

---

ADVANCING QUANTITATIVE  
DNA-MEDIATED SINGLE-MOLECULE  
FLUORESCENCE MICROSCOPY

---

FLORIAN STEHR



München 2021



---

ADVANCING QUANTITATIVE  
DNA-MEDIATED SINGLE-MOLECULE  
FLUORESCENCE MICROSCOPY

---

FLORIAN STEHR

DISSERTATION

*durchgeführt an der*

FAKULTÄT FÜR PHYSIK

*der*

LUDWIG-MAXIMILIANS-UNIVERSITÄT MÜNCHEN

*vorgelegt von*

FLORIAN STEHR

*geb. am 22.04.1989 in Tegernsee*



München, den 24.08.2021

Dissertation eingereicht am: 24.08.2021

Erstgutachter: Prof. Dr. Petra Schwille

Zweitgutachter: Prof. Dr. Ralf Jungmann

Tag der mündlichen Prüfung: 30.11.2021

---

## ZUSAMMENFASSUNG

Die Fluoreszenzmikroskopie ist zu einer der zentralen Untersuchungsmethoden der heutigen Lebenswissenschaften geworden. Den größten Nachteil dieser Methode stellte bisher deren maximal erreichbare räumliche Auflösung dar ( $\approx 250$  nm), die durch die Entwicklung der super-auflösenden (SR) Fluoreszenzmikroskopie und dem dadurch erreichbaren Auflösungsvermögen bis auf die molekulare Ebene überwunden werden konnte. Eine Unterkategorie in der SR-Fluoreszenzmikroskopie stellt die Familie der Einzelmolekül Lokalisierungsmikroskopie (SMLM) dar. Diese erreicht Nanometer-Präzision indem lediglich Subpopulationen der Ziel-Moleküle in der Probe stochastisch angeregt werden, sodass ein statistisches Fit(ing) der "blinkenden" Einzelmolekül-Signale deren Lokalisierung erlaubt. Außerhalb der SMLM wird das Konzept der Lokalisierung auch zum Verfolgen nanoskopischer Bewegungen von Einzelmolekülen genutzt (SPT). Eine quantitative Auswertung von SMLM als auch SPT Experimenten wird dadurch erschwert, dass diese exakte und belastbare Modelle der zugrundeliegenden Einzelmolekül-Photophysik erfordert. Ein SMLM-Verfahren namens DNA-PAINT (Points Accumulation for Imaging in Nanoscale Topography) erreicht das notwendige SMLM-Blinken hingegen, indem es die transiente DNA-Hybridisierung nutzt. DNA-PAINT kann daher weitgehend von der Photophysik der verwendeten Fluorophore entkoppelt werden und bietet somit ein einzigartiges Potential für eine quantitative Interpretation der erhaltenen Daten. In dieser Arbeit konnte herausgearbeitet werden, dass sowohl der photo-induzierte Verlust von Bindesträngen, als auch eine inhomogene Ausleuchtung der Probe, zu Artefakten in der Auswertung von DNA-PAINT Bildrekonstruktionen führen können. Sowohl durch eine Verringerung der verwendeten Anregungs-Intensitäten, als auch durch den Aufbau eines Mikroskops mit "flat-top" Ausleuchtung, konnten hierbei beide Effekte auf ein Minimum reduziert werden. Die Erhöhung der Assoziationsraten der DNA-PAINT Bindungsreaktion erlaubte es schließlich eine Methode zu entwickeln, mit der sowohl die Anzahl der enthaltenen Bindestränge, als auch die lokalen Hybridisierungsraten, in einzelnen Lokalisations-Anhäufungen einer DNA-PAINT Bildrekonstruktion ermittelt werden konnten. Schließlich konnte die DNA-PAINT Bindungsreaktion dazu verwendet werden, um eine 1:1 Molekülmarkierung zu entwickeln, die eine Beobachtung des Fluoreszenzsignals von diffundierenden Einzelmolekülen über mehrere Minuten zuließ. Dies konnte dazu verwendet werden die zugrundeliegenden Diffusionseigenschaften mit hoher Genauigkeit quantitativ zu beschreiben. Zusammenfassend erweitert diese Arbeit die Möglichkeiten einer zuverlässigen, quantitativen Auswertung von Fluoreszenzmikroskopie-Daten auf der Ebene einzelner Moleküle, indem sie das Prinzip eines konstanten Austauschs von Fluorophoren mittels der reversiblen DNA-Hybridisierung nutzt.

---

## ABSTRACT

Fluorescence microscopy has become a standard tool within the life sciences but its major drawback has been its maximum achievable resolution ( $\approx 250$  nm) given by the diffraction limit. The advent of super-resolution (SR) microscopy could overcome this limitation by bringing fluorescence microscopy into the nanoscale, reaching resolutions on the molecular level. The SR methods summarized as Single-Molecule Localization Microscopy (SMLM) circumvent the diffraction limit by acquiring image sequences of stochastically activated subsets of 'blinking' target structures. The subsequent fitting of the recorded fluorescent bursts from individual emitters allows localization of individual fluorophore positions. This concept is similarly applied in Single Particle Tracking (SPT) to monitor the motion of individual biomolecules with nanometer precision. However, a quantitative interpretation of both SMLM and SPT data is often not straightforward since it requires exact modeling of the photo-physics of the used fluorescent labels. The SMLM variant DNA-PAINT (Points Accumulation for Imaging in Nanoscale Topography) achieves the necessary blinking based on the concept of transient DNA hybridization. Hence, DNA-PAINT can in principle be largely decoupled of the photo-physical properties of the fluorophores in use offering a unique potential for quantitative interpretation. In this work, we found that DNA-PAINT still suffers from a photo-induced permanent loss of docking strands and can be prone to remaining photo-physical artifacts caused by inhomogeneous optical excitation. While the first obstacle could be largely reduced by lowering excitation intensities, the latter obstacle could be overcome through the construction of a fluorescence microscope featuring a flat-top illumination profile. Taken together with advancements in the 'speed-up' of the binding reaction, this led to the development of a molecular counting approach able to extract absolute docking strand copy numbers and local hybridization rates of individual DNA-PAINT localization clusters within a single DNA-PAINT image. Finally, the concept of DNA-PAINT was repurposed to generate a live-cell compatible, 1:1 labeling approach for SPT offering observation times in the range of tens of minutes, paving the way for an in-depth quantitative analysis of the underlying motion dynamics. In summary, this thesis extends the possibilities for a robust quantitative interpretation of fluorescence microscopy data at the single-molecule level, by exploiting the concept of DNA-mediated fluorophore exchange.

---

## PUBLICATIONS AND MANUSCRIPTS

### PUBLICATIONS RELATED TO THIS THESIS

**Stehr F\***, Stein J\*, Schueder F, Schwille P, Jungmann R. Flat-top TIRF illumination boosts DNA-PAINT imaging and quantification. *Nature Communications* 2019, 10, 1268

Stein J\*, **Stehr F\***, Schueler P, Blumhardt P, Schueder F, Mücksch J, Jungmann R, Schwille P. Towards absolute molecular numbers in DNA-PAINT. *Nano Letters* 2019, 19, 11, 8182-8190

**Stehr F\***, Stein J\*, Bauer J, Niederauer C, Jungmann R, Ganzinger K, Schwille P. Tracking Single Particles for Hours via continuous DNA-mediated Fluorophore Exchange. *Nature Communications* 2021, 12, 4432

Stein J\*, **Stehr F\***, Jungmann R, Schwille P. Calibration free counting of low molecular copy numbers in single DNA-PAINT localization clusters. *bioRxiv* 2021, doi:10.1101/2021.08.17.456678

### ADDITIONAL PUBLICATIONS AND MANUSCRIPTS

Blumhardt P, Stein J, Mücksch J, **Stehr F**, Bauer J, Jungmann R, Schwille P. Photo-Induced Depletion of Binding Sites in DNA-PAINT Microscopy. *Molecules* 2018, 23, 12, 3165

Wade OK\*, Woehrstein JB\*, Nickels PC\*, Strauss S\*, **Stehr F**, Stein J, Schueder F, Strauss MT, Ganji M, Schnitzbauer J, Grabmeyer H, Yin P, Schwille P, Jungmann R. 124-Color Super-resolution Imaging by Engineering DNA-PAINT Blinking Kinetics. *Nano Letters* 2019, 19, 4, 2641-2646

Schueder F, Stein J, **Stehr F**, Auer A, Sperl B, Strauss MT, Schwille P, Jungmann R. An order of magnitude faster DNA-PAINT imaging by optimized sequence design and buffer conditions. *Nature Methods* 2019, 16, 1101-1104

---

\* These authors contributed equally to this work



# Contents

ZUSAMMENFASSUNG	iii
ABSTRACT	iv
PUBLICATIONS	v
CONTENTS	vii
<b>I Scientific Context</b>	<b>1</b>
1 INTRODUCTION AND OUTLINE	3
1.1 Fluorescence as readout . . . . .	3
1.2 Single-Molecule Localization Microscopy . . . . .	3
1.3 Single Particle Tracking . . . . .	5
1.4 Major obstacle: Fluorophore photo physics . . . . .	6
1.5 DNA-mediated fluorescence microscopy . . . . .	8
1.6 Content of this thesis . . . . .	11
<b>II Peer-Reviewed Research Articles</b>	<b>15</b>
2 HOMOGENEOUS TIRF ILLUMINATION	17
2.1 Motivation and Summary . . . . .	17
2.2 PUBLICATION P1: Flat-top TIRF illumination boosts DNA-PAINT imaging and quantification . . . . .	18
3 LOCALIZATION-BASED FLUORESCENCE CORRELATION SPECTROSCOPY	45
3.1 Motivation and Summary . . . . .	45
3.2 PUBLICATION P2: Toward Absolute Molecular Numbers in DNA-PAINT	46
4 TRACKING SINGLE PARTICLES VIA DNA-MEDIATED FLUOROPHORE EXCHANGE	71
4.1 Motivation and Summary . . . . .	71
4.2 PUBLICATION P3: Tracking Single Particles for Hours via Continuous DNA-mediated Fluorophore Exchange . . . . .	72

---

<b>III</b>	<b>Additional Results and Discussion</b>	<b>107</b>
5	CALIBRATION FREE COUNTING OF LOW MOLECULAR COPY NUMBERS IN SINGLE DNA-PAINT LOCALIZATION CLUSTERS	<b>109</b>
5.1	Motivation and Summary . . . . .	109
5.2	Introduction . . . . .	110
5.3	Methods and Materials . . . . .	111
5.3.1	Brief recap of SMLM & DNA-PAINT binding dynamics . . . . .	111
5.3.2	Counting single molecules in DNA-PAINT localization clusters	112
5.3.3	The analysis approach of lbFCS+ . . . . .	114
5.3.4	Materials and sample preparation . . . . .	115
5.3.5	Imaging . . . . .	116
5.4	Results . . . . .	116
5.4.1	Proof-of-principle demonstration of lbFCS+ on DNA origami .	116
5.4.2	Assessing the working range of lbFCS+ . . . . .	118
5.4.3	Distinction of nanoscopic DNA assemblies via binding dynamics . . . . .	121
5.5	Discussion . . . . .	123
6	SUMMARY AND OUTLOOK	<b>127</b>
<b>IV</b>	<b>Appendix</b>	<b>131</b>
A	APPENDIX TO CHAPTER 5	<b>133</b>
A.1	Supplementary Figures . . . . .	134
A.2	Supplementary Tables . . . . .	140
	LIST OF FIGURES	<b>141</b>
	LIST OF TABLES	<b>143</b>
	LIST OF ABBREVIATIONS	<b>145</b>
	BIBLIOGRAPHY	<b>147</b>
	ACKNOWLEDGEMENTS	<b>155</b>

**Part I**

**Scientific Context**



# 1

## Introduction and Outline

### 1.1 Fluorescence as readout

It is fair to say that the collection of a fluorescence signal has become a standard readout modality of most technical and diagnostic tools within the life sciences [1]. From a vast list of applications it is easy to pick a few prominent examples to underline the use of fluorescence as the ‘workhorse’ of today’s life sciences such as DNA-sequencing [2], optical biosensors for pathogen detection [3], high-throughput pharmaceutical drug screening [4] or fluorescence microscopy [5]. This remarkable success is due to some crucial characteristics of the phenomenon of fluorescence.

First of all, fluorescence is able to provide very sharp contrasts between the measured fluorescent signal and the non-fluorescent background. This is achieved by exploiting the shift in wavelength between the absorbed and re-emitted light of a fluorescent substance, known as Stokes shift [1]. Secondly, a manifold of existing strategies allows researchers to fluorescently label their molecule of interest with very high specificity via classic fluorescent staining or genetic engineering [6]. Further, the recording of a fluorescence signal does neither require expensive equipment [7] nor extreme physical conditions but can instead be carried out under ambient physical conditions (i.e. room temperature and atmospheric pressure) and is as such suited for the observation of living systems [8]. Lastly, the large spectral range of available fluorophores combined with biochemical specificity - i.e. the ability to specifically tag a molecular species of interest - allows to simultaneously record signals from different target molecules paving the way for the study of intramolecular interactions [9, 10].

Despite this, a quantitative interpretation of fluorescence data - especially in the limit of observing the signal from single fluorescent emitters - is usually not straightforward but requires a thorough understanding of the underlying physical principles. Prior knowledge about the photo-physical behavior of the used fluorescent labels, the detector noise statistics and the achievable optical resolution as well as imaging artifacts are usually mandatory [11]. Along this line, the work presented in this thesis is a further attempt to provide a better quantitative understanding for the observation of single molecules using fluorescence microscopy.

### 1.2 Single-Molecule Localization Microscopy

Until recently, the major drawback of fluorescence microscopy was its maximum achievable resolution as given by the Abbe diffraction limit. With a maximum

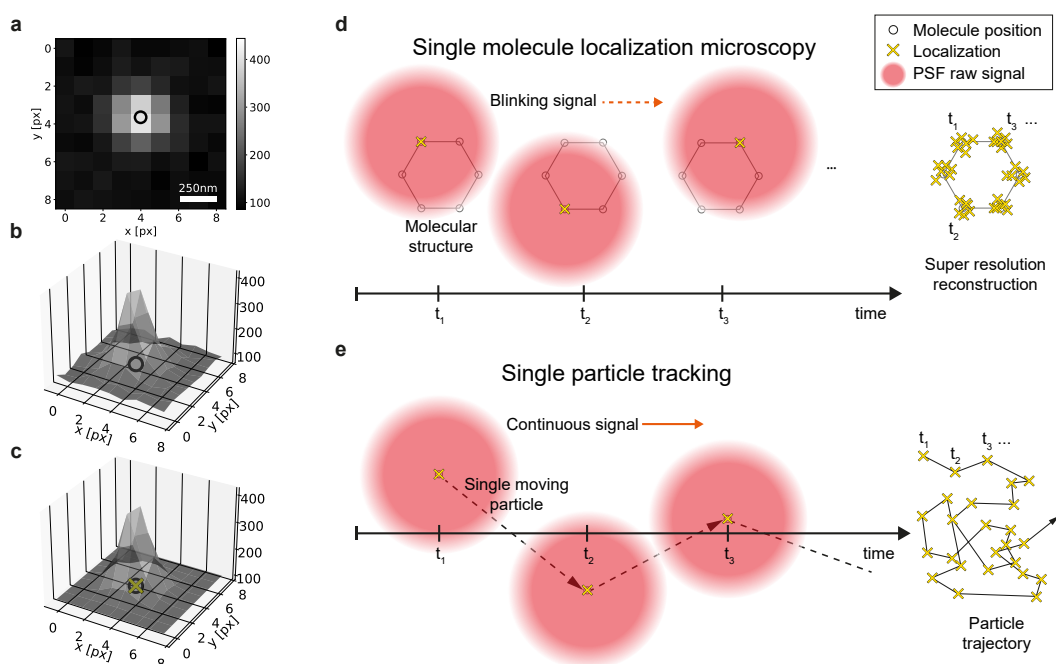


**Figure 1.1. Concept of single molecule localization.** (a) Exemplary raw point-spread function (PSF) originating from the point-like emission of a single fluorescent molecule. The true molecule position is indicated by the black circle. (b) 3D representation of the raw PSF shown in (a). (c) 3D representation of optimum statistical fit of the raw PSF shown in (a-b) using a 2D gaussian model. The center position (localization) obtained from the fit (yellow cross) agrees well with the true molecule position (black circle) enabling sub-diffraction spatial resolution. (d) In SMLM in each frame of the recorded video only a subset of the sub-diffraction sized molecular structure is activated such that each of the active fluorophores PSFs can be optically resolved. After recording and localization of the single molecule blinking events frame by frame the super-resolved molecular structure can be reconstructed. (e) The same principle as in SMLM is applied in SPT to a moving target emitting a continuous fluorescence signal. This finally allows reconstruction of the molecules trajectory with nanometer precision.

obtainable resolution of half the wavelength of light ( $\approx 250$  nm in the visible spectrum) critical length scales within living system (e.g. length of *Escherichia coli*  $\approx 1$   $\mu\text{m}$ ) where not possible to resolve. The advent of super-resolution (SR) microscopy which was honored with the Nobel Prize in Chemistry 2014 circumvented this presumed limitation by bringing optical microscopy down to the nanoscale [12–15].

Especially important for this work are the stochastic approaches to construct super resolved images as applied in Photoactivated Localization Microscopy (PALM) [14], Stochastic Optical Reconstruction Microscopy (STORM) [15] and other variants [16–20]. Since the concepts behind these methods are very similar they are usually combined under the term Single-Molecule Localization Microscopy (SMLM) [21]. There, nanometer resolution can be achieved by determining each molecule’s center of fluorescence emission through a statistical fit of the ideal point-spread function (PSF), usually referred to as ‘localization’ (see Fig.1.1a-c). The core assumption of this approach is, that the recorded PSF is originating from the emission of a *single* fluorophore, since only in this particular case the computationally obtained center of fluorescence emission (localization) agrees with the true position of the molecule [22].

In fact, a similar concept was already applied in 1988 in the field of Single Particle Tracking (SPT) in an attempt to track movements of kinesin along microtubules using Differential Interference Contrast Microscopy (DIC) [23] where already nanometer resolution was demonstrated. The ‘computational trick’ in SMLM only works if just a subset of the fluorophores in the field of view (FOV) are switched on at any point in time, such that each of the active fluorophores is optically resolvable from the rest (see **Fig.1.1d**). In other words, since the diffraction limit does not allow to resolve individual emitters at distances  $\lesssim 250$  nm by optical means, their signal is instead separated in time which is achieved by creating ‘blinking’ fluorescent target molecules [22, 24]. Actually, a more general formulation of this principle says that, if the fluorescent signals form multiple sources within a diffraction-limited volume can be distinguished in any other dimension (e.g. time, wavelength) imaging of the individual emitters becomes possible [25]. Along this line, in SMLM a separation in time is used to ensure that individual fluorescent bursts of *single* emitters are recorded. Finally, after activating different subsets of molecules in each camera frame of the recorded video and subsequent localization, the center positions of all molecules within the FOV can be obtained and a super-resolution (SR) image is reconstructed (see **Fig.1.1d**, right).

In order to obtain a ‘sharp’ final SR image localizations collected from an individual emitter during the image acquisition need to overlap in the final image. Therefore, SMLM is only applied to sufficiently immobile target molecules, meaning that the movement of the individual targets during image acquisition is less than the required resolution. In fact, SR microscopy even requires additional measures to compensate for residual (global) sample or instrument drift caused by temperature changes or mechanical relaxation effects [24, 26, 27]. These residual drifts become especially prominent due to the relatively long measurement times (e.g. tens of minutes) that are usually required in SMLM.

Another important factor to consider for accurate SR reconstruction is a sufficient sampling of the target molecules in the final image (localization density), i.e. how many localizations were collected per target structure during imaging [28, 29]. On the one hand, this is needed to resolve the underlying molecular structure, e.g. visualization of only two corners would not be sufficient to infer about the ring like structure of the example given in **Fig.1.1d**. On the other hand, this is especially important for a robust retrieval of quantitative statements where sufficient statistics are required to adequately map the stochastic nature of the process.

### 1.3 Single Particle Tracking

The concept of single-molecule localization as used in SMLM is similarly applied in the field of Single Particle Tracking (SPT) to capture the movement of single particles with nanometer precision. In order to truthfully reconstruct each molecule’s path, SPT requires a continuous, ideally uninterrupted fluorescence signal for each particle during the observation time (in contrast to the typical SMLM blinking) [30]. If we would take the term ‘Single Particle Tracking’ literally, each position within the trajectory of a *single* moving particle is already ‘separated in time’ (see **Fig.1.1e**) and hence the necessary requirement for truthful localization of the particle position in each camera frame is already given [25]. Unfortunately, the term ‘Single Particle

Tracking' is highly misleading in this regard since SPT usually tries to capture the motion of *more than one* particle within the FOV and hence the term 'multiple particle tracking' would be a better fit. Therefore, in SPT the maximum density of active target molecules within the FOV is ideally limited to levels where the signals from individual emitters in each camera frame can still be resolved optically. Naturally, this requirement can not be completely fulfilled when capturing 'snapshots' of stochastically moving particles. Due to this, one of the highly debated points in the analysis of SPT data is the process of 'particle linking', i.e. the step in which the localizations of the detected particles are connected frame to frame in order to reconstruct each particle's trajectory [31].

To sum this up, while SMLM and SPT are very similar in methodology the main difference between them is that the former asks for structural/spatial information within an immobilized sample while the latter queries for the underlying dynamics behind a moving system. While both methods use the same concept of localization, SMLM requires a *blinking* fluorescence signal while SPT requires a continuous, *uninterrupted* fluorescence signal from each target molecule.

All studies presented in this thesis build on the concept of localization used in both SMLM and SPT and hence provide spatial resolution below the optical diffraction limit. One of the major advantages of this technique is that it provides a true single-molecule signal since it intrinsically relies on the activation of single fluorophores separated in time or space. The localization of individual fluorescent signals originating from single emitters suggests that an inference about the number of fluorophores by analysis of the registered localizations should be feasible [32]. Additionally, the fitting of the single emission events allows to convert the pixel based raw data into a comprehensive list of localizations containing information about the recorded photon levels, noise and shape as well as the temporal information when each fluorescence burst was detected. Hence, the resulting (localized) data in both SMLM and SPT provides a plethora of information about individual, single-molecule emission events. The main objective of the work presented in this thesis was to exploit this underlying information for advanced quantitative analyses.

#### 1.4 Major obstacle: Fluorophore photo physics

As already mentioned in Section 1.1 the complicated photo physics behind fluorophores presents one of the major hurdles for a quantitative treatment of fluorescence data. Whereas in standard fluorescence microscopy the maximum achievable resolution is mainly determined by the quality of the imaging optics in SMLM the brightness of the used fluorophores dictates the maximum achievable resolution for the extracted center positions, commonly referred to as localization precision [33]. Generally, it is required to lift the fluorescence signal above the omnipresent noise level given by both detector readout noise and background fluorescence for a robust extraction of the fitting observables at high signal-to-noise ratio (SNR). Therefore, in SMLM it is always experimentally desirable to harvest as many photons as possible from a single fluorophore within the observation time (e.g. the camera frame exposure time). On the other hand, fluorophores cannot undergo unlimited excitation/emission cycles but will at one point enter a permanent dark state given by the fluorophores specific photon budget. This phenomenon is usually referred to as 'photobleaching' [34]

and represents one of the major constraints in SMLM. As such, conventional SMLM methods using permanently attached dyes such as PALM/STORM are inherently limited by a single fluorophore's photon budget. Explicitly, given a fixed photon budget an experimentalist has to choose between either collecting fewer localizations with better SNR/spatial resolution or more localizations with lower SNR/spatial resolution. A difficult decision, since both localization precision *and* localization density ultimately determine the achievable accuracy of the SR image (see Section 1.2). The fact that each fluorophore contributes a certain number of localizations to the image provides a digital approach for molecular counting (see Section 1.2). Therefore, there have been various attempts to count targeted molecules based on the recorded localizations [32, 35–49]. Practically however, molecular counting turned out to be more difficult than expected due to various reasons. In PALM the required single molecule blinking is achieved by light-induced stochastic photoactivation and subsequent photobleaching (i.e. deactivation) of the fluorophores [14, 16], whereas STORM exploits light-induced photoswitching of the fluorophores between a fluorescent bright state (activation) and a non-fluorescent dark state (deactivation) [15, 18]. Hence, a quantitative understanding in both approaches requires exact knowledge about the photo physical behavior of the used fluorophores and can thus be hampered by many unknowns of the system in use. First, exact modeling of the photobleaching behavior is required which is usually not a simple one-step process [34]. In addition, the unwanted intrinsic blinking of fluorophores in PALM [35, 37] as well as extended blinking after deactivation of fluorophores in STORM [43] leads to overcounting. As a further challenge, photo quenching (e.g. the shortening of the fluorescence life time) induced by fluorophores in close proximity has to be taken into account [48] and the sensitivity of the used label with respect to local changes in pH or ionic strength in its micro environment [42].

In a similar way, photo physical artifacts such as photobleaching and/or blinking represent crucial obstacles in the field of SPT [30]. Again, since the number of collected photons is the decisive parameter for a high localization precision usually bright labels and/or high laser excitation powers are employed, quickly consuming the fixed photon budget of the fluorophore in use. For this reason, commonly used fluorescent labels like organic dyes or fluorescent proteins can only be tracked for a few seconds before they photobleach. The use of quantum dots as fluorescent tags can overcome this limitation allowing observation times in the range of minutes [50]. Unfortunately, quantum dots suffer from heavy photoblinking on various time scales [51, 52] impairing the recording of uninterrupted single particle trajectories over prolonged periods. Both the localization precision and the observed trajectory durations have to be known and taken into account since they can bias the interpretation of the results [53, 54]. Especially short trajectory durations violate the often implicitly applied ergodicity assumption [55], i.e. that the time average of a single particle converges to the average of the ensemble for sufficiently long observation times, potentially leading to erroneous results.

In conclusion, the delicate photo physics of fluorophores represents one of the major obstacles for a quantitative interpretation of both SMLM and SPT experiments. Since many years have passed with inspired researchers dedicating their efforts into deepening our understanding of the mechanisms in process it would be very daring to find a better solution following the same footsteps. Instead this work tries to 'bypass'

the task by reducing the potential influence of photo physical artifact to a minimum through the use of DNA-mediated fluorophore exchange that will be discussed in the next section.

### 1.5 DNA-mediated fluorescence microscopy

A promising approach to decouple the SMLM fluorescence readout from the photo physics of the fluorophore in use is called Points Accumulation for Imaging in Nanoscale Topography (PAINT) [17]. Instead of using a permanent fluorescent label attached to the molecule of interest PAINT uses freely diffusing dyes [17] or fluorescently labeled ligands [56] in solution as fluorescent probes to target the molecules of interest by permanent or transient binding. Whereas in PALM/STORM activation of the target molecule's fluorescence is achieved by photo activation/photo switching in PAINT the detection of a fluorescence burst results only due to the immobilization of the fluorescent probes upon binding to the target molecule. Deactivation of the fluorescence signal however is still achieved by photobleaching of the fluorescent probe. Hence, although activation of the signal in PAINT does not exploit any photo physical property of the used fluorophore it still uses photobleaching for deactivation. This method is therefore still not completely decoupled from the photo physical properties of the used fluorophore. Anyway, it already alleviates the demands on the choice of the fluorescent label since it does not require any photoactivable nor photoswitchable dyes as required for PALM or STORM. In addition, it can be implemented on elementary fluorescence microscopes since a synchronization of different laser lines for activation/deactivation is not necessary. However, the overall simplification in PAINT comes at the cost of introducing a larger fluorescent background due to the usually non-fluorogenic imaging solution restricting these methods to a confined illumination scheme such as Total Internal Reflection Fluorescence (TIRF) [57], Highly Inclined and Laminated Optical Sheet (HILO) [58], Spinning Disc Confocal Microscopy (SDCM) [59, 60] or Selective Plane Illumination Microscopy (SPIM) [61, 62].

The combination of DNA nanotechnology and PAINT resulted in another SMLM derivative called DNA-PAINT [19, 20]. While PAINT suffered from difficulties in establishing a protocol to specifically address a larger variety of molecules DNA-PAINT circumvents this problem by exploiting the specificity and programmability of DNA. The principle of DNA-mediated fluorophore exchange in DNA-PAINT is explained in detail in Fig.1.2. In short, the required SMLM blinking is generated by exploiting the reversible binding of short fluorescently labeled DNA oligonucleotides in solution (imagers) to the target molecule labeled with short DNA oligonucleotides of complementary sequence (docking strand). Therefore, ideally activation/deactivation of the fluorescence signal is only controlled by the association rate  $k_{on}$  and the dissociation rate  $k_{off}$  of the imager/docking strand DNA-hybridization reaction. Explicitly, the association rate  $k_{on}$  determines the average binding frequency at a given imager concentration, i.e. for how long a single docking strand will be in an OFF-state. Vice versa, the dissociation rate  $k_{off}$  determines for how long a single docking strand will remain in an ON-state after activation (i.e. upon imager binding). As such,  $k_{off}$  is the direct measure of the stability of the formed DNA duplex and therefore sets the average dwell time of imagers bound to the docking strands.

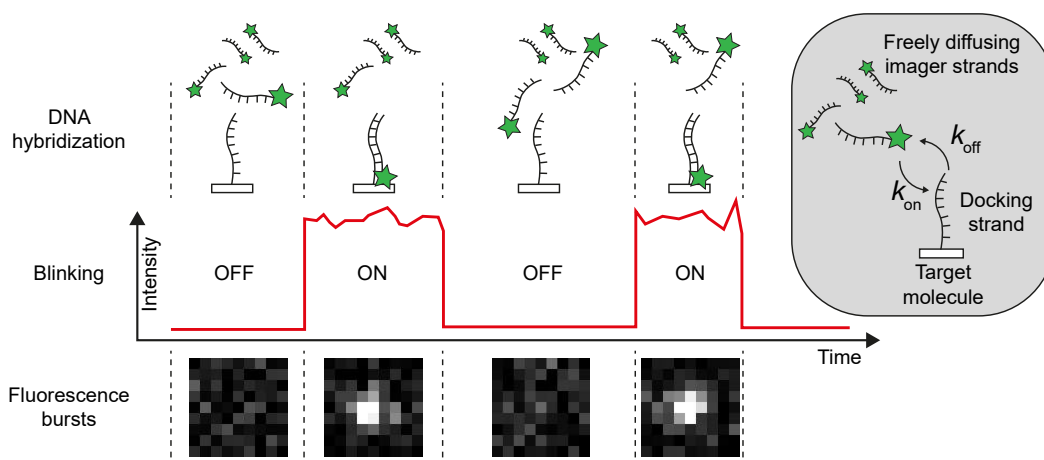


**Figure 1.2. DNA-mediated fluorophore exchange in DNA-PAINT.** In DNA-PAINT short fluorescently labeled single stranded DNA oligonucleotides are used as freely diffusing fluorescent probes, the so called imagers. Vice versa, the target molecule is labeled with a single stranded DNA oligonucleotide of complementary sequence, the so called docking strand. The sequence of the imager is designed in such a way that it does not promote permanent binding but instead only transiently binds to the docking strand. Upon immobilization of the imager at the docking strand enough photons can be collected within the duration of a single camera frame such that the resulting fluorescent spot can be easily distinguished from the fast moving fluorescent background. Hence, in DNA-PAINT the required SMLM blinking is achieved through the reversible imager/docking strand binding reaction characterized by the association rate  $k_{on}$  and dissociation rate  $k_{off}$ .

By choice of the imager sequence, temperature and buffer salinity dwell times in DNA-PAINT are widely tunable ranging from tens of milliseconds up to tens of seconds such that photobleaching of the imager strands before dissociation from the docking strand can be excluded by proper choice of the experimental conditions. In addition, the imaging solution acts as an ‘infinite’ reservoir to provide the target molecules with ‘fresh’ fluorophores upon binding. This allows to harvest the full photon budget of each imager strand within its binding duration. As such, DNA-PAINT can be optimized to reach true molecular spatial resolution with reported localization precisions down to  $\sim 1$  nm [63]. Further, in DNA-PAINT fluorophores do not have to have to comply with any intrinsic prerequisites and hence the full spectrum of available dyes can be used. Finally, in contrast to fixed dye labeling fluorophores in DNA-PAINT arrive ‘just in time’ at the target molecule. Therefore the method is less prone to artifacts effects like self-quenching arising due the close proximity of neighboring dyes in dense molecular clusters.

In conclusion, due its usage of DNA-mediated fluorophore exchange DNA-PAINT is to our knowledge the only SMLM technique that can in principle be fully decoupled from the photo physical properties of the fluorophore in use. Among the different SMLM variants it is therefore probably the most promising candidate for a quantitative analysis since the imager strand/docking strand kinetics can be well characterized [19, 64]. In fact, in qPAINT it was already demonstrated that by calibration of the imager influx on a single docking site counting of target molecule copy numbers in unknown

regions was possible [65]. This was achieved by using the fact that under constant influx the imager binding frequency scales linearly with the number of docking strands contained in nanoscopic volume at a given position.

In addition, the highly programmable and well predictable DNA based target-probe concept might be used beyond the core application of SMLM to achieve super resolved images. For example, in Exchange-PAINT orthogonal imager sequences carrying the same dye were used in sequential imaging rounds to image nine distinct target molecules [66, 67]. Redesign of the docking strands/imager strands allowed researchers to circumvent DNA-PAINT's main limitation of being purely restricted to confined illumination schemes. This was realized by generation of Förster Resonance Energy Transfer (FRET) pairs at the docking strand [68, 69] or the design of self quenching imager strands [70]. The thus generated fluorogenic probes (i.e. only fully fluorescent upon binding to the target) allowed to perform DNA-PAINT even under wide field illumination schemes. Another beautiful example for the creation of 'smart' interrogation probes using a DNA based probe-target system is called Proximity-PAINT [71]. By using a split-docking strand Proximity-PAINT returns essentially a binary output for spatial proximity on molecular interaction scales. A recent development called LIVE-PAINT [72] or Peptide-PAINT [73] transfers the advantages of reversible fluorophore exchange to another set of tunable molecules even enabling its application in living cells. Interestingly, possible advantages of the application of PAINT in the field of SPT were already highlighted in its earliest implementations [56] as well as in later publications [74].

Besides achieving high localization precisions in DNA-PAINT images, the listed works give good evidence that the principle of DNA-mediated fluorophore exchange offers unique features. One of the main advantages of DNA-PAINT compared to other SMLM methods is, that it decouples the fluorescence readout from the complicated photo physics of fluorophores. Instead, a quantitative interpretation of DNA-PAINT data requires exact knowledge about the underlying binding dynamics, which is well-understood and as such poses a more feasible challenge [24]. In fact, the investigation about the truthfulness of this statement was one of the main drivers of this work. Second, the programmability and predictability of the DNA-interaction opens the door for the design of 'smart' labels, which are able to perform simple interrogations (e.g. proximity) on the nanoscale [68–71]. Combined with the first statement this led to the incentive for the development of a SPT labeling approach based on DNA-mediated fluorophore exchange.

## 1.6 Content of this thesis

The starting point for this work can be formulated in three basic questions that served as the guideline for this thesis:

1. *Under which experimental constraints is DNA-PAINT truly decoupled from photo-physical artifacts?*
2. *Is the underlying DNA-hybridization predictable enough to be used for a robust quantitative analysis of DNA-PAINT data?*
3. *Based on DNA-mediated fluorophore exchange, is it possible to create a single molecule label emitting a continuous, ideally uninterrupted, fluorescence signal for prolonged observation times in SPT?*

Two studies initiated a closer look into **Question 1**. In a first study, we used the programmability of the DNA-PAINT binding reaction to create and distinguish unique ‘blinking’ bar-codes [75]. Hence, the motivation of this work was to extend the limits encountered when using imaging approaches based on pure spectral multiplexing. Therefore, the aim was to identify clusters by combinations of the measured fluorescent ON-times (influenced by  $k_{off}$ ) and binding frequencies (influenced by the number of molecules within a cluster and  $k_{on}$ ). The number of unique ‘kinetic’ bar-codes was hereby additionally multiplied by the image acquisition in up to three different color channels (e.g. by using spectrally distinct imagers of same sequence). Naturally, a robust distinction based on the dissociation rate  $k_{off}$  of the binding reaction required to prevent the photobleaching of imagers while residing at the docking strand. Hence, for this study DNA-PAINT images were acquired at lower excitation intensities than usually employed for achieving maximum localization precisions. Since this necessity came with the advantage of a more straightforward quantitative interpretation of the data it marked the beginning of a closer look into how residual photo physical artifacts influence DNA-PAINT.

This was continued in a second study where we could identify the loss of DNA-PAINT docking strands with increasing measurement time [76]. Although residual photobleaching was kept at a minimum we could still clearly observe an irreversible photo induced loss of docking strands over time. Control experiments using oxygen scavenging buffers indicated a permanent damage of the (DNA) docking strands by dye-induced generation of reactive oxygen species.

These two initial studies led to the development and construction of a custom TIRF microscope providing homogeneous illumination throughout the entire FOV which constitutes the first major chapter of this dissertation [77] (see Chapter 2). By introducing a refractive beam shaping device into the excitation path of the microscope the standard Gaussian illumination profile could be converted into a homogeneous flat-top illumination profile. We demonstrated that this resulted in an improved quantitative interpretation of the thus acquired DNA-PAINT data since the remaining artifacts caused by inhomogeneous illumination could be efficiently removed already at the stage of image acquisition without the necessity of complicated post-processing methods.

In our second main publication (see Chapter 3) we searched for an answer to the problem stated in **Question 2**. Building on a previous method to measure hybridization

kinetics termed surface-integrated Fluorescence Correlation Spectroscopy (FCS) [64] and extending its concept to SMLM we developed a method termed localization-based Fluorescence Correlation Spectroscopy (lbFCS). We demonstrated that lbFCS is able to determine the *absolute* number of docking strands contained in DNA-PAINT localization clusters as well as the underlying average hybridization rates (i.e. association rate  $k_{on}$  and dissociation rate  $k_{off}$ ) [78]. This was possible by autocorrelation analysis of the blinking dynamics combined with a three point titration of the imager concentration. As such, it is to our knowledge the first SMLM molecular counting approach that can provide absolute molecular numbers without 1) using any prior knowledge about the blinking dynamics or 2) the need for a calibration to an assumed number of molecules contained in isolated reference localization clusters. Coming back to the stated guideline, this work could give a positive answer to the hypothesis stated in **Question 2**.

While the study in Chapter 3 already included a thorough characterization of the experimental conditions influencing the DNA-PAINT binding dynamics (temperature, ion concentration) we were able to ‘speed-up’ the DNA-PAINT binding reaction demonstrating an increase of the association rate  $k_{on}$  by more than one order of magnitude [79]. This was achieved by 1) usage of a two letter alphabet in the docking/imager strand sequence in order to avoid self-interactions inspired by a previous study [80] and 2) optimization of the buffer conditions. A following study [81] could show that a repetitive concatenated sequence design consisting of short triplets (e.g CTC) could even further increase the association rate  $k_{on}$ . These developments finally brought the idea stated in **Question 3** into reach.

Hence, in our third main publication (see Chapter 4) we were able to develop a single molecule labeling approach for SPT by exploiting the idea of DNA-mediated fluorophore exchange [82]. There, we could show that our DNA based labeling design - referred to as tracking handle (TH) - allowed uninterrupted tracking of single molecules for tens of minutes in live-cell compatible conditions. We gave proof to this in a comparative study by observing both single dye labeled and TH labeled DNA origami both immobilized on glass and moving on a supported lipid bilayer (SLB). Additionally, we could clearly show that the prolonged observation times and improved statistics gained by the TH are crucial for quantitatively assessing questions about the underlying diffusion dynamics (e.g. diffusion mode or the detection of rare motion events).

In our final, yet unpublished work we returned to **Question 2** (see Chapter 5). Our first counting approach lbFCS [78] presented in Chapter 3 was already able to extract absolute molecular numbers without the need for a separate calibration to an assumed number of molecules. But it still lacked some desired features for a straightforward application to unknown targets. First, it required a ‘self-calibration’ step consisting of a minimum of two measurements of the same sample at different imager concentrations. Second, the self-calibration yielded only the *average* hybridization rates ( $k_{off}$ ,  $k_{on}$ ) neglecting possible existing heterogeneities within the ensemble. Third, the self-calibration required exact adjustment of the imager concentration ratios since those were assumed as a priori knowledge. Lastly, the imager sequence used for lbFCS still had a low association rate  $k_{on}$  compared to the ‘speed’ sequences used in later works [79, 81, 82]. Hence, the self-calibration had to be performed at relatively high imager concentrations  $\sim 5 - 20$  nM at levels where unspecific binding of imagers

and low SNR especially in cellular contexts turned out to be problematic. In Chapter 5 we hence present a revised framework lbFCS+ that overcomes the mentioned drawbacks. lbFCS+ yields *absolute* molecular numbers and local hybridization rates of *individual* DNA-PAINT localization clusters requiring only a *single* measurement. In proof of principle experiments on DNA origami we demonstrated that it is able to extract absolute molecular copy numbers in less than 30 min of measurement time at low imager concentrations  $\leq 5$  nM. Our assessment of the working range indicated that lbFCS+ is suited for an application to localization clusters containing up to six docking strands. Further, the high accuracy of lbFCS+ to determine hybridization rates allowed to measure small differences in imager binding dynamics to docking strands of same sequence but placed at different positions of nanoscopic DNA assemblies. Finally, this enabled us to resolve heterogeneous binding dynamics between individual DNA-PAINT clusters allowing for the distinction of stochastically generated and a priori indistinguishable DNA assemblies.

Throughout this thesis, the pronoun ‘we’ includes this author and all contributors to each project, acknowledging the collaborative nature of this field of research. Individual contributions of this author are highlighted for the peer-reviewed journal articles in Part II.



## **Part II**

# **Peer-Reviewed Research Articles**



# 2

## Homogeneous TIRF Illumination

### 2.1 Motivation and Summary

TIRF microscopy offers selective illumination of very thin volumes close to the surface of the sample substrate ( $\leq 200$  nm). It is thus the preferred imaging modality in the case of specimens that are located close to the coverslip surface and require a high rejection of the background fluorescence. Due to this, TIRF microscopy is commonly used for DNA-PAINT imaging since it can efficiently remove the unwanted fluorescent background originating from freely diffusing imagers in solution leading to localization precisions on the order of a few nanometers. However, standard TIRF microscopes only feature an inhomogeneous (Gaussian) lateral excitation profile leading to imaging and quantification artifacts that potentially bias the experimental outcome. In this study, we aimed to quantify artifacts in DNA-PAINT images generated by the image-acquisition with an inhomogeneous TIR illumination. Therefore, we constructed a custom TIRF microscope that could be easily switched between a standard Gaussian excitation profile and a homogeneous 'flat-top' excitation profile using a commercially available refractive beam-shaping device. By using a segment-wise analysis we could clearly demonstrate that an inhomogeneous excitation leads to 1) a non-uniform localization detection efficiency, 2) non-uniform fluorescent ON-times and 3) non-uniform localization precisions throughout the FOV. In addition, we showed that all of these artifacts can already be avoided at the stage of data-acquisition through the simple implementation of a flat-top illumination profile. Finally, we found that homogeneous TIR excitation even allowed to robustly exclude multi-emitter localizations by straight-forward thresholding according to the detected photon levels. This largely improved image quality without sophisticated image post-processing. We hence believe that flat-top TIRF microscopy can not only facilitate a quantitative interpretation of DNA-PAINT data but is actually a useful and easy-to-implement 'upgrade' for any study aiming for a quantitative assessment of fluorescence microscopy images.

2.2 PUBLICATION P1: Flat-top TIRF illumination boosts DNA-PAINT imaging and quantification

# Flat-top TIRF illumination boosts DNA-PAINT imaging and quantification

Florian Stehr, Johannes Stein, Florian Schueder  
Petra Schwille and Ralf Jungmann

*Author contributions:*

**F.St.** and J.S. contributed equally. **F.St.** and J.S. built the microscope, designed and performed experiments, analyzed data, and wrote the manuscript. F.Sc. designed DNA origami structures, performed cell experiments and wrote the manuscript. **F.St.**, J.S., F.Sc., and R.J. conceived of the study. R.J. supervised the study, interpreted data, and wrote the manuscript P.S. supervised the study and wrote the manuscript. **All authors** reviewed and approved the manuscript.

*published in*

Nature Communications 2019, 10, 1268

*Reprinted from [77] under the [CC BY-NC 4.0 license](#).*



## ARTICLE

<https://doi.org/10.1038/s41467-019-09064-6>

OPEN

# Flat-top TIRF illumination boosts DNA-PAINT imaging and quantification

Florian Stehr <sup>1</sup>, Johannes Stein <sup>1</sup>, Florian Schueder <sup>1,2</sup>, Petra Schwille <sup>1</sup> & Ralf Jungmann <sup>1,2</sup>

Super-resolution (SR) techniques have extended the optical resolution down to a few nanometers. However, quantitative treatment of SR data remains challenging due to its complex dependence on a manifold of experimental parameters. Among the different SR variants, DNA-PAINT is relatively straightforward to implement, since it achieves the necessary 'blinking' without the use of rather complex optical or chemical activation schemes. However, it still suffers from image and quantification artifacts caused by inhomogeneous optical excitation. Here we demonstrate that several experimental challenges can be alleviated by introducing a segment-wise analysis approach and ultimately overcome by implementing a flat-top illumination profile for TIRF microscopy using a commercially-available beam-shaping device. The improvements with regards to homogeneous spatial resolution and precise kinetic information over the whole field-of-view were quantitatively assayed using DNA origami and cell samples. Our findings open the door to high-throughput DNA-PAINT studies with thus far unprecedented accuracy for quantitative data interpretation.

<sup>1</sup>Max Planck Institute of Biochemistry, 82152 Martinsried, Munich, Germany. <sup>2</sup>Faculty of Physics and Center for Nanoscience, Ludwig Maximilian University, 80539 Munich, Germany. These authors contributed equally: Florian Stehr, Johannes Stein. Correspondence and requests for materials should be addressed to P.S. (email: [schwille@biochem.mpg.de](mailto:schwille@biochem.mpg.de)) or to R.J. (email: [jungmann@biochem.mpg.de](mailto:jungmann@biochem.mpg.de))

The advent of super-resolution microscopy has revolutionized life science research by providing access to molecular structures with light microscopy, which were previously hidden below the diffraction limit. One of the major branches in the field is referred to as single molecule localization microscopy (SMLM) and includes methods such as photo-activated localization microscopy<sup>1</sup> (PALM), Stochastic optical reconstruction microscopy<sup>2</sup> (STORM), point accumulation in nanoscale topology<sup>3</sup> (PAINT), and their descendants<sup>4</sup>. In STORM and PALM, the blinking required for super-resolution reconstruction is obtained by complex photo-physical switching and activation of target-bound fluorophores. In contrast, PAINT imaging is based on reversible binding of a fluorescent species to the target structure. DNA-PAINT<sup>5</sup> exploits the specificity of DNA by using single-stranded oligonucleotides as labels (“docking strands”) to which fluorescently-labeled complementary “imager” strands bind. Due to the non-fluorogenic nature of imagers (i.e., dye-labeled imager strands do fluoresce if not bound to their respective target strands), DNA-PAINT experiments are typically performed using some sort of selective plane illumination and/or detection, such as total internal reflection fluorescence (TIRF) microscopy<sup>6</sup>, oblique illumination<sup>7</sup>, or spinning disk confocal microscopy<sup>8</sup>. Besides offering spectrally-unlimited multiplexing capabilities (Exchange-PAINT)<sup>9</sup> and quantitative imaging (qPAINT)<sup>10</sup>, DNA-PAINT can achieve spatial resolutions down to ~5 nm using standard TIRF microscopy<sup>5</sup>. As it is the case for all SMLM methods, reconstructed images have to be carefully interpreted, as they can be prone to artifacts arising e.g., from inhomogeneous illumination caused by the Gaussian laser profile<sup>11,12</sup>. This becomes especially important if localization datasets are used to extract quantitative information such as blinking kinetics, absolute molecule numbers, and other parameters beyond “just” binning of localizations to render qualitative images. Furthermore, inhomogeneous illumination can lead to spot-detection and fitting artifacts, ultimately resulting in a non-truthful reconstruction of the image data. One prominent example are false localizations originating from multiple active single emitters in a diffraction-limited area. A manifold of rather sophisticated methods and algorithms have been developed to deal with these multi-emitter localizations in SMLM data<sup>13–17</sup>. However, they are often not straightforward to implement or computationally intense. Approaches for obtaining homogeneous illumination throughout the field-of-view should make it possible to use rather simple global thresholding algorithms to efficiently filter out these mislocalizations and omit them from downstream analysis.

While different solutions for uniform laser excitation have been proposed and applied to SMLM<sup>18–20</sup>, these approaches negatively affect TIRF microscopy, due to their inherent reduction of spatial coherence<sup>18,19</sup>. Although coherent transformation of a Gaussian laser beam into a flat-top intensity profile by means of refractive beam-shaping has been pioneered decades ago<sup>21,22</sup>, only very recently flat-top TIR illumination has been reported with the help of refractive beam-shaping elements, promising clear advantages regarding the interpretation of single molecule experiments<sup>23</sup> and their potential application to SMLM<sup>24</sup>.

In this study, we identify imaging and quantification artifacts introduced by inhomogeneous sample illumination in DNA-PAINT. To achieve this, we present a novel processing metric based on analyzing radial image segments that allows us to quantitatively assess these artifacts and—at least to some extent—overcome the limitation of inhomogeneous sample illumination without the need for sophisticated post-processing of the data. In order to improve on that and to reduce the amount of post-processing necessary to achieve truthful representation of the data, we employ flat-top TIR illumination for DNA-PAINT

microscopy and demonstrate an increased homogeneity of almost all experimental observables when compared to standard Gaussian illumination. This has several implications: first, we achieved the same spot detection efficiency throughout the whole FOV (important for truthful SMLM reconstruction), thus eliminating the necessity for advanced spot finding algorithms, which take non-uniform illumination into account. Second, the uniformity of the excitation field allowed us to obtain accurate and precise binding time distributions for DNA-PAINT, independent of the position in the FOV. We used this predictability to demonstrate improved kinetic analysis of binding durations over the whole FOV. Third, we achieved uniform localization precision allowing spatial resolution better than 10 nm. Lastly, we find that homogeneous TIR excitation enables us to robustly identify multi-emitter localizations simply according to the number of photons detected. By exploiting the advantage of DNA-PAINT that sufficient sampling of the target structure is provided due to reversible binding of new imagers, we can afford to exclude all of these multi-emitter localizations detected by straightforward thresholding and thereby largely improve image quality for artifact-free quantitative statements without sophisticated image post-processing. Combining all advantages, we performed cellular DNA-PAINT imaging of the microtubule network in fixed cells and achieved a significant reduction of artifacts in the periphery compared to Gaussian illumination while preserving the image quality in terms of spatial resolution.

## Results

**Robust spot detection and homogeneous blinking.** To achieve flat-top illumination, we employed a refractive beam-shaping element called piShaper (AdlOptica GmbH, Berlin, Germany), which we placed in the excitation path of a custom-built TIRF microscope (a setup sketch can be found in Supplementary Figure 1). While transforming the profile of the excitation laser, refractive beam-shaping does preserve spatial coherence<sup>23</sup>, which still enables efficient TIRF microscopy in contrast to previously reported flat-field super-resolution studies<sup>18,19</sup>. In order to quantitatively analyze the flat-top TIRF profile, we recorded a sequence of fluorescence images of a sample containing a high surface density of immobilized DNA origami structures, to which freely diffusing imager strands could bind. Figure 1a shows full-chip TIRF images obtained by averaging all acquisition frames for the Gaussian and flat-top profiles (left and right panel, respectively). Exemplary line profiles (Fig. 1b) show the fluorescence intensity variation along the specified axis for Gaussian (upper panel) and flat-top illumination (lower panel), yielding an intensity decrease by nearly a factor of three for Gaussian illumination vs. stable intensity for flat-top illumination.

In DNA-PAINT, blinking is achieved by the transient binding of short fluorescently-labeled DNA oligonucleotide “imager strands” to a DNA “docking” strand which is attached to the target of interest (Fig. 2a). The duration of blinking events is defined as bright time. We designed rectangular DNA origami nanostructures with a 20-nm-spaced pattern of 3 × 4 docking strands (“20-nm-grids”, Fig. 2b) in order to quantitatively characterize the effect of inhomogeneous illumination on DNA-PAINT imaging. Super-resolution images of 20-nm-grids were acquired either using Gaussian or flat-top illumination and subsequently segmented into concentric rings such that each segment contained a similar number of structures (~800 per segment) for subsequent analysis (Fig. 2c).

First, we examined the detection efficiency of our spot finding and single-molecule fitting algorithm during SR reconstruction for a given threshold in the computed net gradient between adjacent pixels in the raw images<sup>5</sup>. Figure 2d compares exemplary

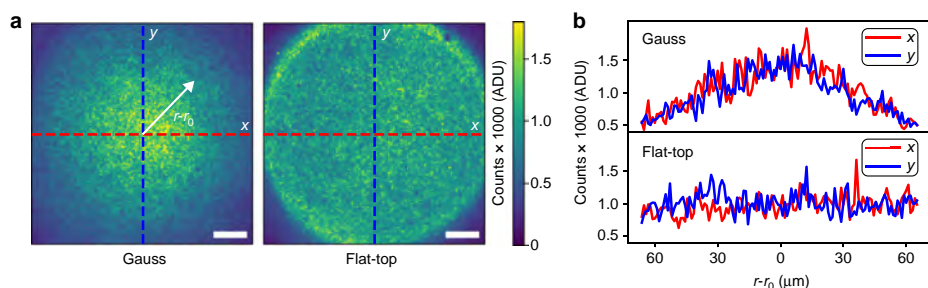


**Fig. 1** Gauss vs. flat-top illumination profiles. **a** Traditional illumination profile for TIRF microscopy with a Gaussian laser beam (left) compared to a flat-top profile created by a refractive beam-shaping device in the excitation path (right). **b** Line plots of fluorescence intensity along x and y axes (red and blue, respectively) for both profiles in **a**. Scale bars, 20  $\mu\text{m}$  in **a**

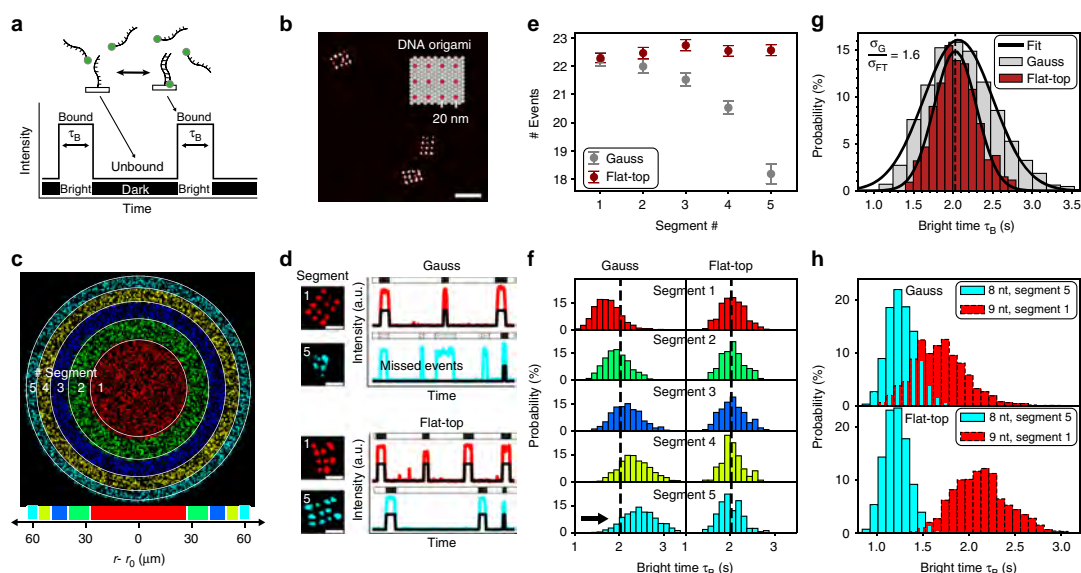


**Fig. 2** Flat-top illumination improves single-molecule detection and enables precise binding time quantification. **a** Schematic of DNA-PAINT: dye-labeled imager strands reversibly bind to complementary docking sites that are attached to the target of interest. Binding events result in apparent target blinking required for single molecule localization microscopy (SMLM). **b** DNA-PAINT image of rectangular DNA origami designed to display a 20-nm-grid pattern of docking strands (inset displaying origami design). **c** Whole-sCMOS-chip field of view (FOV) of several thousand DNA origami. Images acquired with Gaussian and flat-top illumination are both segmented into concentric rings containing equal numbers of origami (~800 origami per segment) for downstream quantification. **d** Exemplary DNA origami and intensity traces from inner and outer segment (red and cyan, respectively) showing that binding events in the outer segment are missed by the spot detection algorithm for Gaussian illumination. **e** The effect illustrated in **d** leads to a decrease in the mean number of binding events per origami with radial distance for the Gaussian profile. Flat-top illumination allows robust spot detection over the whole FOV. **f** Inhomogeneous photobleaching of imager strands increases the mean bright time with radial distance for Gaussian illumination. **g** The effect observed in **f** leads to an overall broadening of the bright time distribution over the whole FOV. **h** Distinction of docking strands of different length via bright times. Position-dependent bright times for Gaussian illumination lead to non-separable populations. Scale bars, 20 nm in **b** and 40 nm in **d**. Error bars in **e** correspond to SEM

intensity traces from 20-nm-grids in segments 1 and 5, highlighting that for Gaussian illumination blinking events in the outer segments were not detected anymore, resulting in poor sampling of the DNA origami image. This is due to the fact that the inhomogeneous profile of Gaussian illumination leads to a systematic decrease of the net gradient in DNA-PAINT raw

images with increasing radial distance from the center (Supplementary Figure 2). The same effect was visible when comparing the average number of apparent binding events per 20-nm-grid between the segments (Fig. 2e). However, images acquired with flat-top illumination showed a constant net gradient resulting in a homogeneous spot detection efficiency (Fig. 2d and

Supplementary Figure 2) and ultimately in a constant number of binding events (Fig. 2e).

Next, we investigated the illumination effects on the bright times of imager binding events using our 20-nm-grids. As the localization precision in SMLM increases with the number of detected photons per acquisition frame<sup>25,26</sup>, it is generally advisable to adapt camera integration times, dye switching duty cycles, and photon emission rates to obtain optimal localization precision. While the finite photon budget of fixed dyes in approaches like STORM or PALM sets a practical limit to the number of photons per switching cycle<sup>27</sup>, PAINT-based approaches have the advantage that every blinking event originates from a “fresh” dye, thus the full photon budget of this dye can be harvested for superior localization precision. However, this comes at the cost of potentially bleaching a certain fraction of imager strands before they have dissociated from their targets. In order to enable precise adjustment of binding and bleaching times for e.g., qPAINT quantification, this bleaching probability should be constant over the FOV. For a Gaussian illumination profile, we observed that imager strands (9 nucleotides in length) binding to the center of the field of view photobleach faster than in the outer segments, as one would expect (Fig. 2f). In contrast, images acquired with flat-top illumination exhibited homogeneous bright times for the same imager species throughout the FOV. The radial bright time dependence for Gaussian illumination resulted in a broadening of the total bright time distribution over the FOV by a factor of  $\sigma_C/\sigma_{FT} = 1.6$  compared to flat-top illumination (Fig. 2g). Inhomogeneous bleaching conditions have direct implications for quantitative statements based on the blinking kinetics from DNA-PAINT images. Figure 2h shows that for DNA-PAINT images of 20-nm-grids with either shorter-binding 8 nucleotide-long (nt) or longer-binding 9-nt-long docking strands acquired with the same imager under identical conditions, it was not possible to distinguish between the two bright time populations comparing segments 1 and 5 for Gaussian illumination (but it still allows for differentiation within each segment, see Supplementary Figure 3a). However, flat-top illumination allowed us to clearly separate bright time distributions over the full FOV. Analogously to Fig. 2g the total bright time distributions for both 8-nt and 9-nt 20-nm-grids are narrower for flat-top illumination (Supplementary Figure 3b). Enhanced control over the bleaching behavior allowed us to both resolve single 20-nm-grid structures (see Supplementary Figure 4) and simultaneously distinguish between short and long binding duration with high fidelity.

**Uniform localization precision and mislocalization filtering.** In order to obtain a measure of how precise a single DNA-PAINT docking strand could be localized, we used a previously developed “averaging” tool in Picasso that allowed us to pick all 20-nm-grids in an image and to align them onto a model grid<sup>28</sup>. Figure 3a displays the averaged images of more than 700 structures each from segments 1 (red) and 5 (cyan) for the same sample imaged with Gaussian and flat-top illumination (a  $20 \times 20$  subset of individual 20-nm-grid images can be found in Supplementary Figure 5). The histograms represent the spatial distribution of localizations along the dashed lines. A double Gaussian fit recovered the designed docking strand spacing of  $\sim 20$  nm. The evident loss of resolution in the Gaussian average from segment 5 compared to segment 1 is confirmed by the broadened peaks in the histograms which increased by almost a factor of two (localization precision from  $\sim 2.0$  to  $\sim 3.5$  nm). On the contrary, in the flat-top image only a minor decrease in localization precision was observed ( $\sim 10\%$ ). As previously mentioned, the localization uncertainty in SMLM is inversely proportional to the square-root

of the number of detected photons. We identified a three-fold decrease in the average number of detected photons per localization event from  $\sim 15,000$  to  $\sim 5,000$  comparing segments 1 and 5 for Gaussian illumination and attributed this as the main cause for the decrease in localization precision (Fig. 3b). Segment-wise calculation of the localization precision based on Nearest Neighbor Analysis<sup>5,29</sup> (NeNA) confirmed this relation (Fig. 3c). Nevertheless, we also observed a radial decrease in photon number and localization precision for the image acquired with flat-top illumination. Since this effect is decoupled from the excitation profile, we attribute this to finite aperture effects that become increasingly apparent in the periphery when increasing the FOV. However, this only leads to minor radial performance and image resolution loss ( $\sim 10\%$ ) compared to the performance decrease due to inhomogeneous excitation in the case of Gaussian illumination.

In order to benchmark the overall localization precision for flat-top illumination, we designed and imaged DNA origami structures with a 10-nm-grid pattern of docking strands. We could resolve the individual docking strands even in segment 5, demonstrating better than 10 nm spatial resolution over the entire FOV,  $\sim 130$   $\mu\text{m}$  in diameter (Fig. 3d).

Straightforward filtering capabilities during image post-processing are an additional advantage of using flat-top illumination. Figure 3e depicts the photon count distribution for a 20-nm-grid sample imaged with Gaussian (top) and flat-top illumination (bottom). In contrast to Gaussian illumination, we were able to identify two distinct peaks in the distribution from the image acquired with the flat-top profile. The first peak at 25,800 photons is attributed to localizations originating from single imager binding events. The second peak is located at roughly twice the number of photons (53,200) and represents localizations originating from two imager strands bound simultaneously to the same structure. The top panel in Fig. 3f illustrates that these multi-emitter events result in mislocalizations, thus degrading the overall image quality. In contrast to the Gaussian profile (only in segment 1 the photon count distribution indicates two peaks, see Supplementary Figure 6), flat-top illumination allowed us to robustly use an upper threshold limit over the whole FOV at the  $1/e^2$  value of the first peak for filtering out these mislocalizations during post-processing and thereby considerably improving the quality of the super-resolved image (Fig. 3f, bottom).

**Improved large field-of-view cellular imaging with DNA-PAINT.** After identifying and quantifying the effects caused by inhomogeneous illumination on DNA origami structures, we applied flat-top illumination for imaging cellular structures with DNA-PAINT to highlight the differences in obtainable overall image quality researchers should expect on common samples. Figure 4a shows SR images of the microtubule network in fixed COS-7 cells labeled using primary and DNA-conjugated secondary antibodies<sup>5,30</sup> and subsequent DNA-PAINT imaging for Gaussian (left) and flat-top illumination (right) acquired with the full camera sensor resulting in a field-of-view of  $130 \times 130$   $\mu\text{m}^2$ . The magnified regions in the center and the border of the image (segment 1 and 5 as defined in Fig. 2c) recorded using Gaussian illumination show an increasing loss of localizations towards the periphery due to the limited spot-detection efficiency (see Fig. 4b, bottom left). In contrast, we obtain a uniform localization density using flat-top illumination, confirming the earlier observations for DNA origami experiments (Fig. 4b, right). Find a detailed two-level zoomed cell image in Supplementary Figure 7). The white arrows point to regions of accumulated multi-emitter mislocalizations in between the densely-labeled microtubules (for

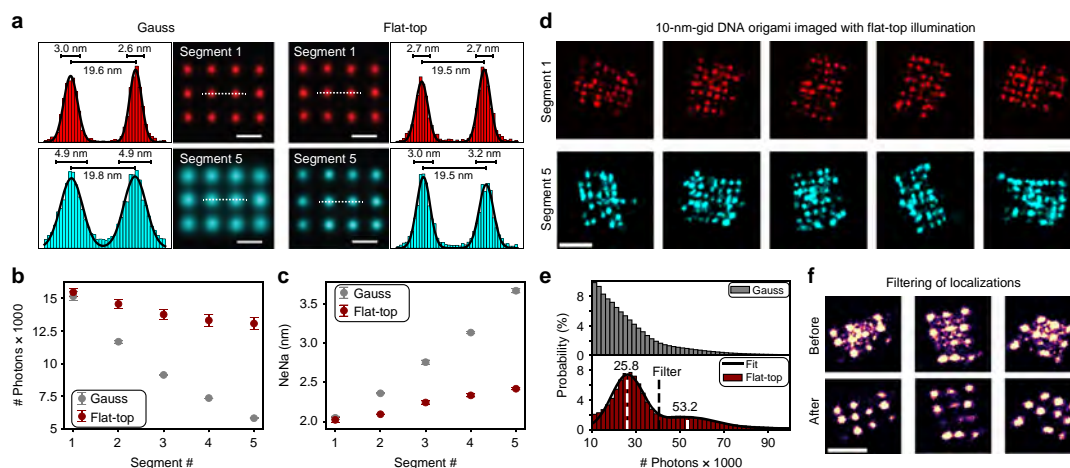


**Fig. 3** Localization precision of 2 nm over  $130 \times 130 \mu\text{m}^2$  FOV with flat-top illumination. **a** Averaged images of 20-nm-grid structures ( $\sim 800$  per segment, see Fig. 2c for definition of segments) show radial decrease in resolution using Gaussian illumination, while flat-top illumination maintains high spatial resolution. Fit results for peak-to-peak distance and standard deviation displayed above. **b** Mean number of detected photons per localization per frame. **c** Localization precision calculated by nearest neighbor analysis (NeNA). **d** 10-nm-grid DNA origami design for whole-chip resolution benchmarking under flat-top illumination. **e** Photon count histogram for flat-top illumination indicating two peaks for the case of single binding and simultaneous binding events of two imager strands to a 20-nm grid. **f** Filtering out simultaneous binding events above single binding threshold (filter in **e** set  $1/e^2$  value of first distribution) allowing the removal of “cross talk” localizations in between two active docking strands. Scale bars, 20 nm in **a**, 50 nm in **d** and **f**. Error bars in **b** and **c** correspond to SEM

magnified illustration see Supplementary Figure 8). These could again be identified in all photon count histograms in Fig. 4c, except for segment 5 of the image acquired using Gaussian illumination. Figure 4d demonstrates the gain in image quality for both segments of the flat-top image after removal of all localizations above the  $1/e^2$  value of the single emitter peak. The distributions of localizations in the boxed regions along the indicated directions in Fig. 4d show two distinct peaks originating from the 2D projection of a homogeneously-labeled rod. Even in the periphery of the full camera sensor image we recovered a peak-to-peak distance of  $\sim 37$  nm which is in good agreement with previously reported values from SR studies<sup>5,19,30,31</sup>. Despite the radial quality loss in the image acquired with Gaussian illumination, we could also identify and remove multi-emitter mislocalizations in the center of the image (Supplementary Figure 9).

Overall, high-throughput DNA-PAINT SMLM employing large FOVs can hence benefit from flat-top illumination without substantial trade-off in image quality.

## Discussion

We here presented a quantitative super resolution study of flat-top TIRF illumination for DNA-PAINT. We demonstrated that flat-top illumination improves the quantification accuracy in DNA-PAINT data by enabling both homogeneous spatial resolution and precise kinetic blinking parameters over large FOVs. In addition, uniform illumination gives rise to new features in the experimental observables, that can be used during straightforward post-processing. This includes a more robust spot detection and enabled us to effectively remove multi-emitter artifacts without the use of computationally demanding multi-emitter localization algorithms<sup>13–17</sup>. We achieved the latter by simple photon number thresholding in the resulting localization datasets. We want to note, that using this threshold to omit multi-emitter mislocalizations does not necessarily lead to a reduced image quality due to missed localizations in DNA-PAINT, as we can collect a considerably

larger amount of total localizations per docking strand due to the repetitive nature of image acquisition.

Furthermore, improved control over the photobleaching conditions allowed us to distinguish apparent identical structures of different docking strand length independent of their position within the FOV. This could be exploited for non-spectral multiplexing in DNA-PAINT super resolution microscopy in the future. We think that these numerous advantages will significantly enhance the statistical treatment of single-molecule microscopy data, since a flat-top illumination allows the use of the complete FOV for further analysis and can hence pave new routes for high-throughput experiments. Furthermore, a uniform TIR excitation will improve single-molecule fluorescence-based binding affinity studies on surfaces, e.g., by SI-FCS<sup>32</sup>, since photophysical effects can be treated globally and can therefore be decoupled from local changes caused by other physical effects. In cases where phototoxicity has to be minimized<sup>33</sup>, flat-top illumination can provide precise control over the whole FOV.

Regarding the comparison of Gaussian and flat-top illumination several of our findings can also directly improve image quality for quantitative DNA-PAINT with a Gaussian excitation profile, when segment-wise analysis of parameters is employed. With regard to biological samples, however, segmented analysis will presumably be most beneficial in the case of compact, separable protein structures such as nuclear pore complexes compared to continuous networks such as the cytoskeleton or large organelle structures. Using this segmentation approach, we showed that in the center segment it is also possible to remove multi-emitter localizations for more precise and quantitative data interpretation. Furthermore, the differentiation between structures with short and long binding docking strands is also possible within each segment, but obviously this comes at the cost that the overall statistics is divided by the number of introduced segments.

In conclusion however, we are convinced that the advantages arising from flat-top TIR illumination—especially with regards to

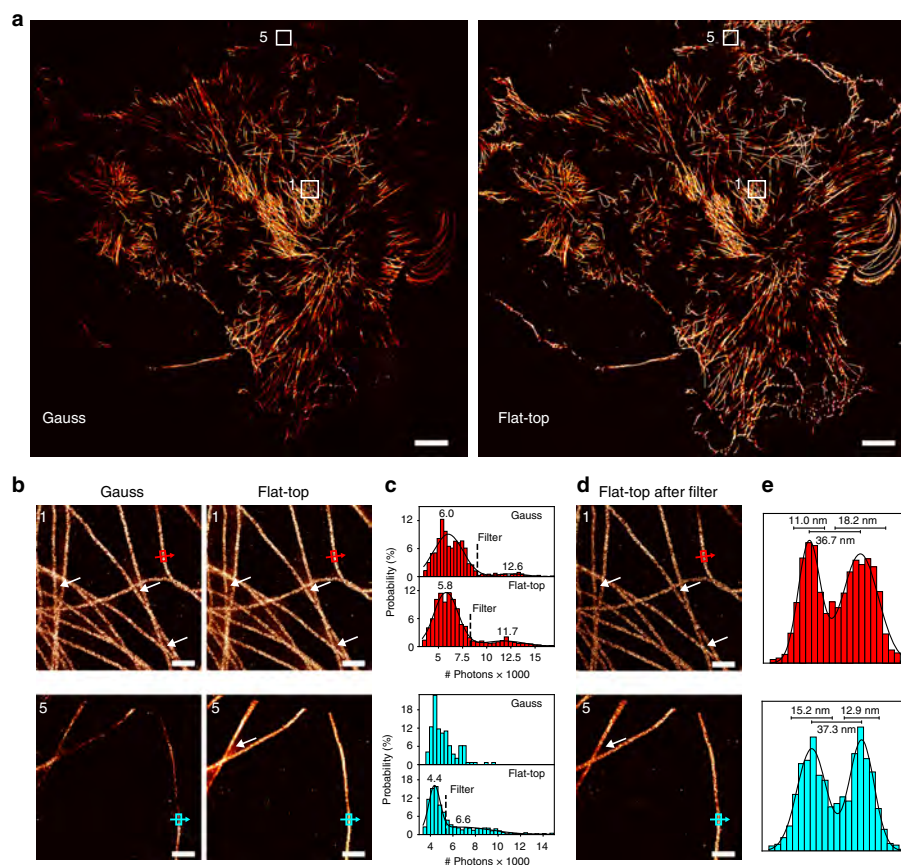


**Fig. 4** Artifact removal for uniform and quantitative cellular DNA-PAINT imaging. **a** Full camera chip ( $130 \times 130 \mu\text{m}^2$ ) DNA-PAINT image of the microtubule network in fixed COS-7 cells acquired using Gauss illumination (left) and the same field of view for flat-top illumination (right). **b** Magnified sections from segment 1 and segment 5 (as defined in Fig. 2a) highlighting the image quality in the center and the border region of the camera chip. White arrows point to artifacts due to multi-emitter mislocalizations. **c** Photon count histograms for box regions in images from **b**. Double Gaussian fit allows identification and removal of multi-emitter mislocalizations (threshold at  $1/e^2$  of first peak) except for segment 5 for Gaussian illumination. **d** Filtered flat-top images from **b** displaying enhanced image quality after removing mislocalization artifacts. **e** Intensity profiles across single microtubules indicated in **d**. Scale bars,  $10 \mu\text{m}$  in **a**,  $500 \text{ nm}$  in **b**, **d**

the ease-of-use and availability of commercial beam shaping devices—are clearly superior and we believe they might become a standard feature for TIRF microscopy.

## Methods

**Materials.** Unmodified, dye-labeled, and biotinylated DNA oligonucleotides were purchased from MWG Eurofins. DNA scaffold strands were purchased from Tilibit (p7249, identical to M13mp18). Streptavidin (cat: S-888) and glass slides (cat: 10756991) were ordered from Thermo Fisher. Coverslips were purchased from Marienfeld (cat: 0107052). PEG-8000 was purchased from Merck (cat: 6510-1KG). Tris 1M pH 8.0 (cat: AM9856), EDTA 0.5M pH 8.0 (cat: AM9261), Magnesium 1M (cat: AM9530G) and Sodium Chloride 5M (cat: AM9759) were ordered from Ambion. Ultrapure water was obtained from a Milli-Q filter machine. Tween-20 (cat: P9416-50ML), Glycerol (cat: G5516-500ML), Methanol (cat: 32213-2.5L), BSA-Biotin (cat: A8549), Protocatechuete 3,4-Dioxygenase Pseudomonas (PCD) (cat: P8279), 3,4-Dihydroxybenzoic acid (PCA) (cat: 37580-25G-F) and (+)-6-Hydroxy-2,5,7,8-tetra-methylchromane-2-carboxylic acid (Trolox) (cat: 238813-5G) were ordered from Sigma-Aldrich. Twinsil two-component glue was purchased from Picodent (cat: 13001000). Monoclonal antibodies against alpha-tubulin (cat: MA1-80017) was purchased from Thermo Scientific. The secondary

antibodies Anti-Rat (cat: 712-005-150) were purchased from Jackson ImmunoResearch.

**Buffers.** Five buffers were used for sample preparation and imaging: Buffer A (10 mM Tris-HCl pH 7.5, 100 mM NaCl, 0.05% Tween 20, pH 7.5); Buffer B (5 mM Tris-HCl pH 8, 10 mM MgCl<sub>2</sub>, 1 mM EDTA, 0.05% Tween 20, pH 8); Buffer C (1× PBS pH 8, 500 mM NaCl, pH 8); 100× Trolox: 100 mg Trolox, 430  $\mu\text{l}$  100% methanol, 345  $\mu\text{l}$  of 1M NaOH in 3.2 ml H<sub>2</sub>O. 40× PCA: 154 mg PCA, 10 ml water, and NaOH were mixed and adjusted to pH 9.0. 100× PCD: 9.3 mg PCD, 13.3 ml of buffer (100 mM Tris-HCl pH 8, 50 mM KCl, 1 mM EDTA, 50% glycerol).

**DNA origami design, assembly, and purification.** DNA origami structures were designed using the design module of Picasso<sup>5</sup> (see Supplementary Figure 10). Folding of structures was performed using the following components: single-stranded DNA scaffold (0.01  $\mu\text{M}$ ), core staples (0.5  $\mu\text{M}$ ), biotin staples (0.5  $\mu\text{M}$ ), modified staples (each 0.5  $\mu\text{M}$ ), 1× folding buffer in a total of 50  $\mu\text{l}$  for each sample. Annealing was done by cooling the mixture from 80 to 25 °C in 3 h in a thermocycler. Structures were purified using PEG-precipitation<sup>34</sup>.

**DNA origami sample preparation.** A glass slide was glued onto a coverslip with the help of double-sided tape (Scotch, cat. no. 665D) to form a flow chamber with inner volume of ~20  $\mu\text{l}$ . First, 20  $\mu\text{l}$  of biotin-labeled bovine albumin (1 mg/ml, dissolved in buffer A) was flushed into the chamber and incubated for 2 min. The chamber was then washed with 40  $\mu\text{l}$  of buffer A. Twenty microliter of streptavidin (0.5 mg/ml, dissolved in buffer A) was then flushed through the chamber and incubated for 2 min. After washing with 40  $\mu\text{l}$  of buffer A and subsequently with 40  $\mu\text{l}$  of buffer B, 20  $\mu\text{l}$  of biotin-labeled DNA structures (1:80 dilution in buffer B from purified DNA-origami stock) were flushed into the chamber and incubated for 10 min. The chamber was washed with 40  $\mu\text{l}$  of buffer B. Finally, 40  $\mu\text{l}$  of the imager solution was flushed into the chamber, which was subsequently sealed with two-component glue before imaging. A list of all staples can be found in Supplementary Tables 1 and 2.

**Cell sample preparation.** COS7 cells were cultured with Eagle's minimum essential medium fortified with 10% FBS with penicillin and streptomycin and incubated at 37 °C with 5% CO<sub>2</sub>. At ~30% confluence, cells were seeded into Eppendorf 8-well chambered cover glass ~24 h before fixation and were grown to ~70% confluence. For fixation, the samples were pre-fixed and pre-permeabilized with 0.4% glutaraldehyde and 0.25% Triton X-100 for 90 s. Next, the cells were quickly rinsed with 1 $\times$  PBS once followed by fixation with 3% glutaraldehyde for 15 min. Afterwards, samples were rinsed twice (5 min) with 1 $\times$  PBS and then quenched with 0.1% NaBH<sub>4</sub> for 7 min. After rinsing four times with 1 $\times$  PBS for 30 s, 60 s, and twice for 5 min, samples were blocked and permeabilized with 3% BSA and 0.25% Triton X-100 for 2 h. Then, samples were incubated with 10  $\mu\text{g}/\text{ml}$  of primary antibodies (1:100 dilution) in a solution with 3% BSA and 0.1% Triton X-100 at 4 °C overnight. Cells were rinsed three times (5 min each) with 1 $\times$  PBS. Next, they were incubated with 10  $\mu\text{g}/\text{ml}$  of labeled secondary antibodies (1:100 dilution) in a solution with 3% BSA and 0.1% Triton X-100 at room temperature for 1 h. For fiducial based drift correction, the samples were incubated with gold nanoparticles with a 1:1 dilution in 1 $\times$  PBS for 5 min. Finally, samples were rinsed three times with 1 $\times$  PBS before adding imager solution.

**Super-resolution microscopy setup.** Fluorescence imaging was carried out on an inverted custom-built microscope (see setup sketch in Supplementary Figure 1) in an objective-type TIRF configuration with an oil-immersion objective (Olympus UAPON, 100 $\times$ , NA 1.49). One laser was used for excitation: 561 nm (1 W, DPSS-system, MPB). Laser power was adjusted by polarization rotation with a half-wave plate (Thorlabs, WPH05M-561) before passing a polarizing beam-splitter cube (Thorlabs, PBS101). To spatially clean the beam-profile the laser light was coupled into a single-mode polarization-maintaining fiber (Thorlabs, P3-488PM-FC-2) using an aspheric lens (Thorlabs, C610TME-A). The coupling polarization into the fiber was adjusted using a zero-order half wave plate (Thorlabs, WPH05M-561). The laser light was re-collimated after the fiber using an achromatic doublet lens (Thorlabs, AC254-050-A-ML) resulting in a collimated FWHM beam diameter of ~6 mm. The laser light was split into two paths of approximately equal length using a combination of two flip mirrors (Thorlabs, FM90/M). In one path the laser light was unaltered resulting in a Gaussian beam profile for excitation. In the other path a diffractive beam shaper device (AdOptica, piShaper 6\_6\_VIS) transformed the Gaussian beam profile in a collimated flat-top profile. Both paths were realigned to each other and passed the same downstream optics. Switching between the two illumination schemes can therefore be achieved by flipping two mirrors simultaneously. The laser beam diameter was magnified by a factor of 2.5 using a custom-built Telescope (Thorlabs, AC254-030-A-ML and Thorlabs, AC508-075-A-ML). The laser light was coupled into the microscope objective using an achromatic doublet lens (Thorlabs, AC508-180-A-ML) and a dichroic beam splitter (AHF, F68-785). Fluorescence light was spectrally filtered with an emission filter (AHF Analysentechnik, 605/64) and imaged on a sCMOS camera (Andor, Zyla 4.2) without further magnification (Thorlabs, TTL180-A) resulting in an effective pixel size of 130 nm (after 2  $\times$  2 binning). Microscopy samples were mounted on a x-y-z stage (ASI, S31121010FT and ASI, FTP2050) that was used for focusing with the microscope objective being at fixed position. Our custom TIRF setup was used for all Figures.

**Imaging conditions.** All fluorescence microscopy data was recorded on the full sensor (2048  $\times$  2048 pixels, pixel size: 6.5  $\mu\text{m}$ ) of our sCMOS camera operated with the open source acquisition software  $\mu\text{Manager}$ <sup>35</sup> at a read out rate of 200 MHz and a dynamic range of 16 bit. Detailed imaging conditions for all main and supplementary figures can be found in Supplementary Table 3. The laser power refers to the power measured after the fiber (see Supplementary Figure 1). As can be seen in Fig. 1b, the mean intensity of the flat-top profile is at around 60 % of the Gaussian peak intensity, when operated at the same power. Supplementary Figure 11 illustrates that by an respective power increase we can adjust the flat-top profile to the Gaussian peak intensity. Sequence design of imager and docking strands can be found in Supplementary Table 4.

**Super-resolution reconstruction.** Raw fluorescence data was subjected to spot-finding and subsequent super-resolution reconstruction using the localize module of the Picasso software package<sup>5</sup>. Localizations were then loaded into Picasso's

render module and drift-corrected. DNA origamis were automatically selected using the "Pick similar" function with the following settings: pick radius: 143 nm; standard deviation: 1.5, 1.7, 1.9 (subsequently). After automated selection, picked areas were saved as "Picked localizations" for further processing.

**Kinetic analysis.** Picasso's render module<sup>5</sup> allows automatic recognition of ROIs within the rendered super-resolution image by searching for similarity in the localization distribution to pre-selected user defined regions of specific size. The resulting ROIs of the complete set of localizations are referred to as "picks" (Supplementary Figure 12a). We calculated characteristic quantities associated with the temporal distribution of localization events within each of these picks with a custom written python script (see Supplementary Figure 12). Since the automated selection of ROIs cannot distinguish between repetitive (specific) and non-repetitive (unspecific) blinking behavior we implemented a filtering procedure based on the temporal distribution of localization events.

**Filtering.** By looking at the temporal distribution of the localization events (trace) associated to a single pick we can define its mean and standard deviation. We refer to these parameters as the mean (localization) frame and its standard deviation (std) in the units of frames. Repetitive transient binding to DNA origami throughout the measurement leads hence to a mean (localization) frame of roughly half the number of total frames in the acquisition window with a large standard deviation (Supplementary Figure 12b, left panel). In contrast non-repetitive binding will result in a mean (localization) frame located within the frames of their unique occurrence randomly distributed throughout the acquisition window and a small standard deviation (Supplementary Figure 12b, right panel). Plotting the distribution of the mean (localization) frame and its standard deviation over all automatically selected ROIs thus allows clear identification of a major population of picked areas showing repetitive blinking while outliers indicating non-repetitive blinking behavior can be disregarded for further analysis (Supplementary Figure 12c and d).

**Averaging.** Picked origami structures were averaged to a designed model structure using the average3 module of Picasso with a pixel oversampling of 40 and setting a custom symmetry of 180 degree<sup>28</sup>.

**Reporting summary.** Further information on experimental design is available in the Nature Research Reporting Summary linked to this article.

**Code availability.** All code supporting the findings of this study is available from the corresponding author upon request.

#### Data availability

The data that support the findings of this study are available from the corresponding authors upon reasonable request.

Received: 29 October 2018 Accepted: 19 February 2019

Published online: 20 March 2019

#### References

- Betzig, E. et al. Imaging intracellular fluorescent proteins at nanometer resolution. *Science* **313**, 1642 LP–1641645 (2006).
- Rust, M. J., Bates, M. & Zhuang, X. Sub-diffraction-limit imaging by stochastic optical reconstruction microscopy (STORM). *Nat. Methods* **3**, 793 (2006).
- Sharonov, A. & Hochstrasser, R. M. Wide-field subdiffraction imaging by accumulated binding of diffusing probes. *Proc. Natl Acad. Sci.* **103**, 18911–18916 (2006).
- Sauer, M. & Heilemann, M. Single-molecule localization microscopy in eukaryotes. *Chem. Rev.* **117**, 7478–7509 (2017).
- Schnitzbauer, J., Strauss, M. T., Schlichthaerle, T., Schueder, F. & Jungmann, R. Super-resolution microscopy with DNA-PAINT. *Nat. Protoc.* **12**, 1198 (2017).
- Axelrod, D. Cell-substrate contacts illuminated by total internal reflection fluorescence. *J. Cell. Biol.* **89**, 141 LP–141145 (1981).
- Tokunaga, M., Imamoto, N. & Sakata-Sogawa, K. Highly inclined thin illumination enables clear single-molecule imaging in cells. *Nat. Methods* **5**, 159 (2008).
- Schueder, F. et al. Multiplexed 3D super-resolution imaging of whole cells using spinning disk confocal microscopy and DNA-PAINT. *Nat. Commun.* **8**, 2090 (2017).
- Jungmann, R. et al. Multiplexed 3D cellular super-resolution imaging with DNA-PAINT and exchange-PAINT. *Nat. Methods* **11**, 313 (2014).

10. Jungmann, R. et al. Quantitative super-resolution imaging with qPAINT. *Nat. Methods* **13**, 439 (2016).
11. Axelrod, D. B. T.-M. in C. B. in *Biophysical Tools for Biologists: In Vivo Techniques*, (eds.) John J. Correia and H. William Detrich, Vol. 2 169–221 (Academic Press, San Diego, 2008). [https://doi.org/10.1016/S0091-679X\(08\)00607-9](https://doi.org/10.1016/S0091-679X(08)00607-9)
12. Yang, Q., Karpikov, A., Toomre, D. & Duncan, J. S. 3-D reconstruction of microtubules from multi-angle total internal reflection fluorescence microscopy using Bayesian framework. *IEEE Trans. Image Process.* **20**, 2248–2259 (2011).
13. Huang, F., Schwartz, S. L., Byars, J. M. & Lidke, K. A. Simultaneous multiple-emitter fitting for single molecule super-resolution imaging. *Biomed. Opt. Express* **2**, 1377–1393 (2011).
14. Holden, S. J., Uphoff, S. & Kapanidis, A. N. DAOSTORM: an algorithm for high-density super-resolution microscopy. *Nat. Methods* **8**, 279 (2011).
15. Zhu, L., Zhang, W., Elnatan, D. & Huang, B. Faster STORM using compressed sensing. *Nat. Methods* **9**, 721 (2012).
16. Burnette, D. T., Sengupta, P., Dai, Y., Lippincott-Schwartz, J. & Kachar, B. Bleaching/blinking assisted localization microscopy for superresolution imaging using standard fluorescent molecules. *Proc. Natl Acad. Sci.* **108**, 21081–21086 (2011).
17. Marsh, R. J. et al. Artifact-free high-density localization microscopy analysis. *Nat. Methods* **15**, 689–692 (2018).
18. Deschamps, J., Rowald, A. & Ries, J. Efficient homogeneous illumination and optical sectioning for quantitative single-molecule localization microscopy. *Opt. Express* **24**, 28080–28090 (2016).
19. Douglass, K. M., Sieben, C., Archetti, A., Lambert, A. & Manley, S. Super-resolution imaging of multiple cells by optimized flat-field epi-illumination. *Nat. Photonics* **10**, 705 (2016).
20. Rowlands, C. J., Ströhl, F., Ramirez, P. P. V., Scherer, K. M. & Kaminski, C. F. Flat-field super-resolution localization microscopy with a low-cost refractive beam-shaping element. *Sci. Rep.* **8**, 5630 (2018).
21. Frieden, B. R. Lossless conversion of a plane laser wave to a plane wave of uniform irradiance. *Appl. Opt.* **4**, 1400–1403 (1965).
22. Hoffnagle, J. A. & Jefferson, C. M. Design and performance of a refractive optical system that converts a Gaussian to a flattop beam. *Appl. Opt.* **39**, 5488–5499 (2000).
23. Khaw, I. et al. Flat-field illumination for quantitative fluorescence imaging. *Opt. Express* **26**, 15276–15288 (2018).
24. Pyle, J. R. & Chen, J. Photobleaching of YOYO-1 in super-resolution single DNA fluorescence imaging. *Beilstein J. Nanotechnol.* **8**, 2296–2306 (2017).
25. Thompson, R. E., Larson, D. R. & Webb, W. W. Precise nanometer localization analysis for individual fluorescent probes. *Biophys. J.* **82**, 2775–2783 (2002).
26. Deschout, H. et al. Precisely and accurately localizing single emitters in fluorescence microscopy. *Nat. Methods* **11**, 253 (2014).
27. Baddeley, D. & Bewersdorf, J. Biological insight from super-resolution microscopy: what we can learn from localization-based images. *Annu. Rev. Biochem.* **87**, 1–25 (2018).
28. Strauss, M. T., Schueder, F., Haas, D., Nickels, P. C. & Jungmann, R. Quantifying absolute addressability in DNA origami with molecular resolution. *Nat. Commun.* **9**, 1600 (2018).
29. Endesfelder, U., Malkusch, S., Fricke, F. & Heilemann, M. A simple method to estimate the average localization precision of a single-molecule localization microscopy experiment. *Histochem. Cell Biol.* **141**, 629–638 (2014).
30. Agasti, S. S. et al. DNA-barcoded labeling probes for highly multiplexed exchange-PAINT imaging. *Chem. Sci.* **8**, 3080–3091 (2017).
31. Dempsey, G. T., Vaughan, J. C., Chen, K. H., Bates, M. & Zhuang, X. Evaluation of fluorophores for optimal performance in localization-based super-resolution imaging. *Nat. Methods* **8**, 1027 (2011).
32. Mücksch, J. et al. Quantifying reversible surface binding via surface-integrated fluorescence correlation spectroscopy. *Nano Lett.* **18**, 3185–3192 (2018).
33. Blumhardt, P. et al. Photo-induced depletion of binding sites in DNA-PAINT microscopy. *Molecules* **23**, 3165 (2018). <https://doi.org/10.3390/molecules23123165>
34. Stahl, E., Martin, T. G., Praetorius, F. & Dietz, H. Facile and scalable preparation of pure and dense DNA origami solutions. *Angew. Chem. Int. Ed.* **53**, 12735–12740 (2014).
35. Edelstein, A. D. et al. Advanced methods of microscope control using µManager software. *J. Biol. Methods* **1**, e10 (2014). <https://doi.org/10.14440/jbm.2014.36>

### Acknowledgements

We thank Julian Bauer, Patrick Schueler, Bianca Sperl and Sigrid Bauer for experimental support. F.St., and J.S. acknowledge support by the QBM graduate school and the Center for Nanoscience Munich. This work has been supported in part by the German Research Foundation through the Emmy Noether Program (DFG JU 2957/1-1 to R.J.), the SFB1032 (projects A11 and A09 to R.J. and P.S.), the European Research Council through an ERC Starting Grant (MolMap; grant agreement number 680241 to R.J.) and the Max Planck Society (P.S. and R.J.).

### Author contributions

F.St. and J.S. built the microscope, designed and performed experiments, analyzed data, and wrote the manuscript. F.Sc. designed DNA origami structures, performed cell experiments and wrote the manuscript. F.St., J.S., F.Sc., and R.J. conceived of the study. R. J. supervised the study, interpreted data, and wrote the manuscript. P.S. supervised the study and wrote the manuscript. All authors reviewed and approved the manuscript.

### Additional information

**Supplementary Information** accompanies this paper at <https://doi.org/10.1038/s41467-019-09064-6>.

**Competing interests:** The authors declare no competing interests.

**Reprints and permission** information is available online at <http://npg.nature.com/reprintsandpermissions/>

**Journal peer review information:** *Nature Communications* thanks the anonymous reviewers for their contribution to the peer review of this work. Peer reviewer reports are available.

**Publisher's note:** Springer Nature remains neutral with regard to jurisdictional claims in published maps and institutional affiliations.



**Open Access** This article is licensed under a Creative Commons Attribution 4.0 International License, which permits use, sharing, adaptation, distribution and reproduction in any medium or format, as long as you give appropriate credit to the original author(s) and the source, provide a link to the Creative Commons license, and indicate if changes were made. The images or other third party material in this article are included in the article's Creative Commons license, unless indicated otherwise in a credit line to the material. If material is not included in the article's Creative Commons license and your intended use is not permitted by statutory regulation or exceeds the permitted use, you will need to obtain permission directly from the copyright holder. To view a copy of this license, visit <http://creativecommons.org/licenses/by/4.0/>.

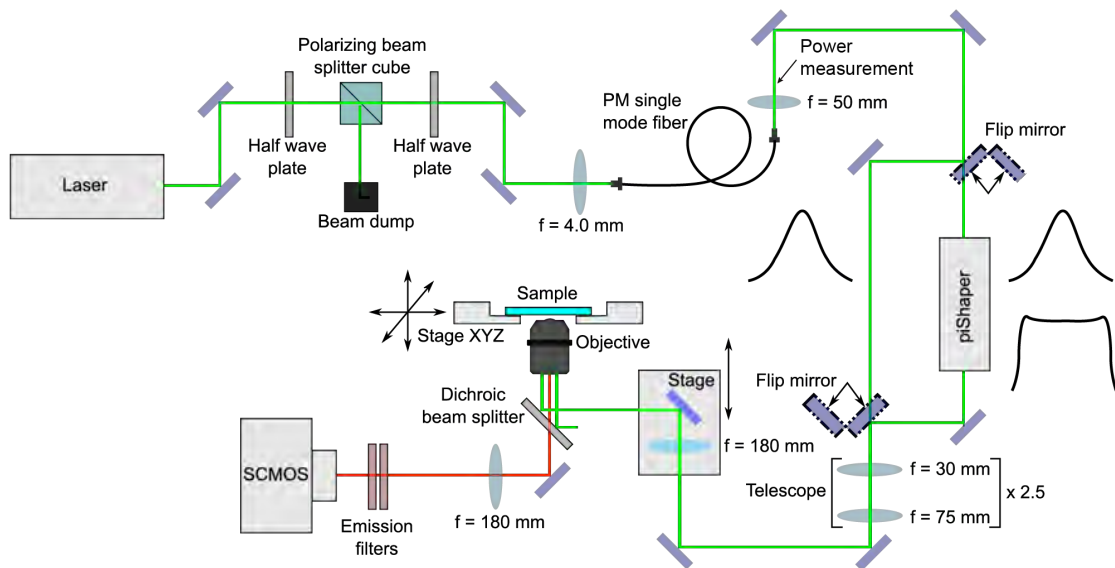
© The Author(s) 2019

## Supplementary Information

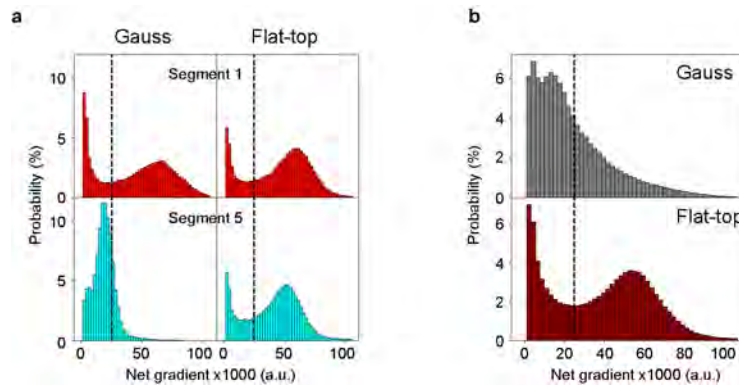
### Flat-top TIRF illumination boosts DNA-PAINT imaging and quantification

Stehr, Stein et al.

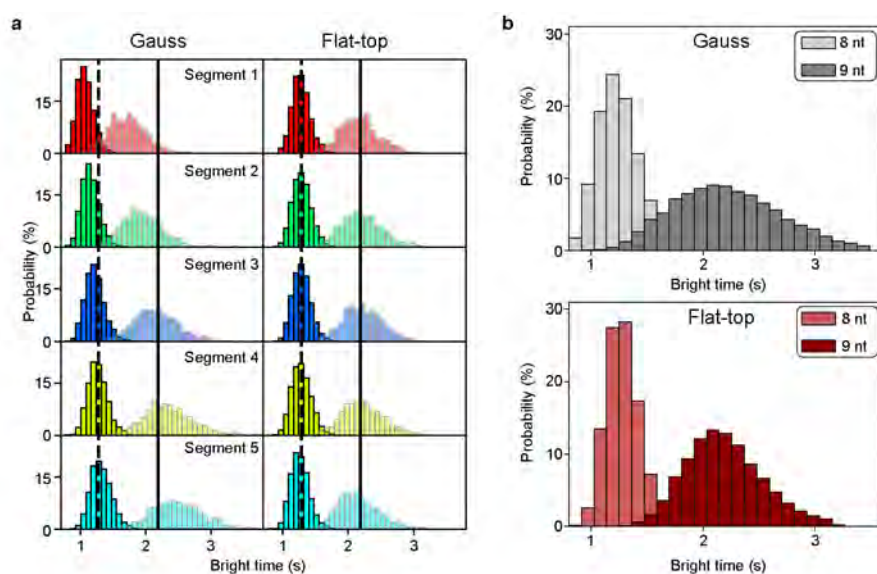
<b>Supplementary Figure 1</b>	Schematic of custom-built super-resolution microscopy setup
<b>Supplementary Figure 2</b>	Spot detection and net gradient
<b>Supplementary Figure 3</b>	Bright time distributions for 8-nt vs. 9-nt docking site length
<b>Supplementary Figure 4</b>	Averaged 20-nm-grid image for 8-nt vs. 9-nt docking sites length for flat-top excitation
<b>Supplementary Figure 5</b>	Individual origami images for averaging
<b>Supplementary Figure 6</b>	Segment-wise photon count distribution Gauss vs. Flat-top
<b>Supplementary Figure 7</b>	Uniform spot-detection efficiency for cellular DNA-PAINT imaging
<b>Supplementary Figure 8</b>	Mislocalization removal by multi-emitter filtering
<b>Supplementary Figure 9</b>	Mislocalization removal by multi-emitter filtering for Gaussian illumination
<b>Supplementary Figure 10</b>	DNA origami grid designs
<b>Supplementary Figure 11</b>	Laser power comparison Gauss vs. Flat-Top
<b>Supplementary Figure 12</b>	Filtering by temporal distribution of localizations
<b>Supplementary Table 1</b>	List of core staples
<b>Supplementary Table 2</b>	List of biotinylated staples
<b>Supplementary Table 3</b>	Imaging parameters
<b>Supplementary Table 4</b>	DNA-PAINT imager sequences



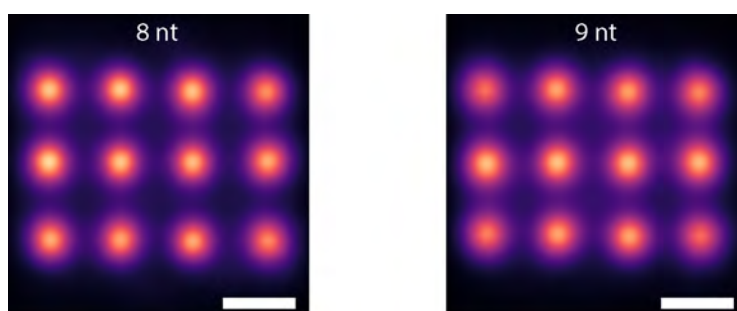
**Supplementary Figure 1 | Schematic of custom-built super-resolution microscopy setup.** Blue rectangles indicate dielectric mirrors, ellipses indicate lenses.



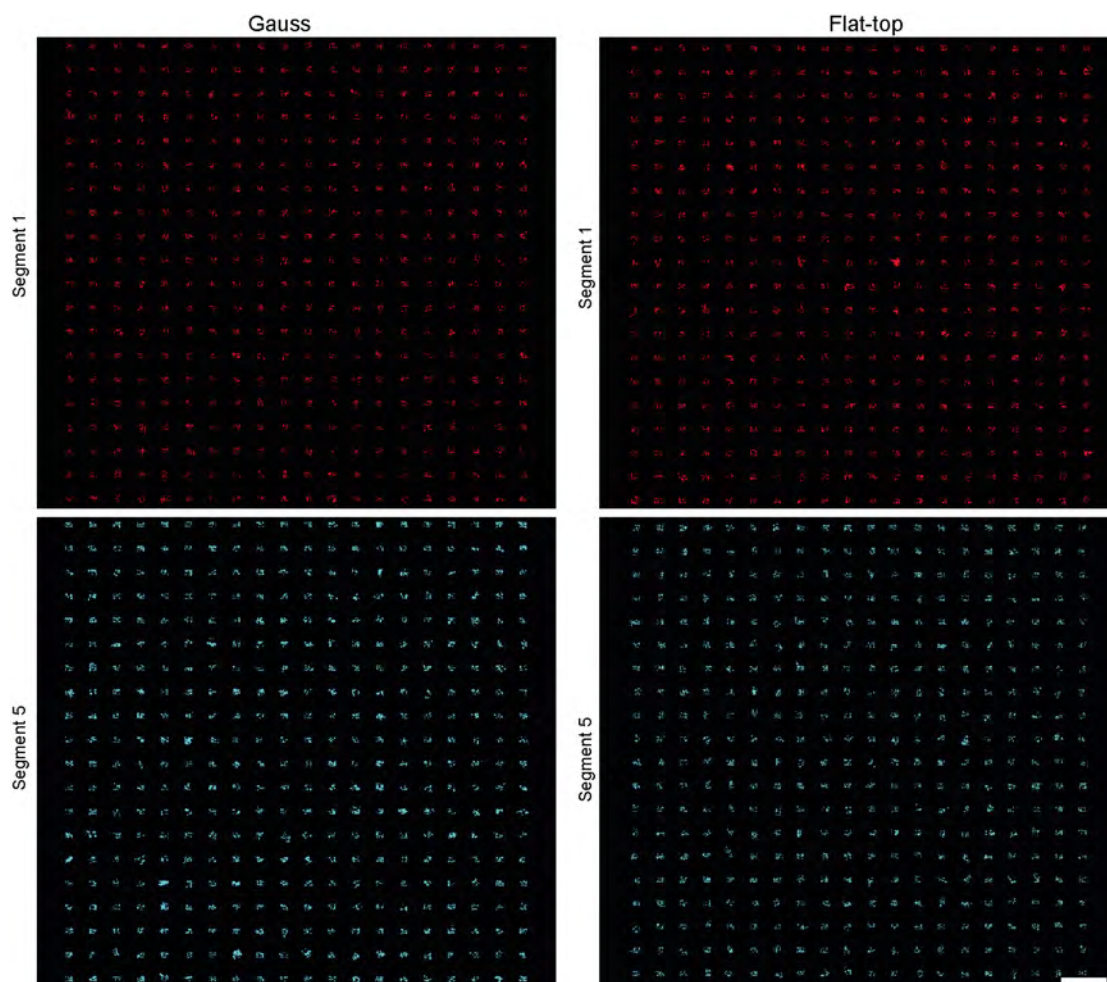
**Supplementary Figure 2 | Spot detection and net gradient.** **a** Net gradient histograms comparing segments 1 and 5 of 20-nm-grid images acquired with Gaussian and flat-top illumination. For DNA-PAINT (but also for SMLM in general) a localization algorithm implemented in Picasso<sup>1</sup> distinguishes between bright blinking events and background noise by computing the net gradient between adjacent pixels in the raw images. A threshold value (dashed line) is chosen manually such that in the center (segment 1) only blinking events and no background is recognized. Due to the inhomogeneous illumination of a Gaussian profile the net gradient in segment 5 does not reach this threshold anymore and blinking events are not recognized. DNA-PAINT data acquired under flat-top illumination show a homogeneous net gradient comparing segments 1 and 5. **b** Net gradient sum histograms for the two images from **a**



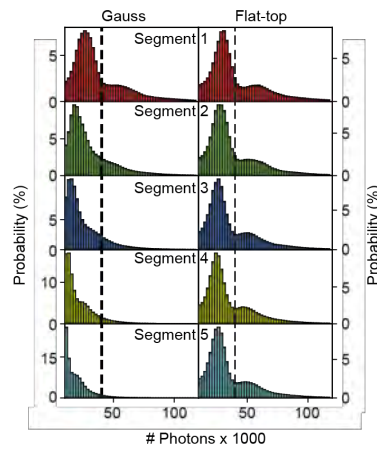
**Supplementary Figure 3 | Bright time distributions for 8-nt vs. 9-nt docking site length.** **a** Segmented bright time histograms for 20-nm-grids with 8-nt docking sites (opaque) and 9-nt docking site length (transparent) for Gauss and flat-top illumination. Mean bright times (over all segments) for flat-top illumination are indicated by dashed lines for 8-nt and solid lines for 9-nt. **b** Total bright time distributions for 8-nt vs 9-nt



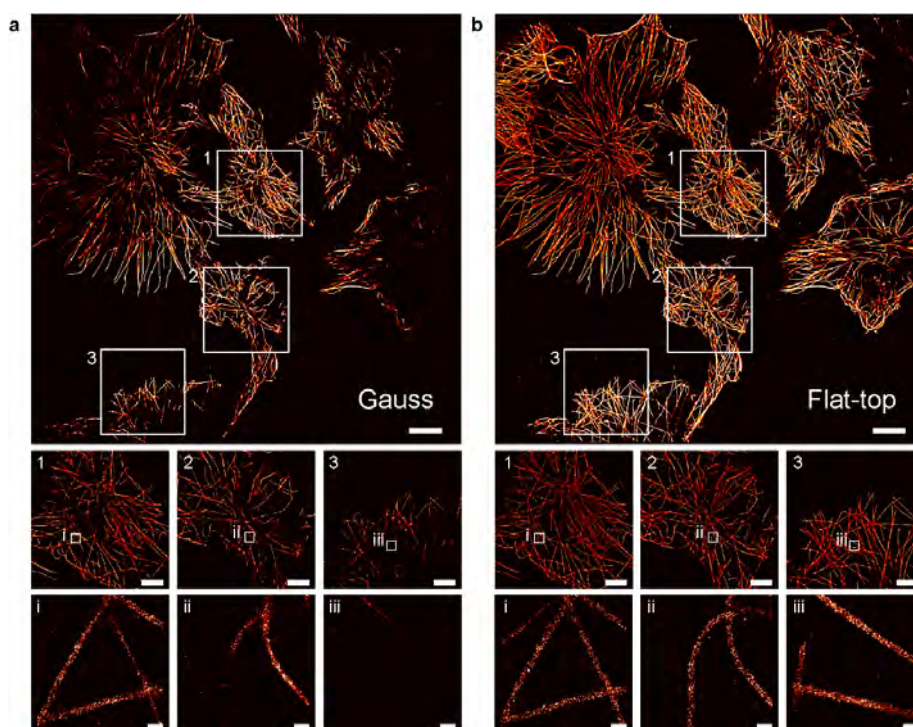
**Supplementary Figure 4 | Averaged 20-nm-grid image for 8-nt vs. 9-nt docking sites for flat-top excitation.** Over 8,000 DNA origami over the whole FOV for the flat-top data sets (8nt and 9nt docking strands) in Figure 2h and Supplementary Figure 5 were averaged and confirms that 20-nm resolution is conserved while origamis can be identified according to their bright times. Scale bars: 20 nm.



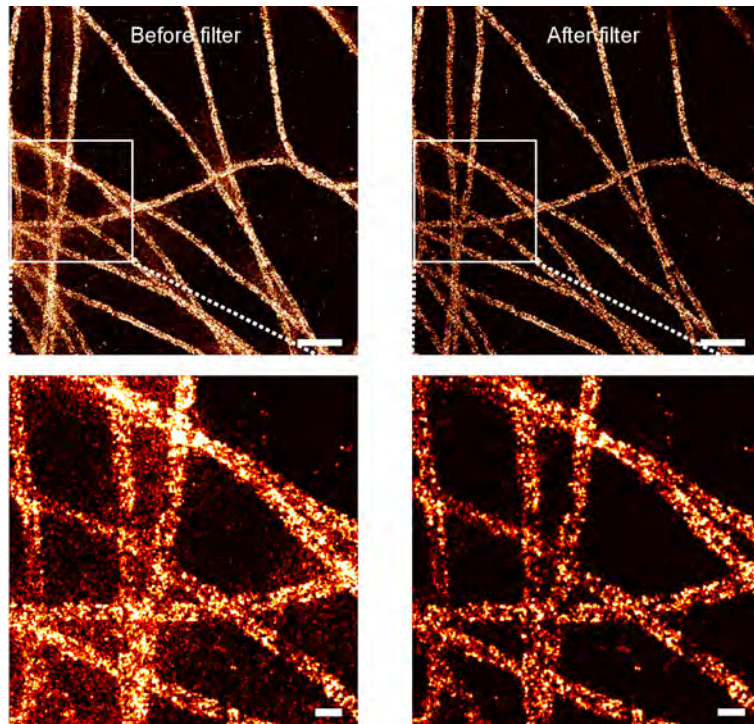
**Supplementary Figure 5 | Individual origami images for averaging.** Image showing 400 DNA origami structures extracted from segment 1 (red) and segment 5 (cyan) for DNA-PAINT images acquired with Gaussian (left) and flat-top illumination (right). In total more than 700 structures were used for averaging in Figure 3a. Scale bar: 500 nm.



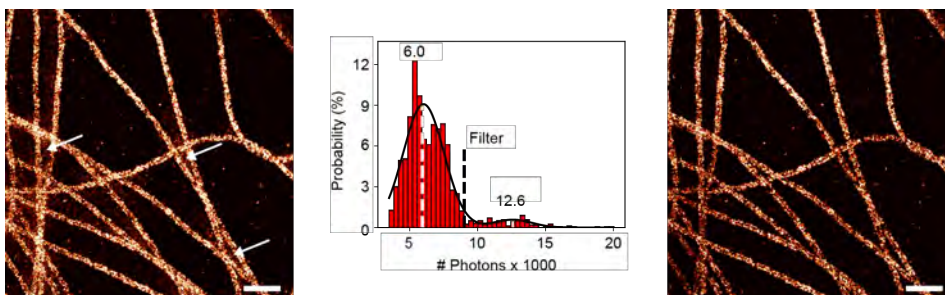
Supplementary Figure 6 | Segment-wise photon count distribution Gauss vs Flat-top.



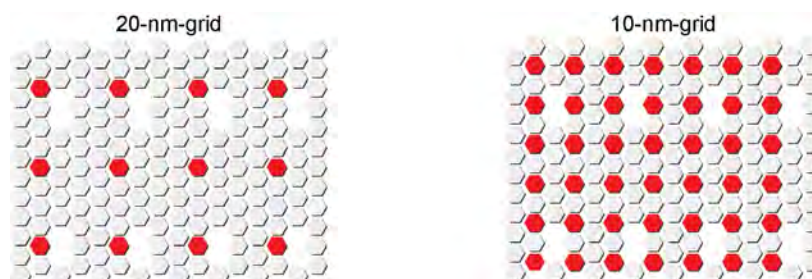
**Supplementary Figure 7 | Uniform spot-detection efficiency for cellular DNA-PAINT imaging.** **a** (top) Full camera chip ( $130 \times 130 \mu\text{m}^2$ ) DNA-PAINT image of the microtubule network in fixed COS-7 cells acquired using Gaussian illumination. (middle row) Three boxes highlighting the image quality in the center, intermediate and border region of the camera chip. (bottom row) Second-level zooms i-iii) highlighting the inhomogeneous localization density over the whole image **b** Image of the same field of view as in **a** acquired with flat-top illumination profile for uniform localization density and image quality. Scale bars,  $10 \mu\text{m}$  top images,  $4 \mu\text{m}$  in middle row and  $200 \text{nm}$  in bottom row.



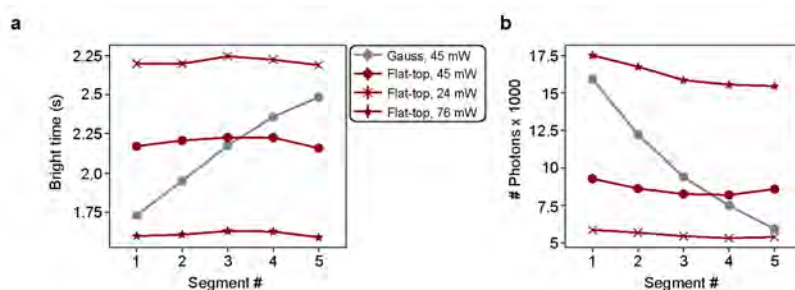
**Supplementary Figure 8 | Mislocalization removal by multi-emitter filtering.** Magnified region of cell image acquired under flat-top illumination (as in Figure 4b). Scale bars, top 500 nm, bottom 100 nm.



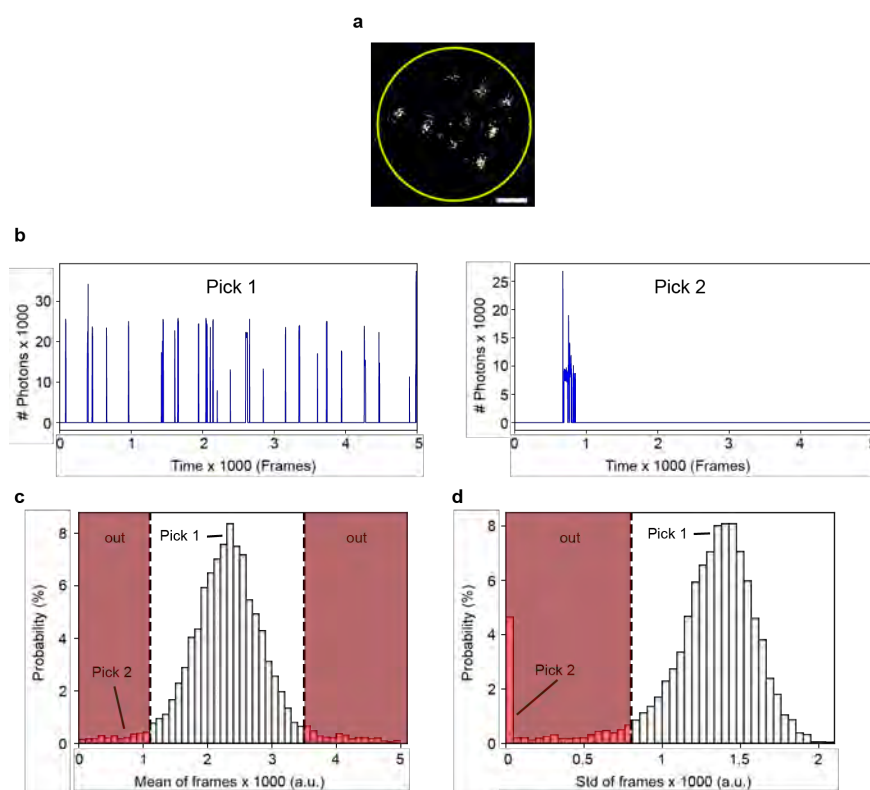
**Supplementary Figure 9 | Mislocalization removal by multi-emitter filtering for Gaussian illumination.** Magnified region of cell image acquired under Gaussian illumination (as in Figure 4b). Scale bars 500 nm.



**Supplementary Figure 10 | DNA origami grid designs.** Picasso Design<sup>1</sup> schematic for 20- and 10-nm-grids. Red hexagons indicate extended staple strands for DNA-PAINT imaging. Missing hexagons indicate the position of extended staple strands on the opposite side, which are functionalized with biotin for surface immobilization.



**Supplementary Figure 11 | Laser power comparison Gauss vs. Flat-Top.** **a** Mean bright time per segment for 9-nt 20-nm-grids **b** Mean number of detected photons per localization with respect to each segment for same data sets as in **a**.



**Supplementary Figure 12 | Filtering by temporal distribution of localizations.** **a** Exemplary auto-selected ROI (yellow circle) of a 20-nm grid in the rendered super-resolution image **b** Typical intensity traces from picks showing repetitive (left) and non-repetitive blinking behavior (right) **c** Exemplary distribution of the mean (localization) frame of all auto-selected picks and **d** the respective distribution for the standard deviation. Values corresponding to picks shown in **b** are indicated. Red areas in both **c** and **d** are discarded before further analysis.

Supplementary Table 1 | List of core staples

Position	Name	Sequence
A1	21[32]23[31]BLK	TTTTCACTCAAAGGGCGAAAAACCATCACC
B1	23[32]22[48]BLK	CAAATCAAGTTTTTTGGGGTCGAAACGTGGA
C1	21[56]23[63]BLK	AGCTGATTGCCCTTCAGAGTCCACTATTAAAGGGTGCCGT
D1	23[64]22[80]BLK	AAAGCACTAAATCGGAACCCTAATCCAGTT
E1	21[96]23[95]BLK	AGCAAGCGTAGGGTTGAGTGTTGTAGGGAGCC
F1	23[96]22[112]BLK	CCCATTAGAGCTTGACGGGGAAAAAGAATA
G1	21[120]23[127]BLK	CCCAGCAGGCGAAAAATCCCTTATAAAATCAAGCCGGCG
H1	21[160]22[144]BLK	TCAATATCGAACCTCAAATATCAATTCCGAAA
I1	23[128]23[159]BLK	AACGTGGCGAGAAAGGAAGGGAAACCAGTAA
J1	23[160]22[176]BLK	TAAAAGGGACATTCTGGCCAACAAAGCATC
K1	21[184]23[191]BLK	TCAACAGTTGAAAGGAGCAAATGAAAAATCTAGAGATAGA
L1	23[192]22[208]BLK	ACCCTTCTGACCTGAAAGCGTAAGACGCTGAG
M1	21[224]23[223]BLK	CTTTAGGGCCTGCAACAGTGCCAATACGTG
N1	23[224]22[240]BLK	GCACAGACAATATTTTTGAATGGGGTCAGTA
O1	21[248]23[255]BLK	AGATTAGAGCCGTCAAAAACAGAGGTGAGGCCTATTAGT
P1	23[256]22[272]BLK	CTTTAATGCGCGAACTGATAGCCCCACCAG
A2	19[32]21[31]BLK	GTCGACTTCGGCCAACGCGCGGGGTTTTTC
B2	22[47]20[48]BLK	CTCCAACGCAGTGAGACGGGCAACCAGCTGCA
D2	22[79]20[80]BLK	TGGAACAACCGCCTGGCCCTGAGGCCCGCT
E2	19[96]21[95]BLK	CTGTGTGATTGCGTTGCGCTACTAGAGTTGC
F2	22[111]20[112]BLK	GCCCGAGAGTCCACGCTGGTTTGCAGCTAACT
H2	19[160]20[144]BLK	GCAATTCACATATTCCTGATTATCAAAGTGTA
I2	22[143]21[159]BLK	TCGGCAAATCCTGTTTGATGGTGGACCCTCAA
J2	22[175]20[176]BLK	ACCTTGCTTGGTCAGTTGGCAAAGAGCGGA
L2	22[207]20[208]BLK	AGCCAGCAATTGAGGAAGGTTATCATCATTTT
M2	19[224]21[223]BLK	CTACCATAGTTTGAGTAACATTTAAAATAT
N2	22[239]20[240]BLK	TTAACACCAGCACTAACAACATAATCGTTATTA
P2	22[271]20[272]BLK	CAGAAGATTAGATAATACATTTGTGACAAA
A3	17[32]19[31]BLK	TGCATCTTTCCAGTCACGACGGCCTGCAG
B3	20[47]18[48]BLK	TTAATGAACTAGAGGATCCCCGGGGGGTAACG
D3	20[79]18[80]BLK	TTCCAGTCGTAATCATGGTCATAAAAGGGG
E3	17[96]19[95]BLK	GCTTTCCGATTACGCCAGCTGGCGGCTGTTTC
F3	20[111]18[112]BLK	CACATTAATAATTGTTATCCGCTCATGCGGGCC
H3	17[160]18[144]BLK	AGAAAACAAGAAGATGATGAAACAGGCTGCG
I3	20[143]19[159]BLK	AAGCCTGGTACGAGCCGGAAGCATAGATGATG
J3	20[175]18[176]BLK	ATTATCATTCAATATAATCCTGACAATTAC

L3	20[207]18[208]BLK	GCGGAACATCTGAATAATGGAAGGTACAAAAT
M3	17[224]19[223]BLK	CATAAATCTTTGAATACCAAGTGTTAGAAC
N3	20[239]18[240]BLK	ATTTTAAAATCAAATTTATTTGCACGGATTG
P3	20[271]18[272]BLK	CTCGTATTAGAAATTGCGTAGATACAGTAC
A4	15[32]17[31]BLK	TAATCAGCGGATTGACCGTAATCGTAACCG
B4	18[47]16[48]BLK	CCAGGGTTGCCAGTTTGAGGGGACCCGTGGGA
C4	15[64]18[64]BLK	GTATAAGCCAACCCGTCGGATTCTGACGACAGTATCGGCCGCAAGGCG
D4	18[79]16[80]BLK	GATGTGCTTCAGGAAGATCGCACAAATGTGA
E4	15[96]17[95]BLK	ATATTTTGGCTTTCATCAACATTATCCAGCCA
F4	18[111]16[112]BLK	TCTTCGCTGCACCGCTTCTGGTGCGGCCTTCC
G4	15[128]18[128]BLK	TAAATCAAAAATAATTCGCGTCTCGGAAACCAGGCAAAGGGAAGG
H4	15[160]16[144]BLK	ATCGCAAGTATGTAATGCTGATGATAGGAAC
I4	18[143]17[159]BLK	CAACTGTTGCGCCATTGCGCATTCAAACATCA
J4	18[175]16[176]BLK	CTGAGCAAAAATTAATTACATTTTGGGTTA
K4	15[192]18[192]BLK	TCAAATATAACCTCCGGCTTAGGTAACAATTTCAATTTGAAGGCGAATT
L4	18[207]16[208]BLK	CGCGCAGATTACCTTTTTAATGGGAGAGACT
M4	15[224]17[223]BLK	CCTAAATCAAAATCATAGGTCTAACAGTA
N4	18[239]16[240]BLK	CCTGATTGCAATATATGTGAGTGATCAATAGT
O4	15[256]18[256]BLK	GTGATAAAAAGACGCTGAGAAGAGATAACCTTGCTTCTGTTCCGGGAGA
P4	18[271]16[272]BLK	CTTTTACAAAATCGTCGCTATTAGCGATAG
A5	13[32]15[31]BLK	AACGCAAAATCGATGAACGGTACCGGTTGA
B5	16[47]14[48]BLK	ACAAACGGAAGCCCAAAAACACTGGAGCA
C5	13[64]15[63]BLK	TATATTTTGCATTGCCTGAGAGTGGAAAGATT
D5	16[79]14[80]BLK	GCGAGTAAAAATTTAAATTGTTACAAAG
E5	13[96]15[95]BLK	TAGGTAAACTATTTTTGAGAGATCAAACGTTA
F5	16[111]14[112]BLK	TGTAGCCATTAATTCGCATTAATGCGGGA
G5	13[128]15[127]BLK	GAGACAGCTAGCTGATAAATTAATTTTTGT
H5	13[160]14[144]BLK	GTAATAAGTTAGGCAGAGGCATTTATGATATT
I5	16[143]15[159]BLK	GCCATCAAGCTCATTTTTAACCACAAATCCA
J5	16[175]14[176]BLK	TATAACTAACAAGAACGCGAGAACGCCAA
K5	13[192]15[191]BLK	GTAAAGTAATCGCCATTTTAACAAAACCTTTT
L5	16[207]14[208]BLK	ACCTTTTTATTTTAGTTAATTTTATAGGGCTT
M5	13[224]15[223]BLK	ACAACATGCCAACGCTCAACAGTCTTCTGA
N5	16[239]14[240]BLK	GAATTTATTTAATGGTTGAAATATTCTTACC
O5	13[256]15[255]BLK	GTTTATCAATATGCGTTATACAAACCGACCGT
P5	16[271]14[272]BLK	CTTAGATTTAAGGCGTTAAATAAAGCCTGT
A6	11[32]13[31]BLK	AACAGTTTTGTACCAAAAACATTTTATTTT
B6	14[47]12[48]BLK	AACAAGAGGGATAAAAATTTTAGCATAAAGC

C6	11[64]13[63]BLK	GATTTAGTCAATAAAGCCTCAGAGAACCCTCA
D6	14[79]12[80]BLK	GCTATCAGAAATGCAATGCCTGAATTAGCA
E6	11[96]13[95]BLK	AATGGTCAACAGGCAAGGCAAAGAGTAATGTG
F6	14[111]12[112]BLK	GAGGGTAGGATTCAAAAGGGTGAGACATCCAA
G6	11[128]13[127]BLK	TTTGGGGATAGTAGTAGCATTAAAAGGCCG
H6	11[160]12[144]BLK	CCAATAGCTCATCGTAGGAATCATGGCATCAA
I6	14[143]13[159]BLK	CAACCGTTTCAAATCACCATCAATTCGAGCCA
J6	14[175]12[176]BLK	CATGTAATAGAATATAAAGTACCAAGCCGT
K6	11[192]13[191]BLK	TATCCGGTCTCATCGAGAACAAGCGACAAAAG
L6	14[207]12[208]BLK	AATTGAGAATTCTGTCCAGACGACTAAACCAA
M6	11[224]13[223]BLK	GCGAACCTCCAAGAACGGGTATGACAATAA
N6	14[239]12[240]BLK	AGTATAAAGTTCAGCTAATGCAGATGTCTTTC
O6	11[256]13[255]BLK	GCCTTAAACCAATCAATAATCGGCACGCGCCT
P6	14[271]12[272]BLK	TTAGTATCACAAATAGATAAGTCCACGAGCA
A7	9[32]11[31]BLK	TTTACCCCAACATGTTTTAAATTTCCATAT
B7	12[47]10[48]BLK	TAAATCGGGATTCCCAATTCTGCGATATAATG
C7	9[64]11[63]BLK	CGGATTGCAGAGCTTAATTGCTGAAACGAGTA
D7	12[79]10[80]BLK	AAATTAAGTTGACCATTAGATACTTTTGCG
E7	9[96]11[95]BLK	CGAAAGACTTTGATAAGAGGTCATATTTGCGA
F7	12[111]10[112]BLK	TAAATCATATAACCTGTTTAGCTAACCTTTAA
G7	9[128]11[127]BLK	GCTTCAATCAGGATTAGAGAGTTATTTTCA
H7	9[160]10[144]BLK	AGAGAGAAAAAATGAAAATAGCAAGCAAAT
I7	12[143]11[159]BLK	TTCTACTACGCGAGCTGAAAAGTTACCGCGC
J7	12[175]10[176]BLK	TTTTATTTAAGCAAATCAGATATTTTTGT
K7	9[192]11[191]BLK	TTAGACGGCCAAATAAGAAACGATAGAAGGCT
L7	12[207]10[208]BLK	GTACCGCAATTCTAAGAACGCGAGTATTATTT
M7	9[224]11[223]BLK	AAAGTCACAAAATAAACAGCCAGCGTTTTTA
N7	12[239]10[240]BLK	CTTATCATTCCCGACTTGCGGGAGCCTAATTT
O7	9[256]11[255]BLK	GAGAGATAGAGCGTCTTTCCAGAGTTTTGAA
P7	12[271]10[272]BLK	TGTAGAAATCAAGATTAGTTGCTCTTACCA
A8	7[32]9[31]BLK	TTTAGGACAAATGCTTTAAACAATCAGGTC
B8	10[47]8[48]BLK	CTGTAGCTTGACTATTATAGTCAGTTCATTGA
C8	7[56]9[63]BLK	ATGCAGATACATAACGGGAATCGTCATAAATAAGCAAAG
D8	10[79]8[80]BLK	GATGGCTTATCAAAAAGATTAAGAGCGTCC
E8	7[96]9[95]BLK	TAAGAGCAAATGTTTAGACTGGATAGGAAGCC
F8	10[111]8[112]BLK	TTGCTCCTTTCAAATATCGCGTTTTGAGGGGT
G8	7[120]9[127]BLK	CGTTTACCAGACGACAAAAGAAGTTTTGCCATAATTCGA
H8	7[160]8[144]BLK	TTATTACGAAGAACTGGCATGATTGCGAGAGG

CHAPTER 2. HOMOGENEOUS TIRF ILLUMINATION

---

I8	10[143]9[159]BLK	CCAACAGGAGCGAACCAGACCGGAGCCTTTAC
J8	10[175]8[176]BLK	TTAACGTCTAACATAAAAAACAGGTAACGGA
K8	7[184]9[191]BLK	CGTAGAAAATACATACCGAGGAAACGCAATAAGAAGCGCA
L8	10[207]8[208]BLK	ATCCCAATGAGAATTAACCTGAACAGTTACCAG
M8	7[224]9[223]BLK	AACGCAAAGATAGCCGAACAAACCCTGAAC
N8	10[239]8[240]BLK	GCCAGTTAGAGGGTAATTGAGCGCTTTAAGAA
O8	7[248]9[255]BLK	GTTTATTTTGTCACAATCTTACCGAAGCCCTTTAATATCA
P8	10[271]8[272]BLK	ACGCTAACACCCACAAGAATTGAAAATAGC
A9	5[32]7[31]BLK	CATCAAGTAAAACGAACTAACGAGTTGAGA
B9	8[47]6[48]BLK	ATCCCCCTATACCACATTCAACTAGAAAAATC
D9	8[79]6[80]BLK	AATACTGCCCAAAGGAATTACGTGGCTCA
E9	5[96]7[95]BLK	TCATTAGATGCGATTTTAAAGAACAGGCATAG
F9	8[111]6[112]BLK	AATAGTAAACACTATCATAACCCTCATTGTGA
H9	5[160]6[144]BLK	GCAAGGCCTACCAGTAGCACCATGGGCTTGA
I9	8[143]7[159]BLK	CTTTTGCAGATAAAAAACCAAATAAAGACTCC
J9	8[175]6[176]BLK	ATACCCAACAGTATGTTAGCAAATTAGAGC
L9	8[207]6[208]BLK	AAGGAAACATAAAGGTGGCAACATTATCACCG
M9	5[224]7[223]BLK	TCAAGTTTCATTAAAGGTGAATATAAAAAGA
N9	8[239]6[240]BLK	AAGTAAGCAGACACCACGGAATAATATTGAGC
P9	8[271]6[272]BLK	AATAGCTATCAATAGAAAATTCAACATTCA
A10	3[32]5[31]BLK	AATACGTTTGAAAGAGGACAGACTGACCTT
B10	6[47]4[48]BLK	TACGTTAAAGTAATCTTGACAAGAACCGAACCT
D10	6[79]4[80]BLK	TTATACCACCAAATCAACGTAACGAACGAG
E10	3[96]5[95]BLK	ACACTCATCCATGTTACTTAGCCGAAAGCTGC
F10	6[111]4[112]BLK	ATTACCTTTGAATAAGGCTTGCCCAAATCCGC
H10	3[160]4[144]BLK	TTGACAGGCCACCACCAGAGCCGCGATTGTGA
I10	6[143]5[159]BLK	GATGGTTTGAACGAGTAGTAAATTTACCATTA
J10	6[175]4[176]BLK	CAGCAAAAGGAAACGTCACCAATGAGCCGC
L10	6[207]4[208]BLK	TCACCGACGCACCGTAATCAGTAGCAGAACCG
M10	3[224]5[223]BLK	TTAAAGCCAGAGCCGCCACCCTCGACAGAA
N10	6[239]4[240]BLK	GAAATTATTGCCTTTAGCGTCAGACCGGAACC
P10	6[271]4[272]BLK	ACCGATTGTCGGCATTTCGGTGCATAATCA
A11	1[32]3[31]BLK	AGGCTCCAGAGGCTTTGAGGACACGGGTAA
B11	4[47]2[48]BLK	GACCAACTAATGCCACTACGAAGGGGTAGCA
C11	1[64]4[64]BLK	TTTATCAGGACAGCATCGGAACGACACCAACCTAAAACGAGGTCAATC
D11	4[79]2[80]BLK	GCGCAGACAAGAGGCAAAAAGAAATCCCTCAG
E11	1[96]3[95]BLK	AAACAGCTTTTTGCGGGATCGTCAACACTAAA
F11	4[111]2[112]BLK	GACCTGCTCTTTGACCCCCAGCGAGGGAGTTA

G11	1[128]4[128]BLK	TGACAACTCGCTGAGGCTTGCATTATACCAAGCGCGATGATAAA
H11	1[160]2[144]BLK	TTAGGATTGGCTGAGACTCCTCAATAACCGAT
I11	4[143]3[159]BLK	TCATCGCCAACAAAGTACAACGGACGCCAGCA
J11	4[175]2[176]BLK	CACCAGAAAGGTTGAGGCAGGTGATGAAAG
K11	1[192]4[192]BLK	GCGGATAACCTATTATTCTGAAACAGACGATTGGCCTTGAAGAGCCAC
L11	4[207]2[208]BLK	CCACCCTCTATTACAAAACAAATACCTGCCTA
M11	1[224]3[223]BLK	GTATAGCAAACAGTTAATGCCCAATCTCTA
N11	4[239]2[240]BLK	GCCTCCCTCAGAATGAAAGCGCAGTAACAGT
O11	1[256]4[256]BLK	CAGGAGGTGGGGTCAGTGCCTTGAGTCTCTGAATTTACCGGAACCAG
P11	4[271]2[272]BLK	AAATCACCTTCCAGTAAGCGTCAGTAATAA
A12	0[47]1[31]BLK	AGAAAGGAACAACTAAAGGAATTCAAAAAAA
B12	2[47]0[48]BLK	ACGGCTACAAAAGGAGCCTTTAATGTGAGAAT
C12	0[79]1[63]BLK	ACAACTTTCAACAGTTTCAGCGGATGTATCGG
D12	2[79]0[80]BLK	CAGCGAAACTTGCTTTCGAGGTGTTGCTAA
E12	0[111]1[95]BLK	TAAATGAATTTTCTGTATGGGATTAATTTCTT
F12	2[111]0[112]BLK	AAGGCCGCTGATACCGATAGTTGCGACGTTAG
G12	0[143]1[127]BLK	TCTAAAGTTTTGTCGTCTTCCAGCCGACAA
H12	0[175]0[144]BLK	TCCACAGACAGCCCTCATAGTTAGCGTAACGA
I12	2[143]1[159]BLK	ATATTCCGAACCATCGCCCACGCAGAGAAGGA
J12	2[175]0[176]BLK	TATTAAGAAGCGGGTTTTGCTCGTAGCAT
K12	0[207]1[191]BLK	TCACCAGTACAACTACAACGCCTAGTACCAG
L12	2[207]0[208]BLK	TTTCGGAAGTGCCGTCGAGAGGGTGAGTTTCG
M12	0[239]1[223]BLK	AGGAACCCATGTACCGTAACACTTGATATAA
N12	2[239]0[240]BLK	GCCCGTATCCGGAATAGGTGTATCAGCCCAAT
O12	0[271]1[255]BLK	CCACCCTCATTTTCAGGGATAGCAACCGTACT
P12	2[271]0[272]BLK	GTTTTAACTTAGTACCGCCACCCAGAGCCA

**Supplementary Table 2 | List of biotinylated staples**

No	Pos	Name	Sequence	Mod
1	C02	18[63]20[56]BIOTIN	ATTAAGTTTTACCGAGCTCGAATTCGGGAAACCTGTCGTGC	5'-BT
2	C09	4[63]6[56]BIOTIN	ATAAGGGAACCGGATATTCATTACGTCAGGACGTTGGGAA	5'-BT
3	G02	18[127]20[120]BIOTIN	GCGATCGGCAATTCACACAACAGGTGCCTAATGAGTG	5'-BT
4	G09	4[127]6[120]BIOTIN	TTGTGTCGTGACGAGAAACACCAAATTTCAACTTTAAT	5'-BT
5	K02	18[191]20[184]BIOTIN	ATTCATTTTTGTTTGGATTATACTAAGAAACCACCAGAAG	5'-BT
6	K09	4[191]6[184]BIOTIN	CACCCTCAGAAACCATCGATAGCATTGAGCCATTTGGGAA	5'-BT

7	O02	18[255]20[248]BIOTIN	AACAATAACGTAAAACAGAAATAAAAATCCTTTGCCCGAA	5'-BT
8	O09	4[255]6[248]BIOTIN	AGCCACCACTGTAGCGCGTTTTCAAGGGAGGGAAGGTAAA	5'-BT

Supplementary Table 3 | Imaging parameters

Figure	Sample	Origami dilution (after PEG purification)	Docking site sequence	Imager concentration (nM)	Imaging Buffer	Laser power before objective (mW)	Exposure time (ms)	Frames	Binning
1	20-nm-grid	1:1	P1 (9 nt)	4	B	Gauss: 1.5 Flat-top: 2.4	200	200	16x16
2c,d,e SI_Fig. 2	20-nm-grid	1:80	P1 (9 nt)	4	B	Gauss: 45 Flat-top: 77	200	5,000	2x2
2f,g 2h (9 nt) SI_Fig. 3,4 (9 nt)	20-nm grid	1:80	P1 (9 nt)	4	B	Gauss: 45 Flat-top: 45	200	13,000	2x2
2h (8 nt) SI_Fig. 3,4 (8 nt)	20-nm-grid	1:80	P1 (8 nt)	4	B	Gauss: 45 Flat-top: 45	200	13,000	2x2
3a,b,c SI_Fig. 5	20-nm-grid	1:80	P1 (9 nt)	4	B	Gauss: 45 Flat-top: 77	200	5,000	2x2
3d	10-nm-grid	1:100	P1 (9 nt)	0.5	1× B 1× Trolox 1× PCA 1× PCD	Flat-top: 77	200	25,000	2x2
3e,f SI_Fig. 6	20-nm-grid	1:80	P1 (9 nt)	20	B	Gauss: 78 Flat-top: 132	200	10,000	2x2
4 SI_Fig. 8,9	COS-7	-	P1 (8 nt)	0.15	1× C 1× Trolox 1× PCA 1× PCD	Gauss: 42 Flat-top: 25	150	60,000	2x2
SI_Fig. 7	COS-7	-	P1 (9 nt)	0.2	1× C 1× Trolox 1× PCA 1× PCD	Gauss: 90 Flat-top: 153	150	13,000	2x2
SI_Fig. 11	20-nm-grid	1:80	P1 (9 nt)	4	B	Gauss: 45 Flat-top: 24, 45, 76	200	5,000	2x2

**Supplementary Table 4 | Used DNA-PAINT sequences**

Shortname (docking site length)	Docking sequence	Imager sequence	Experiment
P1 (9 nt)	TT ATACATCTA	CTAGATGTAT-Cy3b	All except the ones stated below
P1 (8 nt)	TT ATACATCT	CTAGATGTAT-Cy3b	Fig. 2h SI_Fig. 6
P1 (10 nt)	TT ATACATCTAG	AGATGTAT-Cy3b	Fig. 4 SI_Fig. 8

**Supplementary references**

1. Schnitzbauer, J., Strauss, M. T., Schlichthaerle, T., Schueder, F. & Jungmann, R. Super-resolution microscopy with DNA-PAINT. *Nat. Protoc.* **12**, 1198 (2017).





# 3

## Localization-Based Fluorescence Correlation Spectroscopy

### 3.1 Motivation and Summary

Although SMLM is theoretically able to pinpoint the position of individual molecules, the limited photon budgets of dyes, imperfect labeling strategies and the physical size of the label (e.g. antibodies) cause localizations from an individual emitter to be scattered around its true position. Hence, experimentally achieved localization precisions are often not sufficient to visually resolve molecular complexes (e.g. individual monomers in a dimeric complex). However, since in SMLM each targeted molecule contributes a certain number of localizations to the SR image a quantitative analysis of the collected localizations from a specific (nanoscopic) volume in principle allows to infer back on the hidden number of targeted molecules within this volume. Therefore, there has been a multitude of studies dedicated to the problem of ‘molecular counting’ in SMLM based on either (i) a priori knowledge of the blinking dynamics or the number of localizations per fluorescence marker (e.g., via supplementary experiments or theoretical modeling) or (ii) on an initial calibration directly within the sample by using isolated localization clusters originating from an assumed number of fluorescent molecules as a reference. Also for DNA-PAINT a counting approach termed quantitative PAINT (qPAINT) has been developed, based on calibration of the imager influx (to a single docking strand). Here, we introduce lbFCS as the first self-calibrating molecular counting approach in combination with DNA-PAINT. Self-calibration is achieved by imaging the same set of target molecules at three different imager concentrations allowing extraction of average hybridization rates and subsequent counting of docking strands per localization cluster. In order to reduce photo-physical artifacts to a minimum, lbFCS employs much lower excitation intensities than the intensities used to achieve maximum localization precision in DNA-PAINT imaging. In proof-of-principle experiments on DNA origami we demonstrated that lbFCS is able to extract hybridization rates at precisions better than 5 % and is able to determine molecular copy numbers over a wide range starting from a single to 50 docking strands per origami.

3.2 PUBLICATION P2: Toward Absolute Molecular Numbers in DNA-PAINT

# Toward Absolute Molecular Numbers in DNA-PAINT

Johannes Stein, Florian Stehr, Patrick Schueler, Philipp Blumhardt,  
Florian Schueder, Jonas Mücksch, Ralf Jungmann and Petra Schwille

*Author contributions:*

J.S. and **F.St** contributed equally. J.S., **F.St**, R.J., and P.Schwille conceived the study. J.S. designed and performed the experiments, analyzed and interpreted the data, and wrote the manuscript. **F.St** designed and performed the experiments, analyzed and interpreted data, and wrote the manuscript. **F.St** wrote the code and J.S. edited code. P.Schueler. folded DNA origami structures, performed experiments, and analyzed data. P.B., F.Sch. and J.M. performed initial experiments and interpreted the data. R.J. and P.Schwille supervised the study. **All authors** revised the manuscript and have given approval to the final version of the manuscript.

*published in*

Nano Letters 2019, 19, 11, 8182-8190

*Reprinted from [78] under the [CC BY-NC 4.0 license](#).*

This is an open access article published under a Creative Commons Attribution (CC-BY) License, which permits unrestricted use, distribution and reproduction in any medium, provided the author and source are cited.



NANO LETTERS

Cite This: *Nano Lett.* 2019, 19, 8182–8190

Letter

pubs.acs.org/NanoLett

## Toward Absolute Molecular Numbers in DNA-PAINT

Johannes Stein,<sup>†,§</sup> Florian Stehr,<sup>†,§</sup> Patrick Schueler,<sup>†</sup> Philipp Blumhardt,<sup>†</sup> Florian Schueder,<sup>†,‡</sup> Jonas Mücksch,<sup>†</sup> Ralf Jungmann,<sup>†,‡</sup> and Petra Schwille<sup>\*,†,‡</sup>

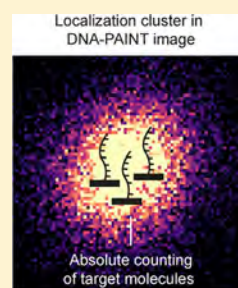
<sup>†</sup>Max Planck Institute of Biochemistry, 82152 Martinsried, Germany

<sup>‡</sup>Faculty of Physics, Ludwig Maximilian University, 80539 Munich, Germany

### Supporting Information

**ABSTRACT:** Single-molecule localization microscopy (SMLM) has revolutionized optical microscopy, extending resolution down to the level of individual molecules. However, the actual counting of molecules relies on preliminary knowledge of the blinking behavior of individual targets or on a calibration to a reference. In particular for biological applications, great care has to be taken because a plethora of factors influence the quality and applicability of calibration-dependent approaches to count targets in localization clusters particularly in SMLM data obtained from heterogeneous samples. Here, we present localization-based fluorescence correlation spectroscopy (lbFCS) as the first absolute molecular counting approach for DNA-points accumulation for imaging in nanoscale topography (PAINT) microscopy and, to our knowledge, for SMLM in general. We demonstrate that lbFCS overcomes the limitation of previous DNA-PAINT counting and allows the quantification of target molecules independent of the localization cluster density. In accordance with the promising results of our systematic proof-of-principle study on DNA origami structures as idealized targets, lbFCS could potentially also provide quantitative access to more challenging biological targets featuring heterogeneous cluster sizes in the future.

**KEYWORDS:** DNA-PAINT, super-resolution microscopy, single-molecule localization microscopy (SMLM), molecular counting, fluorescence correlation spectroscopy (FCS)



The advent of super-resolution (SR) microscopy has revolutionized life science research by providing visual access to specific biological structures at the nanoscale.<sup>1–4</sup> The SR methods summarized as single-molecule localization microscopy (SMLM), such as stochastic optical reconstruction microscopy<sup>3</sup> (STORM), photoactivated localization microscopy<sup>4</sup> (PALM), and (DNA)-points accumulation for imaging in nanoscale topography<sup>5,6</sup> (PAINT) circumvent the diffraction limit by acquiring image sequences of a “blinking” target structure by stochastically activating only a small subset of all fluorescent labels at a time. Thus, these methods enable localization of individual dye molecules in each camera frame and downstream rendering of SR images from the localizations obtained over all frames. Based on the fact that each targeted molecule contributes a certain number of localizations to the SR image, SMLM has been employed as a quantitative tool to count molecules for nearly a decade.<sup>7,8</sup> Extensive efforts have been made in this direction particularly for the methods STORM/PALM<sup>7–22</sup> mostly based on either (i) a priori knowledge of the blinking dynamics or the number of localizations per fluorescence marker (e.g., via supplementary experiments or theoretical modeling) or (ii) on an initial calibration directly within the sample by using isolated localization clusters originating from an assumed number of fluorescent molecules as a reference. Because a multitude of factors can influence the blinking dynamics locally in the sample,<sup>7,8</sup> a calibration directly within the sample as in (ii) is

presumably the preferred option. Either way, however, when applying one of these counting approaches to localization clusters of unknown size, only relative counting results are obtained, determined by the a priori assumptions or by the assumed number of molecules within reference localization clusters.

In the special case of DNA-PAINT, an approach for molecular counting has been proposed, termed quantitative PAINT (qPAINT),<sup>23</sup> which exploits the programmable hybridization of single-stranded and fluorescently labeled DNA probes (“imagers”) to their complementary “docking strands” (DSs) fixed as labels to the target molecules. DNA-PAINT hence decouples the necessary “blinking” in SMLM from the photophysical properties of the fluorescent markers.<sup>7,24</sup> However, when extracting DNA hybridization dynamics from DNA-PAINT data for molecular counting, one still has to consider several pitfalls both at the stage of data acquisition and post processing. On the acquisition side, this includes the choice of optimized illumination schemes for uniform spot detection efficiency<sup>25</sup> as well as minimizing photoinduced damage.<sup>26</sup> As typically high laser intensities are used in order to gain spatial resolution,<sup>27</sup> fluorescence bursts recorded during DNA-PAINT acquisition are usually limited

**Received:** August 28, 2019

**Revised:** September 16, 2019

**Published:** September 19, 2019



ACS Publications

© 2019 American Chemical Society

8182

DOI: 10.1021/acs.nanolett.9b03546  
*Nano Lett.* 2019, 19, 8182–8190

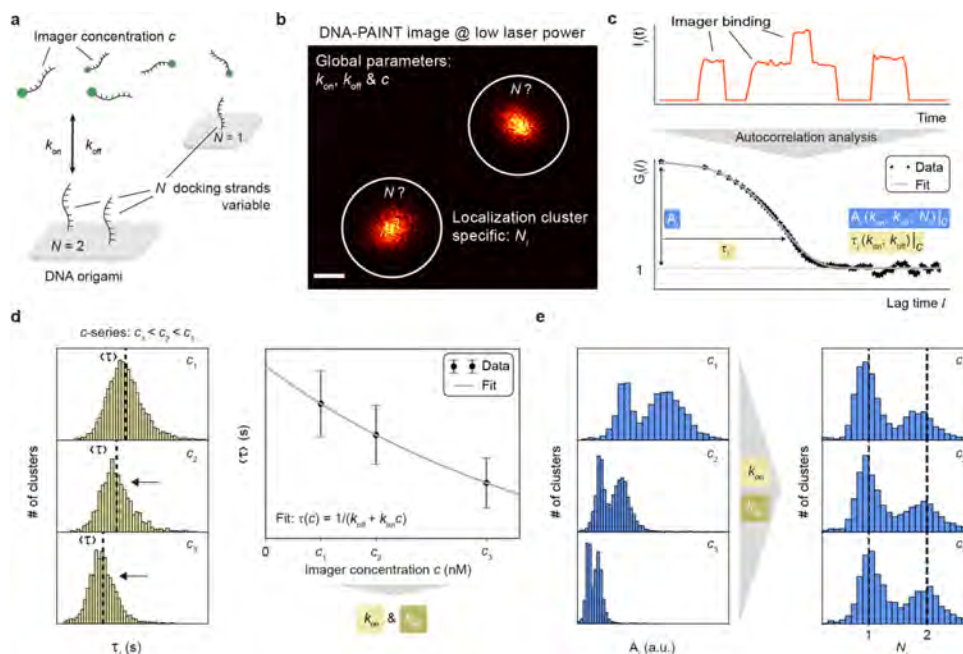


**Figure 1.** Principle of absolute molecular counting with lbFCS. (a) DNA-PAINT schematic for imaging DNA origami nanostructures exhibiting a variable number of docking strands (DSs)  $N$  (either  $N = 1$  or  $N = 2$ ). (b) DNA-PAINT image acquired at low laser power showing the two DNA origami from (a). The spatial resolution does not suffice to robustly distinguish the number of DSs  $N_i$  in the DNA-PAINT image. All localization clusters in an image are automatically detected as circular “picks” (white circles) for downstream DS counting analysis. (c) Top: for each pick, the intensity versus time trace containing the temporal information on imager binding and unbinding is analyzed by computing the autocorrelation function. Bottom: the computed autocorrelation curve of the intensity trace shows a characteristic monoexponential decay and is well described by the fit model with the two parameters amplitude  $A_i$  and characteristic decay time  $\tau_i$  (eqs 1 and 2). (d) Extraction of DNA hybridization rates via imager concentration series. Left: histograms of  $\tau_i$  distributions from all identified localization clusters (passing the filtering procedure as in Supplementary Figure 3) in the DNA-PAINT images of the same target, measured at three different imager concentrations  $c$ . The mean ( $\tau$ ) (black dashed lines) decreases with  $c$ , as expected from eq 2. Right: Fitting eq 2 to  $\langle \tau \rangle$  versus  $c$  yields  $k_{on}$  and  $k_{off}$ . (e) Left: distribution of  $A_i$  obtained from the same clusters as in the histograms in (d). Right: reformulating eq 1 and inserting  $(k_{on}, k_{off}, c)$  allows to convert each  $A_i$  to the number of DSs  $N_i$  in each cluster over all samples with peaks at  $N = 1$  and  $N = 2$  (black dashed lines). Scale bars: 50 nm in (b). Error bars correspond to standard deviation.

by photobleaching of the dye rather than the actual dissociation of the imager strands—an effect that can be accompanied by the photoinduced depletion of DSs during the course of a measurement.<sup>26</sup> Furthermore, qPAINT requires adjustment of the imager concentration to the expected density of DSs, limiting the applicability to biological samples, which might exhibit a heterogeneous distribution of DS densities.<sup>23</sup> On the postprocessing side, counting with qPAINT is also relative as it relies on the calibration to the hybridization kinetics of single DSs.<sup>23</sup>

In this study, we introduce localization-based fluorescence correlation spectroscopy (lbFCS) as a quantitative tool for DNA-PAINT that, to our knowledge, for the first time allows absolute molecular ensemble counting in clusters of SMLM data. We first show that autocorrelation analysis of fluorescence fluctuations similar to classical FCS<sup>28,29</sup> can be applied to localization clusters in DNA-PAINT images (i.e., the rendered localizations) of DNA origami structures<sup>30</sup> allowing the extraction of imager binding kinetics. Following previous work,<sup>31</sup> our approach is based on imaging a sample at three different imager concentrations allowing extraction of the

hybridization rates via lbFCS at a precision of better than 5% and, most importantly, independent of the number of DSs per localization cluster. The DNA hybridization rates obtained over all localization clusters serve as calibration for lbFCS to subsequently count the number of DSs per cluster in each of the three samples. In order to minimize photoinduced damage and to obtain the true imager binding kinetics, we reduce the laser intensity for lbFCS measurements to a minimum while still allowing for efficient spot detection but at the cost of spatial resolution. In a benchmark study of lbFCS on DNA origami structures with a predesigned number of DSs, we additionally image each field of view (FOV) first at a low and then at a high laser power. This allows us to spatially resolve individual DSs as a visual ground truth for the lbFCS counting results over all localization clusters. Finally, we show that via lbFCS we can extend the restriction of qPAINT where the cluster densities (number of DSs) determine the applicable imager concentration. Over a wide range of cluster densities, we show that lbFCS counting results are in good agreement with the visual ground truth.

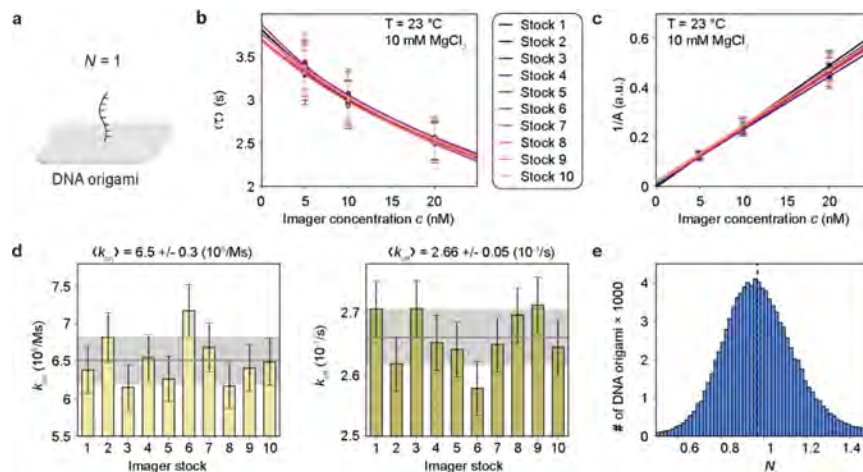


**Figure 2.** Experimental validation of lbFCS. (a) The 1DS structures with  $N = 1$  for testing the lbFCS approach. (b) Repetition of 10 concentration series each with freshly prepared imager stocks ( $10 \times 3$  samples).  $I_i(t)$  versus  $c$  fit for each concentration series demonstrating high reproducibility. (c)  $1/A$  versus  $c$  fits show similar reproducibility. The fits passing through the origin yield that the concentration ratios were adjusted correctly. (d) Sets of  $k_{\text{on}}$  (left, light green) and  $k_{\text{off}}$  (right, dark green) extracted from the fits in (b) for each imager stock. Mean and standard deviation are given as gray line and light gray area, respectively. (e) Histogram of lbFCS counting results  $N$  over all 30 samples from the concentration series on 1DS structures. The black dashed line indicates the median at  $N = 0.97 \pm 0.11$ . Error bars correspond to standard deviation in the case of  $\langle \tau \rangle$ ,  $k_{\text{on}}$ , and  $k_{\text{off}}$  and interquartile range in the case of  $1/A$ .

**Results and Discussion. The Principle of lbFCS.** As model targets for molecular counting with DNA-PAINT in this study we employed DNA origami,<sup>30</sup> a method allowing the precise and large scale production of artificial nanostructures from DNA as building material. In the context of DNA-PAINT, DNA origami have been extensively used for creating nanometer patterns of DSs as ideal benchmarking systems for the obtainable spatial resolution of the used microscope.<sup>6,32,33</sup> In the following, we outline how to count the number of DSs on DNA origami structures in DNA-PAINT images with lbFCS (a detailed step-by-step description of all analysis steps can be found in Supplementary Figure 1). Figure 1a shows a DNA-PAINT schematic of two surface-immobilized DNA origami, one with two DSs ( $N = 2$ ) and the other with a single DS ( $N = 1$ ). Freely diffusing imagers bind to the DSs at association rate  $k_{\text{on}}$  and unbind at dissociation rate  $k_{\text{off}}$ , thereby generating the characteristic blinking required for downstream SMLM reconstruction. The concentration of imager strands is denoted as  $c$ . DNA-PAINT imaging was performed on a custom-built total internal reflection fluorescence (TIRF) microscope with a homogeneous (“flat-top”) intensity profile for optimized acquisition conditions<sup>25</sup> and temperature control (see Supplementary Figure 2a for a detailed setup sketch). A low laser power was selected to obtain imager dissociation rates unbiased by photobleaching (Supplementary Figure 2b) while still preserving the ability of robust spot detection. Albeit the reduction in laser power minimizes photoinduced damage during acquisition, it comes at the cost of reduced spatial resolution leaving clusters of localizations that do not allow counting of the number of DSs by eye (Figure 1b). However, lbFCS allows to count the number of DSs per structure solely based on the assumptions that (1) every target structure in the sample is subject to the same imager concentration  $c$  and (2) all individual DSs of the

target structures bind imager strands with equal hybridization rates given by  $k_{\text{on}}$  and  $k_{\text{off}}$ . This implies that the values  $k_{\text{on}}$  and  $k_{\text{off}}$  are determined for all structures in one sample (i.e., globally) by the designed sequence of the DS and the imager strand for a fixed set of environmental conditions (temperature, buffer, and so forth). Around each automatically detected cluster  $i$  in an image we define a circular region referred to as “pick” (white circles in Figure 1b) for which we plot the respective intensity versus time trace  $I_i(t)$  containing the temporal information on imager binding and unbinding to the specific target structure (Figure 1c, top). From these, we subsequently compute the autocorrelation curves  $G_i(l)$  (Figure 1c, bottom) which are well described by the monoexponential fit model previously derived for surface-integrated (SI)-FCS:<sup>31,34,35</sup>  $G_i(l) = A_i e^{-l/\tau_i} + 1$ . Here,  $l$  is defined as the autocorrelation lag time,  $A_i$  as the amplitude of the autocorrelation function at zero lag time  $G_i(l = 0)$  and  $\tau_i$  as the characteristic exponential decay constant. Following previous derivations,<sup>31,34,35</sup> the model parameters are defined as

$$A_i(k_{\text{on}}, k_{\text{off}}; N_i)_c = \frac{1}{N_i} \frac{k_{\text{off}}}{k_{\text{on}} c} \quad (1)$$

and

$$\tau_i(k_{\text{on}}, k_{\text{off}})_c = \frac{1}{k_{\text{on}} c + k_{\text{off}}} \quad (2)$$

Referring to the previous assumptions of global hybridization rates and imager concentration, one can readily see that  $\tau_i$  is only a function of the global rate constants  $k_{\text{on}}$  and  $k_{\text{off}}$  meaning that all picks in one sample of imager concentration  $c$  should yield the same value of  $\tau_i$  within the uncertainty of the measurement. As a consequence the mean value  $\langle \tau \rangle$  over all

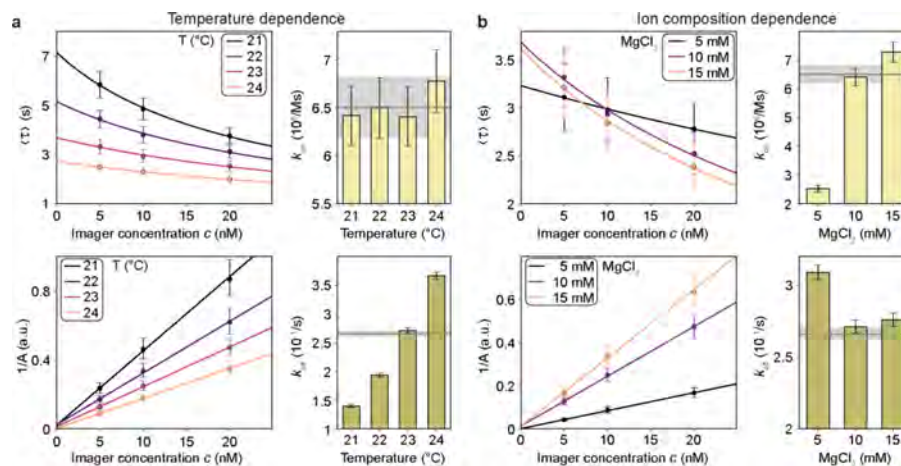


**Figure 3.** Temperature and ion composition affecting DNA hybridization rates. (a) lbfCS concentration series with 1DS samples at different temperatures, highlighting the temperature dependence of DNA hybridization rates (at fixed  $[MgCl_2] = 10$  mM). (b) lbfCS concentration series with 1DS samples at different  $MgCl_2$  concentrations affecting the DNA hybridization rates (at fixed  $T = 23$  °C). Gray lines and light gray shaded areas correspond to the mean and the standard deviation, respectively, of the hybridization rates at standard conditions ( $T = 23$  °C and  $[MgCl_2] = 10$  mM, see Figure 2d). Error bars correspond to standard deviation in the case of  $\langle \tau \rangle$ ,  $k_{on}$ , and  $k_{off}$  and interquartile range in the case of  $1/A$ .

picks suffices for the extraction of the rate constants. The amplitude  $A_i$  in contrast is subject to the same global parameters but additionally depends on the number of DSs  $N_i$  in each pick. lbfCS makes use of these dependencies in order to extract both the hybridization rate constants  $k_{on}$  and  $k_{off}$  and the number of DSs  $N_i$  in each pick by the following procedure. First, we prepare and image three DNA origami samples (here exemplarily containing both  $N = 1$  and  $N = 2$  DNA origami structures) at three different imager concentrations ( $c_1 < c_2 < c_3$ ) and automatically detect all clusters in the three resulting SR images (see Supplementary Figure 1). Next, we autocorrelate all intensity traces and remove clusters exhibiting nonrepetitive binding and/or binding dynamics deviating from a clear monoexponential behavior in a filtering step before further analysis (see Supplementary Figure 3). The left panel in Figure 1d shows the resulting  $\tau_i$  histograms for all remaining clusters in each of the three images. As expected from eq 2, we observe a shift of the distributions toward lower values with increasing  $c$  corresponding to a decrease of the mean value  $\langle \tau \rangle$ . Following the aforementioned reasoning, the mean value  $\langle \tau \rangle$  for each imager concentration  $c$  (Figure 1d, right panel) yields the global rate constants  $k_{on}$  and  $k_{off}$  by fitting eq 2. An analogous approach has been previously demonstrated using SI-FCS for the same system (i.e., DNA-PAINT on surface immobilized DNA origami) using an ensemble autocorrelation analysis of the raw intensity fluctuations integrated over larger arrays of camera pixels (originating from thousands of DNA origami), which allowed for the extraction of imager hybridization rates via a concentration series.<sup>31</sup> Here, we show that this approach can be directly transferred to each localization cluster in a DNA-PAINT image of subdiffraction spatial resolution. This allows one to make further use of the amplitude  $A_i$  of each pick for molecular counting. According to eq 1,  $A_i$  depends on the number of DSs in each cluster resulting in a distribution exhibiting two peaks (for DNA origami either with  $N = 1$  or

$N = 2$ ) in addition to the also concentration-dependent shift, as can be seen in the left panel of Figure 1e. Each  $A_i$  value can be converted into  $N_i$  by reformulating eq 1 to  $N_i = \frac{1}{A_i} \frac{k_{off}}{k_{on}c}$  (Figure 1e, right) and inserting the now available rate constants  $k_{on}$  and  $k_{off}$  together with the respective imager concentration  $c$  of each measurement. Figure 1e, right, shows the distribution of the number of DSs present in each localization cluster (i.e., either one or two DSs).

**Validation of lbfCS.** In order to demonstrate the ability of lbfCS to extract DNA hybridization rates and to count DSs in DNA-PAINT images acquired at low laser power, we first explored the case of a DNA origami design exhibiting just a single DS ( $N = 1$ , referred to as “1DS”), as depicted in Figure 2a, because it is the only case of an implicit counting ground truth. In 10 repetitions of the same experiment over the course of 2 months, we prepared fresh imager stocks at 5, 10, and 20 nM for subsequent low laser power imaging on 1DS samples ( $10 \times 3$  samples, standard conditions: imaging buffer containing 10 mM  $MgCl_2$  and temperature controlled at  $23 \pm 0.1$  °C). lbfCS analysis of the localization clusters showed a good reproducibility with respect to the output parameters  $\tau_i$  and  $A_i$  (Figure 2b,c). The mean (error bar, standard deviation) denoted as  $\langle \tau \rangle$  of the  $\tau_i$  distribution and the median (error bar, interquartile range) denoted as  $A$  of the  $A_i$  distribution ( $N$  and  $N_i$ ) are shown whenever a statistical quantity of an ensemble is presented. The representation of  $1/A$  in Figure 2c is chosen to verify the linear dependency on  $c$  (see eq 1). In addition, the plot serves as a control for whether the imager concentrations have been adjusted in the correct ratios when the fit of eq 1 intersects the y-axis at the origin. Figure 2d shows the scatter in  $k_{on}$  and  $k_{off}$  resulting from the 10 fits in Figure 2b. Over all measurements, we obtained the mean hybridization rates of  $\langle k_{on} \rangle = (6.5 \pm 0.3) \times 10^6 \text{ M}^{-1} \text{ s}^{-1}$  and  $\langle k_{off} \rangle = (2.66 \pm 0.05) \times 10^{-1} \text{ s}^{-1}$  with standard deviations below 5% and 2%, respectively, proving high reproducibility. We attribute this

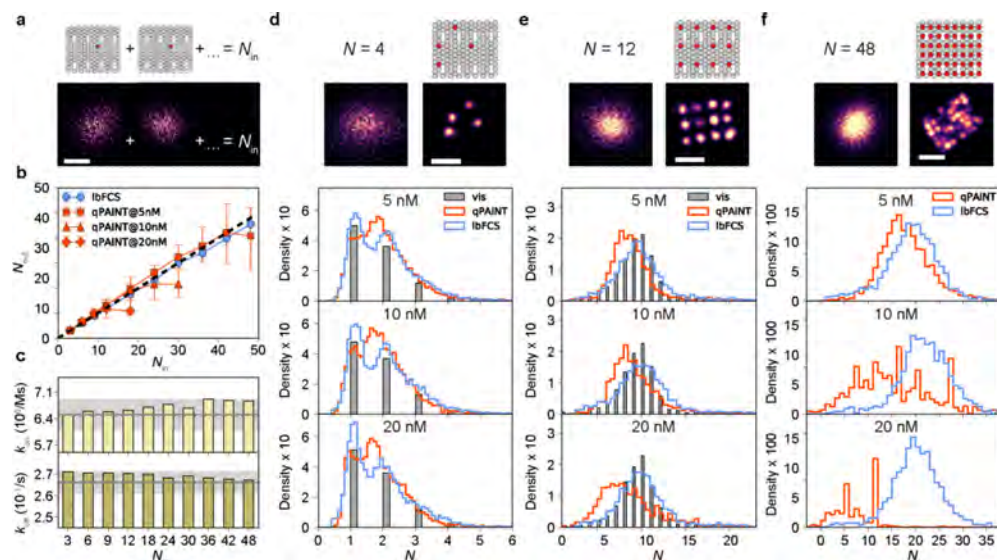


**Figure 4.** Counting of docking strands on DNA origami. (a) Binning of experimental 1DS localization clusters (taken from stock measurements 1–3, see Figure 2) for computationally increasing the number of DSs  $N_{in}$  as input for further testing of counting performance. (b) Median of the counting result  $N_{out}$  versus  $N_{in}$  comparing the counting results obtained via qPAINT at different imager concentrations (red) versus lbFCS (blue); sum over all imager concentrations displayed (see Supplementary Figure 9 for individual lbFCS and qPAINT results). The black dashed line displays a line through the origin of slope one as expected for ideal counting results (i.e.,  $N_{out} = N_{in}$ ). (c) lbFCS extracts correct hybridization rates within the measurement uncertainty independent of  $N_{in}$  ( $k_{on}$  and  $k_{off}$  means (gray lines) and STDs (light gray areas) from Figure 2d). (d) Top: DNA origami design with  $N = 4$  DSs. Exemplary image of the same structure from the low laser power image (left) and the high laser power image for visual counting (right). Bottom: counting results for visual counting (gray), qPAINT (red) and lbFCS (blue). (e) Same as (d), but for  $N = 12$  DSs DNA origami design. Intensity traces that do not exhibit dark times anymore (see Supplementary Figure 7) cannot be analyzed via qPAINT and are not shown in the histograms. Refer to Supplementary Table 1 for total numbers of analyzable clusters per histogram. (f) Same as (d,e) but for  $N = 48$  DSs DNA origami design (no visual count histogram due to too tight DS spacing (10 nm) for robust spot detection). Scale bars: 40 nm in (a,d–f). Error bars in (b) correspond to interquartile range.

high precision to the fact that we are able to minimize the influence of unspecific binding to the surface (Supplementary Figure 4) by only analyzing detected clusters which, in addition, passed the filter criteria (see Supplementary Figure 3). Next, the values ( $k_{on}$ ,  $k_{off}$ ) for each stock were used to count the number of DSs in each of the three samples of the respective concentration series. Figure 2e shows the histogram of  $N_i$  over all 30 samples (>90% of all data points lie within the  $x$ -axis limits; >97 k localization clusters in total) with the median at  $N = 0.97 \pm 0.11$ , which is in good agreement with the initial design of the 1DS structures.

The counting ability of lbFCS is based on the assumption that  $k_{on}$  and  $k_{off}$  are global parameters which do not change during the course of the concentration series measurements. It is hence essential to precisely control the experimental conditions affecting DNA hybridization, such as temperature and buffer ion composition. In order to quantitatively assay these effects, we first repeated the concentration series on 1DS samples at 21–24 °C (1 °C increments, all at 10 mM MgCl<sub>2</sub>), a temperature range which we observed due to the heating of the often enclosed sample space of commercial microscopes during imaging. As reported in many DNA hybridization studies before,<sup>32,36–38</sup> Figure 3a shows that the dissociation rates change considerably (up to ~2.5-fold) over this temperature range, whereas the association rates do not change within the measurement error and show no observable

trend. We also varied the ion composition by changing the standard of 10 mM MgCl<sub>2</sub> by  $\pm 5$  mM (at 23 °C) and again used lbFCS to monitor the effects on both rates, such as the 3-fold increase in  $k_{on}$  between 5 and 10 mM (Figure 3b). However, as long as the rates are kept constant for all three concentration measurements, lbFCS yields the correct counting result of  $N_i = 1$ , independent of the actual temperature or ion composition (Supplementary Figure 5). Finally, the question of how precisely the absolute imager concentrations must be controlled needs to be addressed. In Supplementary Figure 6, we reanalyzed one of the stock measurement series at standard conditions as presented in Figure 1b–e by intentionally assuming higher or lower absolute imager concentrations while keeping the correct concentration ratios. The results clearly show that wrong absolute imager concentrations neither affect the absolute counting ability of lbFCS nor the resulting dissociation rate  $k_{off}$  as long as the correct concentration ratios are preserved (for which the  $1/A$  fit provides control when crossing the origin). However, due to the product  $k_{on}c$  in eq 2, assumed imager concentrations deviating from the “true” value by a factor of  $x$  will result in an obtained association rate multiplied by the inverse factor  $x^{-1}$ . To avoid this ambiguity in order to (relatively) compare obtained association rates we performed a control concentration series on 1DS origamis using the same

imager stock at standard conditions (see Figure 2b–e) for every measurement in this study.

**Molecular Counting.** As a next step, we tested the performance of lbFCS by arbitrarily grouping clusters of  $N = 1$  obtained from earlier 1DS experiments (data taken from stock measurements 1–3; see Figure 2) into clusters of defined  $N > 1$  ( $\equiv N_{\text{in}}$ ) which is equivalent to the simple computational addition of their respective intensity versus time traces (see Figure 4a). This way, we created localization clusters of up to  $N_{\text{in}} = 48$  for each imager concentration ( $c = 5, 10, \text{ and } 20 \text{ nM}$ ) and analyzed them using lbFCS and qPAINT. It should be mentioned at this point that in contrast to lbFCS the counting of DSs with qPAINT needs a calibration<sup>23</sup> by the influx rate  $k_{\text{on}}^{\text{qPAINT}} c$  obtained from clusters containing a single DS only (see Supplementary Figure 7 for the principle of the qPAINT approach). Supplementary Figure 8 displays the results as obtained by qPAINT analysis of the 1DS experiments of Figure 2b–e. The following results from molecular counting with qPAINT hence rely on a calibration association rate of  $k_{\text{on}}^{\text{qPAINT}} = (7.7 \pm 0.2) \times 10^6 \text{ M}^{-1} \text{ s}^{-1}$ . With respect to the error we would like to note that also  $k_{\text{on}}^{\text{qPAINT}}$  is profiting from the filtering procedure introduced in Supplementary Figure 3, which in turn is based on the unique property of the autocorrelation analysis of lbFCS to identify and exclude clusters exhibiting dynamics that deviate from a clear monoexponential behavior.

Figure 4b displays the analysis results  $N_{\text{out}}$  versus  $N_{\text{in}}$  for both analysis methods (for lbFCS the sum over all three imager concentrations is displayed. See Supplementary Figure 9a–c for individual results at  $c = 5, 10, \text{ and } 20 \text{ nM}$ , respectively). As expected, lbFCS does not show any concentration dependence and yields the correct counting results ( $N_{\text{out}} = N_{\text{in}}$ , indicated by black dashed line) over the whole range of  $N_{\text{in}}$ . In contrast, qPAINT starts underestimating the correct number of DSs at a certain cluster size, an effect depending on the imager concentration (whereas for  $c = 5 \text{ nM}$  qPAINT starts deviating from the linear relation at  $N_{\text{in}} \sim 48$ , for  $c = 20 \text{ nM}$  the deviation already occurs at  $N_{\text{in}} \sim 12$ ). As explained in Supplementary Figure 10, this is due to the increasing occurrence of simultaneous imager binding to multiple DSs within the same cluster. Because the qPAINT algorithm is based on the extraction of dark times from the intensity versus time trace of a cluster, its intrinsic limit given a certain imager concentration is determined by the maximum number of DSs per cluster  $N$  at which the corresponding intensity trace exhibits only few and, ultimately, no dark times at all anymore (in other words, the cluster is continuously fluorescing during data acquisition due to constant imager turnover). In accordance with this consideration, Figure 4b shows that the higher the imager concentration, the faster this limit determined by  $N$  is reached (see Supplementary Figure 9 for a detailed analysis of the number of unique dark times extracted per cluster for the last qPAINT data points for  $c = 5, 10, \text{ and } 20 \text{ nM}$  at  $N = 48, 30, \text{ and } 18$ , respectively). It should be discussed, however, that our DNA-PAINT data deviates from the type of data previously subjected to qPAINT analysis<sup>23</sup> in two aspects: (i) due to the low laser intensity, the bright times are an order of magnitude longer (i.e., not limited by fast photobleaching as in classical high-resolution DNA-PAINT) and (ii) the imager-DS sequence design employed in this study has a significantly higher  $k_{\text{on}}^{\text{qPAINT}}$  (here  $7.7 \times 10^6 \text{ M}^{-1} \text{ s}^{-1}$  versus previously<sup>23</sup>  $1 \times 10^6 \text{ M}^{-1} \text{ s}^{-1}$ ). Hence, our probability of simultaneous binding events is

largely increased for a given  $N$  and imager concentration  $c$  (i.e., the limit of qPAINT is reached already for much smaller  $N$  compared to the previous study<sup>23</sup>).

Having confirmed that lbFCS allows molecular counting over this wide range of DS densities independent of the imager concentration, we next validated the assumption that lbFCS can extract the correct DNA hybridization rates independent of  $N$ . Figure 4c displays that for all  $N_{\text{in}}$  we obtained the same hybridization rates within the measurement uncertainty verifying eq 2 and confirming that  $\tau_i$  is indeed independent of the number of DSs per cluster.

In order to fully experimentally benchmark the counting performance of lbFCS, we designed DNA origami species with higher numbers of DSs ( $N = 4, 12, \text{ and } 48$ ). Like for the 1DS structures, we prepared three samples per DNA origami species at  $c = 5, 10, \text{ and } 20 \text{ nM}$  and measured each sample first at low laser power. Directly after each low power measurement, we imaged the same FOV at high laser power in order to obtain visual references at high resolution assignable to each of the localization clusters from the low power measurement. The top panel in Figure 4d depicts the  $N = 4$  DNA origami design, an example DNA-PAINT image of a single structure acquired at low laser power (left) and the respective high power image exhibiting the four DSs in the designed pattern (right). We subsequently applied a spot detection algorithm to the high power image in order to automatically count the number of present DSs as a ground truth for the lbFCS and qPAINT results from the low laser power images. The efficiency by which individual staple strands are incorporated into each DNA origami during the folding process is limited and also position dependent,<sup>39</sup> that is, only very few structures feature all DSs from the initial design. The lower panel in Figure 4d shows the counting results of lbFCS (blue) and qPAINT (red) from the low power measurements as well as the visual counting results (gray) from the high power measurements for the three samples of  $N = 4$  structures. Folding of this DNA origami design resulted in structures primarily exhibiting one or two DSs, which can be seen at the distinct peaks in all lbFCS distributions and which is furthermore in good agreement with the visual reference (refer to Supplementary Figure 11a for a comparison of the lbFCS/qPAINT performance with respect to individual integers from the visual inspection). Also qPAINT yields a distribution covering the lbFCS and visual results, even for the sample imaged at  $c = 20 \text{ nM}$  (as expected from Figure 4b for the regime  $N < 6$ ). In contrast, the qPAINT distribution does not feature clear and distinct peaks. Figure 4e illustrates the counting results for the measurement series on the  $N = 12$  structures. Again lbFCS produces counting results which correlate well with the visual counting reference (see Supplementary Figure 11b for integer-wise comparison with visual inspection), both peaking at around  $N \approx 10$  and both exhibiting the same distribution shape. However, for qPAINT we obtained a slightly left-shifted distribution even for the sample imaged at  $c = 5 \text{ nM}$ , which further increased and broadened for the  $c = 10$  and  $20 \text{ nM}$  samples. As expected from Figure 4b, intensity traces extracted from these samples started to lack enough unique dark times for qPAINT analysis (compare Supplementary Figures 7 and 9. The total number of analyzable clusters in each data set from Figure 4d–f are given in Supplementary Table 1). At last, we imaged the series of samples containing  $N = 48$  structures (Figure 4f). As can be seen in the top panel, we were able to partially resolve the DSs tightly packed at a  $10 \text{ nm}$  spacing in

the DNA-PAINT images. However, the spatial resolution did not suffice to robustly run the spot detection algorithm earlier employed for the  $N = 4$  and  $N = 12$  origami for an unbiased visual ground truth. The DS incorporation efficiency leads to a broader spread in the actual number of DSs over all DNA origami structures with increasing  $N$ , which is in agreement with a broadening in the distribution of counted DSs by lbFCS compared to the previous DNA origami designs with less DSs. However, for all three imager concentrations lbFCS yielded the same counting results with a median of around  $N \approx 25$ . Although for the  $c = 5$  nM sample the qPAINT results are in relatively good agreement with lbFCS, the distribution for the 10 nM sample is broadened and again shifted to the left due to lacking unique dark times extractable from the respective intensity versus time traces. As expected from Figure 4b, for  $c = 20$  nM the DS density of the DNA origami design is already beyond the applicable limit of qPAINT since almost 75% of all clusters did not exhibit a single dark time anymore (see Supplementary Table 1).

Finally, we investigated whether even during the low laser power measurements the effect of photoinduced DS depletion via reactive oxygen species (ROS) generated upon excitation of dye molecules can be observed, as previously described by Blumhardt et al.<sup>26</sup> For the  $N = 12$  structure, we repeated the concentration series with fresh samples this time measuring four times longer than a usual low power measurement without the use of an oxygen scavenging and triplet state quenching system ( $4 \times 30$  min). We then temporally segmented the total data set into four subsets and analyzed each subset individually via lbFCS. Supplementary Figure 12a depicts the resulting  $\langle \tau \rangle$  versus  $c$  dependencies for all segments. We observed no significant difference between the time segments indicating that hybridization rates were unaffected and giving direct evidence that there was no bleaching of the imager solution (i.e., decreasing  $c$ ) during the course of the 2 h measurement. Bearing this in mind, the clear change in  $1/A$  versus  $c$  as shown in Supplementary Figure 12b is a direct consequence of the depletion of DSs leading to a decrease in  $N$  (compare eq 1). Supplementary Figure 12c shows the counting results over all segments normalized to the value of the first segment for every concentration. For an imager concentration of 20 nM, more than 20% of the DSs were depleted after 2 h of measurement. Furthermore, we observed an increase of the depletion rate with increasing imager concentration which is in agreement with previous results showing that the probability of photo-induced damage scales with the DS occupancy.<sup>26</sup> With respect to the results in Supplementary Figure 12b, this additionally explains why an offset in  $1/A$  is becoming apparent for the later segments, as the  $1/A$  values of different concentrations already originate from origamis of different  $N$  due to different depletion rates.

One of the proposed strategies to circumvent DS depletion is the use of oxygen scavenging systems such as pyranose oxidase, catalase, and glucose (POC) to directly remove ROS from the solution upon generation.<sup>26</sup> We repeated the same extended low power measurement series with POC and Trolox (a commonly used triplet state quencher) added to the imaging buffer. Subsequent lbFCS analysis revealed neither changes in  $\langle \tau \rangle$  nor in  $1/A$  over the four time segments (Supplementary Figure 12d,e). Hence, usage of oxygen scavenging systems allows one to virtually eliminate DS depletion during the low laser power measurements for lbFCS (Supplementary Figure 12e,f).

In conclusion, we presented lbFCS as an absolute counting approach for DNA-PAINT microscopy in a proof-of-principle study targeting DNA origami structures as ideal samples. On the basis of imaging a target of interest at several imager concentrations, we showed that lbFCS allows the extraction of imager hybridization rates at high precision from target clusters independent of the number of DSs within a cluster, which subsequently serves as calibration for counting of DS numbers within all clusters. We first confirmed the measurement principle on DNA origami exhibiting only a single DS and assayed the measurement uncertainty and the influence of experimental conditions such as temperature and buffer ion concentration. Next, we examined the performance of lbFCS to count the increasing number of DSs per cluster and compared the obtained results to the state-of-the-art DNA-PAINT counting approach qPAINT. We first increased the cluster size in a controlled way by grouping experimentally obtained clusters containing only a single DS into clusters of defined  $N$ . The obtained results show that lbFCS yields the correct counts over a range of more than 40 DSs for various imager concentrations in contrast to qPAINT. In addition, the extracted hybridization rates were unaffected by the number of DSs per cluster within the measurement uncertainty. Subsequent experimental benchmarking of lbFCS on DNA origami structures exhibiting multiple DSs yielded counts in good agreement with the visual ground truth obtained from high-resolution images from the respective FOVs. Finally, we could confirm previous results regarding the depletion of DSs in DNA-PAINT.<sup>26</sup> lbFCS is sensitive enough to detect slight changes in  $N$  due to depleted DSs and gave direct evidence that neither the hybridization rates nor the “effective” imager concentrations were affected by the employed low laser intensities during image acquisition. The usage of oxygen scavenging systems helped to virtually eliminate the depletion of DSs, underlining the applicability of our approach.

The work presented in this study was based on surface-immobilized DNA origami structures as model targets for DNA-PAINT microscopy. It should be highlighted that in this case all presented counting results here could also be obtained correctly via qPAINT when the imager concentration is adjusted according to the DS density. qPAINT could in principle also deal with samples containing heterogeneous cluster densities by imaging the sample at different imager concentrations. We particularly see the strength of lbFCS in future applications to DNA-PAINT data of biological samples, where it might be hard to identify enough single DSs for a robust calibration of the qPAINT influx rate. Additionally, local factors such as charge differences or steric hindrance effects introduced, for example, by the labeling linker to the target molecule, might lead to changes in the imager association rate limiting the applicability of the calibration rate obtained from DSs on DNA origami. While lbFCS could potentially solve these problems, the way toward cellular samples bears several difficulties that still remain to be tested. These include, among others, the effects of elevated background fluorescence, robust cluster identification and demands on achievable spatial resolution. We further would like to point out that lbFCS in its current state relies on the identification of spatially well-separated clusters and is hence not applicable to continuous structures (e.g., filaments).

Despite the focus on molecular counting presented here, the scope of lbFCS essentially exceeds the study of specific DNA–DNA interactions as in DNA-PAINT. We see promising

applications translating the high precision of lbFCS to study specific and reversible DNA–protein and protein–protein interactions with one of the species immobilized on a surface. In addition, lbFCS could also find application in structural in vitro studies to count subunits of immobilized multimeric complexes.

When targeting fixed cells, however, future work needs to address possible local changes in DNA hybridization rates, which might lead to large deviations between DSs and clusters. A next step in this direction will be combining lbFCS with Exchange-PAINT<sup>40</sup> in order to acquire the imager concentration series at the same FOV of a sample, potentially providing access to local changes in hybridization rates and allowing direct calibration with the cluster-specific rates for more robust counting. Finally, the same FOV would be imaged at high laser intensity for obtaining a DNA-PAINT image at highest spatial resolution. Complementing high-resolution DNA-PAINT images with an additional layer of robust quantitative information obtained via lbFCS has the potential to move the technology away from artificial or well-studied structures toward physiologically relevant targets and, ultimately, biological discovery.

#### ■ ASSOCIATED CONTENT

##### 📄 Supporting Information

The Supporting Information is available free of charge on the ACS Publications website at DOI: 10.1021/acs.nanolett.9b03546.

Supplementary methods and figures (PDF)

#### ■ AUTHOR INFORMATION

##### Corresponding Author

\*E-mail: [schwille@biochem.mpg.de](mailto:schwille@biochem.mpg.de).

##### ORCID

Johannes Stein: 0000-0002-1335-1120

Florian Schueder: 0000-0003-3412-5066

Jonas Mücksch: 0000-0002-1469-6956

Ralf Jungmann: 0000-0003-4607-3312

Petra Schwille: 0000-0002-6106-4847

##### Author Contributions

J.S., F.Stehr, R.J., and P.Schwille conceived the study. J.S. designed and performed the experiments, analyzed and interpreted the data, and wrote the manuscript. F.Stehr designed and performed the experiments, analyzed and interpreted data, and wrote the manuscript. F.Stehr wrote the code and J.S. edited code. P.Schueler folded DNA origami structures, performed experiments, and analyzed data. P.B., F.Schueder and J.M. performed initial experiments and interpreted the data. R.J. and P.Schwille supervised the study. All authors revised the manuscript and have given approval to the final version of the manuscript.

##### Author Contributions

§J.S. and F. Stehr contributed equally.

##### Funding

This work has been supported in part by the German Research Foundation through the Emmy Noether Program (DFG JU 2957/1-1 to R.J.), the SFB1032 (projects A11 and A09 to R.J. and P. Schwille), the European Research Council through an ERC Starting Grant (MolMap; Grant Agreement 680241 to R.J.) and the Max Planck Society (P.Schwille and R.J.).

#### Notes

The authors declare no competing financial interest.

#### ■ ACKNOWLEDGMENTS

We thank Julian Bauer, Tamara Heermann, Henri Franquelim, Sigrid Bauer, and Katharina Nakel for experimental assistance and helpful discussions. J.S. and F. Stehr acknowledge support from Graduate School of Quantitative Bioscience Munich (QBM). P.B. and J.M. acknowledge support from the International Max Planck Research School for Molecular and Cellular Life Sciences (IMPRS-LS). All authors acknowledge support from the Center for Nano Science (CeNS).

#### ■ ABBREVIATIONS

SMLM, single-molecule localization microscopy; (q)PAINT, (quantitative) points accumulation for imaging in nanoscale topography; DS, docking strand; FCS, fluorescence correlation spectroscopy; lbFCS, localization-based FCS; TIRF, total internal reflection fluorescence; SI-FCS, surface-integrated FCS; FOV, field of view; ROS, reactive oxygen species; POC, pyranose oxidase, catalase, and glucose

#### ■ REFERENCES

- (1) Hell, S. W.; Wichmann, J. Breaking the diffraction resolution limit by stimulated emission: stimulated-emission-depletion fluorescence microscopy. *Opt. Lett.* **1994**, *19*, 780–782.
- (2) Hell, S. W.; et al. The 2015 super-resolution microscopy roadmap. *J. Phys. D: Appl. Phys.* **2015**, *48*, 443001.
- (3) Rust, M. J.; Bates, M.; Zhuang, X. Sub-diffraction-limit imaging by stochastic optical reconstruction microscopy (STORM). *Nat. Methods* **2006**, *3*, 793.
- (4) Betzig, E.; et al. Imaging Intracellular Fluorescent Proteins at Nanometer Resolution. *Science (Washington, DC, U. S.)* **2006**, *313*, 1642–1645.
- (5) Sharonov, A.; Hochstrasser, R. M. Wide-field subdiffraction imaging by accumulated binding of diffusing probes. *Proc. Natl. Acad. Sci. U. S. A.* **2006**, *103*, 18911–18916.
- (6) Schnitzbauer, J.; Strauss, M. T.; Schlichthaerle, T.; Schueder, F.; Jungmann, R. Super-resolution microscopy with DNA-PAINT. *Nat. Protoc.* **2017**, *12*, 1198.
- (7) Baddeley, D.; Bewersdorf, J. Biological Insight from Super-Resolution Microscopy: What We Can Learn from Localization-Based Images. *Annu. Rev. Biochem.* **2018**, *87*, 965–989.
- (8) Nicovich, P. R.; Owen, D. M.; Gaus, K. Turning single-molecule localization microscopy into a quantitative bioanalytical tool. *Nat. Protoc.* **2017**, *12*, 453.
- (9) Annibale, P.; Vanni, S.; Scarselli, M.; Rothlisberger, U.; Radenovic, A. Quantitative Photo Activated Localization Microscopy: Unraveling the Effects of Photoblinking. *PLoS One* **2011**, *6*, No. e22678.
- (10) Annibale, P.; Vanni, S.; Scarselli, M.; Rothlisberger, U.; Radenovic, A. Identification of clustering artifacts in photoactivated localization microscopy. *Nat. Methods* **2011**, *8*, 527.
- (11) Hummer, G.; Fricke, F.; Heilemann, M. Model-independent counting of molecules in single-molecule localization microscopy. *Mol. Biol. Cell* **2016**, *27*, 3637–3644.
- (12) Laplante, C.; Huang, F.; Tebbs, I. R.; Bewersdorf, J.; Pollard, T. D. Molecular organization of cytokinesis nodes and contractile rings by super-resolution fluorescence microscopy of live fission yeast. *Proc. Natl. Acad. Sci. U. S. A.* **2016**, *113*, E5876–LP-E5885.
- (13) Nino, D.; Rafiei, N.; Wang, Y.; Zilman, A.; Milstein, J. N. Molecular Counting with Localization Microscopy: A Bayesian Estimate Based on Fluorophore Statistics. *Biophys. J.* **2017**, *112*, 1777–1785.

- (14) Golfetto, O.; et al. A Platform To Enhance Quantitative Single Molecule Localization Microscopy. *J. Am. Chem. Soc.* **2018**, *140*, 12785–12797.
- (15) Coltharp, C.; Kessler, R. P.; Xiao, J. Accurate Construction of Photoactivated Localization Microscopy (PALM) Images for Quantitative Measurements. *PLoS One* **2012**, *7*, No. e51725.
- (16) Lee, S.-H.; Shin, J. Y.; Lee, A.; Bustamante, C. Counting single photoactivatable fluorescent molecules by photoactivated localization microscopy (PALM). *Proc. Natl. Acad. Sci. U. S. A.* **2012**, *109*, 17436–17441.
- (17) Nan, X.; et al. Single-molecule superresolution imaging allows quantitative analysis of RAF multimer formation and signaling. *Proc. Natl. Acad. Sci. U. S. A.* **2013**, *110*, 18519–18524.
- (18) Puchner, E. M.; Walter, J. M.; Kasper, R.; Huang, B.; Lim, W. A. Counting molecules in single organelles with superresolution microscopy allows tracking of the endosome maturation trajectory. *Proc. Natl. Acad. Sci. U. S. A.* **2013**, *110*, 16015–16020.
- (19) Ehmann, N.; et al. Quantitative super-resolution imaging of Bruchpilot distinguishes active zone states. *Nat. Commun.* **2014**, *5*, 4650.
- (20) Fricke, F.; Beaudouin, J.; Eils, R.; Heilemann, M. One, two or three? Probing the stoichiometry of membrane proteins by single-molecule localization microscopy. *Sci. Rep.* **2015**, *5*, 14072.
- (21) Ricci, M. A.; Manzo, C.; García-Parajo, M. F.; Lakadamyali, M.; Cosma, M. P. Chromatin Fibers Are Formed by Heterogeneous Groups of Nucleosomes In Vivo. *Cell* **2015**, *160*, 1145–1158.
- (22) Rollins, G. C.; Shin, J. Y.; Bustamante, C.; Pressé, S. Stochastic approach to the molecular counting problem in superresolution microscopy. *Proc. Natl. Acad. Sci. U. S. A.* **2015**, *112*, E110–LP-E118.
- (23) Jungmann, R.; et al. Quantitative super-resolution imaging with qPAINT. *Nat. Methods* **2016**, *13*, 439.
- (24) Nikić, I.; et al. Debugging Eukaryotic Genetic Code Expansion for Site-Specific Click-PAINT Super-Resolution Microscopy. *Angew. Chem., Int. Ed.* **2016**, *55*, 16172–16176.
- (25) Stehr, F.; Stein, J.; Schueder, F.; Schwille, P.; Jungmann, R. Flat-top TIRF illumination boosts DNA-PAINT imaging and quantification. *Nat. Commun.* **2019**, *10*, 1268.
- (26) Blumhardt, P. Photo-Induced Depletion of Binding Sites in DNA-PAINT Microscopy. *Molecules* **2018**, *23*, 3165.
- (27) Deschout, H.; et al. Precisely and accurately localizing single emitters in fluorescence microscopy. *Nat. Methods* **2014**, *11*, 253.
- (28) Magde, D.; Elson, E.; Webb, W. W. Thermodynamic Fluctuations in a Reacting System—Measurement by Fluorescence Correlation Spectroscopy. *Phys. Rev. Lett.* **1972**, *29*, 705–708.
- (29) Eigen, M.; Rigler, R. Sorting single molecules: application to diagnostics and evolutionary biotechnology. *Proc. Natl. Acad. Sci. U. S. A.* **1994**, *91*, 5740–5747.
- (30) Rothemund, P. W.; Folding, K. DNA to create nanoscale shapes and patterns. *Nature* **2006**, *440*, 297.
- (31) Mücksch, J.; et al. Quantifying Reversible Surface Binding via Surface-Integrated Fluorescence Correlation Spectroscopy. *Nano Lett.* **2018**, *18*, 3185–3192.
- (32) Jungmann, R.; et al. Single-Molecule Kinetics and Super-Resolution Microscopy by Fluorescence Imaging of Transient Binding on DNA Origami. *Nano Lett.* **2010**, *10*, 4756–4761.
- (33) Steinhauer, C.; Jungmann, R.; Sobey, T. L.; Simmel, F. C.; Tinnefeld, P. DNA Origami as a Nanoscopic Ruler for Super-Resolution Microscopy. *Angew. Chem., Int. Ed.* **2009**, *48*, 8870–8873.
- (34) Thompson, N. L.; Burghardt, T. P.; Axelrod, D. Measuring surface dynamics of biomolecules by total internal reflection fluorescence with photobleaching recovery or correlation spectroscopy. *Biophys. J.* **1981**, *33*, 435–454.
- (35) Starr, T. E.; Thompson, N. L. Total Internal Reflection with Fluorescence Correlation Spectroscopy: Combined Surface Reaction and Solution Diffusion. *Biophys. J.* **2001**, *80*, 1575–1584.
- (36) Howorka, S.; Movileanu, L.; Braha, O.; Bayley, H. Kinetics of duplex formation for individual DNA strands within a single protein nanopore. *Proc. Natl. Acad. Sci. U. S. A.* **2001**, *98*, 12996–13001.
- (37) Dupuis, N. F.; Holmstrom, E. D.; Nesbitt, D. J. Single-molecule kinetics reveal cation-promoted DNA duplex formation through ordering of single-stranded helices. *Biophys. J.* **2013**, *105*, 756–766.
- (38) Ouldrige, T. E.; Sulc, P.; Romano, F.; Doye, J. P. K.; Louis, A. A. DNA hybridization kinetics: Zippering, internal displacement and sequence dependence. *Nucleic Acids Res.* **2013**, *41*, 8886–8895.
- (39) Strauss, M. T.; Schueder, F.; Haas, D.; Nickels, P. C.; Jungmann, R. Quantifying absolute addressability in DNA origami with molecular resolution. *Nat. Commun.* **2018**, *9*, 1600.
- (40) Jungmann, R.; et al. Multiplexed 3D cellular super-resolution imaging with DNA-PAINT and Exchange-PAINT. *Nat. Methods* **2014**, *11*, 313.

## Supporting Information

### Towards absolute molecular numbers in DNA-PAINT

Johannes Stein<sup>†,‡</sup>, Florian Stehr<sup>†,‡</sup>, Patrick Schueler<sup>†</sup>, Philipp Blumhardt<sup>†</sup>, Florian Schueder<sup>†,§</sup>, Jonas Mücksch<sup>†</sup>, Ralf Jungmann<sup>†,§</sup> and Petra Schwille<sup>†,\*</sup>

<sup>†</sup>Max Planck Institute of Biochemistry, 82152 Martinsried near Munich, Germany.

<sup>§</sup>Faculty of Physics, Ludwig Maximilian University, 80539 Munich, Germany.

Supplementary Methods	
Supplementary Figure 1	Step-by-step guide through lbFCS analysis
Supplementary Figure 2	Custom-built TIRF microscope and laser power series
Supplementary Figure 3	Filtering out clusters whose intensity vs. time traces exhibit flawed dynamics
Supplementary Figure 4	Unspecific surface binding interactions
Supplementary Figure 5	1DS counting results for lbFCS at varying temperature and MgC <sub>2</sub> concentration
Supplementary Figure 6	Self-calibrating counting independent of absolute imager concentration
Supplementary Figure 7	The qPAINT approach
Supplementary Figure 8	qPAINT calibration from single docking strands
Supplementary Figure 9	$N_{out}$ vs. $N_{in}$ at varying imager concentrations
Supplementary Figure 10	Simultaneous binding in dense clusters limits qPAINT
Supplementary Figure 11	$N_{out}$ vs. $N_{vis}$ comparison per integer from visual counting results
Supplementary Figure 12	Depletion of docking strands for DNA-PAINT imaging at low laser power
Supplementary Table 1	Total number of analyzed clusters for lbFCS/qPAINT counting
Supplementary Table 2	Used DNA-PAINT sequences
Supplementary Table 3	Parameters for analysis steps

## Supplementary methods

### Materials

Unmodified, dye-labeled, and biotinylated DNA oligonucleotides were purchased from MWG Eurofins. DNA scaffold strands were purchased from Tilibit (p7249, identical to M13mp18). Streptavidin was purchased from Thermo Fisher (cat: S-888). BSA-Biotin was obtained from Sigma-Aldrich (cat: A8549). Glass slides were ordered from Thermo Fisher (cat: 10756991) and coverslips were purchased from Marienfeld (cat: 0107032). Freeze 'N Squeeze columns were ordered from Bio-Rad (cat: 732-6165). Tris 1M pH 8.0 (cat: AM9856), EDTA 0.5M pH 8.0 (cat: AM9261), Magnesium 1M (cat: AM9530G) and Sodium Chloride 5M (cat: AM9759) were ordered from Ambion. Ultrapure water (cat: 10977-035) was purchased from Thermo Fisher Scientific. Tween-20 (cat: P9416-50ML), Glycerol (cat: 65516-500ml) and (+)-6-Hydroxy-2,5,7,8-tetra-methylchromane-2-carboxylic acid (Trolox) (cat: 238813-5G) were purchased from Sigma-Aldrich. Two-component epoxy glue (cat: 886519 - 62) was purchased from Conrad Electronic SE.

### Buffers

Four buffers were used for sample preparation and imaging: Buffer A+ (10 mM Tris-HCl pH 7.5, 100 mM NaCl, 0.05% Tween 20, pH 7.5); Buffer B+ (5 mM Tris-HCl pH 8.0, 10 mM MgCl<sub>2</sub>, 1 mM EDTA, 0.05% Tween 20, pH 8); Enzyme buffer for POC oxygen scavenging system (10 mM Tris pH 7.5, 50 mM KCl, 20% glycerol); 10x folding buffer (100 mM Tris, 10 mM EDTA pH 8.0, 125 mM MgCl<sub>2</sub>).

### DNA origami design, assembly and purification

DNA origami structures were designed using the design module of Picasso<sup>1</sup> (see **Figure 4**, top for docking strand positions). Folding of structures was performed using the following components: single-stranded DNA scaffold (0.01  $\mu$ M), core staples (0.5  $\mu$ M), biotin staples (0.5  $\mu$ M), modified staples (each 0.5  $\mu$ M), 1x folding buffer in a total of 50  $\mu$ l for each sample. Annealing was done by cooling the mixture from 80 to 25 °C in 3 h in a thermocycler. Structures were purified using gel electrophoresis (3 h at 60 V). For detailed instructions see<sup>1,2</sup>.

### DNA origami sample preparation

DNA origami samples were prepared as described before<sup>1</sup>. A glass slide was glued onto a coverslip with the help of double-sided tape (Scotch, cat. no. 665D) to form a flow chamber with inner volume of ~20  $\mu$ l. First, 20  $\mu$ l of biotin-labeled bovine albumin (1 mg/ml, dissolved in buffer A+) was flushed into the chamber and incubated for 3 min. The chamber was then washed with 40  $\mu$ l of buffer A+. 20  $\mu$ l of streptavidin (0.5 mg/ml, dissolved in buffer A+) was then flushed through the chamber and incubated for 3 min. After washing with 40  $\mu$ l of buffer A+ and subsequently with 40  $\mu$ l of buffer B+, 20  $\mu$ l of biotin-labeled DNA structures (dilution from DNA origami stock dependent on origami yield after gel purification. Adjusted for each origami species individually to obtain sparse DNA origami surface density. Starting dilution ~1:4) were flushed into the chamber and incubated for 10 min. The chamber was washed with 40  $\mu$ l of buffer B+. Finally, 40  $\mu$ l of the imager solution was flushed into the chamber, which was subsequently sealed with two-component epoxy glue before imaging. Adjustment of imager concentrations: The imager concentrations used for all experiments were  $c = 5, 10$  and  $20$  nM. As described in **Supplementary Figure 6**, we first prepared a larger volume of 20 nM imager solution, from which in two subsequent 1:1 dilution steps the 10 nM and 5 nM solutions were prepared. Sequence design of imager and docking strands can be found in **Supplementary Table 2**.

### Super-resolution microscopy setup

Fluorescence imaging was carried out on an inverted custom-built microscope<sup>3</sup> (see setup sketch in **Supplementary Figure 2a**) in an objective-type TIRF configuration with an oil-immersion objective (Olympus UAPON, 100x, NA 1.49). One laser was used for excitation: 561 nm (1 W, DPSS-system, MPB). Laser power

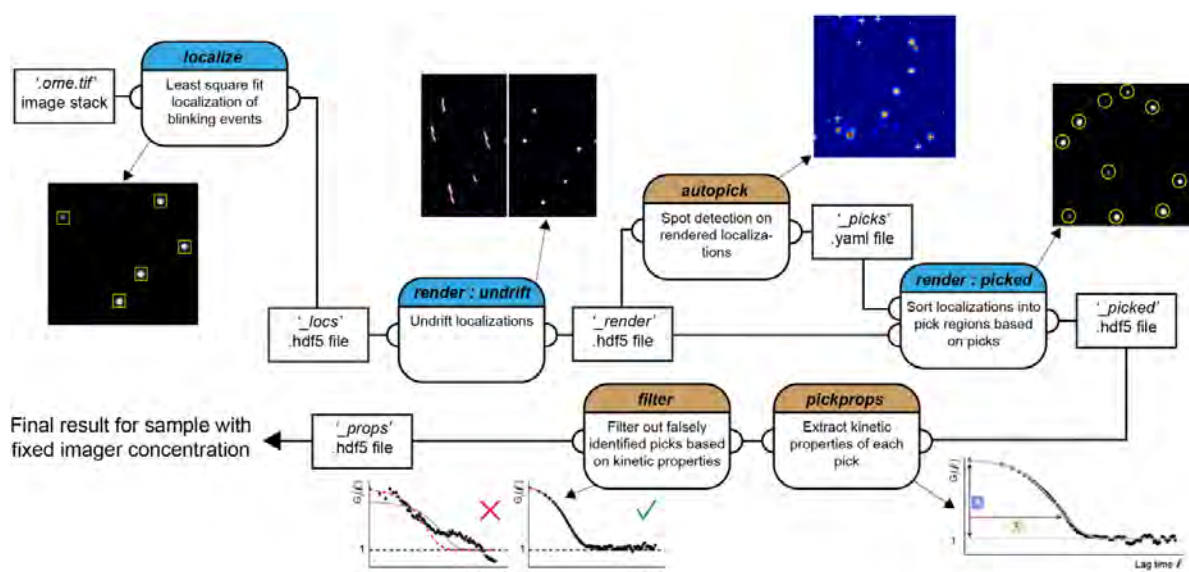
was adjusted by polarization rotation with a half-wave plate (Thorlabs, WPH05M-561) before passing a polarizing beam-splitter cube (Thorlabs, PBS101). To spatially clean the beam-profile the laser light was coupled into a single-mode polarization-maintaining fiber (Thorlabs, P3-488PM-FC-2) using an aspheric lens (Thorlabs, C610TME-A). The coupling polarization into the fiber was adjusted using a zero-order half wave plate (Thorlabs, WPH05M-561). The laser light was re-collimated after the fiber using an achromatic doublet lens (Thorlabs, AC254-050-A-ML) resulting in a collimated FWHM beam diameter of ~6 mm. The Gaussian laser beam profile was transformed into a collimated flat-top profile using a refractive beam shaping device (AdlOptica, piShaper 6\_6\_VIS). The laser beam diameter was magnified by a factor of 2.5 using a custom-built telescope (Thorlabs, AC254-030-A-ML and Thorlabs, AC508-075-A-ML). The laser light was coupled into the microscope objective using an achromatic doublet lens (Thorlabs, AC508-180-A-ML) and a dichroic beam splitter (AHF, F68-785). Fluorescence light was spectrally filtered with a laser notch filter (AHF, F40-072) and a bandpass filter (AHF Analysentechnik, 605/64) and imaged on a sCMOS camera (Andor, Zyla 4.2) without further magnification (Thorlabs, TTL180-A) resulting in an effective pixel size of 130 nm (after  $2 \times 2$  binning). Microscopy samples were mounted into a closed water-based temperature chamber (Okolab, H101-CRYO-BL) on a x-y-z stage (ASI, S31121010FT and ASI, FTP2050) that was used for focusing with the microscope objective being at fixed position. The temperature of the objective was actively controlled using the same water cycle as the temperature chamber. Focus stabilization was achieved via the CRISP autofocus system (ASI @ 850 nm) in a feedback loop with a piezo actuator (Piezoconcept, Z-INSERT100) moving the sample. The CRISP was coupled into the excitation path of the microscope using a long pass dichroic mirror (Thorlabs, DMLP650L). Our custom TIRF setup was used for all Figures.

### Imaging conditions

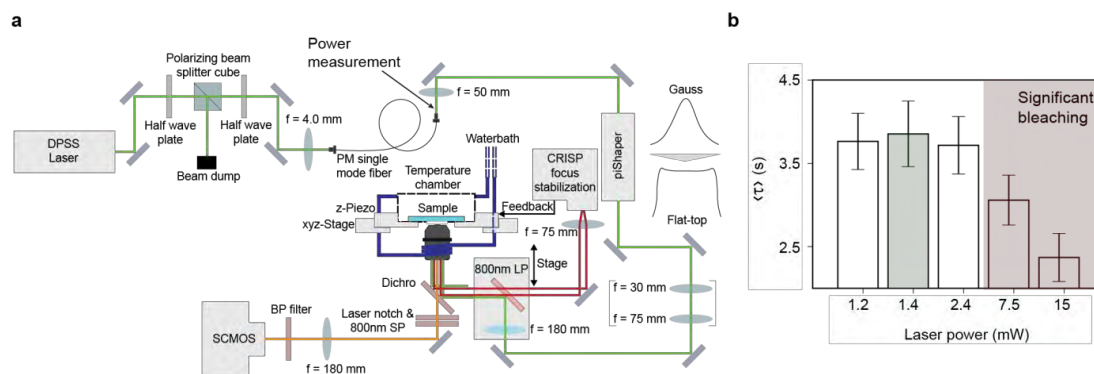
All fluorescence microscopy data was recorded with our sCMOS camera ( $2048 \times 2048$  pixels, pixel size:  $6.5 \mu\text{m}$ ). The camera was operated with the open source acquisition software  $\mu\text{Manager}^4$  at  $2 \times 2$  binning and cropped to the center  $700 \times 700$  pixel FOV. The exposure time was set to 200 ms, the read out rate to 200 MHz and the dynamic range to 16 bit. For lbFCS measurements the laser power was set to 1.4 mW (see **Supplementary Figure 2**), corresponding to an average intensity of  $\sim 10 \text{ W/cm}^2$  over the circular illuminated area of  $130 \mu\text{m}$  in diameter. The acquisition lengths for lbFCS measurements were set to: 9,000 frames ( $c = 20$  &  $10 \text{ nM}$ ) and 18,000 frames ( $c = 5 \text{ nM}$ ). Longer acquisition lengths at lower imager concentrations ensure that sufficient imager binding events are registered from each DS cluster as a prerequisite for robust autocorrelation analysis<sup>5</sup>. For high resolution imaging the laser power was set to 70 mW (intensity of  $\sim 500 \text{ W/cm}^2$ ) and the acquisition length to 5,000 frames.

### Super-resolution reconstruction & data analysis

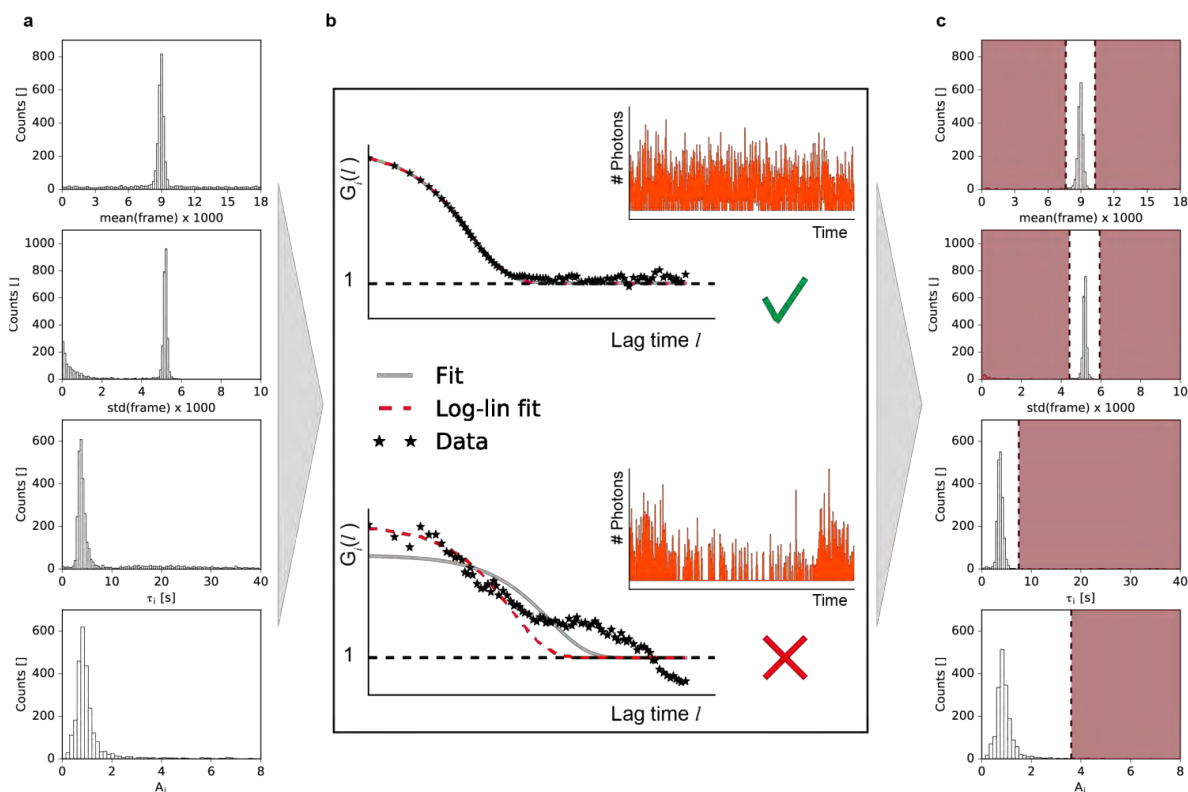
Refer to **Supplementary Figure 1** for a detailed step-by-step guide through all processing steps after data acquisition. The lbFCS software package and installation instructions are available at <https://github.com/schwille-paint/lbFCS>. A full integration in the Picasso<sup>1</sup> software package is currently under construction.



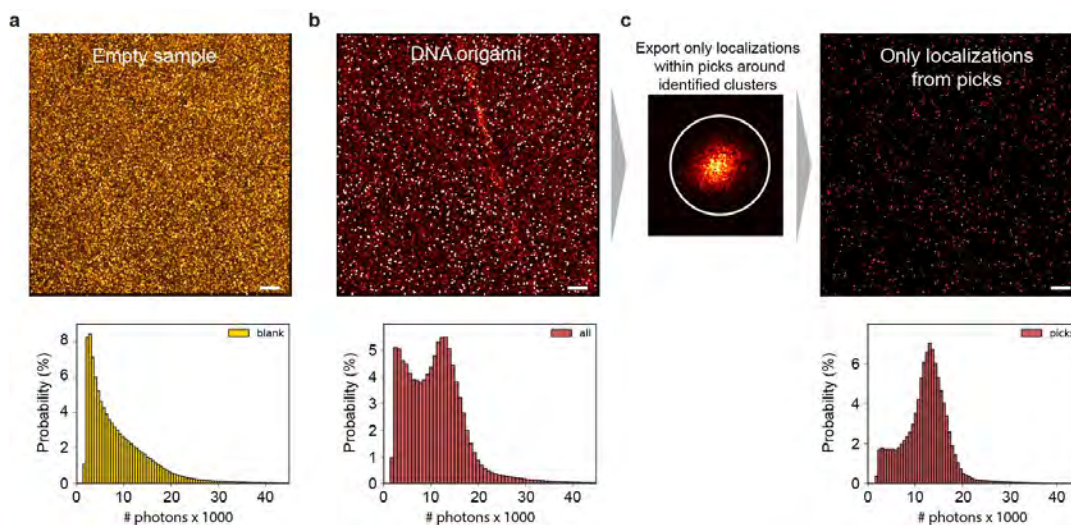
**Supplementary Figure 1. Step-by-step guide through IbFCS analysis.** (a) Software flow diagram depicting how final autocorrelation analysis result is obtained from DNA-PAINT raw-data. Rectangles represent saved data containing custom file extension and data format. Rounded boxes represent modules from ‘picasso’ python package<sup>1</sup> (blue) (<https://github.com/jungmannlab/picasso>) or custom python modules (ocher) (see **Supplementary Materials**) with half open circles indicating either input or output files according to flow direction. All additional input parameters of the modules used are listed in **Supplementary Table 3**. For a detailed description on the ‘filter’ module see **Supplementary Figure 3**.



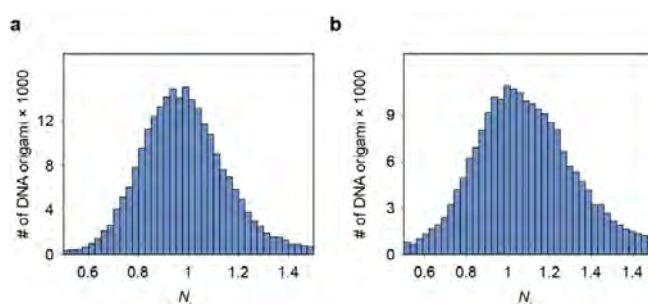
**Supplementary Figure 2. Custom-built TIRF microscope and laser power series.** (a) Sketch of custom-built TIRF microscope. See Supplementary Methods for details on components. (b). Power series on sample containing single docking strand DNA origami at 21°C (the temperature condition yielding the longest imager residence times, i.e. lowest  $k_{off}$ ). The laser power was measured after the fiber exit (see (a)). The red area highlights the regime where the laser power is high enough to photobleach the dye molecules of bound imager strands before dissociation which therefore significantly affects the extracted values of  $\langle \tau \rangle$ . We chose a laser power at ~1.4 mW (green), where we did not affect the extracted rates but were still able to robustly detect fluorescence bursts for super-resolution reconstruction.



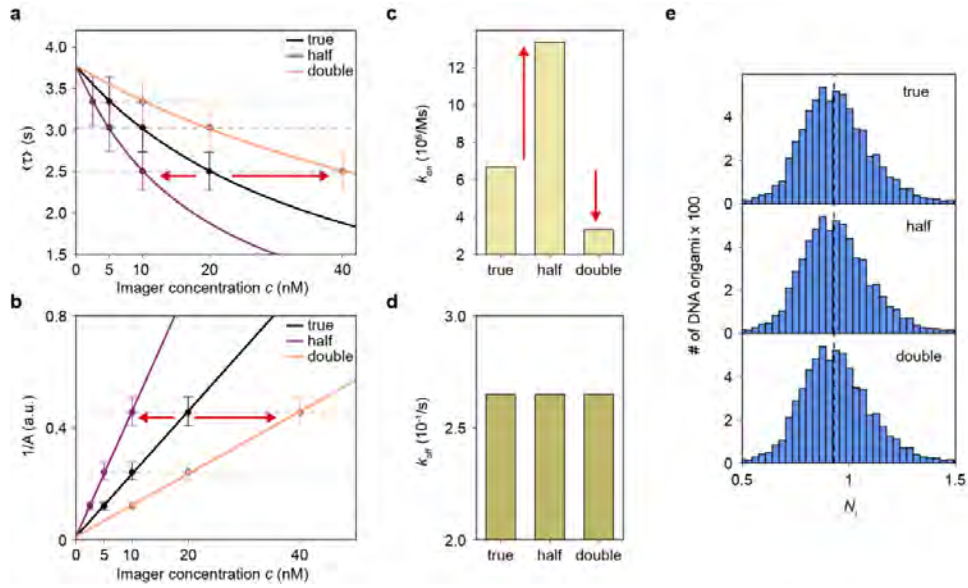
**Supplementary Figure 3. Filtering out clusters whose intensity vs. time traces exhibit flawed dynamics.** (a) Final distributions of kinetic variables as obtained before ‘filter’ module (see **Supplementary Figure 1**) over all picks of a sample containing DNA origami with 12 DSs at  $c = 5$  nM. The variable mean(frame) and std(frame) refer to the mean (standard deviation) of the timestamp (frame) of all localizations in a pick. (b) The ‘pickprops’ module (see **Supplementary Figure 1**) applies two fitting procedures to the autocorrelated intensity vs. time trace (black stars): (1) a non-linear least square fit according to the equation  $G_i(l) = A_i e^{l/\tau_i} + 1$  (gray) and, (2) a linear fit to the logarithmized autocorrelation function using the logarithmic form of the same equation  $\log(G_i(l) - 1) = A_i + l/\tau_i$  (red dashed). The linearized logarithmic fit does only take into account the first 10 data points of the autocorrelation. In the first filtering step the two different  $\tau_i$  for each pick obtained by the two fitting approaches are compared. If the value  $\tau_i$  as resulting by (2) deviates more than 20 % of the value  $\tau_i$  as resulting by (1) the pick is disregarded for further analysis. The resulting distributions over all picks after this filtering step are shown in (c). In the second filtering step the median over all picks for each of the variables mean(frame), std(frame),  $\tau_i$  and  $A_i$  is calculated. Picks with the following attributes are disregarded for further analysis (indicated by the red area): mean(frame)  $< 0.85 \times$  median or  $> 1.15 \times$  median, std(frame)  $< 0.85$  median,  $\tau_i > 2 \times$  median,  $A_i > 4 \times$  median.



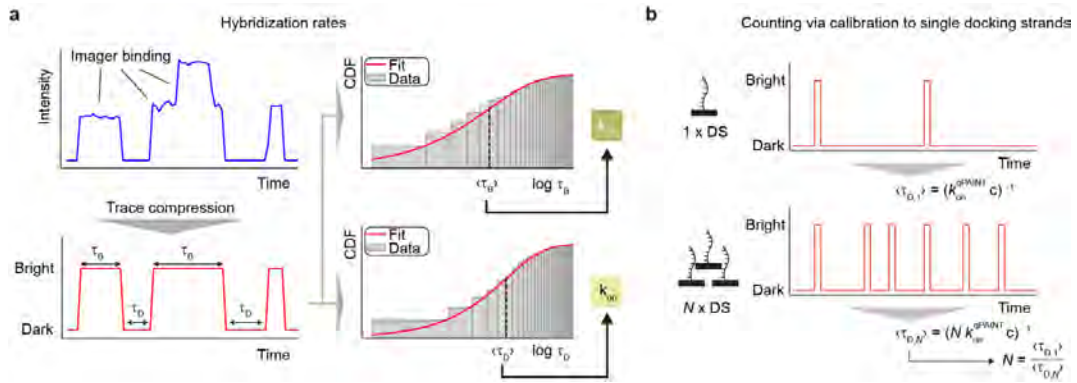
**Supplementary Figure 4. Unspecific surface binding interactions.** (a) DNA-PAINT image of a surface-passivated sample (BSA-Biotin-Streptavidin, see sample preparation in **Supplementary Methods**) containing no DNA origami but only 10 nM imager in the solution. Unspecific binding of imager to the surface is registered as blinking events leading to a homogeneous distribution of localizations over the surface. The histogram below shows the number of photons counted in each localization event. (b) DNA-PAINT image of sample containing DNA origami acquired under the same conditions as (a). DNA origami appear as bright spots whereas unspecific binding still leads to a homogeneous surface coverage of localizations. The photon count histogram now displays a distinct peak around 13,000 originating from specific binding interactions to DNA origami in addition to the same unspecific distribution as in (a). (c) For further lbfCS analysis we only process localizations within identified localization clusters (picks, white circle, see also **Figure 1b**). The photon count histogram of the localizations from all picks exhibits the same peak as in (b) from specific binding interactions but localizations originating from unspecific binding are minimized. Scale bars, 5  $\mu\text{m}$ .



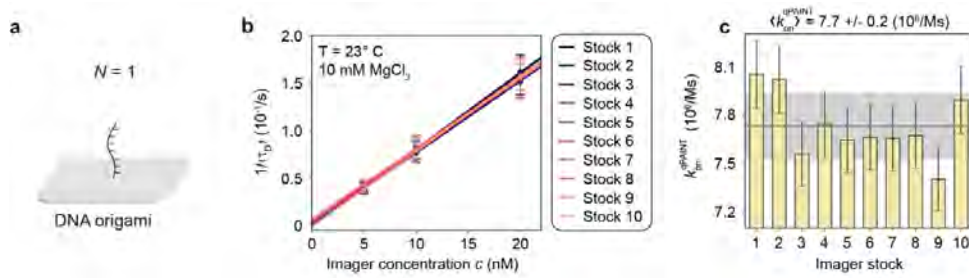
**Supplementary Figure 5. 1DS counting results for lbfCS at varying temperature and  $\text{MgCl}_2$  concentration.** (a) Sum of the counting results for lbfCS measurements at 21 - 24  $^{\circ}\text{C}$  (see **Figure 3a**). (b) Sum of the counting results for lbfCS measurements at 5-15 mM  $\text{MgCl}_2$  (see **Figure 3b**).



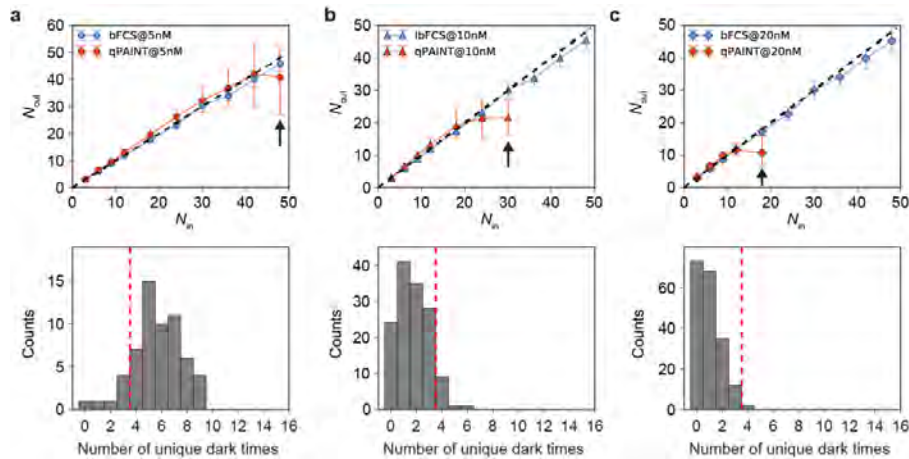
**Supplementary Figure 6. Self-calibrating counting independent of absolute imager concentration.** (a) As described in the **Supplementary Methods** (sample preparation) we adjusted the imager concentrations to  $c = 5, 10$  and  $20$  nM starting with the highest concentration  $c = 20$  nM which we subsequently diluted twice at a ratio 1:1. Here, we illustrate that the counting ability of lbFCS does in fact not depend on the absolute imager concentration. The black  $\langle \tau \rangle$  vs.  $c$  fit shows the results of the lbFCS measurement series on samples containing 1DS origami structures (referred to as “true” due to  $c = 5, 10$  and  $20$  nM). Next, we assume that we actually failed to adjust the first dilution by a factor of 2 to  $40$  nM instead of  $20$  nM resulting in a horizontal shift of the three measurement points to the right (red arrow). The orange  $\langle \tau \rangle$  vs.  $c$  curve hence fits the data points at  $c = 10, 20$  and  $40$  nM (“double”). Similarly, we go through the “half” scenario where we started with  $10$  nM and ended up with  $5$  and  $2.5$  nM shifting the data points horizontally to the left (red arrow, purple fit). (b) Same as (a) but for  $1/A$  obtained from the three data sets. As described in the main text, all three fits cross pass through the origin since the concentration ratios are still conserved. (c)  $k_{on}$  obtained from the three  $\langle \tau \rangle$  vs.  $c$  fits in (a). The relative offset in the imager concentration  $c$  inversely translates into an offset in  $k_{on}$  (i.e.  $k_{on}$  doubles for “half” and halves for “double”. See **eq. 2**) (d)  $k_{off}$  obtained from the three  $\langle \tau \rangle$  vs.  $c$  fits in (a).  $k_{off}$  is unaffected by the introduced offset in  $c$  (also visible at the identical y-axis intersections in (a)). Compare **eq. 2** for  $c \rightarrow 0$ ). (e) lbFCS yields identical counting results (sum  $N_i$  over the three measurements displayed) independent of the introduced offset in  $c$  as it cancels out when multiplied by  $k_{on}$ :  $N_i = \frac{1}{A_i} \frac{k_{off}}{k_{on} c}$ .



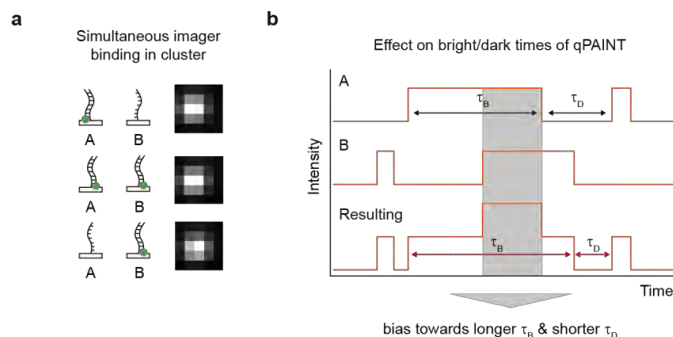
**Supplementary Figure 7. The qPAINT approach.** (a) Current standard for extracting imager hybridization kinetics from DNA-PAINT data. The intensity vs. time trace (blue) is compressed into a system of two states (red): i) Bright (bound imager) and ii) Dark (no imager). Here, information regarding simultaneous binding of multiple imagers resulting in higher intensity values is lost. All dwell times in both states, referred to as bright times  $\tau_B$  and dark times  $\tau_D$ , are extracted from the compressed trace and processed into cumulative histograms. Short disruptions of fluorescence bursts in the intensity trace (i.e. between two bright times) less than a predefined 'ignore' parameter are discarded (i.e. the two bright times are treated as one bright time with the combined duration. Standard: ignore = 1 frame). The histograms are fitted with the fit model<sup>1</sup>  $F(\tau_m) = \left(1 - \exp\left(-\frac{\tau_m}{\langle \tau_m \rangle}\right)\right) a + b$ , where  $m = B, D$  and the angle brackets denote the mean of the respective distribution.  $a$  and  $b$  are empirical fit parameters introduced for improved qPAINT counting performance (see implementation at <https://github.com/jungmannlab/picasso><sup>1</sup>). In order to apply this fit model with three parameters to an intensity vs. time trace from a localization cluster, the trace needs to exhibit at least three unique dark times (e.g. two dark times of lengths = 2 frames, three dark time of lengths = 5 frames and one dark time of length 11 frames. See **Supplementary Figure 9**). The imager hybridization rates can be obtained via the following relations<sup>1,6,7</sup>:  $k_{off} = \langle \tau_B \rangle^{-1}$  and  $k_{on}c = \langle \tau_D \rangle^{-1}$ . (b) Counting with qPAINT relies on calibration to the imager influx rate during a DNA-PAINT measurement obtained from single docking strands (1DS). The influx rate is defined as the inverse mean dark time obtained from a 1DS fluorescence vs. intensity trace  $\langle \tau_{D,1} \rangle^{-1} = k_{on}^{qPAINT} c$ . qPAINT is based on the assumption that a cluster of  $N$  DS will produce an intensity vs. time trace with a mean dark time  $\langle \tau_{D,N} \rangle$  shortened by a factor of  $N$  compared to a 1DS. Hence, qPAINT counting results for each localization cluster  $i$  are obtained via the relation:  $N_i = (k_{on}^{qPAINT} c \times \langle \tau_{D,i} \rangle)^{-1} = \langle \tau_{D,1} \rangle / \langle \tau_{D,i} \rangle$ .



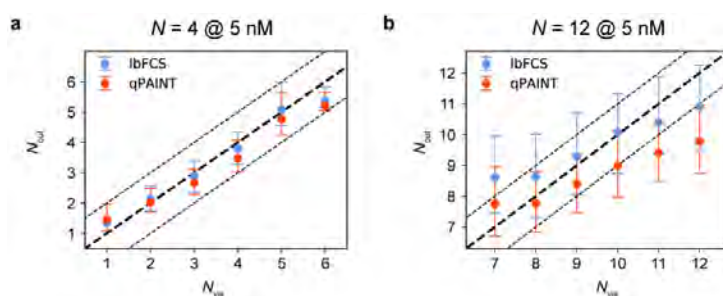
**Supplementary Figure 8. qPAINT calibration from single docking strands.** (a) For qPAINT calibration we used the measurements obtained on 1DS structures as in **Figure 2a-e**. (b)  $1/\langle\tau_D\rangle$  vs.  $c$  fit for the 10 concentration series. As defined in **Supplementary Figure 7**,  $1/\langle\tau_D\rangle = k_{on}^{qPAINT} c$  which means that  $k_{on}^{qPAINT}$  required for qPAINT calibration can directly be read off the slope of the fit. (c) Scatter in  $k_{on}^{qPAINT}$  obtained from fits in (b). Mean and standard deviation are indicated as grey line and light grey area, respectively. The mean of  $\langle k_{on}^{qPAINT} \rangle = (7.7 \pm 0.2 \times 10^6) \text{ M}^{-1}\text{s}^{-1}$  was used as calibration for all qPAINT counting results. We would like to note that the high precision in  $k_{on}^{qPAINT}$  is due to profiting from the filtering procedure introduced in **Supplementary Figure 3**, which in turn is based on the unique property of the autocorrelation analysis of lbFCS to identify and exclude docking strands exhibiting flawed dynamics.



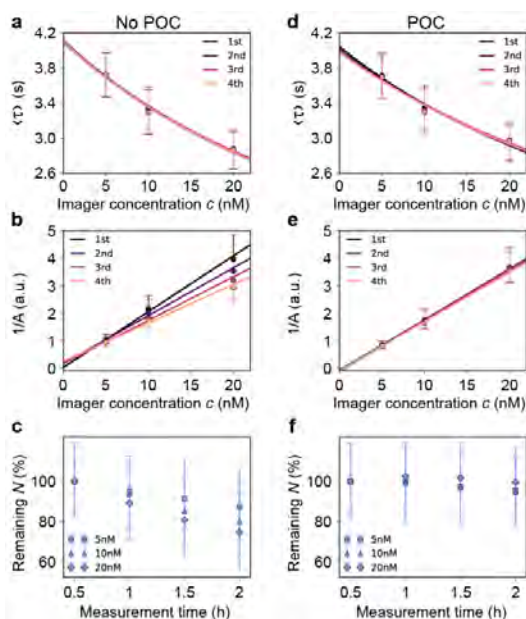
**Supplementary Figure 9.  $N_{out}$  vs.  $N_{in}$  at varying imager concentrations.** (a) Top: median of the counting results  $N_{out}$  vs.  $N_{in}$  plot comparing the results obtained via qPAINT (red) vs. lbFCS (blue) at  $c = 5 \text{ nM}$  as in **Figure 4b**. The black dashed line displays a line through the origin of slope one as expected for ideal counting results (i.e.  $N_{out} = N_{in}$ ). The first qPAINT data point at  $N = 48$  deviating from the ideal behavior is indicated by a black arrow. Bottom: histogram showing the number of unique dark times per intensity vs. time trace for the  $N = 48$  qPAINT data point. The dashed red line indicates the minimum of three unique dark times per intensity trace required for the fit described in **Supplementary Figure 7**. In case a trace exhibited less than three unique dark times, we assigned the mean dark time obtained over all fits to the cluster. Clusters, i.e. traces featuring no dark time at all were discarded from further analysis. (b) Top: same as in (a), but for  $c = 10 \text{ nM}$ . Bottom: the majority of clusters in the data set indicated by the black arrow at  $N = 30$  exhibit less than the required three unique dark times. (c) Same as in (a-b), but for  $c = 20 \text{ nM}$ . Histogram of unique dark times displayed for the data point at  $N = 18$ .



**Supplementary Figure 10. Simultaneous binding in dense clusters limits qPAINT.** (a) Schematic of the case of simultaneous binding of imagers to two docking strands A and B in close proximity. The diffraction limited images indicate an increase in fluorescence intensity when an imager is bound to both docking strands compared to when only a single imager is bound. (b) Individual intensity vs. time traces for DS A and B. The duration of simultaneous binding is shaded in grey. The resulting intensity vs. time trace (bottom) extracted from the localization cluster of the two DSs exhibits an extended bright event and shortened dark event (black-red dashed double arrows) when analyzed according to qPAINT (see **Supplementary Figure 7**). To avoid simultaneous binding events limiting this approach the imager concentration has to be adjusted accordingly to the expected target density.



**Supplementary Figure 11.  $N_{out}$  vs.  $N_{vis}$  comparison per integer from visual counting results.** (a) IbFCS/qPAINT counting results for the  $N = 4$  data set at  $c = 5$  nM compared to visual counting results. The bold black line indicates the line through the origin of slope one as expected for ideal counting (i.e.  $N_{out} = N_{vis}$ ). The light black dashed lines indicate a counting error of  $\pm 1$ . This implies that for each  $N_{vis}$  more than 50 % of all clusters fulfill the criterion  $abs(N_{out} - N_{vis}) < 1$ . (b) Same as in (a) but for the  $N = 12$  data set at  $c = 5$  nM. Error bars correspond to interquartile range.



**Supplementary Figure 12. Depletion of docking strands for DNA-PAINT imaging at low laser power.** (a) Three-point concentration series for DNA origami samples ( $N = 12$ ) each measured for 2 h ( $4 \times$  longer than standard lbFCS measurement time). The data sets were temporally divided into 4 segments and each analyzed via lbFCS. The four respective overlapping  $\langle \tau \rangle$  vs.  $c$  fits yield that neither of the global parameters  $k_{on}$ ,  $k_{off}$  and  $c$  changed over the acquisition time. (b) In contrast, the four  $1/A$  vs.  $c$  fits clearly change over time as a result of DS depletion occurring even at low laser power. (c) DS depletion rate normalized to the lbFCS counting results from the first segment. (d) Repeat of the same concentration series as in (a) with POC + Trolox added to the imaging solution also indicating constant global parameters over time. (e) In contrast to (b) with POC + Trolox  $1/A$  does also not change over time. (f) Negligible depletion rate of DS for POC + Trolox. Error bars in (c) and (f) correspond to interquartile range.

**Supplementary Table 1 | Total number of analyzed clusters for lbFCS/qPAINT counting**

<i>N</i>	<i>c</i> (nM)	No. of automatically detected clusters	No. of clusters after filtering	No. of clusters after removal of $N_{vis} = 0$	No. of clusters for lbFCS analysis	No. of clusters for qPAINT analysis	Reference
4	5	28,166	12,815	10,963	10,963	10,963	Figure 4d (top)
4	10	18,824	6,343	5,245	5,245	5,245	Figure 4d (middle)
4	20	24,775	7,399	6,090	6,090	6,090	Figure 4d (bottom)
12	5	3,825	1,782	1,781	1,781	1,781	Figure 4e (top)
12	10	4,288	1,779	1,778	1,778	1,777	Figure 4e (middle)
12	20	3,662	1,200	1,200	1,200	1,171	Figure 4e (bottom)
48	5	9,743	3,829	n.a.	3,829	3,822	Figure 4f (top)
48	10	3,899	1,653	n.a.	1,653	1,496	Figure 4f (middle)
48	20	9,949	1,584	n.a.	1,584	419	Figure 4f (bottom)

**Supplementary Table 2 | Used DNA-PAINT sequences**

Shortname (docking strand length)	Docking strand sequence	Imager sequence	Experiment
PS6 (8 nt)	TT TCCTCCTC	GAGGAGGA-Cy3b	All experiments

**Supplementary Table 3 | Parameters for analysis steps**

Module	Parameters
localize	Net gradient = 400 Quantum efficiency = 0.82 (from Camera Specs) Sensitivity = 0.53 (from Camera Specs) Box size = 5 pixel Background = 70
render : undrift	No of segments for RCC drift correction: 500
autopick	Oversampling = 5 Net gradient = 300
render : picked	Pick diameter = 2 pixel
pickprops	Ignore = 1 (for qPAINT analysis, see <b>Supplementary Figure 7</b> )
filter	n.a.

**Supplementary references**

1. Schnitzbauer, J., Strauss, M. T., Schlichthaerle, T., Schueder, F. & Jungmann, R. Super-resolution microscopy with DNA-PAINT. *Nat. Protoc.* **12**, 1198 (2017).
2. Strauss, M. T., Schueder, F., Haas, D., Nickels, P. C. & Jungmann, R. Quantifying absolute addressability in DNA origami with molecular resolution. *Nat. Commun.* **9**, 1600 (2018).
3. Stehr, F., Stein, J., Schueder, F., Schwille, P. & Jungmann, R. Flat-top TIRF illumination boosts DNA-PAINT imaging and quantification. *Nat. Commun.* **10**, 1268 (2019).
4. Edelstein, A. D. *et al.* Advanced methods of microscope control using  $\mu$ Manager software. *J. Biol. Methods; Vol 1, No 2* (2014).
5. Mücksch, J. *et al.* Quantifying Reversible Surface Binding via Surface-Integrated Fluorescence Correlation Spectroscopy. *Nano Lett.* **18**, 3185–3192 (2018).
6. Jungmann, R. *et al.* Single-Molecule Kinetics and Super-Resolution Microscopy by Fluorescence Imaging of Transient Binding on DNA Origami. *Nano Lett.* **10**, 4756–4761 (2010).
7. Jungmann, R. *et al.* Quantitative super-resolution imaging with qPAINT. *Nat. Methods* **13**, 439 (2016).





# 4

## Tracking Single Particles via DNA-mediated Fluorophore Exchange

### 4.1 Motivation and Summary

Monitoring biomolecules in Single Particle Tracking (SPT) experiments is typically achieved by employing fixed organic dyes or fluorescent fusion proteins linked to the target of interest. However, photobleaching typically limits observation times to merely a few seconds, restricting downstream statistical analysis and observation of rare biological events. The use of quantum dots (QDs) as fluorescent tags can overcome this limitation allowing observation times in the range of minutes. Unfortunately, QDs suffer from heavy photoblinking on various time scales, impairing the recording of uninterrupted single particle trajectories over prolonged periods. In addition, bio-compatible QDs are large ( $\approx 10 - 40$  nm in diameter), potentially influencing the dynamics of the labeled molecules, and are difficult to functionalize at the desired 1:1 stoichiometry. Based on DNA mediated fluorophore exchange we developed a labeling approach to generate fluorescent labels with increased lifetimes, while maintaining live-cell compatibility, 1:1 labeling, and smaller sizes than QDs. The rejuvenating nature of our labeling approach not only yielded multiple recorded trajectories per particle but also prolonged trajectory durations in the range of tens of minutes. The observation of DNA origami on SLBs showed that the large number of recorded trajectories per particle nearly covered the FOV, which allowed mapping of the entire accessible membrane with an actual low number of particles. Finally, the ability to divide long trajectories into sub-trajectories opened the door for a in-depth, more robust quantitative analysis of the underlying motion dynamics. Although this work demonstrated the strengths of our approach using an in vitro reconstituted system, we believe that the principle can be translated also to cellular targets, such as genetically-tagged membrane proteins with accessible extra-cellular modification sites.

4.2 PUBLICATION P3: Tracking Single Particles for Hours via Continuous DNA-mediated Fluorophore Exchange

# Tracking Single Particles for Hours via Continuous DNA-mediated Fluorophore Exchange

Florian Stehr, Johannes Stein, Julian Bauer, Christian Niederauer,  
Ralf Jungmann, Kristina Ganzinger and Petra Schwillie

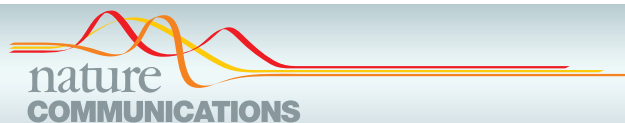
*Author contributions:*

**F.S.**, J.S., R.J., K.G. and P.S. conceived the study. **F.S.**, J.S. and J.B. designed experiments. J.S. performed the experiments. J.B. devised the concept of the tracking handle sequence, prepared DNA origami and performed initial experiments. C.N. performed initial experiments. **F.S.** and J.S. designed and performed data analysis. **F.S.** wrote the analysis code. **F.S.**, J.S., R.J., K.G. and P.S. wrote the manuscript. K.G. and P.S. supervised the study. **All authors** discussed and interpreted results and revised the manuscript.

*published in*

Nature Communications 2021, 12, 4432

*Reprinted from [82] under the [CC BY-NC 4.0 license](#).*



## ARTICLE

<https://doi.org/10.1038/s41467-021-24223-4>

OPEN

# Tracking single particles for hours via continuous DNA-mediated fluorophore exchange

Florian Stehr <sup>1,4</sup>, Johannes Stein <sup>1,4</sup>, Julian Bauer <sup>1</sup>, Christian Niederauer <sup>2</sup>, Ralf Jungmann <sup>1,3</sup>,  
Kristina Ganzinger <sup>2</sup>✉ & Petra Schwillle <sup>1</sup>✉

Monitoring biomolecules in single-particle tracking experiments is typically achieved by employing fixed organic dyes or fluorescent fusion proteins linked to a target of interest. However, photobleaching typically limits observation times to merely a few seconds, restricting downstream statistical analysis and observation of rare biological events. Here, we overcome this inherent limitation via continuous fluorophore exchange using DNA-PAINT, where fluorescently-labeled oligonucleotides reversibly bind to a single-stranded DNA handle attached to the target molecule. Such versatile and facile labeling allows uninterrupted monitoring of single molecules for extended durations. We demonstrate the power of our approach by observing DNA origami on membranes for tens of minutes, providing perspectives for investigating cellular processes on physiologically relevant timescales.

<sup>1</sup>Max Planck Institute of Biochemistry, Martinsried, Germany. <sup>2</sup>AMOLF, Amsterdam, The Netherlands. <sup>3</sup>Faculty of Physics, Ludwig Maximilian University, Munich, Germany. <sup>4</sup>These authors contributed equally: Florian Stehr, Johannes Stein. ✉email: [k.ganzinger@amolf.nl](mailto:k.ganzinger@amolf.nl); [schwillle@biochem.mpg.de](mailto:schwillle@biochem.mpg.de)

Single-Particle Tracking (SPT) is a powerful technique to study the motion and interactions of biomolecules in cellular or biomimetic environments<sup>1,2</sup>. Following dynamics and orchestration of molecular processes one molecule at a time has been key for developing the mechanistic concept of proteins as molecular machines<sup>3</sup>. Already since the use of colloidal gold particles as SPT labels<sup>4,5</sup>, it became clear that both label size, photostability and target attachment are crucial factors to extract biologically meaningful data. To date, SPT mainly employs single fluorophores or quantum dots (QDs) as labels. More recently, also advanced multi-fluorophore labeling implementations have been developed<sup>6,7</sup>. Organic dyes are small and straightforward to attach to a target, but as their photon budget is limited, observations are only possible for a few seconds at 20–50 nm spatial precision before they photobleach<sup>1</sup>. Oxygen scavenging systems can improve the photon yield of organic dyes<sup>8–12</sup>, but they are mostly incompatible with live-cell experiments<sup>13</sup>. QDs can overcome this limitation of fluorophores, as they are brighter and resistant to photobleaching<sup>14</sup>. However, QDs blink, and bio-compatible QDs are large (~10–40 nm), potentially impairing the dynamics of the labeled molecules<sup>1,14</sup>. Furthermore, they are difficult to functionalize at the desired 1:1 stoichiometry<sup>1</sup>, possibly resulting in artificial cross-linking of multiple molecules. Observing particle trajectories for an extended amount of time with high spatiotemporal resolution is however key to further our ability to extract physiologically meaningful data to observe rare biological events and improve theoretical models in the future<sup>15</sup>.

Here, we introduce a labeling approach by re-purposing DNA-PAINT<sup>16</sup> (Points Accumulation for Imaging in Nanoscale Topography) to generate fluorescent labels with increased lifetimes, while maintaining live-cell compatibility, 1:1 labeling, and smaller sizes than QDs (see Supplementary Fig. 1 for size comparison). The key principle is DNA-mediated fluorophore exchange: short fluorescently-labeled oligonucleotides (‘imagers’, 8 bp; sequence: 5'-GAGGAGGA-3'-Cy3B) transiently bind a complementary single, long DNA strand attached to the molecule of interest (‘tracking handle’ TH, 54 base pairs, Fig. 1a). Imagers bind *via* reversible DNA hybridization of their short complementary oligonucleotide part, and both TH’s 3' and 5' ends can be modified with functional groups for target labeling (e.g., thiol or click-chemistry, SNAP/HALO-tag, etc.). TH and imager sequences are designed such that one imager is bound to the TH at all times, with turnover being sufficiently fast to replace imagers before photobleaching occurs. This is achieved by allowing multiple (max. 6, see Supplementary Fig. 2) imagers to bind simultaneously, maximizing their association rate ( $k_{on}$ )<sup>17–21</sup>, and optimizing their dwell times ( $k_{off}$ ) (see Fig. 1b for schematic depiction).

## Results

**A continuously rejuvenating fluorescent label.** To demonstrate the improved properties of the TH, we compared it to single Cy3B molecules fixed to DNA origami (‘single-dye origami’ or SD origami). We acquired images of immobilized target molecules at low surface densities via TIRFM<sup>22</sup> (Total Internal Reflection Fluorescence Microscopy; see Supplementary Table 1 for imaging conditions of all presented data). Both SD and TH origami data sets were then subjected to the same post-processing procedure (Supplementary Fig. 3 & 4). While SD origami bleached on the time scale of tens of seconds—after 2 min, nearly all dyes had entered a permanent dark state—a large fraction of TH origami was still observable even after 30 min, using identical acquisition conditions (Fig. 1c, d).

For quantitative comparison of single dyes and THs, we distinguish between the full trajectory ( $x, y, t$ ) of a molecule and the sections where this molecular path can be visualized by detecting a fluorescence signal (see Fig. 1e), leading to the recording of (potentially) a multitude of trajectories per particle. Irrespective of the position coordinates ( $x, y$ ), we hence introduce a metric that reflects not only on the measured trajectory durations ( $\tau$ ) but also on the number of recorded trajectories per particle ( $TPP$ ). We hence calculate  $TPP_i(\tau \geq T)$ , i.e., the number of trajectories with durations  $\tau$  longer or equal to arbitrary query times  $T$  for each immobilized DNA origami  $i$  ( $i = 1, 2, \dots, M$ , where  $M$  denotes the total number of molecules after filtering). In contrast to permanent labeling with a single dye, where  $TPP$  is ideally expected to be 1, for the TH origami the  $TPP$  will grow with the duration of the measurement, as imagers are continuously replenished and a single TH can be repeatedly observed. Thus, a typical SD origami fluoresces from the start of image acquisition until it abruptly photobleaches (Fig. 1f), while a typical fluorescence trace of a TH origami shows an almost continuous signal of fluctuating intensities with short interruptions of a few frames (when no emitting imager is bound) resulting in five trajectories of durations  $\tau_{1-5}$  in the range of ~10–200 s in the example shown (Fig. 1g; a 10 min subset of the trace is displayed for illustration purposes). Calculation of  $TPP_i(\tau \geq T)$  for all  $M$  fluorescence traces of the data set and subsequent averaging yielded the ensemble mean  $TPP(\tau \geq T) = \frac{1}{M} (\sum_{i=1}^M TPP_i(\tau \geq T))$  (Fig. 1h,i black line). We refer to the time at which the ensemble mean falls below one-half (i.e.,  $TPP(\tau \geq T_{1/2}) = 0.5$ ) as the characteristic half-life time  $T_{1/2}$ . Hence, the mean  $TPP(\tau \geq T)$  and its corresponding  $T_{1/2}$  simultaneously allow both a quantitative description of the number of trajectories obtained per particle/origami and their expected average duration. In other words, all ~3000 SD origami in the data set produced on average a single trajectory (Fig. 1h, y-axis intercept at 1) and half of these (i.e., 1500) had a duration of at least 11 s ( $T_{1/2} = 11$  s). In contrast, each of the ~2500 TH origami yielded ~22 trajectories on average over a measurement duration of 10 min and  $T_{1/2}$  analysis revealed that we registered 1250 trajectories with a duration of at least 200 s (>3 min), resulting in an increase in both the number of tracks and in  $T_{1/2}$  of a factor of ~20× compared to SD origami (Fig. 1i). When the number of trajectories per frame was normalized to the first frame, we found that more than 80% of all THs were still detectable (fluorescent) when imaging for 30 min, while this was true for only ~3% of the SD origami already after 120 s (Fig. 1j). The 20% decrease in TH detection over time is likely due to photo-induced damage to the DNA caused by reactive oxygen species<sup>21,23</sup> during imaging (see Supplementary Note 1). To assess the number of imagers simultaneously bound to the TH, we analyzed the photon count distribution, which yielded distinct, equidistant single dye steps with the first step exhibiting the same photon count value in the TH and SD origami data sets (Supplementary Fig. 5). The increase in photons per localization in the TH case also resulted in a twofold increase in localization precision compared to SD origami (5.6 nm and 9.0 nm, respectively, Supplementary Fig. 5). In summary, compared to a single dye, a single TH produces: (1) more trajectories, which on average have (2) a longer duration and (3) a higher fluorescence brightness. Using a buffer compatible with live-cell imaging and optimized imaging conditions ( $T = 21^\circ$  and 40 nM imager concentration), we obtained a 26-fold increase in  $T_{1/2}$  for TH compared to SD origami (Fig. 1k, see Supplementary Note 1 for a

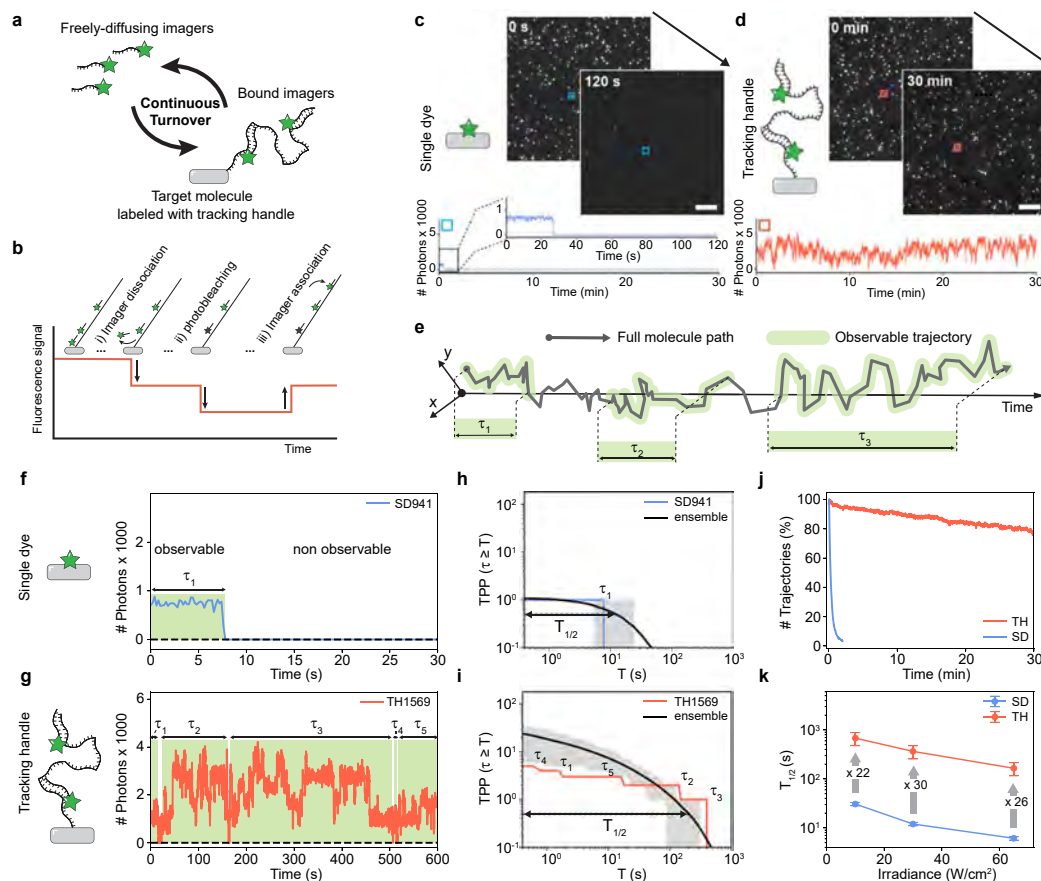


**Fig. 1** DNA-mediated continuous fluorophore exchange leads to long observations times for labeled molecules. **a** Principle of re-purposing DNA-PAINT for single-particle tracking experiments. Freely-diffusion imagers are binding and unbinding in a continuous turnover to the TH attached to the target molecule. **b** Schematic of intensity fluctuations recorded from a TH caused by imager dissociation, association and photobleaching. **c** TIRFM imaging of static DNA origami labeled with single-dye (left) and fluorescence traces corresponding to the marked particle. **d** Same as **(c)** but for TH origami under equal imaging conditions and 40 nM of imager in solution. **e** Distinction between full molecular path ( $x$ - $y$ - $t$ ) and its observable sections by means of a detectable fluorescence signal. This leads to the recording of a multitude of trajectories per particle of durations  $\tau_i$ . **f** SD example fluorescence trace (SD941 arbitrarily selected out of all  $\sim 3000$  SD origami surpassing the filter criteria described in Supplementary Fig. 4). **g** Arbitrarily selected TH example fluorescence trace (analogous to **f**). **h** Plot of  $TPP(\tau \geq T)$  vs.  $T$  for the SD fluorescence trace in **(f)** (blue) and averaged over all SD origami in the data set (black). **i** Plot of  $TPP(\tau \geq T)$  vs.  $T$  for the TH fluorescence trace in **(g)** (orange) and averaged over all TH origami in the data set (black). **j** Number of trajectories per frame (i.e., emitting labels) vs. measurement time normalized to initial trajectory number. Total number of recorded trajectories:  $n \sim 149,000$  (TH) and  $n \sim 3700$  (SD) **(k)**  $T_{1/2}$  vs. irradiance plots for SD origami (blue) and TH origami (orange) imaged at varying irradiances without using an oxygen scavenging system (after filtering, SD data sets contained at least  $n \sim 3000$  origami and TH data sets at least  $n \sim 700$  origami). Arrows indicates factors of increase of TH vs. SD. Scale bars,  $5 \mu\text{m}$  in **(c, d)**. Error in **(h, i)** refers to interquartile range indicated as gray shaded area. Error bars in **(k)** correspond to relative standard deviation (see Supplementary Fig. 6).

detailed description and analysis of the optimization process). For instance, for an irradiance of  $30 \text{ W/cm}^2$ , we obtained  $T_{1/2}$  of 365 s ( $>6 \text{ min}$ ) for TH compared to only 12 s for SD origami in live-cell-compatible conditions.

**Single particle tracking on supported lipid bilayers.** Next, we investigated the improvement of TH labeling for SPT of moving origami. We used eight biotin anchors to attach the origami *via* streptavidin to biotinylated lipids in supported lipid bilayers (SLB), mimicking two-dimensional diffusion (Supplementary

Movies 1 & 2; see Supplementary Fig. 7 for the analysis workflow). Comparing the 16 longest trajectories for SD and TH under identical conditions, we could readily observe that even the shortest trajectory measured for a TH origami (244 s) was two-times longer than any of the SD origami trajectories ( $<120 \text{ s}$ , Fig. 2a, Supplementary Fig. 8 for different irradiances). Remarkably, we were able to track single TH origami for more than 18 min during a 30 min measurement. Similar to immobilized origami (see Fig. 1i), diffusing TH origami still yielded  $>50\%$  of the initial trajectory number at the end of the measurement duration of 30 min (half time decay  $\sim 33 \text{ min}$ , Fig. 2b,

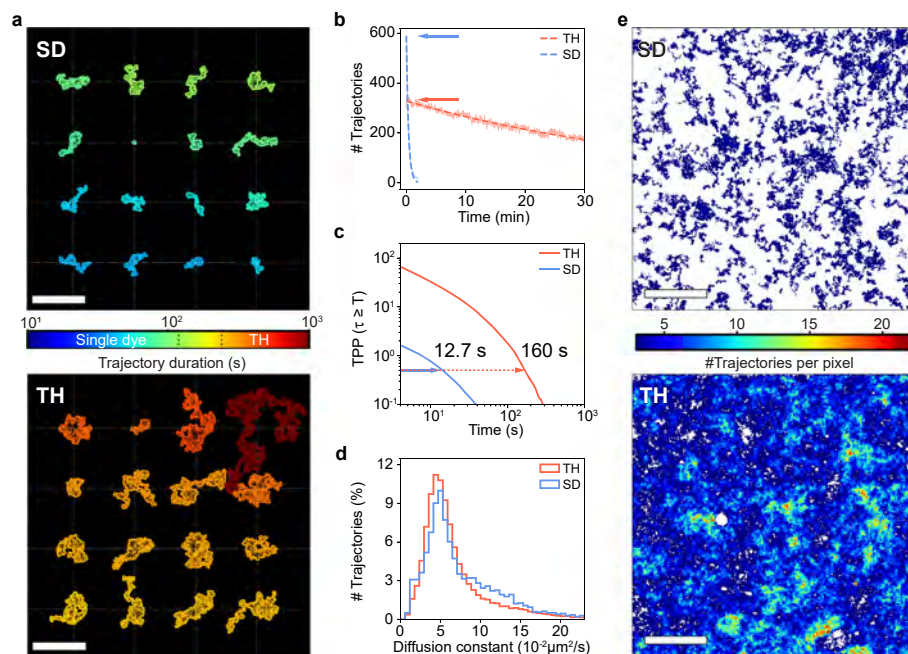


**Fig. 2 Probing 2D diffusion of DNA origami on lipid membranes.** **a** The 16 trajectories of longest duration of both SD origami (top) and TH origami (bottom) floating on an SLB. The trajectories were shifted according to their mean position indicated by the joints of the white dashed lines and were color-coded by duration for better visibility. **b** Number of trajectories per frame for SD origami (solid blue) and TH origami (solid orange). The curves were fitted by an exponential decay function (dashed). The arrows indicate the initial track number ( $\sim$  number of Origami)  $M$  within the FOV. **c** Average number of tracks per Origami  $TPP(\tau_n \geq T)$  as obtained by normalization to the initial track number  $M$  (arrows in **b**, see Supplementary Note 2). **d** Diffusion constants as obtained by linear iterative fitting of the individual MSD curves. Histograms represent the total distribution of three different samples imaged under three different irradiances. Only trajectories with more than 20 localizations were included giving a total of  $n \sim 61,000$  trajectories for the TH origami and  $n \sim 9,000$  trajectories for the SD origami. **e** Number of unique trajectories per  $2 \times 2$  binned pixel (complete FOV). For each binned pixel we counted the number of unique trajectories passing through it during the entire measurement (i.e., a unique trajectory having at least one localization within the pixel boundaries increases its count by one). The TH origami allowed an almost complete mapping of the SLB (bottom) in contrast to only sparse sampling for the SD origami (top). White areas indicate that no trajectory passed these pixels over the complete measurement time. SLB tracking experiments were repeated at least three times for TH origami and at least nine times for SD origami yielding similar results (compare also varying irradiances in Supplementary Figs. 8 and 9). Scale bars,  $10 \mu\text{m}$  in (**a**),  $20 \mu\text{m}$  in (**e**).

Supplementary Fig. 9 for different irradiances). In total, we collected  $\sim 19,000$  trajectories for TH origami compared to only  $\sim 900$  for SD origami, representing a 20-fold increase in statistical sampling. For mobile SD origami we obtained a  $T_{1/2}$  value of  $\sim 12.7$  s (Fig. 2c; see Supplementary Note 2 for mobile TPP calculation) which is in good agreement with the  $T_{1/2}$  of  $\sim 11$  s for immobilized SD origami (Fig. 1g; see Supplementary Fig. 9 for different irradiances). In contrast, we measured a  $T_{1/2}$  of  $\sim 160$  s for TH origami, translating into more than 12-fold longer trajectories on average (Fig. 2c). The  $\sim 2$ -fold reduction in TH trajectory lengths (observation times) compared to immobilized samples imaged under identical conditions is likely due to imperfect trajectory linking at the given particle densities (Supplementary Fig. 10). Even moving particles allowed to observe up to six discrete photon levels—corresponding to the number of imagers bound to the TH—which could potentially be used to resolve ambiguities during trajectory linking (Supplementary Fig. 11). The diffusion constant histograms of both SD and TH origami diffusing on SLBs, as obtained by linear (iterative) fitting of the individual mean square displacement (MSD) curves, agree well with each other, indicating that diffusion properties of origami are not altered by the TH (Fig. 2d). The relatively broad

range of diffusion constants ranging from  $0.02$  to  $0.06 \mu\text{m}^2/\text{s}$  is likely caused by varying numbers of biotinylated anchors per TH origami due to a limited incorporation efficiency<sup>24</sup>. Finally, when we created spatially-resolved maps of single-molecule motions<sup>25,26</sup> of the entire FOV, both the high number of trajectories obtained per TH origami and the long duration of the individual trajectories allowed an almost complete mapping of SLB morphology with only  $\sim 350$  origami present in the FOV at the start of the measurement, in stark contrast to SD origami even when present at much higher initial particle densities (Fig. 2e; arrows in Fig. 2b).

**Long particle trajectories enable advanced quantitative analyses.** Apart from allowing us to efficiently map diffusional patterns in space, the significantly longer particle trajectories for TH origami also allowed us to analyze the motion of sub-trajectories to capture changes within a single trajectory. While promising important biological insights, such an analysis is statistically impossible for trajectories obtained from single-dye-labelled molecules. We divided all trajectories exceeding 120 s (600 frames) in duration into sub-trajectories of 10 s (50 frames), and applied the same MSD fitting algorithm to both the complete

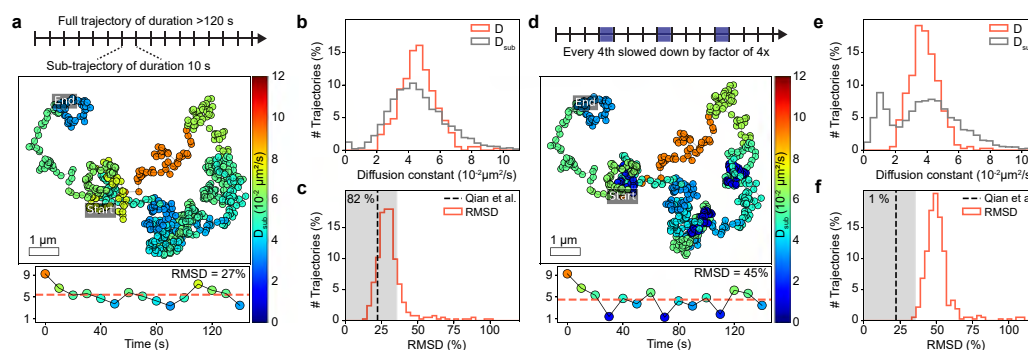


**Fig. 3 Subtrajectory analysis of TH origami diffusion on SLB.** Trajectories exceeding 120 s in duration were divided into sub-trajectories of duration 10 s and analyzed by the same MSD fitting procedure. **a** In the exemplary trajectory each localization is color-coded according to the obtained diffusion constant  $D_{\text{sub}}$  of the corresponding subtrajectory. Time dependent scatter of  $D_{\text{sub}}$  (see colorbar in **a**) around the diffusion constant  $D$  (red dashed) as obtained from analysis of the full trajectory. **b** Total distribution of  $D$  and the corresponding subtrajectory diffusion constants  $D_{\text{sub}}$ . **c** Root-mean-square deviation (RMSD) distribution of  $D_{\text{sub}}$  to  $D$  of all trajectories exceeding 120 s (red). RMSD was normalized to  $D$  and should hence be close to the theoretical limit for the relative standard deviation of  $D_{\text{sub}}$  (black dashed) if the TH origami are subject to a time-invariant Brownian motion (Supplementary Note 3). Gray area indicates deviation of <60% to the theoretical limit. **(d, e, f)** same as **(a, b, c)** but with sub-trajectories computationally slowed down as indicated in **(d)**.

trajectory ( $D$ ) and all of its sub-trajectories ( $D_{\text{sub}}$ , Fig. 3a). The diffusion coefficient distribution for both complete and sub-trajectories overlap perfectly indicating Brownian motion. The  $D_{\text{sub}}$  distribution was 1.5-fold broadened due to the larger statistical uncertainty with decreasing trajectory lengths<sup>27–29</sup> (Fig. 3b, Supplementary Fig. 12). Indeed, we find that the scatter of  $D_{\text{sub}}$  agrees very well with the statistically expected uncertainty for the given subtrajectory durations<sup>27</sup>, confirming a time-invariant Brownian motion of the origami (Fig. 3c, Supplementary Fig. 13, see Supplementary Note 3 for details on the calculations). While time-invariant Brownian motion is expected for our experimental system, we tested if the applied analysis would indeed be capable of detecting motion changes between sub-trajectories, by computationally slowing down individual sub-trajectories (Fig. 3d). Such mobility changes are frequently observed in cell membranes and usually point to physiologically relevant local events<sup>30</sup>. A fourfold speed decrease in every fourth subtrajectory resulted in a second peak in the  $D_{\text{sub}}$  distribution for the slower motion mode (Fig. 3e), and the scatter of  $D_{\text{sub}}$  with respect to  $D$  now clearly deviated from the statistically allowed limits for time-invariant Brownian motion (Fig. 3f, Supplementary Fig. 14).

**A practical handout—limitations and considerations.** In this study, we focused on reconstituted 2D systems that (1) featured a very thin excitation volume (TIRF) and (2) showed very low levels of unspecific binding<sup>21</sup>. This enabled us to use rather high imager concentrations of up to 40 nM. When shifting to cellular targets, one will most likely find a situation that deviates from these ideal conditions more or less strongly. In fact, fluorescence background from unbound diffusing imagers in solution and unspecific binding will dictate the upper bound of the imager concentration at which the TH can be operated in any biological system of interest. However, reducing the imager concentration also comes at the cost of shorter observation times of the TH. We characterized the effects on both the TH key observables and background fluorescence levels caused by either altering the excitation volume via variation of the TIRF angle (Supplementary Fig. 21) or by reducing imager concentrations (Supplementary Fig. 22).

One approach to regain longer trajectory durations even at lower imager concentrations is to label each target molecule with multiple THs. We therefore designed DNA origami with two TH extensions ( $2 \times \text{TH}$ ) and compared the effect on the recorded trajectory durations to standard TH origami ( $1 \times \text{TH}$ ) for varying imager concentrations (Supplementary Fig. 23). While the weight imposed on the target molecule by the  $2 \times \text{TH}$  labeling is only doubled, the observation times are dramatically increased, allowing an eightfold reduction in imager concentration to measure similar observation times as for the  $1 \times \text{TH}$  labeling. We reason that we can achieve a similar effect by extending the  $1 \times \text{TH}$  handle sequence by multiples of the triplet CTC (e.g., from  $18 \times$  to  $36 \times$ ). Naturally, both ways lead to an increased size and weight of the label, potentially interfering with the dynamics of the target molecules at a certain point or reducing the achievable localization precision. However, we think that this approach can be a viable starting point for further optimization, especially in cases where background fluorescence and/or unspecific binding are the limiting factors.

In applications where live-cell compatibility is not required, usage of oxygen scavenging systems and triplet state quenchers strongly boost the performance of single dye molecules (Supplementary Fig. 15). In combination with increased imager dwell times at the TH (e.g., by increasing the imager length to  $3 \times \text{GAG}$ ) this is an additional option to reduce the required imager concentrations.

## Discussion

In summary, our labeling strategy for fluorescence-based SPT, using a 1:1 functionalization with a DNA-based TH and exploiting DNA-mediated fluorophore exchange largely decouples trajectory lengths from the photon budget of single dye molecules, allowing for observations of target particles from minutes to hours depending on the experimental conditions. At the example of 2D diffusion on SLBs, we showed that the large number of trajectories nearly covered the FOV, which allowed mapping of the entire accessible membrane with an actual low number of particles. Even for moving THs, the number of currently bound imagers can be recovered from step-like intensity fluctuations in the fluorescence trace, which provides the

potential for intensity barcoding<sup>31</sup> and multiplexing<sup>32</sup> in the future beyond the use of orthogonal DNA sequences<sup>33</sup>. The ability to divide long trajectories into sub-trajectories paves the way for a robust quantitative analysis of the underlying motion dynamics<sup>34–36</sup>, both in time and in space, and of molecular interactions, paramount to gaining mechanistic information into the biological systems studied by SPT.

We here demonstrated the strengths of our approach using an *in vitro* reconstituted system. However, we believe that the principle can be translated also to cellular targets, such as genetically-tagged<sup>37,38</sup> membrane proteins with accessible extracellular modification sites. Along this way, it will become particularly important to assess and minimize unspecific binding of negatively charged imagers with extracellular components. While intracellular targets of living cells are inaccessible to DNA-PAINT (due to degradation of imager strands by DNase), recently a peptide-based PAINT approach has been successfully demonstrated inside living cells<sup>39,40</sup>, which could potentially enable genetic engineering of a peptide-based TH for intracellular targets.

A key challenge to overcome is the elevated background fluorescence currently limiting the tracking experiments to selective plane illumination schemes such as TIRF microscopy. Here, we have demonstrated that doubling the number of binding sites per particle (labeling with  $2 \times$  TH) allowed a reduction in both imager concentration and background fluorescence, by eightfold and sixfold, respectively, without any loss in performance. Of course, this comes at the cost of additional load to the target molecules. A promising complementary solution to the problem of background fluorescence has recently been proposed in a study using self-quenching fluorogenic imagers for DNA-PAINT<sup>41</sup>. A combined implementation of fluorogenic imagers with our TH in a widefield configuration could allow, for instance, tracking of molecules also in 3D using point spread function engineering<sup>42,43</sup>.

To conclude, our detailed analysis of the key parameters of DNA-PAINT based SPT will allow researchers to adapt the TH to their specific systems of interest, ranging from *in vitro* applications to potentially tracking receptors in the plasma membrane of living cells. We believe that due to its modularity and ease-of-use, our DNA-PAINT adaptation for SPT will become a valuable tool for studying dynamic processes at the single-molecule level.

## Methods

**Materials.** Unmodified, dye-labeled, and biotinylated DNA oligonucleotides were purchased from MWG Eurofins. DNA scaffold strands were purchased from Tilibit (cat. p7249, identical to M13mp18). Streptavidin was purchased from Thermo Fisher (cat. S-888). BSA-Biotin was obtained from Sigma-Aldrich (cat. A8549). All lipids were purchased from Avanti Polar Lipids. Glass slides were ordered from Thermo Fisher (cat. 10756991) and coverslips were purchased from Marienfeld (cat. 0107032). Freeze 'N Squeeze columns were ordered from Bio-Rad (cat. 732-6165). Tris 1M pH 8.0 (cat. AM9856), EDTA 0.5M pH 8.0 (cat. AM9261), Magnesium 1M (cat. AM9530G) and Sodium Chloride 5M (cat. AM9759) were ordered from Ambion. Ultrapure water (cat. 10977-035) was purchased from Thermo Fisher Scientific. Tween-20 (cat. P9416-50ML), Glycerol (cat. 65516-500ml), (+)-6-Hydroxy-2,5,7,8-tetra-methylchromane-2-carboxylic acid (Trolox) (cat. 238813-5G), pyranose oxidase (PO, cat. P4234) and catalase (C, cat. C40) were purchased from Sigma-Aldrich. Two-component epoxy glue (cat. 886519 - 62) was purchased from Conrad Electronic SE.

**Buffers.** Seven buffers were used for sample preparation and imaging: Buffer A (10 mM Tris-HCl pH 7.5, 100 mM NaCl); Buffer B (5 mM Tris-HCl pH 8.0, 10 mM MgCl<sub>2</sub>, 1 mM EDTA); Buffer L (20 mM HEPES pH 7.6, 140 mM NaCl, 3 mM MgCl<sub>2</sub>); Buffer POCT (5 mM Tris-HCl pH 8.0, 10 mM MgCl<sub>2</sub>, 1 mM EDTA, incubated 1 h prior to measurement with  $1 \times$  PO,  $1 \times$  C, 0.8% Glucose and  $1 \times$  Trolox as previously described<sup>23</sup>);  $10 \times$  folding buffer (100 mM Tris, 10 mM EDTA pH 8.0, 125 mM MgCl<sub>2</sub>); Buffer M (25 mM Tris-HCl pH 7.5, 150 mM KCl, 5 mM MgCl<sub>2</sub>); SLB buffer (25 mM Tris-HCl pH 7.5, 150 mM KCl).

**DNA origami design and assembly and purification.** DNA origami structures were designed using the design module of Picasso<sup>16</sup>. Our DNA origami design is identical to the one used in previous work<sup>44</sup>, i.e., of flat rectangular geometry with just a single extension on the top side (at position 2B07 of Picasso Design). At this position, we as the label either incorporated the TH or a Cy3B molecule permanently attached to a short T-spacer, or a single DNA-PAINT docking strand (1DS) (see Supplementary Table 2 for sequences). On the bottom side, eight biotinylated extensions were incorporated for surface immobilization/SLB binding. Folding of structures was performed using the following components: single-stranded DNA scaffold (0.01  $\mu$ M), core staples (0.1  $\mu$ M), biotin staples (1  $\mu$ M for SD origami and 0.01  $\mu$ M for TH origami and 1DS origami), TH/SD/1DS strands (1  $\mu$ M),  $1 \times$  folding buffer in a total of 50  $\mu$ l for each sample. Annealing was done by cooling the mixture from 80 to 25 °C in 3 h in a thermocycler. TH origami and 1DS were not purified after folding. SD origami were purified using PEG precipitation<sup>45</sup>.

## Sample preparation

**Surface-immobilized DNA origami.** DNA origami samples were prepared as described before<sup>16</sup>. A glass slide was glued onto a coverslip with the help of double-sided tape (Scotch, cat. no. 665D) to form a flow chamber with inner volume of  $\sim 20 \mu$ l. First, 20  $\mu$ l of biotin-labeled bovine albumin (1 mg/ml, dissolved in buffer A) was flushed into the chamber and incubated for 3 min. The chamber was then washed with 40  $\mu$ l of buffer A. 20  $\mu$ l of streptavidin (0.5 mg/ml, dissolved in buffer A) was then flushed through the chamber and incubated for 3 min. After washing with 40  $\mu$ l of buffer A and subsequently with 40  $\mu$ l of buffer B, 20  $\mu$ l of biotin-labeled DNA origami (dilution from DNA origami stock dependent on origami yield after gel purification. Adjusted for each origami species individually to obtain a sparse DNA origami surface density. Starting dilution  $\sim 1:200$ ) were flushed into the chamber and incubated for 10 min. The chamber was washed with 80  $\mu$ l of imaging buffer (L/B/POCT) to remove unbound DNA origami. SD origami samples were sealed with two-component epoxy glue before imaging. For TH and 1DS origami samples, 40  $\mu$ l of the imager solution was flushed into the chamber before sealing.

**DNA origami diffusing on supported lipid bilayers.** A glass slide was rubbed and rinsed with EtOH and ddH<sub>2</sub>O and subsequently plasma cleaned using a plasma cleaner (Zepto, Diener Electronic, Germany) for 40 s at 50% power and 0.3 mbar with oxygen as process gas. The glass slide was glued onto a coverslip with the help of double-sided tape (Scotch, cat. no. 665D) to form a flow chamber with inner volume of  $\sim 20 \mu$ l. Small unilamellar vesicles (SUVs) were prepared at a concentration of 4 mg/ml in buffer M from a lipid composition of 99 mol % DOPC/1 mol % Biotinyl-CAP-PE. Lipids dissolved in chloroform were dried under a stream of nitrogen. Vials were placed in a desiccator for 30 min to remove residual chloroform. After lipids were rehydrated in 200  $\mu$ l of buffer M, the vials were placed in a sonicator bath to generate SUVs until the solution appeared transparent (storage of SUV solution aliquots possible at  $-30 \text{ }^\circ\text{C}$  for several weeks. After thawing of an aliquot it was placed in the sonication bath for 30 min). SUV solution was diluted to 0.5 mg/ml in buffer M. 20  $\mu$ l of SUV dilution was flushed into the chamber and incubated for 3 min. The chamber was then washed with  $5 \times 80 \mu$ l of SLB buffer to remove excess vesicles and  $1 \times 80 \mu$ l with buffer B. 20  $\mu$ l of streptavidin (0.5 mg/ml, dissolved in buffer A) was then flushed through the chamber and incubated for 5 min. After washing with 80  $\mu$ l of buffer B, 20  $\mu$ l of biotin-labeled DNA origami was flushed into the chamber and incubated for 3 min (origami dilution after folding  $\sim 1:1,000$ ). Excess DNA origami were washed with 80  $\mu$ l of buffer L. SD origami samples were sealed with two-component epoxy glue before imaging. For TH origami samples 40  $\mu$ l of the imager solution were flushed into the chamber before sealing.

**Super-resolution microscopy setup.** Fluorescence imaging was carried out on an inverted custom-built microscope (see supplementary references<sup>44,46</sup> for detailed sketches) in an objective-type TIRF configuration with an oil-immersion objective (Olympus UAPON, 100 $\times$ , NA 1.49). One laser was used for excitation: 561 nm (1 W, DPSS-system, MPB). The laser power was adjusted via polarization rotation using a half-wave plate (Thorlabs, WPH05M-561) before passing a polarizing beam-splitter cube (Thorlabs, PBS101). The laser light was coupled into a single-mode polarization-maintaining fiber (Thorlabs, P3-488PM-FC-2) using an aspheric lens (Thorlabs, C610TME-A) in order to spatially clean the beam-profile. Using a zero-order half-wave plate (Thorlabs, WPH05M-561) the coupling polarization into the fiber was adjusted. The laser light was re-collimated after the fiber using an achromatic doublet lens (Thorlabs, AC254-050-A-ML) resulting in a collimated FWHM beam diameter of  $\sim 6$  mm. The Gaussian laser beam-profile was transformed into a collimated flat-top profile using a refractive beam shaping device (AdlOptica, piShaper 6\_6\_VIS). The laser beam diameter was magnified by a factor of 2.5 using a custom-built telescope (Thorlabs, AC254-030-A-ML and Thorlabs, AC508-075-A-ML). The laser light was coupled into the microscope objective using an achromatic doublet lens (Thorlabs, AC508-180-A-ML) and a dichroic beam splitter (AHF, F68-785). Fluorescence light was spectrally filtered with a laser notch filter (AHF, F40-072) and a bandpass filter (AHF Analy-sentechnik, 605/64) and imaged on a sCMOS camera (Andor, Zyla 4.2) using a tube lens without further magnification (Thorlabs, TTL180-A) resulting in an effective pixel size of 130 nm (after  $2 \times 2$  binning). Microscopy samples were

mounted into a closed water-based temperature chamber (Okolab, H101-CRYO-BL) on an x-y-z stage (ASI, S31121010FT and ASI, FTP2050) that was used for focusing with the microscope objective being at fixed position. The temperature of the objective was actively controlled using the same water cycle as the temperature chamber. Focus stabilization was achieved via the CRISP autofocus system (ASI @ 850 nm) in a feedback loop with a piezo actuator (Piezoconcept, Z-INSERT100) moving the sample. The CRISP was coupled into the excitation path of the microscope using a long pass dichroic mirror (Thorlabs, DMLP650L). Our custom TIRF setup was used for all presented data.

**Imaging conditions.** All fluorescence microscopy data was recorded with our sCMOS camera (2048 × 2048 pixels, pixel size: 6.5 μm). The camera was operated with the open source acquisition software μManager<sup>47</sup> at 2 × 2 binning and cropped to the center 700 × 700 pixel FOV. The exposure time was set to 200 ms, the read out rate to 200 MHz and the dynamic range to 16 bit. The laser power was set to a homogeneous (flat-top profile, see setup description) with a measured excitation beam diameter of  $d \sim 130 \mu\text{m}$ <sup>46</sup>. We performed all experiments at laser excitation powers  $P$  of 1.4 mW, 4.1 mW and 8.9 mW (as measured at the fiber exit port). We hence calculated an (upper limit) homogeneous excitation irradiance  $E$  at the sample space of 10 W/cm<sup>2</sup>, 30 W/cm<sup>2</sup> and 65 W/cm<sup>2</sup> by using  $E = 4P/\pi d^2$ . SD origami samples were imaged repeatedly at 3× field of views (FOVs) for increased statistics, TH origami samples only at 1× FOV. For detailed imaging parameters specific to the data presented in all main and supplementary figures refer to Supplementary Table 1.

**Image processing & single particle tracking analysis.** Please refer to Supplementary Fig. 3, Supplementary Fig. 4 and Supplementary Fig. 7 for a step-by-step illustration through all processing steps of immobilized and diffusing DNA origami data, respectively. In any case, a standard single molecule localization algorithm was applied to the raw image stack to obtain a pointillist super-resolution image of the DNA origami<sup>16</sup> (*picasso*, see below). Immobile DNA origami appeared as localization clusters after image correlation based undrifting<sup>48</sup>. Subsequently, we automatically detected all localization clusters as previously described<sup>44</sup> and extracted the corresponding fluorescence traces (see e.g., Fig. 1f,g) for further analysis (*spt*, see below). Note that for all surface-immobilized experiments (for both SD origami and TH origami) we ignored interruptions in the fluorescence trace of just a single frame when determining the trajectory durations (i.e., ‘ignore’ in Supplementary Fig. 3). In the case of moving origami a nearest neighbor based linking algorithm (*trackpy*, see below) was applied to the localized raw image stack to obtain particle trajectories. Subsequent MSD analysis of the individual trajectories was carried out using custom python code (*spt*, see below).

The described analysis workflow was completely based on two custom written python packages [https://github.com/schwille-paint/picasso\\_addon](https://github.com/schwille-paint/picasso_addon) (*picasso\_addon*<sup>48</sup>) and <https://github.com/schwille-paint/SPT> (*spt*). These packages integrate <https://github.com/jungmannlab/picasso> (*picasso*<sup>49</sup>) for localization of raw image stacks and on <https://soft-matter.github.io/trackpy/v0.4.2/> (*trackpy*<sup>50</sup>) for linking of localizations into particle trajectories. The custom packages *picasso\_addon* and *spt* hence provide a complete single particle tracking analysis suite for both mobile and immobilized particles. Please visit <https://picasso-addon.readthedocs.io/en/latest/index.html> and <https://spt.readthedocs.io/en/latest/index.html> for detailed information about the *picasso\_addon* and *spt* API.

**Reporting summary.** Further information on research design is available in the Nature Research Reporting Summary linked to this article.

#### Data availability

Source data are provided with this paper. The raw data that support the findings of this study are available from the corresponding authors upon reasonable request. Source data are provided with this paper.

#### Code availability

Custom written python modules packages were employed in this study, which are available in public repositories: [https://github.com/schwille-paint/picasso\\_addon](https://github.com/schwille-paint/picasso_addon)<sup>48</sup> and <https://github.com/schwille-paint/SPT><sup>49</sup>.

Received: 27 January 2021; Accepted: 7 June 2021;

Published online: 21 July 2021

#### References

- Manzo, C. & Garcia-Parajo, M. F. A review of progress in single particle tracking: from methods to biophysical insights. *Rep. Prog. Phys.* **78**, 124601 (2015).
- Kusumi, A., Suzuki, K. G. N., Kasai, R. S., Ritchie, K. & Fujiwara, T. K. Hierarchical mesoscale domain organization of the plasma membrane. *Trends Biochem. Sci.* **36**, 604–615 (2011).
- Mallik, R., Petrov, D., Lex, S. A., King, S. J. & Gross, S. P. Building Complexity: an In Vitro Study of Cytoplasmic Dynein with In Vivo Implications. *Curr. Biol.* **15**, 2075–2085 (2005).
- Geerts, H. et al. Nanovid tracking: a new automatic method for the study of mobility in living cells based on colloidal gold and video microscopy. *Biophys. J.* **52**, 775–782 (1987).
- De Brabander, M., Nuydens, R., Geerts, H. & Hopkins, C. R. Dynamic behavior of the transferrin receptor followed in living epidermoid carcinoma (A431) cells with nanovid microscopy. *Cell Motil.* **9**, 30–47 (1988).
- Ghosh, R. P. et al. A fluorogenic array for temporally unlimited single-molecule tracking. *Nat. Chem. Biol.* **15**, 401–409 (2019).
- Niekamp, S., Stuurman, N. & Vale, R. D. A 6-nm ultra-photostable DNA FluoroCube for fluorescence imaging. *Nat. Methods* (2020). <https://doi.org/10.1038/s41592-020-0782-3>
- Patil, P. V. & Ballou, D. P. The Use of Protocatechuate Dioxygenase for Maintaining Anaerobic Conditions in Biochemical Experiments. *Anal. Biochem.* **286**, 187–192 (2000).
- Aitken, C. E., Marshall, R. A. & Puglisi, J. D. An Oxygen Scavenging System for Improvement of Dye Stability in Single-Molecule Fluorescence Experiments. *Biophys. J.* **94**, 1826–1835 (2008).
- Swoboda, M. et al. Enzymatic Oxygen Scavenging for Photostability without pH Drop in Single-Molecule Experiments. *ACS Nano* **6**, 6364–6369 (2012).
- Rasnik, I., McKinney, S. A. & Ha, T. Nonblinking and long-lasting single-molecule fluorescence imaging. *Nat. Methods* **3**, 891–893 (2006).
- Dave, R., Terry, D. S., Munro, J. B. & Blanchard, S. C. Mitigating Unwanted Photophysical Processes for Improved Single-Molecule Fluorescence Imaging. *Biophys. J.* **96**, 2371–2381 (2009).
- Magidson, V. & Khodjakov, A. Chapter 23—Circumventing Photodamage in Live-Cell Microscopy. in *Methods in Cell Biology* (eds. Sluder, G. & Wolf, D. E.) 114, 545–560 (Academic Press, 2013).
- Pinaud, F., Clarke, S., Sittner, A. & Dahan, M. Probing cellular events, one quantum dot at a time. *Nat. Methods* **7**, 275–285 (2010).
- Shen, H. et al. Single Particle Tracking: from Theory to Biophysical Applications. *Chem. Rev.* **117**, 7331–7376 (2017).
- Schnitzbauer, J., Strauss, M. T., Schlichthaerle, T., Schueder, F. & Jungmann, R. Super-resolution microscopy with DNA-PAINT. *Nat. Protoc.* **12**, 1198–1228 (2017).
- Schickinger, M., Zacharias, M. & Dietz, H. Tethered multifluorophore motion reveals equilibrium transition kinetics of single DNA double helices. *Proc. Natl Acad. Sci.* **115**, E7512–E7521 (2018).
- Schueder, F. et al. An order of magnitude faster DNA-PAINT imaging by optimized sequence design and buffer conditions. *Nat. Methods* **16**, 1101–1104 (2019).
- Strauss, S. & Jungmann, R. Up to 100-fold speed-up and multiplexing in optimized DNA-PAINT. *Nat. Methods* 1–3 (2020). <https://doi.org/10.1038/s41592-020-0869-x>
- Civiti, F. et al. Fast and multiplexed superresolution imaging with DNA-PAINT-ERS. *Nat. Commun.* **11**, 4339 (2020).
- Clowsley, A. H. et al. Repeat DNA-PAINT suppresses background and non-specific signals in optical nanoscopy. *Nat. Commun.* **12**, 501 (2021).
- Thompson, N. L., Burghardt, T. P. & Axelrod, D. Measuring surface dynamics of biomolecules by total internal reflection fluorescence with photobleaching recovery or correlation spectroscopy. *Biophys. J.* **33**, 435–454 (1981).
- Blumhardt, P. et al. Photo-Induced Depletion of Binding Sites in DNA-PAINT Microscopy. *Molecules* **23**, 3165 (2018).
- Strauss, M. T., Schueder, F., Haas, D., Nickels, P. C. & Jungmann, R. Quantifying absolute addressability in DNA origami with molecular resolution. *Nat. Commun.* **9**, 1600 (2018).
- Manley, S. et al. High-density mapping of single-molecule trajectories with photoactivated localization microscopy. *Nat. Methods* **5**, 155–157 (2008).
- Johnson-Buck, A., Jiang, S., Yan, H. & Walter, N. G. DNA-Cholesterol Barges as Programmable Membrane-Exploring Agents. *ACS Nano* **8**, 5641–5649 (2014).
- Qian, H., Sheetz, M. P. & Elson, E. L. Single particle tracking. Analysis of diffusion and flow in two-dimensional systems. *Biophys. J.* **60**, 910–921 (1991).
- Michalet, X. Mean square displacement analysis of single-particle trajectories with localization error: Brownian motion in an isotropic medium. *Phys. Rev. E* **82**, 041914 (2010).
- Kerkhoff, Y. & Block, S. Analysis and refinement of 2D single-particle tracking experiments. *Biointerphases* **15**, 021201 (2020).
- Egeling, C. et al. Direct observation of the nanoscale dynamics of membrane lipids in a living cell. *Nature* **457**, 1159–1162 (2009).
- Woehrstein, J. B. et al. Sub-100-nm metafluorophores with digitally tunable optical properties self-assembled from DNA. *Sci. Adv.* **3**, e1602128 (2017).

32. Wade, O. K. et al. 124-Color Super-resolution Imaging by Engineering DNA-PAINT Blinking Kinetics. *Nano Lett.* **19**, 2641–2646 (2019).
33. Jungmann, R. et al. Multiplexed 3D cellular super-resolution imaging with DNA-PAINT and Exchange-PAINT. *Nat. Methods* **11**, 313–318 (2014).
34. Simson, R., Sheets, E. D. & Jacobson, K. Detection of temporary lateral confinement of membrane proteins using single-particle tracking analysis. *Biophys. J.* **69**, 989–993 (1995).
35. Block, S., Zhdanov, V. P. & Höök, F. Quantification of Multivalent Interactions by Tracking Single Biological Nanoparticle Mobility on a Lipid Membrane. *Nano Lett.* **16**, 4382–4390 (2016).
36. Huet, S. et al. Analysis of Transient Behavior in Complex Trajectories: application to Secretory Vesicle Dynamics. *Biophys. J.* **91**, 3542–3559 (2006).
37. Schlichthaerle, T. et al. Direct Visualization of Single Nuclear Pore Complex Proteins Using Genetically-Encoded Probes for DNA-PAINT. *Angew. Chem. Int. Ed.* **58**, 13004–13008 (2019).
38. Strauss, S. et al. Modified aptamers enable quantitative sub-10-nm cellular DNA-PAINT imaging. *Nat. Methods* **15**, 685–688 (2018).
39. Oi, C. et al. LIVE-PAINT allows super-resolution microscopy inside living cells using reversible peptide-protein interactions. *Commun. Biol.* **3**, 1–10 (2020).
40. Eklund, A. S., Ganji, M., Gavins, G., Seitz, O. & Jungmann, R. Peptide-PAINT Super-Resolution Imaging Using Transient Coiled Coil Interactions. *Nano Lett.* **20**, 6732–6737 (2020).
41. Chung, K. K. H. et al. Fluorogenic probe for fast 3D whole-cell DNA-PAINT. *bioRxiv* 2020.04.29.066886 (2020). <https://doi.org/10.1101/2020.04.29.066886>
42. Huang, B., Wang, W., Bates, M. & Zhuang, X. Three-dimensional super-resolution imaging by stochastic optical reconstruction microscopy. *Sci.* (80-) **319**, 810–813 (2008).
43. Pavani, S. R. P. et al. Three-dimensional, single-molecule fluorescence imaging beyond the diffraction limit by using a double-helix point spread function. *Proc. Natl Acad. Sci. U. S. A.* **106**, 2995–2999 (2009).
44. Stein, J. et al. Toward Absolute Molecular Numbers in DNA-PAINT. *Nano Lett.* **19**, 8182–8190 (2019).
45. Stahl, E., Martin, T. G., Praetorius, F. & Dietz, H. Facile and Scalable Preparation of Pure and Dense DNA Origami Solutions. *Angew. Chem. Int. Ed.* **53**, 12735–12740 (2014).
46. Stehr, F., Stein, J., Schueder, F., Schwille, P. & Jungmann, R. Flat-top TIRF illumination boosts DNA-PAINT imaging and quantification. *Nat. Commun.* **10**, 1268 (2019).
47. Edelstein, A. D. et al. Advanced methods of microscope control using µManager software. *J. Biol. Methods* **1**, e10 (2014).
48. Stehr, F. & Stein, J. *picasso\_addon*. (2021). <https://doi.org/10.5281/ZENODO.4792396>
49. Stehr, F. & Stein, J. SPT. (2021). <https://doi.org/10.5281/ZENODO.4792495>
50. Crocker, J. C. & Grier, D. G. Methods of Digital Video Microscopy for Colloidal Studies. *J. Colloid Interfac. Sci.* **179**, 298–310 (1996).

#### Acknowledgements

We thank Beatrice Ramm, Tamara Heermann, Henri Franquelim, Patrick Schueler, Sigrid Bauer and Katharina Nakel for experimental support and helpful discussions. J.S. and F.S. acknowledge support from Graduate School of Quantitative Bioscience Munich (QBM). All authors acknowledge support from the Center for Nano Science (CeNS).

This work has been supported in part by the German Research Foundation through the Emmy Noether Program (DFG JU 2957/1-1 to R.J.), the SFB1032 (projects A11 and A09 to R.J. and P.S.), the European Research Council through an ERC Starting Grant (MolMap; grant agreement number 680241 to R.J.) and the Max Planck Society (P.S. and R.J.).

#### Author contributions

F.S., J.S., R.J., K.G. and P.S. conceived the study. F.S., J.S. and J.B. designed experiments. J.S. performed the experiments. J.B. devised the concept of the tracking handle sequence, prepared DNA origami and performed initial experiments. C.N. performed initial experiments. F.S. and J.S. designed and performed data analysis. F.S. wrote the analysis code. F.S., J.S., R.J., K.G. and P.S. wrote the paper. K.G. and P.S. supervised the study. All authors discussed and interpreted results and revised the paper.

#### Funding

Open Access funding enabled and organized by Projekt DEAL.

#### Competing interests

The authors declare no competing interests.

#### Additional information

**Supplementary information** The online version contains supplementary material available at <https://doi.org/10.1038/s41467-021-24223-4>.

**Correspondence** and requests for materials should be addressed to K.G. or P.S.

**Peer review information** *Nature Communications* thanks David Baddeley and the other, anonymous, reviewer(s) for their contribution to the peer review of this work. Peer reviewer reports are available.

**Reprints and permission information** is available at <http://www.nature.com/reprints>

**Publisher's note** Springer Nature remains neutral with regard to jurisdictional claims in published maps and institutional affiliations.



**Open Access** This article is licensed under a Creative Commons Attribution 4.0 International License, which permits use, sharing, adaptation, distribution and reproduction in any medium or format, as long as you give appropriate credit to the original author(s) and the source, provide a link to the Creative Commons license, and indicate if changes were made. The images or other third party material in this article are included in the article's Creative Commons license, unless indicated otherwise in a credit line to the material. If material is not included in the article's Creative Commons license and your intended use is not permitted by statutory regulation or exceeds the permitted use, you will need to obtain permission directly from the copyright holder. To view a copy of this license, visit <http://creativecommons.org/licenses/by/4.0/>.

© The Author(s) 2021

## Supporting Information

### Tracking Single Particles for Hours via continuous DNA-mediated Fluorophore Exchange

Florian Stehr<sup>1,\*</sup>, Johannes Stein<sup>1,\*</sup>, Julian Bauer<sup>1</sup>, Christian Niederauer<sup>3</sup>, Ralf Jungmann<sup>1,2</sup>, Kristina Ganzinger<sup>3</sup> and Petra Schwillie<sup>2</sup>

#### Supplementary Figures

Supplementary Figure 1	Size comparison between SPT labels
Supplementary Figure 2	Sequence design
Supplementary Figure 3	Data analysis workflow - immobilized
Supplementary Figure 4	Filter - immobilized
Supplementary Figure 5	Photon counts & localization precision - immobilized
Supplementary Figure 6	Error estimation for $T_{1/2}$ results
Supplementary Figure 7	Data analysis workflow - mobile
Supplementary Figure 8	Longest trajectories at varying irradiances
Supplementary Figure 9	Tracks, TPP and diffusion constant for varying irradiances
Supplementary Figure 10	Linking and particle density
Supplementary Figure 11	Photons counts - mobile
Supplementary Figure 12	$D$ vs. $D_{\text{sub}}$ for varying subtrajectory durations
Supplementary Figure 13	RMSD of $D_{\text{sub}}$ for varying subtrajectory durations
Supplementary Figure 14	2-fold slowdown of every fourth subtrajectory

**Supplementary Note 1: Tracking handle key parameters**

Supplementary Figure 15	Tracking handle key parameters overview
Supplementary Figure 16	Extended 3-hour measurement using POCT
Supplementary Figure 17	$k_{\text{photodamage}}$ vs. irradiance
Supplementary Figure 18	Temperature effect on DNA hybridization rates
Supplementary Figure 19	Ion concentration effect on DNA hybridization rates

**Supplementary Note 2: TPP calculus for mobile particles**

**Supplementary Note 3: Statistical treatment of diffusion coefficients**

Supplementary Figure 20	Mobile analysis control with immobilized data set
-------------------------	---

**Supplementary Note 4: Potential limitations and workarounds**

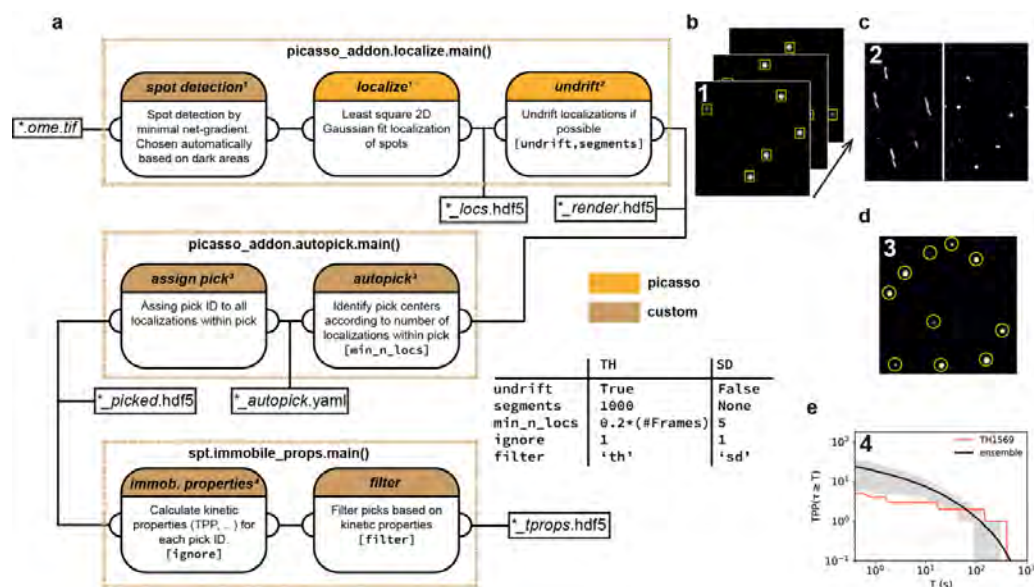
Supplementary Figure 21	Performance of tracking handle at varying TIRF angles
Supplementary Figure 22	Performance of tracking handle at varying imager concentrations
Supplementary Figure 23	2×TH vs. 1×TH labeling

**Supplementary Tables**

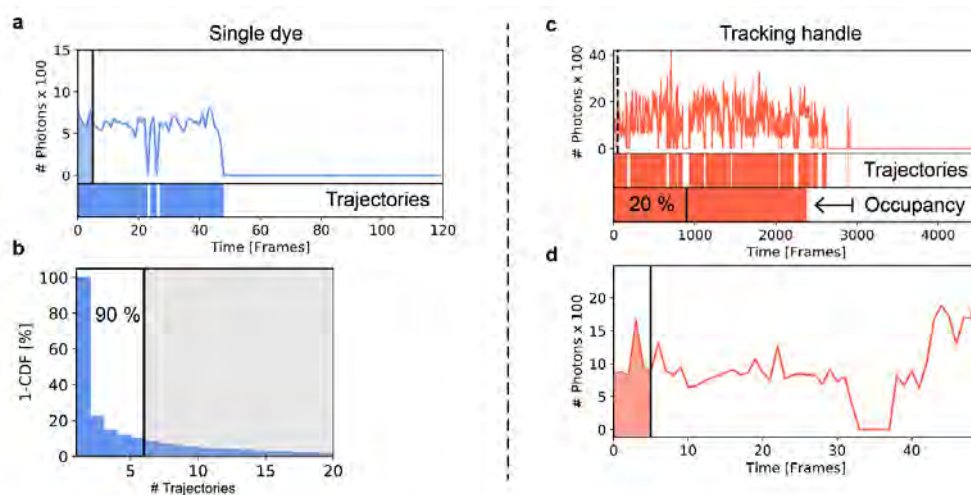
Supplementary Table 1	Imaging parameters
Supplementary Table 2	Used DNA oligonucleotide sequences as labels

**Supplementary References**

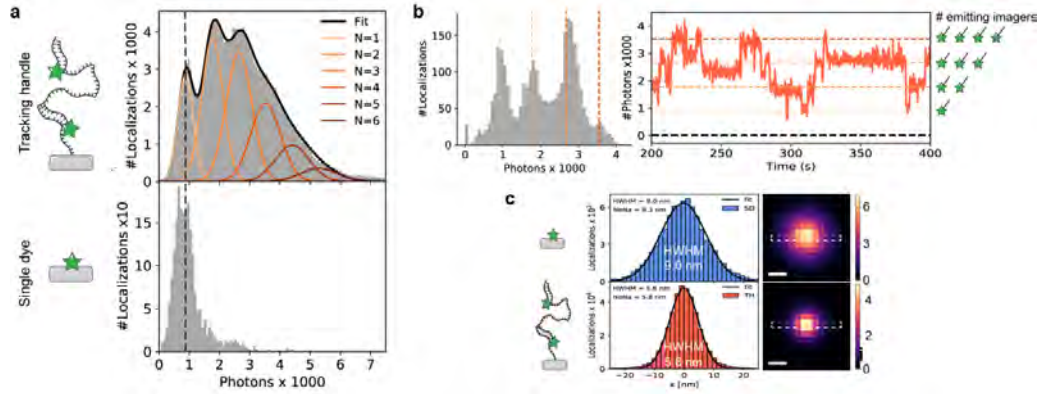




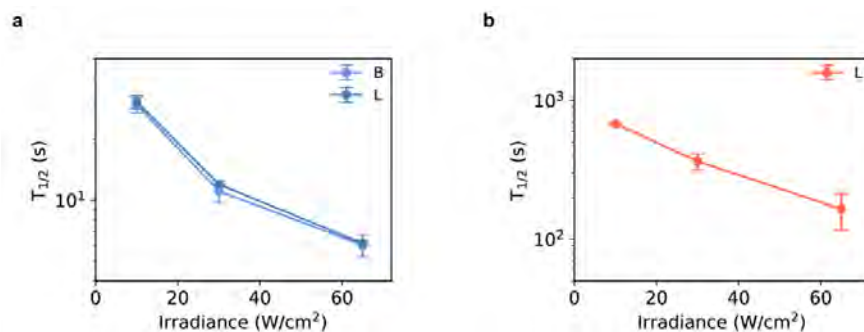
**Supplementary Figure 3. Data analysis workflow - immobilized.** (a) Data analysis workflow from raw movies (\*.ome.tif) to final result (\*\_tprops.hdf5). Dashed boxes indicate employed main functions - e.g. `picasso_addon.localize.main()` - of the `picasso_addon` and `spt` python package. Rounded boxes illustrate provided functionalities of each main function. The header color code indicates from which python package the functionality was adapted (e.g. `picasso` or `custom` for extended functionalities within `picasso_addon` or `spt`). The text within the rounded boxes gives a short description of the provided functionality and parameters (brackets) for execution of the main function. The table summarizes all parameters used for evaluation of immobilized SD or TH experiments. The small boxes branching of the main flow represent which files are saved during execution. Please visit the links provided in the section “Image processing & single particle tracking analysis” for further information. (b) Illustration of spot detection (boxes) and localization of individual emitters in raw images. (c) Illustration of image correlation based undrift of the rendered localization lists (parameters: `undrift`, `segments`). (d) Illustration of localization cluster detection based on number of localizations within the localization cluster (parameter: `min_n_locs`). We follow the Picasso nomenclature referring to a detected localization cluster as ‘pick’ with a unique pick ID. (e) Final result is obtained by calculating kinetic properties for each pick (e.g. TPP, number of localizations, photon counts etc.) by employing `spt.immobile_props.main()` (parameters: `ignore`, `filter`). For a detailed description of our final filtering procedure for each pick please refer to **Supplementary Fig. 4**.



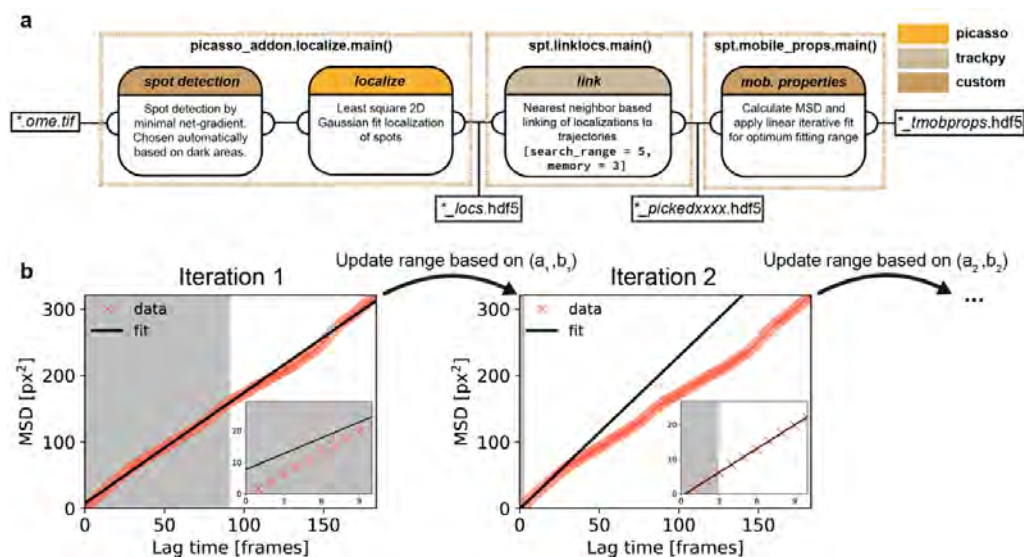
**Supplementary Figure 4. Filter - immobilized.** (a) The filtering procedure (see **Supplementary Fig. 3**) for immobilized SD origami is illustrated for an exemplary fluorescence trace (blue line). Valid picks (i.e. picks passing the filter criteria) yielded fluorescence traces with at least one localization within the first 5 frames (black line) of the measurement (blue area below trace). The bar below indicates the number of trajectories, i.e., continuous and uninterrupted fluorescence signal (here 3 trajectories). (b) Cumulative distribution function of number of trajectories per SD origami for an exemplary data set. As expected, the majority of SD origami yielded only a single trajectory before undergoing photobleaching. However, a small fraction of SD origami exhibited blinking behavior, causing interruptions in the fluorescence trace and hence an increased number of registered trajectories (as in the example in a). To remove potentially damaged/imperfect dye molecules, we discarded all picks exceeding the 90%-percentile (black line) of the distribution of number of trajectories of all picks, in this case picks exhibiting more than 5 trajectories. (c) For immobilized TH origami we calculated the ratio between the total time of a TH in the fluorescent state (i.e. the sum over all trajectory durations) and the total measurement time, which we define as the occupancy. In other words, the occupancy indicates the total time in which a TH is occupied with a fluorescing imager as a percentage of measurement time. Only picks with an occupancy of more than 20 % (black line) were used for further analysis. The black dashed line indicates a zoom into the fluorescence signal shown in (d). Analogous to (a), we additionally only considered TH origami picks yielding at least one localization within the first 5 frames (black line) of the measurement (red area below trace).



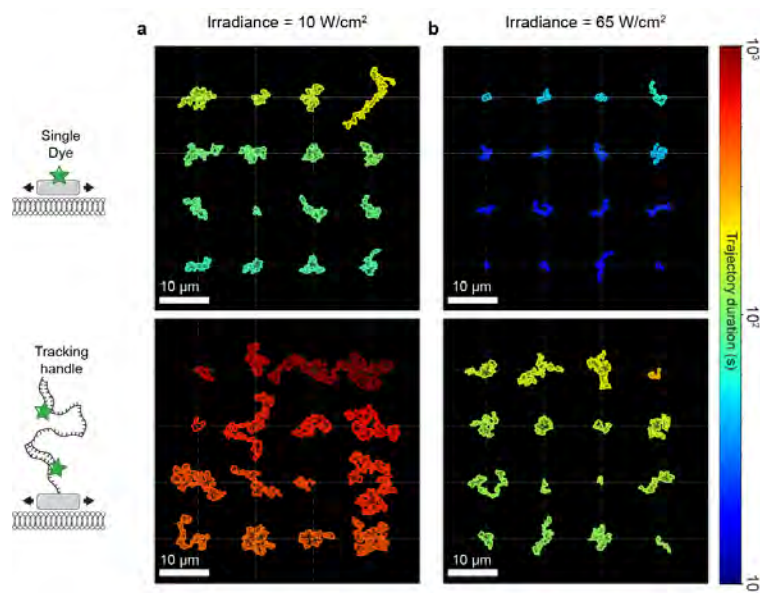
**Supplementary Figure 5. Photon counts & localization precision - immobilized.** (a) Ensemble photon count distributions as obtained from localizations corresponding to immobilized TH origami (top) and SD origami (bottom). The TH origami showed a multimodal distribution with distinct peaks in an equidistant spacing and located at multiples of the lowest peak's center value. We hence fitted the data with the sum (solid black) of 6 Gaussian functions  $g_i$  (colored) of the form  $g_i(x; A_i, x_0, \sigma) = A_i \exp\left[-\frac{(x - ix_0)^2}{i\sigma^2}\right]$  with freely floating amplitudes  $A_i$  for each  $g_i$  but global parameters  $x_0$  and  $\sigma$  for the sum, corresponding to the center and width of the lowest order peak. The amplitudes  $A_i$  can thus directly be translated into a probability of  $i$  emitting imager strands being bound to the TH. Notice that the fit result for the center of lowest peak  $x_0$  coincides with the single peak obtained for the photon distributions of SD origami localizations (dashed black line). In order to account for imaging artifacts causing variations in the number of detected photons<sup>5</sup>, we only used origami lying within the central circular region of the FOV (diameter = 200 px). (b) Photon count histogram (left) and zoom into the fluorescence trace (right) of the individual TH origami TH1569 displayed in Fig. 1g. The dashed colored lines indicate the photon levels  $ix_0$  as obtained from the fit of the ensemble distribution (a, top). For individual origami, the equidistant peaks in the photons count histogram (left) revealing the number of currently bound and emitting imagers (here 1-4x imagers) are more clearly separable than in the ensemble histogram from all TH origami (a, top). The zoom-in (right) illustrates that the fluorescence trace indeed follows a step-like behavior dependent on the number of emitting imagers bound to the TH at every time point. (c) Analysis of the effect of the increased brightness of the TH compared to SD origami with respect to the localization precision. The left panel depicts cross-sectional histograms through the aligned and averaged images of several hundreds of both SD origami (top image and blue histogram) and TH origami (bottom image and orange histogram). The visual impression of sharper localization distribution for THs compared to SDs is confirmed by comparing the half width half maximum (HWHM) of the Gaussian fits to the two histograms (5.6 nm and 9.0 nm, respectively), which are in good agreement with the localization precision results based on Nearest-Neighbor Analysis<sup>7</sup> (NeNA; 5.8 nm and 9.3 nm, respectively). Particle averaging was repeated over at least  $n \sim 2,000$  origami. Scale bars, 10 nm in (c).



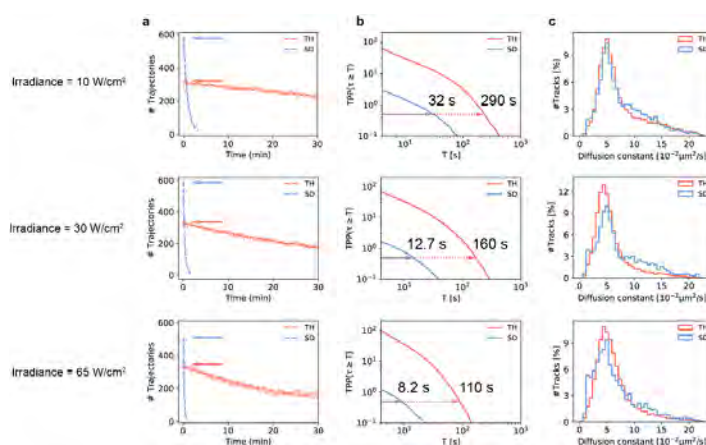
**Supplementary Figure 6. Error estimation for  $T_{1/2}$  results.** (a) Repeated irradiance series for fresh samples of SD origami in buffer B (light blue; 4x samples; each sample imaged at 3x field of views (FOVs)) and buffer L (dark blue; 1x samples, 3x FOVs). The plots display the mean  $T_{1/2}$  values averaged over all repeats per buffer condition. Error bars correspond to the standard deviation (std). The largest relative standard deviation (i.e. std/mean) was  $\sim 8\%$ , which was used to display error bars of the SD origami results shown in Fig. 1k and Supplementary Fig. 15. It should also be noted that the buffer ion composition did not influence the photobleaching behavior of Cy3B, since both irradiance series yielded almost the same results. (b) Repeated irradiance series for fresh samples of TH origami under the conditions buffer L,  $T=21^\circ\text{C}$  and  $[\text{imager}]=40\text{ nM}$  (2x samples). The plots display the mean  $T_{1/2}$  values averaged over the two repeats. Error bars correspond to the standard deviation (std). The largest relative standard deviation was  $\sim 30\%$ , which was used to display error bars to the TH origami results shown in Fig. 1k, Supplementary Fig. 15b and Supplementary Fig. 23b. After filtering, SD data sets contained at least  $n\sim 3,000$  origami and TH data sets at least  $n\sim 700$  origami.



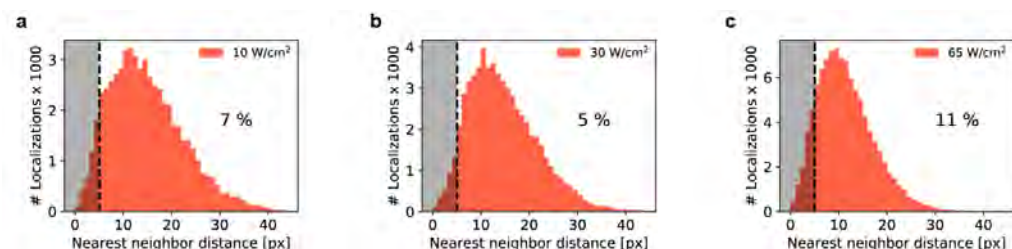
**Supplementary Figure 7. Data analysis workflow - mobile.** (a) Data analysis workflow from raw movies (`*.ome.tif`) to final result (`*_tmobprops.hdf5`). Dashed boxes indicate employed main functions - e.g. `picasso_addon.localize.main()` - of the `picasso_addon` and `spt` python package. Rounded boxes illustrate provided functionalities of each main function. The header color code indicates from which python package the functionality was adapted (e.g. `picasso`, `trackpy` or `custom` for extended functionalities within `picasso_addon` or `spt`). The text within the rounded boxes gives a short description of the provided functionality and parameters (brackets) for execution of the main function. For all evaluations of mobile origami a `search_range` value of 5 and a `memory` value of 3 was used (please refer to <http://soft-matter.github.io/trackpy/v0.4.2/generated/trackpy.link.html#trackpy.link>). The small boxes branching of the main flow represent which files are saved during execution. Please visit the links provided in the section “Image processing & single particle tracking analysis” for further information. Note that for all the mobile origami data presented only trajectories having more than 20 localizations were included in the analysis (b) We followed a linear iterative fitting procedure of the individual MSD curves as proposed by Michalet *et al.*<sup>8</sup> to find the optimum fitting range. For the following description we define the total trajectory length as  $N$  and the maximum lag time  $l$  up to which the MSD curve is fitted as  $N_p$ . In every step we fit the MSD with the linear fit model  $\text{MSD}(l) = a \cdot l + b$  up to  $N_p$ . For the first iteration we set  $N_{p,1} = 0.125 \cdot N$  (nearest integer) and perform an unweighted least square fit giving  $(a_1, b_1)$ . The left panel shows the fitting result of the first iteration. The grey area indicates the fitting range as given by  $N_{p,1}$ . The zoom-in illustrates poor fitting of the MSD values for short lag times  $l$  which constitute the MSD values of lowest (statistical) uncertainty<sup>9</sup>. For the next iteration we hence update the fitting range as given by  $N_{p,2}$  using the rule<sup>8</sup>  $N_{p,2} = 2 + 2.3(b_1/a_1)^{0.52}$  (rounded integer). The right panel shows the fitting result of the second iteration with an updated  $N_{p,2}$  of 3. The zoom-in indicates that now the (low uncertainty) MSD values for short lag times  $l$  are fitted well hence leading to a more precise determination of the diffusion constant. We usually observed a fast convergence in  $N_p$  after 2 or 3 iterations and we only allowed up to five iterations.



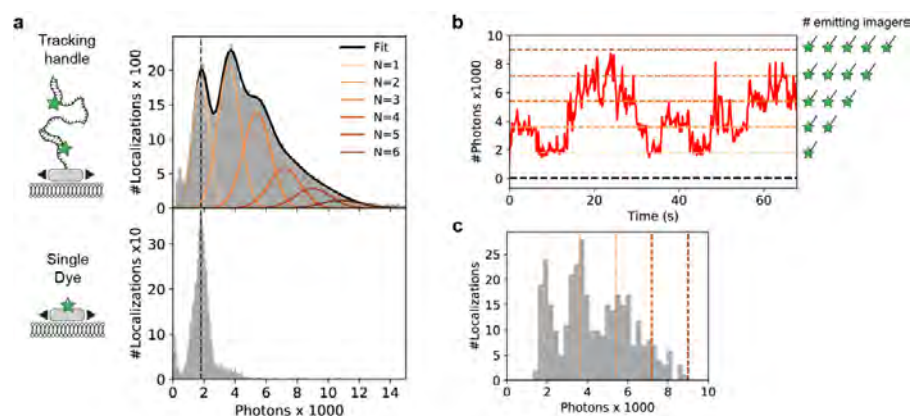
**Supplementary Figure 8. Longest trajectories at varying irradiances.** The 16 particle trajectories of longest durations of SD origami (top) and TH origami (bottom) floating on SLBs analogous to Fig. 2a but measured with (a) lower irradiance and (b) higher irradiance. Longest observed TH trajectory duration (top right trajectory) for an irradiance of  $10 \text{ W/cm}^2$  was  $\sim 30 \text{ min}$  and  $\sim 4 \text{ min}$  for  $65 \text{ W/cm}^2$ , respectively.



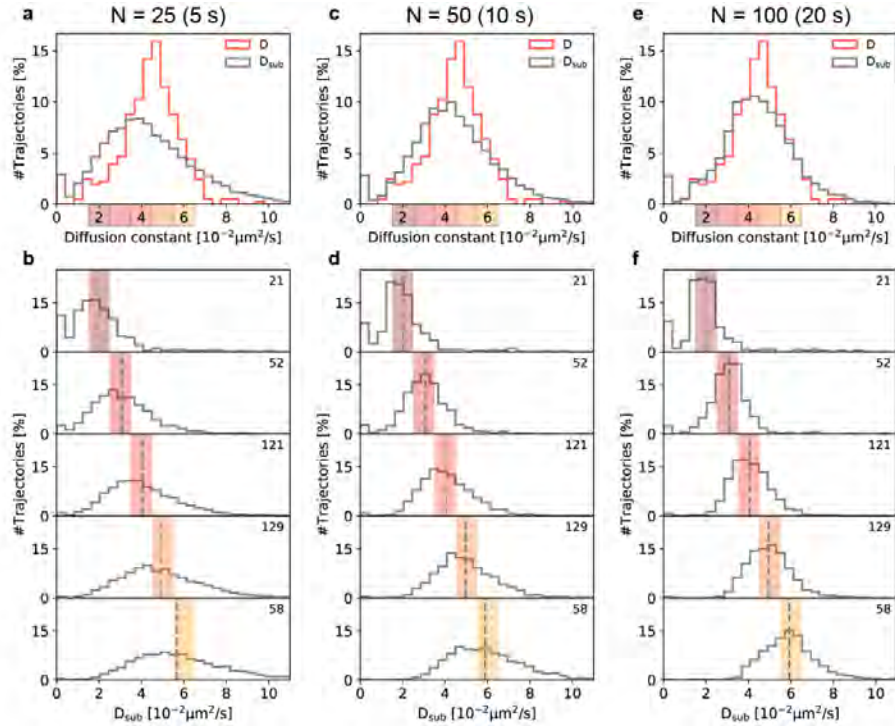
**Supplementary Figure 9. Tracks, TPP and diffusion constant at varying irradiances.** (a) Number of trajectories per frame analogous to Fig. 2b. (b) Average number of tracks per origami  $TPP(\tau_n \geq T)$  analogous to Fig. 2c. (c) Diffusion constants as obtained by linear iterative fitting of the individual MSD curves analogous to Fig. 2d. Floating TH origami results are indicated by orange color, floating SD origami results are indicated by blue color. Rows represent results as obtained for varying irradiances.



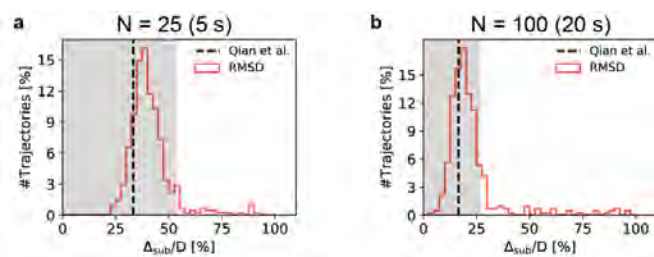
**Supplementary Figure 10. Linking and particle density.** (a) The data shown refers to TH origami measurements at an irradiance of  $10 \text{ W/cm}^2$ . It shows the nearest neighbor distance distribution between all localizations corresponding to the same frame of the recorded movie. The histogram represents the total distribution as calculated for each of the first 100 frames of the movie. The black dashed line indicates the range used as parameter for the nearest neighbor based linking algorithm ('search\_range', see **Supplementary Fig. 7**). 7% of all nearest neighbor distances between localizations of one frame lie within the search range of the linking algorithm, potentially impairing its linking ability and thus leading to trajectories of shorter duration when compared to the immobilized samples. (b,c) Same as (a) but at an irradiance of  $30 \text{ W/cm}^2$  and  $65 \text{ W/cm}^2$ , respectively.



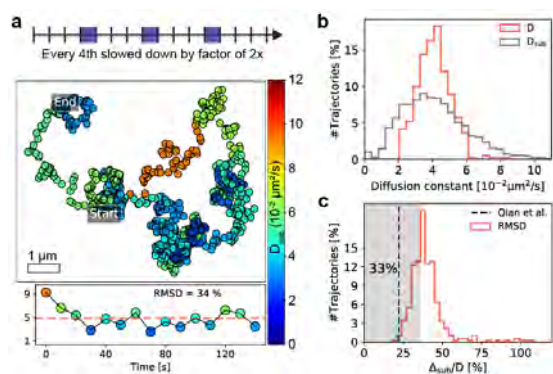
**Supplementary Figure 11. Photons counts - mobile.** (a) Ensemble photon count distributions as obtained from localizations corresponding to mobile TH origami (top) and SD origami (bottom) measured at irradiance =  $65 \text{ W/cm}^2$ . Both histograms refer to localizations from the central circular region of the FOV (diameter =  $200 \text{ px}$ ) of the first 40 frames, 1000 frames of the measurement for SD origami and TH origami, respectively. Analogous to **Supplementary Fig. 5** the TH histogram was fitted with sum (solid black) of 6 Gaussian functions (colored). The dashed black line - corresponding to the center of the first peak of the TH distribution (top) - coincides with the peak of the unimodal SD origami distribution (bottom). (b) Fluorescence trace of an exemplary TH trajectory illustrating step-like behavior dependent on the number of emitting imagers bound to the TH at every time point. The dashed colored lines indicate the photon levels  $i x_0$  as obtained from the fit of the ensemble distribution (a, top). (c) Photon count histogram of the trajectory shown in (b).



**Supplementary Figure 12.  $D$  vs.  $D_{\text{sub}}$  for varying subtrajectory durations.** (a) Total distribution of  $D$  and the corresponding subtrajectory diffusion constants  $D_{\text{sub}}$  for subtrajectories of duration 5 s. We define the broadening factor  $B$  of the  $D_{\text{sub}}$  distribution with respect to the  $D$  distribution as  $B = \sigma_{\text{rel}}(D_{\text{sub}})/\sigma_{\text{rel}}(D)$  with  $\sigma_{\text{rel}}$  being the relative standard deviation divided by the respective mean of the distribution and obtained a broadening factor  $B = 1.7$ . (b) We selected five subsets of trajectories yielding a value of  $D$  within the ranges 1.5 - 2.5, ..., 5.5 - 6.5  $10^{-2} \mu\text{m}^2/\text{s}$  (colored boxes in a) and plotted the corresponding  $D_{\text{sub}}$  distribution. The mean value of  $D_{\text{sub}}$  (grey dashed) agrees well with the selected central  $D$ . The top right number indicates how many (full) trajectories were part of the selected subsets in  $D$ . The same calculus as in (a) for every subset yielded an average broadening factor  $B = 6.1$  (theoretical: 6.7, see **Supplementary Note 3**). (c) Same as (a) but with a subtrajectory duration of 10 s yielding broadening factor  $B = 1.5$ . (d) Same as (b) but with a subtrajectory duration of 10 s yielding subset average broadening factor of  $B = 4.9$  (theoretical: 4.9). (e) Same as (a) but with a subtrajectory duration of 20 s yielding broadening factor  $B = 1.4$ . (f) Same as (b) but with a subtrajectory duration of 20 s yielding subset average broadening factor of  $B = 4.0$  (theoretical: 3.4).



**Supplementary Figure 13. RMSD of  $D_{\text{sub}}$  for varying subtrajectory durations.** (a) RMSD distribution of  $D_{\text{sub}}$  to  $D$  of all trajectories exceeding 120 s split into subtrajectories of 5 s (red). RMSD was normalized to  $D$  and should hence be close to the theoretical limit<sup>9</sup> (black dashed line) if the TH origami are subject to a time-invariant Brownian motion (see **Supplementary Note 3**). Grey area indicates deviation of less than 60 % to the theoretical limit. (b) Same as (a) but with a subtrajectory duration of 20 s.



**Supplementary Figure 14. Two-fold slowdown of every fourth subtrajectory.** (a,b,c) same as Fig.3a,b,c but with sub-trajectories computationally slowed down as indicated in (a).

### Supplementary Note 1: Tracking handle key parameters

We investigated the various factors determining the function and performance of the TH under ideal surface-immobilized conditions. The four main kinetic rates that control continuous imager exchange are: i) the rate of photobleaching  $k_{\text{photobleaching}}$ , ii) the rate of photo-induced damage  $k_{\text{photodamage}}$ , iii) the effective imager association rate  $k_{\text{on}}$  and iv) the dissociation rate  $k_{\text{off}}$  (**Supplementary Fig. 15a**). Depending on the experimental conditions, such as the temperature or the imaging buffer composition as well as the excitation laser power (irradiance) at which imaging is performed, either of these rates can play a more or less dominant role for the TH. We optimized the experimental conditions for SPT experiments in a live-cell compatible buffer L (see **Supplementary Methods**), at temperature  $T=21$  °C and at an imager concentration of 40 nM (if data was acquired at deviating conditions this is explicitly stated).

First, we examined to what extent photobleaching as a function of irradiance is a limiting factor to the TH performance. To do so, we first had to assay the average bleaching rate of single Cy3B dye molecules (remember that each imager carries a single Cy3B molecule, i.e. the average time it takes a dye molecule to photobleach should be larger than the average binding time or  $k_{\text{off}} > k_{\text{photobleach}}$ ) by imaging immobilized SD origami at increasing irradiances ( $E=10$  W/cm<sup>2</sup>, 30 W/cm<sup>2</sup> and 65 W/cm<sup>2</sup>). Faster photobleaching of Cy3B molecules was observed with increasing irradiance, as one would expect ( $T_{1/2} = 30$  s, 12 s and 6 s, respectively blue decaying curve in the left panel in **Supplementary Fig. 15b**). Next, we imaged TH origami at the same irradiances. Despite a similar decay with increasing irradiance, we on average obtained a 26-fold increase in  $T_{1/2}$  compared to SD origami (orange curve in **Supplementary Fig. 15b**, left panel). For instance, in 30 minutes imaging of TH origami at 30 W/cm<sup>2</sup>, we obtained  $T_{1/2}$  of 365 s (> 6 minutes) compared to only 12 s for SD origami.

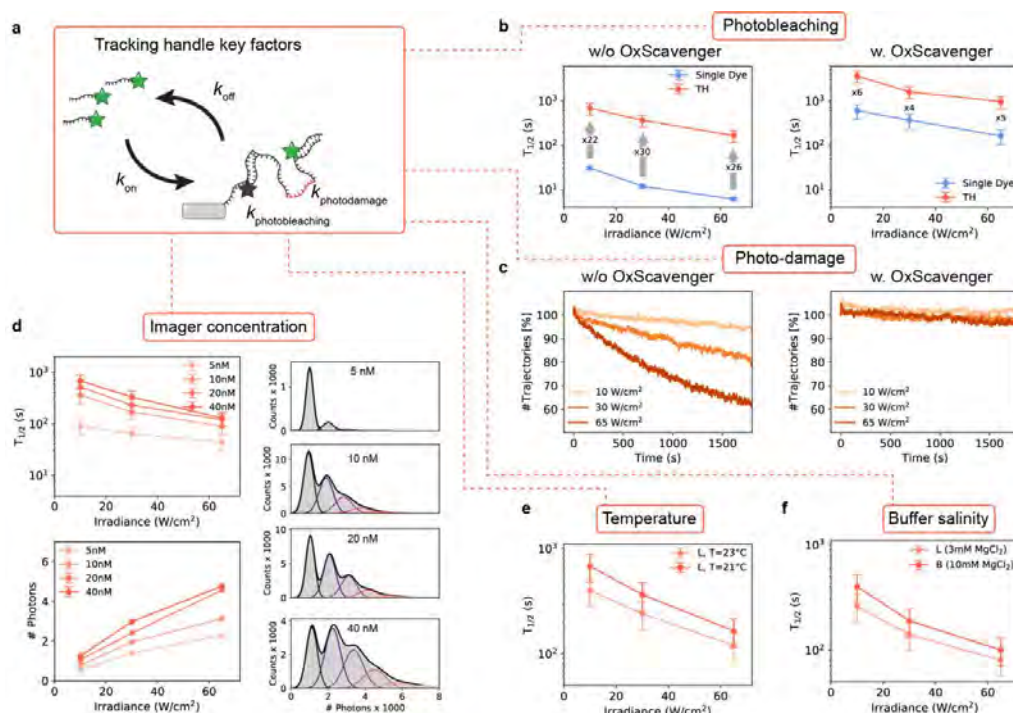
In order to suppress fast photobleaching, we repeated the irradiance series in the presence of the oxygen scavenging system POC (pyranose oxidase, catalase and glucose) and the triplet state quencher trolox (imaging buffer POCT, acquisition length: 30 min for SD origami and at least 60 min for TH origami). To our surprise, even for SD origami we obtained  $T_{1/2}$  values in the range of hundreds of seconds (blue curve in **Supplementary Fig. 15b**, right panel). However, for TH origami we even obtained another 5-fold increase in comparison to SD origami (orange curve). With POCT, in 60 minutes imaging at  $E=30$  W/cm<sup>2</sup>, we obtained a  $T_{1/2}$  of ~26 minutes. Repeating the measurement at  $E=10$  W/cm<sup>2</sup> with an extended measurement time of 3 hours we even obtained a  $T_{1/2}$  value of more than 1 hour (see also **Supplementary Fig. 16**).

We also investigated the effect of photo-induced damage to the survival time of the TH. Analyzing the number of trajectories per frame for the TH data sets of the irradiance series clearly indicates that  $k_{\text{photodamage}}$  increases with higher irradiances (**Supplementary Fig. 15c**, left panel). In **Supplementary Fig. 17** we show that  $k_{\text{photodamage}}$  follows a linear dependence on the irradiance. However, despite this damage occurring over time, even at  $E=65$  W/cm<sup>2</sup> (where SD origami had a  $T_{1/2}$  of 6 s) on average more than 60 % of all THs were detected in every frame over 30 minutes. The source of the damage lies in reactive oxygen species, confirming previous results<sup>1,3,10</sup> (**Supplementary Fig. 15c**, right panel). These can be efficiently

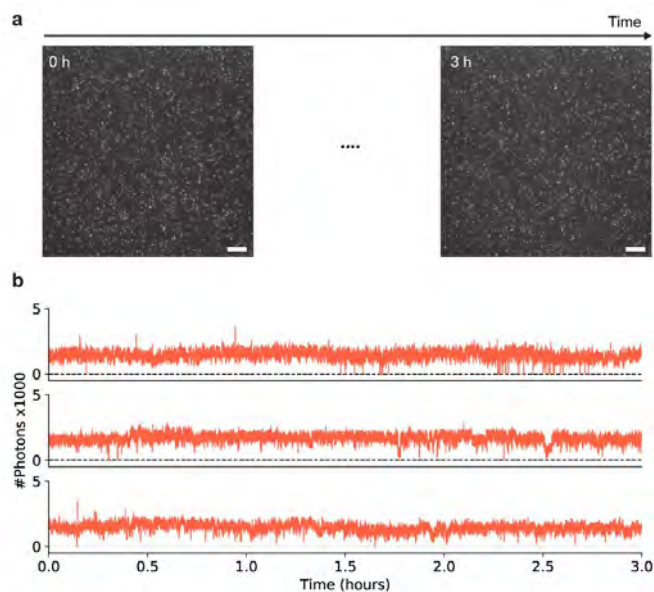
removed using POCT maintaining a constant level of detected THs independent of the applied irradiance over the same time interval. As previously mentioned, we optimized the TH performance in a buffer compatible with live cell conditions (buffer L,  $T=21\text{ }^{\circ}\text{C}$ , 40 nM imager). For future specific SPT problems, one or more of these conditions might have to be adapted. In the following, we therefore analyzed the effect of changes to imager concentration, temperature and buffer composition (salt), keeping the other parameters fixed, with respect to TH function.

First, we varied the imager concentration for samples with immobilized TH origami ( $[\text{imager}] = 5\text{ nM}, 10\text{ nM}, 20\text{ nM}$  and  $40\text{ nM}$ , at  $T=21\text{ }^{\circ}\text{C}$ , buffer L). As one would expect, increasing the imager concentration resulted in an increase in trajectory durations due to a higher probability of binding to an unoccupied site on the TH (**Supplementary Fig. 15d**, top left panel). However, increasing from 20 to 40 nM imager concentration, the increase in  $T_{1/2}$  is close to saturation, particularly at high irradiances. Looking at the number of photons detected per localization (**Supplementary Fig. 15d**, bottom left panel), we similarly observed an increase with imager concentration because multiple emitting imagers simultaneously bind the TH. The corresponding distributions of photon counts illustrates how the probability of higher order occupancies of bound imagers increases with concentration (**Supplementary Fig. 15d**, right panel).

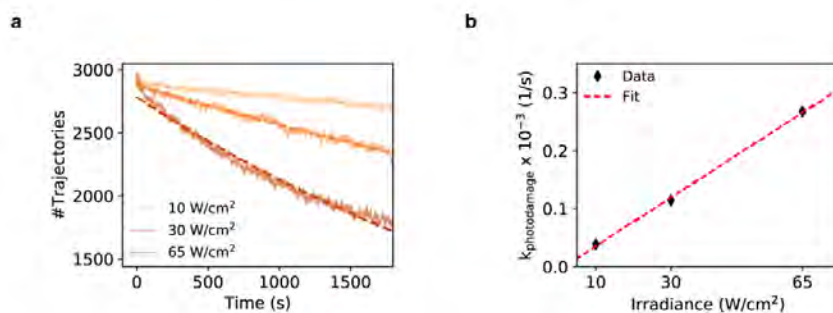
Third, we highlight the influence of temperature on TH performance. Increasing the temperature from  $21\text{ }^{\circ}\text{C}$  to  $23\text{ }^{\circ}\text{C}$  (fix: buffer L, 40 nM imager concentration) had a large effect on the average trajectory duration despite this small temperature difference, as  $T_{1/2}$  dropped on average by  $\sim 30\%$  (**Supplementary Fig. 15e**). The drop is due to an increased  $k_{\text{off}}$ , which results in faster imager dissociation and thus more frequent interruptions in the fluorescence signal (**Supplementary Fig. 18**). Lastly, we emphasize the effect of ion composition (salt) onto the TH. We performed the same irradiance series for TH origami samples using two buffers with different ion compositions: buffer L (3 mM  $\text{MgCl}_2$  + 140 mM NaCl) and buffer B (10 mM  $\text{MgCl}_2$ ) at  $T=21\text{ }^{\circ}\text{C}$  and 5 nM imager concentration. The buffer with the higher amount of  $\text{Mg}^{2+}$  ions, buffer B, resulted in longer trajectories by  $\sim 40\%$  compared to buffer L due to the beneficial effect of higher  $\text{MgCl}_2$  concentrations to both  $k_{\text{on}}$  and  $k_{\text{off}}$  (**Supplementary Fig. 15f**, **Supplementary Fig. 19**).



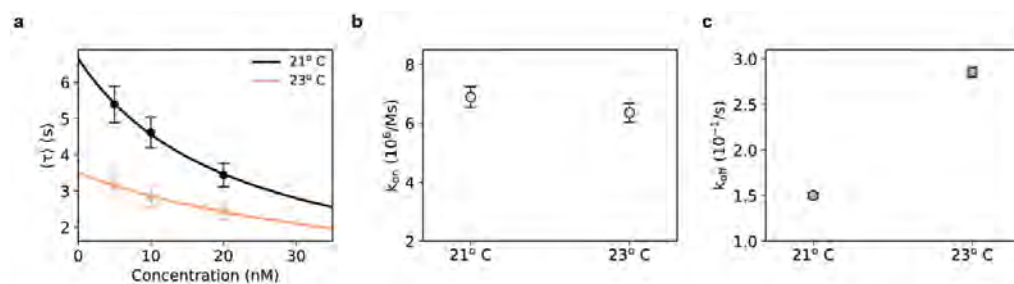
**Supplementary Figure 15. Tracking handle key parameters overview.** (a) Main rates determining the TH function (b) Mean  $T_{1/2}$  vs. irradiance plots for SD origami (blue) and TH origami (orange) imaged at varying irradiances. Left and right panels show the case without and with using an oxygen scavenging system, respectively. Arrows indicates factors of increase of TH vs SD. SD data sets contained at least  $n \sim 3,000$  origami and TH data sets at least  $n \sim 700$  origami after filtering. (c) Number of trajectories per frame (i.e. emitting labels) vs. measurement time normalized to initial trajectory number. Left and right panels show the case without (a total of at least  $n \sim 109,000$  trajectories per data set) and with using an oxygen scavenging system (a total of at least  $n \sim 241,000$  trajectories per data set), respectively. (d) Top left panel: Mean  $T_{1/2}$  vs. irradiance plot for TH origami samples imaged at varying imager concentrations. Bottom left panel: Plot of mean number of detected photons per localization. Right panels: Distributions of number of photons detected per localization corresponding to concentration series imaged at  $E=30$  W/cm<sup>2</sup>. All data sets contained at least  $n \sim 400$  origami after filtering. (e) Mean  $T_{1/2}$  vs. irradiance plots for TH origami imaged at varying temperature (All data sets contained at least  $n \sim 2,300$  origami after filtering). (f) Mean  $T_{1/2}$  vs. irradiance plots for TH origami imaged at varying buffer ion compositions (All data sets contained at least  $n \sim 1,400$  origami after filtering). Error bars in b,c,d,e,f correspond to relative standard deviation (see **Supplementary Fig. 6**).



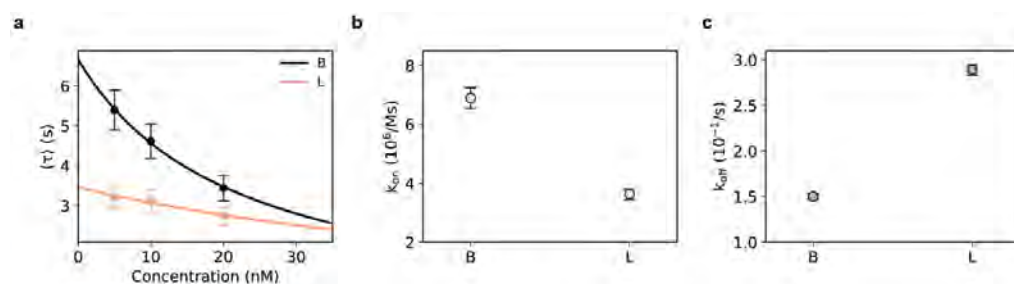
**Supplementary Figure 16. Extended 3-hour measurement using POCT.** (a) First and last frame of the 3h TIRFM acquisition of static TH origami still emitting after the course of the measurement. Parameters: buffer POCT, [imager]=40 nM, T=21 °C, E=10 W/cm<sup>2</sup>. (b) Three exemplary fluorescence traces exhibiting continuous intensity fluctuations over 3 h. The combination POC and trolox suppresses photobleaching and photodamage to the TH. However, still short interruptions due to the stochastic nature of DNA association and dissociation occur. Scale bars, 10 μm in (a).



**Supplementary Figure 17.  $k_{\text{photodamage}}$  vs irradiance.** (a) Number of trajectories per frame vs. measurement time normalized to initial trajectory number (transparent fluctuating curves) from DNA origami samples imaged at varying irradiances, as shown in left panel in **Supplementary Fig. 15c**. An exponential model  $f(x) = ae^{-x/\tau_{\text{photodamage}}}$  was fitted to the data (dashed curves), where  $\tau_{\text{photodamage}}$  denotes the characteristic decay constant over which photodamage occurs and  $a$  the initial number of trajectories. (b) The inverse of  $\tau_{\text{photodamage}}$  yielded the rate  $k_{\text{photodamage}} = 1/\tau_{\text{photodamage}}$  for each irradiance. Plotting  $k_{\text{photodamage}}$  vs. irradiance was well described by a line fit (red dashed line) confirming a linear relation of the two quantities over the here applied irradiance range.



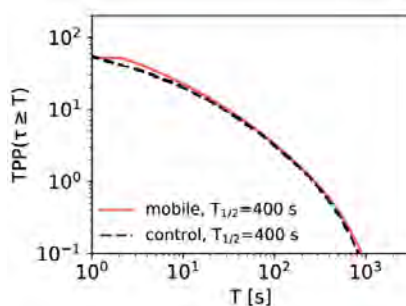
**Supplementary Figure 18. Temperature effect on DNA hybridization rates.** (a) As previously described<sup>3</sup>, we performed localization-based Fluorescence Correlation Spectroscopy (lbFCS) measurements on DNA origami labeled with just a single docking strand fully complementary to the imager sequence (see **Supplementary Table 2**). By performing an imager concentration series ([imager]=5 nM, 10 nM and 20 nM) lbFCS allows to precisely measure the DNA hybridization rates  $k_{on}$  and  $k_{off}$ . Here, we conducted the imager concentration series in buffer B at T=21 °C and T=23 °C. Fitting eq. 2 in ref. 3 to the mean characteristic decay constant ( $\tau$ ) plotted vs. the imager concentration yielded  $k_{on}$  and  $k_{off}$ . (b)  $k_{on}$  results from the two fits in (a) indicating only minor changes due to the temperature variation. (c)  $k_{off}$  results from the two fits in (a) highlighting the drastic temperature effect on the dissociation rate.  $k_{off}$  increased almost by a factor of x2 when increasing the temperature from 21 °C to 23 °C. Error bars correspond to standard deviation in (a) and to the lbFCS uncertainty range<sup>3</sup> of 5 % and 2 % in  $k_{on}$  and  $k_{off}$ , respectively, in (b). All data sets contained at least  $n \sim 5,500$  origami after filtering.



**Supplementary Figure 19. Ion concentration effect on DNA hybridization rates.** (a) Analogously to **Supplementary Fig. 18**, we repeated the same lbFCS imager concentration series on single-docking-strand origami samples using buffer B and buffer L (at T=21 °C). (b)  $k_{on}$  results from the two fits in (a) exhibiting a decreased association rate due to a lower  $MgCl_2$  concentration in buffer L. (c)  $k_{off}$  results from the two fits in (a). In contrast to  $k_{on}$ ,  $k_{off}$  increased nearly by a factor of 2x using buffer L compared to buffer B. Error bars correspond to standard deviation in (a) and to the lbFCS uncertainty range<sup>3</sup> of 5 % and 2 % in  $k_{on}$  and  $k_{off}$ , respectively, in (b). All data sets contained at least  $n \sim 535$  origami after filtering.

### Supplementary Note 2: TPP calculus for mobile particles

Since in SPT, it is generally not possible to unambiguously identify multiple appearances of the same mobile particle in a data set, we calculated  $TPP(\tau_n \geq T) = \frac{N_{\text{tot}}(\tau_n \geq T)}{M}$  for trajectories with duration  $\tau_n$  longer or equal to the time  $T$  by normalizing the total number of trajectories  $N_{\text{tot}}(\tau_n \geq T)$  to the initial trajectory number  $M$  (arrows in **Fig. 2b**) in order to directly compare trajectory durations of both immobile and mobile origami. Note that  $M$  should give a good estimate for the number of particles within the FOV for sufficiently low particle densities.  $TPP(\tau_n \geq T)$  was  $< 1.5$  for the SD origami, confirming the validity of our approach since we ideally would expect only one trajectory per single dye before it photobleaches (see **Fig. 2c**). To test the applicability of this approach we reanalyzed the immobilized TH origami using this procedure and obtained almost identical results as for the immobilized origami analysis workflow (**Supplementary Fig. 20**).



**Supplementary Figure 20. Mobile analysis control with immobilized data set.** In order to verify our approach of TPP calculation for the mobile case (see **Fig. 2b,c**) we reanalyzed an immobilized TH origami sample using the mobile analysis workflow described in **Supplementary Fig. 7**. The orange curve displays the corresponding TPP results. The black dashed line displays the TPP results as obtained via the immobile analysis workflow described in **Supplementary Fig. 3** and serves as a control. Both curves evolve almost identically and yield the same average TPP of  $\sim 50$  and a  $T_{1/2}$  value of 400 s. This confirms our approach for the mobile case to normalize the total number of detected trajectories to the number of trajectories (i.e. particles) in the first frame of the data set.

### Supplementary Note 3: Statistical treatment of diffusion coefficients

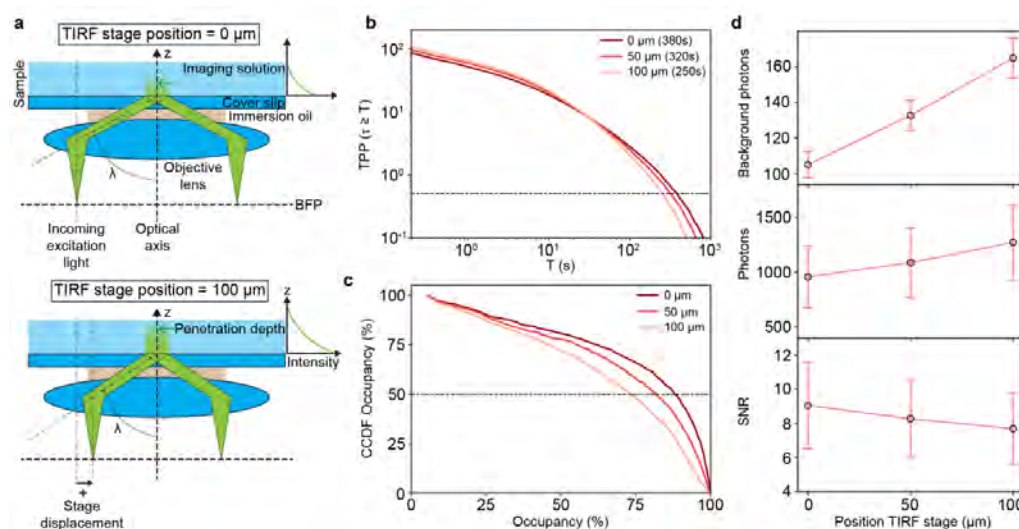
A theoretical expression for the relative standard deviation of the diffusion coefficient as obtained by fitting of the MSD curve was derived by Qian et al.<sup>9</sup>:

$$\frac{\sigma_D}{D} = \sqrt{\frac{2N_p}{3(N - N_p)}} \quad \text{Eq. (1)}$$

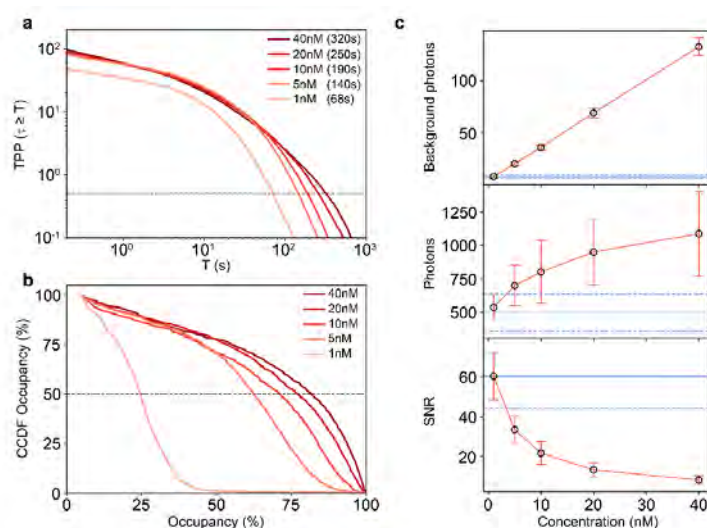
with  $N$  being the total duration of the trajectory in frames (e.g.  $N = 600$  for full trajectories,  $N = 50$  for subtrajectories in **Fig. 3**) and  $N_p$  being the maximum lag time (in frames) up to which the MSD curve was fitted (see **Supplementary Fig. 7**).

In our case  $N_p$  was chosen automatically during the iterative fitting process<sup>8</sup> resulting in a median value of  $N_p = 3$  on average. To test whether the scatter of  $D_{\text{sub}}$  is only governed by the random nature of the motion according to Eq. 1, we calculated the root-mean-square deviation  $\text{RMSD} = \sqrt{\langle (D_{\text{sub}} - D)^2 \rangle}$  of  $D_{\text{sub}}$  to  $D$  for each trajectory<sup>11</sup>. **Fig. 3c** shows the distribution of the thus obtained RMSD normalized to the diffusion coefficient  $D$  of the full trajectory for  $N = 50$ . If the movement of the TH origami is indeed governed by the same 2D Brownian motion with a diffusion coefficient  $D$  at any time the RMSD should correspond to the standard deviation  $\sigma_D$  (for  $N = 50$ ) and should hence yield a value close to theoretically achievable limit given by Eq. 1 (black dashed line, in **Fig. 3c**). **Fig. 3c** shows that around 86 % of the analyzed trajectories do not deviate from the expected statistical uncertainty by more than 60 % (grey area) suggesting that the TH origami are indeed subject to a time-invariant Brownian motion on the SLB. This statement is further supported by division into longer ( $N = 100$ ) or shorter ( $N = 25$ ) subtrajectories (see **Supplementary Fig. 13**).

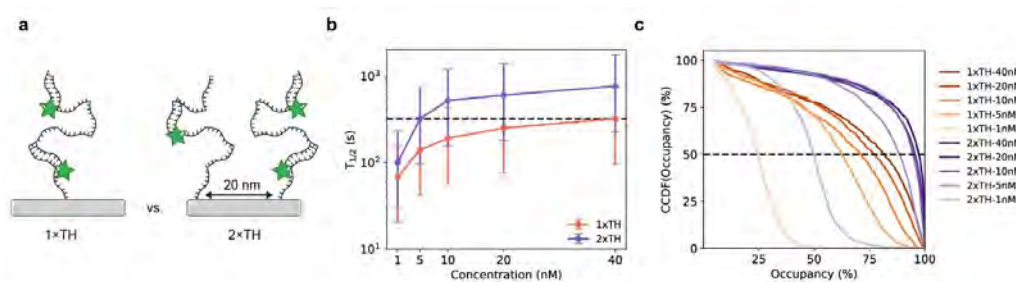
## Supplementary Note 4: Potential limitations and workarounds



**Supplementary Figure 21. Performance of tracking handle at varying TIRF angles.** (a) Sketch to illustrate the variation of the TIRF angle  $\lambda$  defined as the angle of incidence of the excitation light with respect to the optical axis. In order to vary  $\lambda$ , a linear stage bearing the coupling lens focusing the laser into the back focal plane (BFP) of the objective was moved to laterally decrease the offset from the optical axis within the BFP. In our case, a positive displacement of the TIRF stage (bottom) with respect to the zero position (top) resulted in a decrease of  $\lambda$ . According to literature<sup>12</sup>, a decrease in  $\lambda$  leads to an increasing penetration depth of the resulting evanescent field and hence a larger excitation volume (indicated by green arrows). Additionally, a decrease in  $\lambda$  results in higher excitation intensities (relative to the incoming light) of the resulting evanescent field (indicated by intensity vs.  $z$  plots to the right). (b) Plot of  $TPP(\tau \geq T)$  vs.  $T$  for immobilized TH origami acquired at different stage displacements (i.e., varying  $\lambda$ ). We observed shorter  $T_{1/2}$ -values (given in brackets in the legend) with increased displacements (i.e., decreased  $\lambda$ ) indicating a higher irradiance (compare **Supplementary Fig. 15** and see **Supplementary Table 1** for imaging conditions). (c) As explained in **Supplementary Fig. 4**, we calculated the occupancy for immobilized TH origami. The plot shows the complementary cumulative distribution function (CCDF=1-CDF) of the calculated occupancies for the three data sets in (a). As expected from (a), the occupancy decreases with increasing TIRF angle. (d) Top: Plot of mean registered background photons per localization vs. TIRF stage position for the three data sets in (b-c). A larger displacement (i.e., a smaller  $\lambda$ ) results in higher background due to the increased excitation volume within the non-fluorogenic imaging solution. Middle: Plot of mean photons detected per localization vs. TIRF stage position also showing an increase with larger displacements (i.e., smaller  $\lambda$ ), indicating an increased intensity of the evanescent (excitation) field. Bottom: Plot of signal-to-noise ratio (SNR) vs. TIRF stage position. Overall, the SNR (detected TH photons/background photons) decreases due to the more pronounced background with larger displacements (i.e., smaller  $\lambda$ ). All data sets contained at least  $n \sim 1,300$  origami after filtering. Error bars in d correspond to standard deviation.



**Supplementary Figure 22. Performance of tracking handle at varying imager concentrations.** (a) Plot of  $TPP(\tau \geq T)$  vs.  $T$  for immobilized TH origami acquired at different imager concentrations. As expected we observed shorter  $T_{1/2}$ -values (given in brackets in the legend) for decreasing imager concentration. (b) Complementary cumulative distribution function (CCDF) of occupancies for immobilized TH origami acquired at different imager concentrations (equivalent to **Supplementary Fig. 21, b**). (c) Top: Plot of mean registered background photons per localization vs. imager concentration for the data shown in (a-b) indicating linear response of the background fluorescence vs. imager concentration. The blue line indicates the measured value for SD origami for the same imaging conditions. Middle: Plot of mean photons detected per localization vs. imager concentration indicating saturation behavior for higher imager concentrations. Bottom: Plot of signal-to-noise ratio (SNR) vs. imager concentration. Overall, the SNR (detected TH photons/background photons) decreases due to the more pronounced background with higher imager concentrations. All data sets contained at least  $n \sim 460$  origami after filtering. Error bars and dashed blue lines in c correspond to relative standard deviation.



**Supplementary Figure 23. 2xTH vs. 1xTH labeling.** (a) Standard TH origami design with a single TH (1xTH) vs. origami featuring two TH labels at a 20 nm spacing (2xTH). (b) Mean  $T_{1/2}$  vs. imager concentration for immobilized 1xTH origami (standard, orange) and 2xTH origami (purple). Labeling with two THs dramatically increases observation times. The black dashed line highlights that using an imager concentration of 5 nM with 2xTH origami yields a similar  $T_{1/2}$  compared to 1xTH origami at an imager concentration of 40 nM, hence, allowing an 8-fold reduction in imager concentration. (c) Complementary cumulative distribution functions (CCDF) of the occupancy for 1xTH origami (orange shades) and 2xTH (purple shades) for the same data sets as in (b). All data sets contained at least  $n \sim 430$  origami after filtering. Error bars in b correspond to relative standard deviation (see **Supplementary Fig. 6**).

## Supplementary Tables

Supplementary Table 1 | Imaging parameters

Figure	Sample	Imager concentration (nM)	Imaging Buffer	Temperature (°C)	Irradiance (W/cm <sup>2</sup> )	Frames (wrt. Irradiance)
1c,f,h,j,k SI_Fig. 5	SD origami, static	-	L	21	30	600
1d,g,i,j,k SI_Figs. 5,20	TH origami, static	40	L	21	30	9,000
2 SI_Figs. 9	SD origami, diffusing on SLB	-	L	21	30	600 (3x FOVs)
2 3 SI_Figs. 9,10,12,13,14	TH origami, diffusing on SLB	40	L	21	30	9,000
SI_Fig 6a	SD origami, static	-	B (4x samples), L (1x sample)	21	10 30 65	2,000 (3x FOVs) 600 (3x FOVs) 300 (3x FOVs)
SI_Fig 6b	TH origami, static	40	L (2x samples)	21	10 30 65	9,000 9,000 9,000
SI_Figs. 8,9,11	SD origami, diffusing on SLB	-	L	21	10 65	1,000 (3x FOVs) 300 (3x FOVs)
SI_Figs. 8,9,10,11	TH origami, diffusing on SLB	40	L	21	10 65	9,000 9,000
SI_Fig 15b, left panel	SD origami, static	-	L	21	10 30 65	2,000 (3x FOVs) 600 (3x FOVs) 300 (3x FOVs)
SI_Fig 15b, left panel SI_Fig 15c, left panel SI_Fig 17	TH origami, static	40	L	21	10 30 65	9,000 9,000 9,000

Figure	Sample	Imager concentration (nM)	Imaging Buffer	Temperature (°C)	Irradiance (W/cm <sup>2</sup> )	Frames (wrt Irradiance)
SI_Fig 15b, right panel	SD origami, static	-	POCT	21	10 30 65	9,000 9,000 9,000
SI_Fig 15b, right panel SI_Fig 15c, right panel	TH origami, static	40	POCT	21	10 30 65	18,000 18,000 18,000
SI_Fig. 15d	TH origami, static	5, 10, 20, 40 (4 samples)	L	21	10 30 65	9,000 9,000 9,000
SI_Fig. 15e	TH origami, static	40 nM	L	21, 23	10 30 65	9,000 9,000 9,000
SI_Fig. 15f	TH origami, static	5 nM	L, B (2 samples)	21	10 30 65	9,000 9,000 9,000
SI_Fig 16	TH origami, static	40	POCT	21	10	54,000
SI_Fig. 18	1DS origami	5, 10, 20 (3 samples)	B	21, 23	10	9,000 (6x)
SI_Fig. 19	1DS origami	5, 10, 20	B, L (2x3=6 samples)	21	10	9,000 (6x)
SI_Fig. 21	TH origami, static	40	L	21	30 (varying TIRF angles)	9000 (3x)
SI_Fig. 22	TH origami, static	1,5,10,20,40	L	21	30	9000 (5x)
SI_Fig. 23	TH & 2xTH origami, static	1,5,10,20,40 (TH & 2xTH)	L	21	30	9000 (10x)

Supplementary Table 2 | Used DNA oligonucleotide sequences as labels

Name (oligo length)	Docking strand sequence (5' – 3')	Imager sequence (5' – 3')	Experiment
TH (54 bp)	TT- CTCCTCCTCCTCCTCCTCCTCCTC CTCCTCCTCCTCCTCCTCCTCCTC CTCCTC	GAGGAGGA-Cy3B	All TH experiments
SD (5 bp)	TT TTT-Cy3B	-	All SD experiments
1DS (8 nt)	TT TCCTCCTC	GAGGAGGA-Cy3B	lbFCS series in SI_Fig. 18 & 19

## Supplementary References

- Blumhardt, P. *et al.* Photo-Induced Depletion of Binding Sites in DNA-PAINT Microscopy. *Molecules* **23**, 3165 (2018).
- Schnitzbauer, J., Strauss, M. T., Schlichthaerle, T., Schueder, F. & Jungmann, R. Super-resolution microscopy with DNA-PAINT. *Nat. Protoc.* **12**, 1198 (2017).
- Stein, J. *et al.* Toward Absolute Molecular Numbers in DNA-PAINT. *Nano Lett.* **19**, 8182–8190 (2019).
- Stahl, E., Martin, T. G., Praetorius, F. & Dietz, H. Facile and Scalable Preparation of Pure and Dense DNA Origami Solutions. *Angew. Chemie Int. Ed.* **53**, 12735–12740 (2014).
- Stehr, F., Stein, J., Schueder, F., Schwille, P. & Jungmann, R. Flat-top TIRF illumination boosts DNA-PAINT imaging and quantification. *Nat. Commun.* **10**, 1268 (2019).
- Edelstein, A. D. *et al.* Advanced methods of microscope control using  $\mu$ Manager software. *J. Biol. Methods; Vol 1, No 2* (2014).
- Endesfelder, U., Malkusch, S., Fricke, F. & Heilemann, M. A simple method to estimate the average localization precision of a single-molecule localization microscopy experiment. *Histochem. Cell Biol.* **141**, 629–638 (2014).
- Michalet, X. Mean square displacement analysis of single-particle trajectories with localization error: Brownian motion in an isotropic medium. *Phys. Rev. E* **82**, 41914 (2010).
- Qian, H., Sheetz, M. P. & Elson, E. L. Single particle tracking. Analysis of diffusion and flow in two-dimensional systems. *Biophys. J.* **60**, 910–921 (1991).
- Clowsley, A. H. *et al.* Repeat DNA-PAINT suppresses background and non-specific signals in optical nanoscopy. *Nat. Commun.* **12**, 501 (2021).

11. Block, S., Zhdanov, V. P. & Höök, F. Quantification of Multivalent Interactions by Tracking Single Biological Nanoparticle Mobility on a Lipid Membrane. *Nano Lett.* **16**, 4382–4390 (2016).
12. MARTIN-FERNANDEZ, M. L., TYNAN, C. J. & WEBB, S. E. D. A ‘pocket guide’ to total internal reflection fluorescence. *J. Microsc.* **252**, 16–22 (2013).



## **Part III**

# **Additional Results and Discussion**



# 5

## Calibration free counting of low molecular copy numbers in single DNA-PAINT localization clusters

### 5.1 Motivation and Summary

SMLM has revolutionized light microscopy by enabling optical resolutions down to a few nanometer. Yet, localization precisions commonly not suffice to visually resolve single subunits in molecular assemblies or multimeric complexes. Since each targeted molecule contributes localizations during image acquisition, molecular counting approaches to reveal the target copy numbers within localization clusters have been continuously proposed since the early days of SMLM, most of which rely on preliminary knowledge of the dye photo-physics or on a calibration to a reference. Previously, we developed lbFCS as an absolute ensemble counting approach for the SMLM-variant DNA-PAINT, for the first time circumventing the necessity for reference calibrations. Here, we present a revised framework termed lbFCS+ which allows absolute counting of copy numbers for individual localization clusters in a single DNA-PAINT image. In lbFCS+, absolute counting in individual clusters is achieved via precise measurement of the local hybridization rates of the fluorescently-labeled oligonucleotides ('imagers') employed in DNA-PAINT imaging. In proof-of-principle experiments on DNA origami nanostructures, we demonstrate the ability of lbFCS+ to truthfully determine molecular copy numbers and imager association and dissociation rates in well-separated localization clusters containing up to six docking strands. We show that lbFCS+ allows to resolve heterogeneous binding dynamics enabling the distinction of stochastically generated and *a priori* indistinguishable DNA assemblies. Beyond advancing quantitative DNA-PAINT imaging, we believe that lbFCS+ could find promising applications ranging from bio-sensing to DNA computing.

A preprint of this work can be found on the bioRxiv, doi:10.1101/2021.08.17.456678 [83].

## 5.2 Introduction

The advent of SR microscopy has revolutionized life science research by allowing to visualize specific biological structures at the nanoscale [12–15]. The SR methods summarized as SMLM, such as PALM [14], STORM [15], and (DNA)-PAINT [17, 19, 20] circumvent the diffraction limit by acquiring image sequences of a ‘blinking’ target structure by stochastically activating only a small subset of all fluorescent labels at a time. Thus, these methods enable localization of individual dye molecules in each camera frame and downstream rendering of SR images from all obtained localizations. However, the limited photon budgets of dyes [33], imperfect labeling strategies and the physical size of the label (e.g. antibodies) cause these localizations to be scattered around the true position of the targeted molecule (forming a ‘localization cluster’) [84]. Within fixed cells, single molecules can thus only be pinpointed at lateral localization precisions of up to 10 nm [81], which is often not sufficient to reach molecular resolution and to visually resolve molecular complexes. To give an example, it is not possible to visually distinguish the two monomers within a dimer, because the localizations obtained from both molecules overlap within a localization cluster. However, since in SMLM each targeted molecule contributes a certain number of localizations to the SR image a quantitative analysis of the collected localizations from a specific (nanoscopic) volume in principle allows to infer back on the hidden number of targeted molecules within this volume [32].

Based on this concept, there has been a multitude of studies dedicated to the problem of ‘molecular counting’ since the early beginnings of SMLM, especially for the methods PALM and STORM [35–49]. While the required single molecule blinking in PALM is achieved by light-induced stochastic photoactivation and subsequent photobleaching of the fluorophores [14, 16], STORM exploits the light-induced photoswitching of fluorophores between a fluorescent bright state and a non-fluorescent dark state [15, 18]. Hence, for both methods, the success of a quantitative analysis of localization clusters critically depends on an exact photo-physical modeling of the specific system with respect to photobleaching [34], intrinsic and/or extended blinking [35, 37, 43] as well as photo-quenching [48] of the fluorophores in use.

In contrast to a direct and permanent dye labeling as used in STORM/PALM, DNA-PAINT exploits the transient hybridization of short single-stranded and fluorescently-labeled DNA probes (‘imagers’) to their complementary ‘docking strands’ attached as labels to the target molecules [19, 20]. Because the required blinking is generated by the stochastic imager-docking strand binding reaction, DNA-PAINT is largely independent of the photo-physical properties of fluorophores under appropriate experimental conditions (e.g. sufficiently low excitation intensities to reduce any residual photobleaching or the permanent photo-induced damage of docking strands) [20, 76–78]. In this case, localization clusters in DNA-PAINT data offer a unique potential for a quantitative interpretation, since the underlying bimolecular hybridization reaction between imager/docking strands is highly programmable and well-understood [24, 32, 48]. In fact, an approach termed qPAINT has been successfully used for molecular counting in localization clusters by using the imager influx rate as a calibration [65]. So far, all of the approaches to the problem of molecular counting in any of the SMLM variants were based on either (i) a priori knowledge of the blinking dynamics or the number of localizations per fluorescence marker (e.g., via supplementary

experiments or theoretical modeling) or (ii) on an initial calibration directly within the sample by using isolated localization clusters originating from an assumed number of fluorescent molecules as a reference. Hence, those approaches only allow *relative* counting compared to a reference sample or given by the model assumptions.

In a previous study we introduced an approach termed lbFCS which allows *absolute* molecular counting in localization clusters in DNA-PAINT images, without the need of a separate reference measurement and using only minimal theoretical assumptions [78]. However, lbFCS required at least two measurements of the same sample at distinct and correctly adjusted imager concentrations, making an experiment rather tedious and time consuming. Additionally, lbFCS could only yield average values for both the underlying hybridization rates and the counted copy numbers and was hence not suited for the detection of possible heterogeneities between clusters. Finally, since its first implementation, several studies worked on the ‘speed-up’ of the DNA-PAINT reaction [79–81, 85] promising benefits on the achievable statistics (e.g. more binding events can now be recorded in the same amount of time).

Overcoming these limitations, we here present a revised framework lbFCS+ which allows extraction of *absolute* molecular numbers and hybridization rates of *single* DNA-PAINT clusters requiring only a *single* DNA-PAINT image acquisition. In proof-of-principle experiments on DNA origami nanostructures [86], we demonstrate the ability of lbFCS+ to truthfully determine molecular copy numbers and dissociation/association rates  $k_{\text{off}}$  &  $k_{\text{on}}$  of the imager/docking strand reaction in well-separated localization clusters containing up to six docking strands. We further thoroughly assess its applicable working range for reliable counting which is largely determined by the experimentally used imager concentrations and image acquisition length. Using lbFCS+ we could clearly give proof of changes in the imager/docking strand binding dynamics solely induced by placing docking strands at different positions of the DNA origami. Exploiting this effect we were even able to resolve heterogeneous binding dynamics within individual DNA-PAINT clusters allowing for the distinction of stochastically generated and a priori indistinguishable DNA assemblies.

### 5.3 Methods and Materials

#### 5.3.1 Brief recap of SMLM & DNA-PAINT binding dynamics

This section reviews the fundamental principles of DNA-PAINT binding kinetics, which constitute the basis of lbFCS+. For a detailed description of the working principles of SMLM in general and DNA-PAINT in particular, the reader is referred to [24] and [20], respectively.

A DNA-PAINT experiment [19, 20] is characterized by the transient binding reaction of short fluorescently-labeled DNA oligonucleotides in solution (‘imager strands’, short: ‘imagers’) to complementary ‘docking strands’ which are attached as labels to the target molecules of interest (see schematic in Fig.5.1a). At a given imager concentration  $c$  (typically on the order of  $\approx 10$  nM), the binding and unbinding reaction between imagers and docking strands is governed by the association rate  $k_{\text{on}}$  and the dissociation rate  $k_{\text{off}}$ . While the dissociation reaction is a zero-order chemical reaction and thus independent of the reactant concentrations, the association reaction leading to the formation of the docking/imager strand duplex is a first order chemical

reaction. Due to the ‘infinite reservoir’ of imagers in solution their concentration can be assumed to be constant during DNA-PAINT image acquisition. This leads to a constant effective association rate  $\tilde{k}_{\text{on}} \equiv k_{\text{on}}c$  dependent on the imager concentration. The schematic in **Fig.5.1a** depicts  $N$  docking strands spaced at only a few nanometer due to an exemplary local assembly of target molecules within the sample. During image acquisition, the ‘blinking’ raw signal recorded over time from this position consists of a series of bright frames (at least one imager strand bound to any of the  $N$  docking strands) and dark frames (no imager strand bound to any of the  $N$  docking strands), as illustrated in **Fig.5.1b**. As common for SMLM, the raw signal is converted into a list of localizations during post-processing, commonly referred to as super-resolution reconstruction. This is achieved by fitting a 2D Gaussian function to each of the identified diffraction limited spots, thereby pinpointing the fluorophore’s center coordinates (i.e. localization; red dots in **Fig.5.1b**). An exemplary list of localizations as obtained from the  $N$  docking strands by this procedure is shown in **Fig.5.1c**. Each localization carries information about the  $x$  and  $y$  coordinates of the identified spot (i.e. its spatial information) and a time stamp  $t$  of its occurrence as well as the total amount of recorded photo-electrons  $I(t)$  contained within the spot (i.e. its temporal intensity information). The spatial information contained in this list can be used to reconstruct a super-resolved image from our exemplary molecular assembly in form of a  $x - y$ -scatter plot for all localizations (see **Fig.5.1d**). However, due to the close docking strand spacing below the achievable localization precision it is not possible to visually distinguish individual docking strands and localizations overlap within the localization cluster.

### 5.3.2 Counting single molecules in DNA-PAINT localization clusters

The central question to which lbFCS+ aims to provide an answer is depicted in **Fig.5.1d**. In cases of molecular assemblies such as multimers, the spatial representation of localizations in a DNA-PAINT image often cannot reveal how many docking strands  $N$  are contained within a single localization cluster. Furthermore, the spatial representation does not reflect in any sense on the temporal information of imager binding (as given by  $\tilde{k}_{\text{on}}$  &  $k_{\text{off}}$ ) to the docking strands during image acquisition. Therefore, the quantities  $N$ ,  $\tilde{k}_{\text{on}}$  &  $k_{\text{off}}$  for each localization cluster must be considered unknown. It might further be the case that localization clusters feature distinct values in both  $N$  (e.g. due to varying degrees of multimerization or docking strand labeling efficiency) and in  $\tilde{k}_{\text{on}}$  &  $k_{\text{off}}$  (e.g. due to the local sample environment affecting the imager accessibility). Hence, an ensemble measurement of  $\langle N \rangle$ ,  $\langle \tilde{k}_{\text{on}} \rangle$  &  $\langle k_{\text{off}} \rangle$  would not be able to detect existing heterogeneities in either variable within the sample.

In contrast, the temporal intensity representation of a single localization cluster  $I(t)$  (referred to as ‘intensity trace’; see **Fig.5.1e**) contains the full information of imager binding under appropriately chosen experimental conditions during image acquisition. These conditions include that the reaction of imager-docking strand binding is at equilibrium (e.g. constant imager concentration  $c$  and temperature). Sufficiently low excitation intensities have to be employed in order to reduce possible photo-physical artifacts to a minimum such that the binding/blinking kinetics are solely determined by the hybridization rates  $\tilde{k}_{\text{on}}$  &  $k_{\text{off}}$ . Explicitly, fluorophore photobleaching of bound imagers needs to be avoided by adjusting laser excitation with respect to  $k_{\text{off}}$  [78, 82]. Similarly, the photo induced loss of docking strands [76, 78] (leading to a decrease in

$N$  over the measurement time) has to be countered by appropriate measures (low excitation intensities, oxygen scavenger systems). Given that the stated conditions are fulfilled, lbFCS+ is able to find a separate solution  $N$ ,  $\tilde{k}_{\text{on}}$  &  $k_{\text{off}}$  for individual localization clusters solely based on the information contained in their intensity traces.

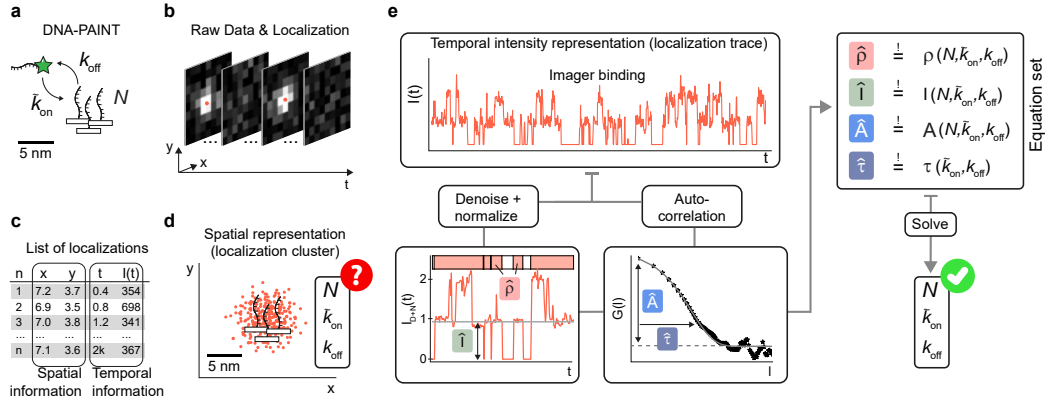


**Figure 5.1. Absolute counting of molecular copy numbers in a single DNA-PAINT experiment.** (a) Schematic of DNA-PAINT. The transient binding of fluorescently-labeled imager strands to complementary docking strands attached to the target molecules of interest. The binding reaction is governed by reaction rates  $k_{\text{off}}$  and  $\tilde{k}_{\text{on}}$ . Multimeric organization of the target molecules can lead to accumulations of  $N$  docking strands at very close spacing ( $< 5$  nm). (b) Sparse transient imager binding ensures the detection of single-molecule fluorescence signals during data acquisitions of typically several thousand frames. Fitting the center coordinates of each single-molecule detection during post-processing allows to obtain a localization that pinpoints the actual position of the underlying docking strand at nanometer precision (red points). (c) A processed DNA-PAINT data set consists of a list that contains all  $n$  obtained localizations (typically on the order of  $10^6$ ). Each localization is associated to accessible quantities such as its spatial coordinates ( $x, y$ ; in case of a 2D image), the frame  $t$  in which it was localized and its intensity  $I(t)$  as the number of detected photo-electrons. (d) An  $x$ - $y$  scatter plot allows to render a super-resolved image as the spatial representation of the localization list (red dots). Ideally, the position of each docking strand is revealed by a clearly-distinguishable localization cluster. In case of multimeric targets, however, localizations obtained from multiple tightly-spaced docking strands can overlap in a not-resolvable localization cluster in the DNA-PAINT image. We are asking the question whether it is possible to derive the unknown physical quantities  $N$ ,  $\tilde{k}_{\text{on}}$  and  $k_{\text{off}}$  based on a single localization cluster, but for all localization clusters contained in the overall DNA-PAINT image. (e) Starting point of our solution to this problem is the intensity vs. time information that is associated to each localization cluster (compare (c)). This ‘intensity trace’ contains the temporal intensity fluctuations due to imager binding and unbinding that were detected from the position of the localization cluster during data acquisition. The intensity trace of each localization cluster is subject to two parallel analysis work streams (see 5.3.3 for detailed description): i) *Denoising & Normalization* which yields the two observables mean intensity  $\hat{I}$  and occupancy  $\hat{\rho}$  of the intensity trace as well as ii) *Autocorrelation* analysis which yields the two observables amplitude  $\hat{A}$  and decay constant  $\hat{\tau}$  of the computed autocorrelation curve. Lastly, the four observables  $\hat{\rho}$ ,  $\hat{I}$ ,  $\hat{A}$ ,  $\hat{\tau}$  are input to a least square optimization of a defining set of equations to find a solution for the unknowns  $N$ ,  $\tilde{k}_{\text{on}}$  &  $k_{\text{off}}$

We want to highlight that the applicability of lbFCS+ is intrinsically limited to targets which give rise to *distinct* and *well-separated* localization clusters in a DNA-PAINT

image. Potential cellular targets are well-separated target molecule assemblies such as nuclear pore complexes in the nuclear envelope. We have previously published a python package, which allows automated detection and isolation of all localization clusters within a DNA-PAINT image [82] (available at <https://doi.org/10.5281/zenodo.4792396>), constituting the starting point of lbFCS+ analysis.

### 5.3.3 The analysis approach of lbFCS+

The concept of the lbFCS+ analysis framework is illustrated in **Fig.5.1e** and is applied in parallel to all detected localization clusters in a DNA-PAINT image. In case of a localization cluster originating from multiple docking strands, the intensity trace  $I(t)$  can show intensity fluctuations depending on the number of bound imagers at each time point. First, a step preserving non-linear de-noising filter [87] is applied to the intensity trace to generate a close to step-like behavior according to the number of simultaneously bound imagers (see **Supplementary Fig.A.1a**). Next, the de-noised intensity trace is normalized by the intensity recorded when only a single imager was bound (i.e. to the first intensity level). Hence, after normalization first level intensity values have a unit-less value of '1' instead of an arbitrary photo-electron count, the second level has a value of '2' and so forth. Further details about the normalization procedure are illustrated in **Supplementary Fig.A.1b**. Based on the de-noised and normalized intensity trace  $I_{D+N}(t)$  the occupancy  $\hat{\rho}$  and the mean intensity  $\langle I_{D+N}(t) \rangle = \hat{I}$  are computed (see lower left panel in **Fig.5.1e**). The occupancy  $\hat{\rho}$  corresponds to the total time a signal was recorded at the position of the localization cluster divided by the total measurement time, i.e. the fraction the intensity trace was in a fluorescing state.

Analytic expressions for both  $\hat{\rho}$  and  $\hat{I}$  can be derived under the assumption of equal and independent binding with  $\tilde{k}_{\text{on}}$  &  $k_{\text{off}}$  of each imager strand to each of the  $N$  docking strands. Then, the probability  $P_k$  to find  $k$  imager strands simultaneously bound to  $N$  docking strands at an arbitrary point in time is given by a binomial distribution:

$$P_k = \binom{N}{k} p^k (1-p)^{N-k} \quad \text{with} \quad p = \frac{1/k_{\text{off}}}{1/k_{\text{off}} + 1/\tilde{k}_{\text{on}}} \quad (5.1)$$

Intuitively,  $p$  corresponds to the probability to find a single docking strand in a fluorescing state, i.e. with an imager bound. The occupancy  $\hat{\rho}$  then corresponds to the inverse of the probability  $P_0$  of no imagers bound to the  $N$  docking strands:

$$\hat{\rho} = 1 - P_0 = 1 - (1-p)^N \quad (5.2)$$

The mean intensity  $\hat{I}$  is simply given by:

$$\hat{I} = \sum_{k=0}^N k \binom{N}{k} p^k (1-p)^{N-k} = Np \quad (5.3)$$

Hence, the expressions for both  $\hat{\rho}$  and  $\hat{I}$  solely depend on the unknowns  $N$ ,  $\tilde{k}_{\text{on}}$  &  $k_{\text{off}}$ . Second, the autocorrelation function  $G(l)$  of the original localization trace  $I(t)$  is computed and  $G(l)$  is fitted with a mono exponential decay function yielding the amplitude  $\hat{A}$  and the characteristic decay time  $\hat{\tau}$  (see lower right panel in **Fig.5.1e**).



Next, 200  $\mu\text{l}$  of streptavidin solution was flushed into the well, incubated for 2 min, removed and washed 1 $\times$  with 200  $\mu\text{l}$  buffer A and subsequently 1 $\times$  with 200  $\mu\text{l}$  buffer B. DNA origami solution (diluted 1:200 in buffer B after folding) was flushed into the well, incubated for 5 min, removed and washed 2 $\times$  with 200  $\mu\text{l}$  buffer B. Lastly, the desired imager strand concentration was directly adjusted in the well first adding the required amount of buffer B.

As mentioned in Section 5.3.3, pipetting errors directly translate into the obtained result for  $k_{\text{on}}$ . Therefore, all samples contained a subpopulation of reference origami consisting of  $N = 1$  origami carrying a single Pm2\* docking strand. Since Pm2\* is a subset of our standard docking strand 5xCTC, the same imager Pm2 binds to both Pm2\* (reference) and 5xCTC (target) docking strands but at a lower  $k_{\text{on}}$  (repetitive docking strands such as 5xCTC with multiple imager binding sites increase  $k_{\text{on}}$  [81, 82, 85]). Therefore, Pm2 reference localization clusters could be easily separated from 5xCTC clusters by using the occupancy  $\hat{\rho}$  during analysis. After separation, resulting variations in  $k_{\text{on}}$  as obtained from Pm2 reference localization clusters were used as global calibration of the imager concentration.

### 5.3.5 Imaging

Imaging of DNA origami samples was performed on a custom-built flat-top TIRF microscope described in previous studies [77, 78, 82]. All fluorescence microscopy data was recorded with a sCMOS camera (2048  $\times$  2048 pixels, pixel size: 6.5  $\mu\text{m}$ ; Andor Zyla 4.2). The camera was operated with the open source acquisition software  $\mu\text{Manager}$  [88] at 2 $\times$ 2 binning and cropped to the center 700  $\times$  700 pixel FOV. The exposure time was set to 400 ms corresponding to the acquisition duty cycle. The read out rate was 200 MHz and the dynamic range was set to 16 bit. The nearly homogenous excitation irradiance [77] at the sample was set to  $\approx 10 \text{ W}/\text{cm}^2$ . For detailed imaging parameters specific to the data presented in all main and supplementary figures refer to **Supplementary Table A.1**.

## 5.4 Results

### 5.4.1 Proof-of-principle demonstration of lbFCS+ on DNA origami

As in our previous work [78], we first tested lbFCS+ on DNA origami as synthetic targets that allow precise control of the number of docking strands per target. We designed four DNA origami variants carrying up to six docking strands  $N = 1, 2, 4, 6$  of the sequence 5xCTC ( $\equiv$  5 repetitions of the triplet CTC). Note that here  $N$  is an upper bound due to the limited docking strand incorporation efficiency [74], i.e. a sample of  $N = 4$  origami will also contain origami carrying only three, two or even one docking strand/s. We recorded a 30-min DNA-PAINT acquisition at 5 nM imager concentration for each origami variant immobilized on the cover glass of distinct wells of a microscopy slide (see Section 5.3.5 and **Supplementary Table A.1** for detailed imaging conditions of all presented data). After localizing and rendering of the DNA-PAINT images, all localization clusters were automatically detected (see Section 5.3.3) and subject to lbFCS+ analysis.

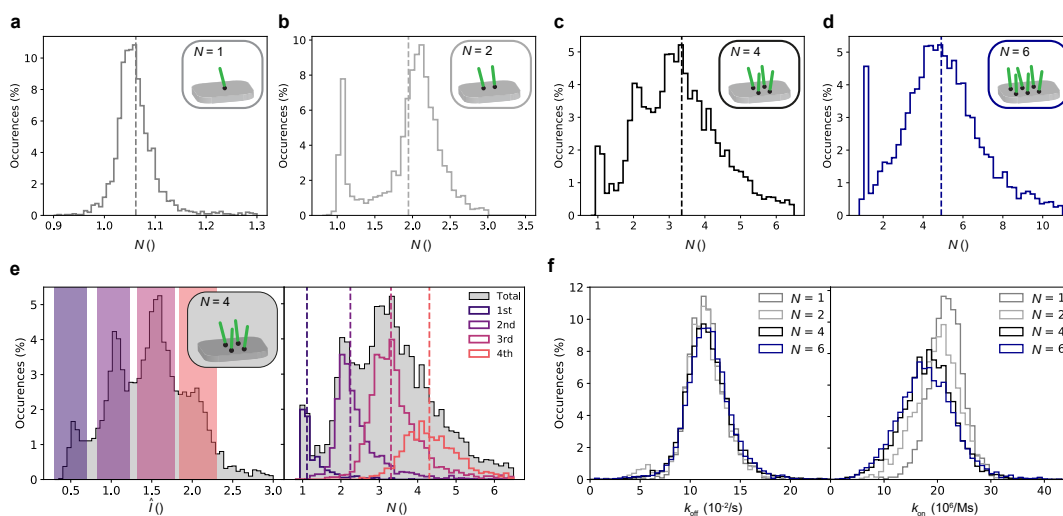


**Figure 5.2. Proof-of-principle demonstration on DNA origami.** (a) Counting results for DNA origami carrying a single docking strand ( $N = 1$ ; # clusters = 1,994 ) with a mean of  $\langle N \rangle = 1.06$  (dashed line). (b) Same as (a) but for DNA origami carrying two docking strands ( $N = 2$ ; # clusters = 2,582;  $\langle N \rangle = 1.95$ ). (c) Same as (a) but for DNA origami carrying four docking strands ( $N = 4$ ; # clusters = 7,232;  $\langle N \rangle = 3.35$ ). (d) Same as (a) but for DNA origami carrying six docking strands ( $N = 6$ ; # clusters = 5,038;  $\langle N \rangle = 4.91$ ). (e)  $\hat{I}$  distribution (grey; left panel) and  $N$  distribution (grey; right panel) for the  $N = 4$  origami data set shown in (c). We defined subpopulations by selection of intervals in  $\hat{I}$  (colored intervals; left panel) and plotted their corresponding counting results  $N$  (colored solid lines) and mean values  $\langle N \rangle$  (colored dashed lines, right panel). (f) Dissociation rates  $k_{\text{off}}$  (left panel) and association rates  $k_{\text{on}}$  (right panel) obtained via lfFCS+ analysis of all data sets shown in (a-d).

**Fig.5.2a** shows the obtained counting results for  $N = 1$  origami (# clusters = 1,994). The mean of the distribution at  $\langle N \rangle = 1.06$  is in close agreement with the expected value of 1, but indicates a slight tendency of over counting.

The counting results for the DNA-PAINT image of  $N = 2$  origami (# clusters = 2,582) in **Fig.5.2b** features a prominent peak at  $N = 2$  but also a smaller peak at  $N = 1$  corresponding to origami with one of the two docking strands missing. 82 % of all localization clusters lie within  $1.5 < N < 3$  which corresponds to an average incorporation efficiency for any of the two docking strands of around 90 % (in good agreement with [74]).

The counting results obtained from the  $N = 4$  origami image in **Fig.5.2c** (# clusters = 7,232) yielded a distribution with clearly distinguishable peaks located at  $N = 1, 2$  and 3. Based on the mean of the distribution  $\langle N \rangle = 3.35$  (dashed line) we estimated a slightly lower incorporation efficiency of around 84 % [74]. However, we observed a broadening of the distribution toward higher  $N$ , hindering a visual distinction of the peak at  $N = 4$ .

This is further confirmed when looking at the counting results derived from the  $N = 6$  origami data set (see **Fig.5.2d**). While for  $N \geq 5$  it is not possible to visually distinguish incremental copy numbers, the mean of the distribution at  $\langle N \rangle = 4.91$  (dashed line) still yields a reasonable ensemble average result (corresponding to an incorporation efficiency of around 82 %) [74].

Next, we turned back to the  $N = 4$  data set in order to find out whether it is possible

to achieve a clear distinction between  $N = 3$  and  $N = 4$ . Remarkably, we found that the distribution of mean intensities  $\hat{I}$  obtained from all localization clusters exhibited four peaks, as depicted in the left panel of **Fig.5.2e**. Intuitively, the leftmost peak, i.e. the lowest mean intensity should correspond to  $N = 1$  origami, since increasing numbers of docking strands lead to higher values of  $\hat{I}$  due to the increasing probability of simultaneous binding of multiple imagers (see Eq. 5.3). We confirmed this by selecting localization clusters lying within the colored intervals in  $\hat{I}$  and by comparing the corresponding subpopulations in  $N$  to the overall obtained distribution (**Fig.5.2e**, left and right, respectively). This selection in  $\hat{I}$  allowed us to obtain mean counting results for the subpopulations that are close to the expected values of  $N = 1, 2, 3$  and  $4$  (colored dashed lines). The visual inspection of exemplary intensity traces from the selected intervals in  $\hat{I}$  confirms the applicability of this approach (see **Supplementary Fig.A.2**). Again, we observed a slight over counting that is more prominent for increasing  $N$ .

After inspection of the counting results, we turned our attention to the imager hybridization rates obtained via lbFCS+ analysis of the same four data sets as in **Fig.5.2a-d**. **Fig.5.2f** shows the corresponding  $k_{\text{off}}$  distributions (left) and  $k_{\text{on}}$  distributions (note that lbFCS+ yields  $\tilde{k}_{\text{on}}$ , from which  $k_{\text{on}} = \tilde{k}_{\text{on}}/c$  was calculated using the absolute imager concentration, see Section 5.3.1). Overall,  $k_{\text{off}}$  shows very good agreement for all four data sets independent of the number of docking strands per origami with a relative width of  $\text{STD}(k_{\text{off}})/\langle k_{\text{off}} \rangle \approx 18\%$ .

In  $k_{\text{on}}$ , however, we observed broader distributions compared to  $k_{\text{off}}$  with relative widths  $\text{STD}(k_{\text{on}})/\langle k_{\text{on}} \rangle$  increasing from 14% for  $N = 1$  to 30% for  $N=6$ . Additionally, we observed a slight, but systematic decrease with increasing numbers of docking strands with  $\langle k_{\text{on}} \rangle$  decreasing from  $22 \times 10^6$  1/Ms for  $N = 1$  to  $18 \times 10^6$  1/Ms for  $N = 6$ . As described in Section 5.3.4, reference origami allowed for a calibration of the imager concentrations to minimize pipetting errors affecting  $k_{\text{on}}$  (see **Supplementary Fig.A.3** for the calibration results of the  $N = 1, 2, 4, 6$  datasets shown in **Fig.5.2a-d**).

Both the experimentally observed upper limit in distinguishing copy numbers of  $N \geq 4$  and the apparent dependence of  $k_{\text{on}}$  on  $N$  led us to further assess the applicable working range of lbFCS+.

#### 5.4.2 Assessing the working range of lbFCS+

To investigate the applicable working range of lbFCS+ and possible systematic artifacts it was obligatory to perform the analysis on a data set of known ground truth. Therefore, we computationally combined arbitrary localization clusters from the  $N = 1$  data set (see **Fig.5.2a**) into clusters of user-defined  $N_{\text{in}} = k \times (N = 1)$ , a concept we already applied in an earlier study [78]. This ‘regrouping’ is equivalent to the computational addition of intensity traces  $I(t)$  of the individual clusters. To exclude varying intensity levels between the original clusters (e.g., caused by speckles in the illumination profile) the intensity traces  $I(t)$  were normalized prior to addition (see **Supplementary Fig.A.1**). We want to highlight, that this procedure completely preserved the experimental intensity noise distribution.

**Fig.5.3a** shows the counting results obtained from computationally regrouped clusters consisting of up to eight experimental  $N = 1$  clusters (i.e.  $N_{\text{in}} = k \times (N = 1)$  up to  $k = 8$ ). Overall, the counting results  $N$  agree very well with the expected  $N_{\text{in}}$ . Again, we observed a slight systematic offset of the resulting means  $\langle N \rangle$  (colored dashed

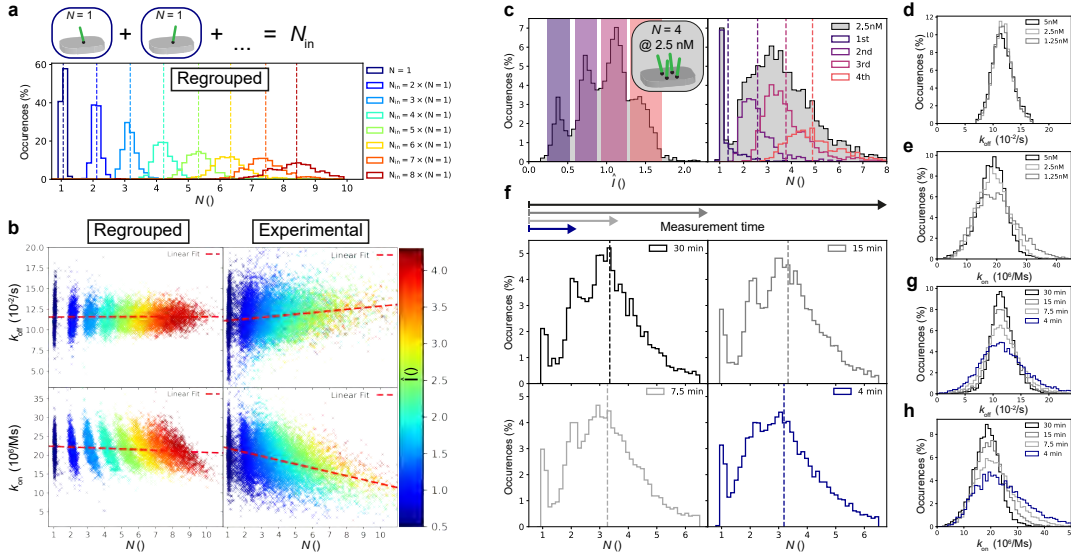


**Figure 5.3. Assessing the working range of lbFCS+.** Localization clusters from the  $N = 1$  data set (see Fig.5.2a) were selected at random and subsequently computationally combined into clusters of user-defined  $N_{in} = k \times (N = 1)$  and subject to lbFCS+ analysis (# clusters = 1,000 for each  $N_{in}$ ). (a) Counting results  $N$  obtained from computationally-combined clusters consisting of up to eight experimental  $N = 1$  clusters (i.e.  $N_{in} = k \times (N = 1)$  up to  $k = 8$ ) and their corresponding means  $\langle N \rangle$  (dashed lines). (b) Scatter plot  $k_{off}$  vs.  $N$  (upper panels) and scatter plot  $k_{on}$  vs.  $N$  (lower panels) for all computationally-combined clusters (left panels) shown in (a) and for all experimental clusters from  $N = 1, 2, 4, 6$  origami (right panels) shown in Fig.5.2a-d. Each cluster was color-coded according to its mean intensity  $I$  (which is linearly proportional to  $N$ , see Eq.5.3). The red dashed lines indicate the optimum linear fits over all data points in each panel. (c) Analysis analogous to Fig.5.2e for DNA origami containing four docking strands ( $N = 4$ ), but measured at a reduced imager concentration of 2.5 nM (# clusters = 3,697). (d) Dissociation rates  $k_{off}$  obtained via lbFCS+ analysis for DNA origami containing four docking strands ( $N = 4$ ) measured at varying imager concentrations (# clusters = 5,834 for 1.25 nM). (e) Association rates  $k_{on}$  for the same data sets as in (d). (f) Counting results for the  $N = 4$  origami data set shown in Fig.5.2c for varying measurement times. The original data set (30 min measurement time) was reduced to the first 15 min, 7.5 min and 4 min, respectively, prior to analysis. The dashed lines indicate the mean  $\langle N \rangle$  of each distribution. (g) Dissociation rates  $k_{off}$  obtained via lbFCS+ analysis for the data shown in (f). (h) Association rates  $k_{on}$  obtained via lbFCS+ analysis for the data shown in (f).

lines) towards higher  $N$ . Although this effect seemed to increase with  $N_{in}$  in absolute terms, the relative offsets ( $(\langle N \rangle - N_{in})/N_{in}$ ) remained constant at  $\approx 6\%$  (compare to Fig.5.2a). Similar to the experimental results the width of the  $N$  distributions broadened with increasing  $N_{in}$  (compare to Fig.5.2a-e). The relative width of each distribution defined as  $STD(N)/\langle N \rangle$  increased proportional to  $\sqrt{N_{in}}$ , starting with a value of 4% for  $N = 1$ . This broadening behavior is in line with the experimental  $N$  results displayed in Fig.5.2a-d. However, from our regrouping analysis we would expect that it should be possible to clearly distinguish the peaks between  $N = 3$  and  $N = 4$ , which is not the case for DNA origami (see Fig.5.2c). This indicates an additional source of uncertainty of lbFCS+ counting towards higher  $N$ .

Next, we focused on the hybridization rates obtained from the regrouped data sets. The upper left panel of Fig.5.3b shows a scatter plot of the obtained  $k_{off}$  vs.  $N$  result

for all localization clusters from the eight regrouped data sets. Each cluster was color coded using its respective mean intensity value  $\hat{I}$  (which is linearly proportional to  $N$ , see Eq.5.3). Contrarily to the broadening in  $N$ , we observed a narrowing of the  $k_{\text{off}}$  distributions for increasing  $N_{\text{in}}$ . Both the shape of the distributions with respect to  $k_{\text{off}}$  and  $N$  as well as the negligible slope of a linear fit of all data points (red dashed line) indicated that the solutions for  $k_{\text{off}}$  and  $N$  are largely decoupled.

Similarly, the lower left panel of **Fig.5.3b** shows the analogous scatter plot for  $k_{\text{on}}$  vs.  $N$ . Here, the linear fit over all clusters exhibited a minor, but negligible decrease in  $k_{\text{on}}$  for increasing  $N$  with respect to experimental measurement errors (see description of **Fig.5.2f** in Section 5.4.1). Furthermore, we observed a hyperbolic shape of the  $k_{\text{on}}$  vs.  $N$  distributions for increasing  $N_{\text{in}}$ . This is due to the fact that three of the four observables ( $\hat{\rho}$ ,  $\hat{I}$  and  $\hat{A}$ ) used as input to the final set of equations (see **Fig.5.1e**, right) are in first order approximation proportional/indirect proportional to the product  $N\tilde{k}_{\text{on}}$  (see Eq.5.2,5.3 and 5.4). Additionally, the observable  $\hat{\rho}$  only contains valuable information for fluorescence traces featuring interruptions, thereby constituting an upper operational limit of lbFCS+ at a given imager concentration. For increasing  $N$ , almost uninterrupted intensity traces lead to saturation of  $\hat{\rho}$  (e.g.  $\hat{\rho} \approx 99\%$  for  $N_{\text{in}} = 8$ ) and as such to a loss of information for the defining set of equations. For this reason, lbFCS+ is designed for the application to targets containing low copy numbers of docking strands  $N \lesssim 4 - 8$  (depending on the used imager concentration and  $k_{\text{on}}$ ). To experimentally assess its upper limit we imaged and analyzed origami containing 12 docking strands, still yielding reasonable ensemble results when imaged at a concentration of 2.5 nM (see **Supplementary Fig.A.4**).

To compare the findings obtained from computational regrouping to the experimental data we depicted the combined results from  $N = 1, 2, 4, 6$  origami (see **Fig.5.2a-d**) in an analogous  $k_{\text{off}}$  vs.  $N$  scatter plot in the upper right panel of **Fig.5.3b**. In contrast to the computationally combined clusters, linear fitting over all experimental clusters (red dashed line) indicated an increase in  $k_{\text{off}}$  with  $N$ . On the other hand, the experimentally obtained  $k_{\text{on}}$  vs.  $N$  scatter plot in the lower right panel of **Fig.5.3b** similarly yields increasingly hyperbolic distributions as observed for the regrouped clusters. Linear fitting of all data points (red dashed line) showed a clear decrease in  $k_{\text{on}}$  with increasing  $N$ , as already observed in **Fig.5.2f**. This decrease in  $k_{\text{on}}$  with increasing  $N$  is significantly larger compared to the regrouped data sets (see lower left panel).

The observations in both  $k_{\text{on}}$  and  $k_{\text{off}}$  indicated that intensity traces recorded from origami containing multiple docking strands are not exactly equal to the simple addition of the individual single docking strand signals. We suspected that the docking strand position on the DNA origami could lead to local changes in  $k_{\text{on}}$  and  $k_{\text{off}}$ , thereby possibly giving rise to a measurement bias for higher  $N$ . Remarkably, when performing four control experiments, each time only with one of the four docking strands of the  $N = 4$  origami incorporated, we could not observe any position dependence neither in  $k_{\text{on}}$  nor in  $k_{\text{off}}$  (see **Supplementary Fig.A.5**). We hypothesize that cooperative binding due to the spatial proximity of the docking strands could be a possible explanation for this behavior. However, over the applicable range of  $N \lesssim 4 - 8$ , this does not affect the ability of lbFCS+ to obtain correct counting results and only causes minor deviations in the measured hybridization rates ( $\leq 2\%$  and  $\leq 20\%$  in  $k_{\text{off}}$  and  $k_{\text{on}}$ , respectively).

As a next step we assessed the lower limit of the applicable working range by measuring  $N = 4$  origami at reduced imager concentrations. Analogous to **Fig.5.2e** it was still possible to clearly distinguish subpopulations in  $\hat{I}$  in order to identify the corresponding result in  $N$ , but at a reduced imager concentration of 2.5 nM (see **Fig.5.3c**). It was even possible to repeat the same analysis for a sample imaged at an imager concentration of 1.25 nM (see **Supplementary Fig.A.6**). The shapes of the  $N$  distributions are in close agreement with the results obtained from the computational combination of experimental  $N = 1$  clusters measured at a concentration of 1.25 nM to clusters of defined  $N_{\text{in}} = k \times (N = 1)$  as presented in **Supplementary Fig.A.7** (analogous to **Fig.5.3a,b**).

Surprisingly, imaging  $N = 4$  origami at lower imager concentrations had no significant effect on the resulting  $k_{\text{off}}$  values as shown in **Fig.5.3d**. However, we observed a broadening in  $k_{\text{on}}$  with decreasing imager concentrations as expected from the broadening in  $N$  (see **Fig.5.3e**).

Finally, we investigated the effects of the measurement time on lbFCS+ analysis (i.e. the image acquisition time). We therefore reduced the original  $N = 4$  data set (30 min measurement time) to the first 15 min, 7.5 min and 4 min prior to analysis. Remarkably, it was only possible to observe significant changes in the resulting  $N$  distribution at measurement times  $\lesssim 8$  min (see **Fig.5.3f**). A measurement time of 4 min would correspond to an expectation value of only  $\approx 13$  imager binding events per single docking strand. We observed a broadening in both  $k_{\text{off}}$  and  $k_{\text{on}}$  for reduced measurement times as apparent from **Fig.5.3g** and **Fig.5.3h**, respectively. Finally, our optimization of the required measurement times allowed us to image 18 FOVs containing a total of  $\approx 50.000$  origami in  $\approx 3$  h of total measurement time, still yielding robust quantitative results (see **Supplementary Fig.A.8**).

#### 5.4.3 Distinction of nanoscopic DNA assemblies via binding dynamics

Driven by the high accuracy of lbFCS+ to determine hybridization rates we hypothesized that it might be possible to distinguish DNA constructs via detection of slight changes in the position dependent imager-docking strand binding dynamics.

Besides the direct incorporation of 5xCTC docking strands as used in the preceding experiments, we designed DNA origami carrying a single 20 base 'adapter' docking strand of sequence A20 (see Section 5.3.4 for exact sequences). Addition of oligos carrying both the complementary adapter region and the docking strand sequence (A20\*+5xCTC, referred to as 'linker strand') allowed us to permanently install the docking strand further away from the origami surface via the double-stranded link A20+A20\* ( $\approx 10$  nm at full elongation), as depicted in **Fig.5.4a**. We distinguished between the 'Direct' configuration (5xCTC incorporated; grey box) and the 'Link' configuration (5xCTC on top of the double-stranded A20 linker; orange box). We want to highlight that both configurations are not rigid but experience rotational freedom introduced by single stranded TT-spacers (black dots; one for Direct and two for Link, respectively).

We subsequently imaged three samples containing 1) only Direct origami, 2) only Link origami or 3) a mixture of both configurations. lbFCS+ analysis yielded the expected number of docking strands  $N = 1$  (see **Fig.5.4b**) in all cases and we could not observe any alteration of  $k_{\text{off}}$  between the different configurations (see **Fig.5.4c**).

In contrast, we observed an increased  $k_{\text{on}}$  for the Link configuration compared to the Direct configuration (see **Fig.5.4d**). We suppose that both the increased mobility of the docking strand and larger distance from the origami surface promote a higher chance of imager binding for the Link configuration. This shift was large enough to clearly identify the Link/Direct origami in the bimodal  $k_{\text{on}}$  distribution of the sample containing both configurations (Mix).

Following the same reasoning, we designed DNA origami similar to the Link assembly (see **Fig.5.4a**) but now providing a second possible binding site for the A20 adapter (referred to as '2xLink', see **Fig.5.4e**). Due to the stochastic nature of linker strand binding, this origami configuration can be observed in one of three possible states. The first two states consist of a single linker strand (i.e.,  $N = 1$ ) bound to the 2xLink origami at either the bottom or the top (blue box in **Fig.5.4e**). The third state corresponds to both A20 sites (i.e.,  $N = 2$ ) being occupied by a linker strand (dark-red box in **Fig.5.4e**). Since the ratio of origami in a  $N = 1$  or  $N = 2$  configuration should be manipulable via variation of linker strand concentrations, we imaged four samples of 2xLink origami which were previously incubated for 3 min at 100 nM, 40 nM, 5 nM and 2 nM linker strand concentrations.

**Fig.5.4f** shows the total  $N$  distribution obtained from lbFCS+ analysis of the four data sets (grey), confirming the expected counting result of either  $N = 1$  or  $N = 2$ . While for a 100 nM linker strand concentration  $\approx 80\%$  of all origami had bound two linkers, at 2 nM it was only  $\approx 60\%$ , validating the concentration dependence during incubation on the probability of 2xLink origami to be found in an  $N = 1$  or  $N = 2$  state (see **Supplementary Fig.A.9**).

Again, we were interested in potential variations in the measured hybridization rates depending on the state of each 2xLink origami. For this reason, we isolated the  $N = 1$  and  $N = 2$  configurations by separating localization clusters that yielded either  $N < 1.2$  (blue) or  $N > 1.6$  (dark red), respectively (see **Fig.5.4f**). Already the total  $k_{\text{off}}$  distribution of all 2xLink origami (grey) presented in **Fig.5.4g** revealed two subpopulations located at  $k_{\text{off}} \approx 7 \times 10^{-2}$  1/s and  $k_{\text{off}} \approx 11 \times 10^{-2}$  1/s. These two subpopulations became especially prominent when looking at only  $N = 1$  localization clusters (blue), confirming the existence of a top and a bottom state of  $N = 1$  origami that give rise to a distinct  $k_{\text{off}}$ . In contrast, the  $N = 2$  clusters yielded a homogeneous  $k_{\text{off}}$  distribution with a median (dark red arrow) nearly identical to the median of previous Link origami (orange arrow, obtained from orange distribution shown in **Fig.5.4c**).

Inspection of the  $k_{\text{on}}$  results yielded a similar behavior, as depicted **Fig.5.4h**. While the total  $k_{\text{on}}$  distribution showed a somewhat broadened shape (grey), selection of  $N = 1$  origami clearly revealed two subpopulations located at  $k_{\text{on}} \approx 17 \times 10^6$  M/s and  $k_{\text{on}} \approx 31 \times 10^6$  M/s. This suggested that for  $N = 1$  origami the top and bottom states also give rise to a different  $k_{\text{on}}$ . The  $k_{\text{on}}$  values obtained from  $N = 2$  origami resulted in a broad distribution with a skew toward lower  $k_{\text{on}}$  values. However, its median (dark red arrow) was again close to the median in  $k_{\text{on}}$  as obtained for the Link origami (orange arrow, obtained from orange distribution shown in **Fig.5.4d**).

In conclusion, this suggests that the signal from  $N = 2$  origami is actually a superposition of heterogeneous signals due to the distinct binding dynamics of the top/bottom  $N = 1$  states. Strictly speaking, here  $N = 2$  origami hence violate our assumption of equal and independent binding rates used in the derivation of Section 5.3.3. The

coincidence of the  $N = 2$  peak (dark red) with the right peaks of the two possible  $N = 1$  configurations (blue) indicates that in case of heterogeneous rates lbFCS+ analysis is dominated by the larger value in both  $k_{\text{off}}$  and  $k_{\text{on}}$  (see **Fig.5.4g** and **h**, respectively). Regardless of heterogeneous rates, lbFCS+ analysis still yielded the correct counting results (compare **Fig.5.4f**).

Finally, we aimed to exploit the heterogeneous binding kinetics to identify the (otherwise indistinguishable) top/bottom states within the  $N = 1$  subpopulation. Indeed, hierarchical density based clustering (hdbscan) [89] allowed us to classify two distinct states in the scatter plot of  $k_{\text{off}}$  vs.  $k_{\text{on}}$  over all  $N = 1$  localization clusters (see **Fig.5.4i**). Intuitively, the bottom  $N = 1$  state of the 2xLink origami should be close to the Link configuration depicted in **Fig.5.4a**. Comparison of the median  $k_{\text{off}}$  &  $k_{\text{on}}$  of each class (white crosses) with the median  $k_{\text{off}}$  &  $k_{\text{on}}$  as obtained for the Link origami (orange lines, obtained from **Fig.5.4b** and **d**) hence allowed to associate the top right class (square) with the bottom  $N = 1$  state and the top left class with the top  $N = 1$  state (diamonds). We classified almost three times as many origami in a top state (# clusters = 2630) as in a bottom state (# clusters = 981) suggesting a lower binding probability of linker strands to the bottom position. Interestingly, we observed a significantly lower  $k_{\text{off}}$  (i.e. a longer binding duration) and a lower  $k_{\text{on}}$  for docking strands placed at the top position when compared to the bottom position.

## 5.5 Discussion

In summary, lbFCS+ is, to our knowledge, the first method capable of extracting both absolute molecular copy numbers and DNA hybridization rates of individual DNA-PAINT localization clusters within a single DNA-PAINT image. Based on only minimal experimental requirements and theoretical assumptions it thus provides a solution to the long prevailing problem of ‘molecular counting’ in SMLM without the need of any initial calibration or modeling [24, 32, 48].

In proof-of-principle experiments on DNA origami we demonstrated that lbFCS+ yields truthful docking strand copy numbers  $N$  and dissociation/association rates  $k_{\text{off}}$  &  $k_{\text{on}}$  of the underlying imager/docking strand binding reaction from DNA-PAINT data sets acquired at moderate imager concentrations ( $\leq 5$  nM) and measurement times  $\leq 30$  min). Our assessment of the working range indicated that lbFCS+ is suited for an application to localization clusters containing up to six docking strands. The high accuracy of lbFCS+ to determine hybridization rates allowed to measure small differences in imager binding dynamics to docking strands of same sequence but placed at different positions of nanoscopic DNA assemblies. Finally, this enabled us to resolve heterogeneous binding dynamics between individual DNA-PAINT clusters allowing for the distinction of stochastically generated and a priori indistinguishable DNA assemblies.

We want to stress that although lbFCS+ is in principle equally applicable to 3D data sets this work was limited to planar samples imaged in TIRF configuration. Usually, a 3D DNA-PAINT image acquisition requires a confined illumination scheme (e.g. HILO or SDCM) to suppress the fluorescent background from the imaging solution. Since lbFCS+ is not relying on any ensemble averaging it would be ideally suited for the study of heterogeneous samples as expected in e.g. cellular environments. Heterogeneities might emerge from diffusional barriers due to compartmentaliza-

tion or steric hindrance in densely-packed molecular environments. lbFCS+ could hence map the accessibility of imagers to different cellular parts (decoupled from the molecular copy numbers) which could be of general interest for the interpretation of DNA-PAINT images. Due to its accuracy in the determination of low molecular copy numbers especially studies aiming for the distinction of monomers, dimers or tetramers are a feasible first step. We reason that high target molecule densities[32], pronounced unspecific binding of imager strands [85, 90] and the optical sectioning capabilities of the used microscope will be major challenges when applying lbFCS+ to cellular targets. We want to highlight that DNA-PAINT (and hence lbFCS+) is generally not designed for living cells but requires fixed specimens. Finally, lbFCS+ requires the presence of well-separable localization clusters in the DNA-PAINT image and can as such not be readily transferred to an analysis of e.g. continuous objects. We demonstrated that lbFCS+ is capable of detecting/distinguishing small differences in imager/docking strand binding dynamics in nanoscopic volumes containing low numbers of molecules requiring only moderate measurement times. Hence, lbFCS+ provides a highly-parallelized and easy-to-implement readout for potential on-chip bio-sensing applications. Especially interesting are applications requiring a direct detection of molecules in low concentration regimes without amplification steps [91, 92]. Additionally, our study of varying DNA-assemblies already suggests that lbFCS+ might readily serve as a readout to determine the state of logic gates (e.g. hairpins) in DNA-based logical circuits [93, 94]. However, we want to highlight that lbFCS+ is in principle not limited to the study of DNA hybridization reactions, but can applied to any reversible binding reaction of fluorescently-labeled ligands to immobilized receptors.

In conclusion, we believe that lbFCS+ provides a powerful tool with promising applications beyond its initial purpose of advancing quantitative DNA-PAINT imaging.

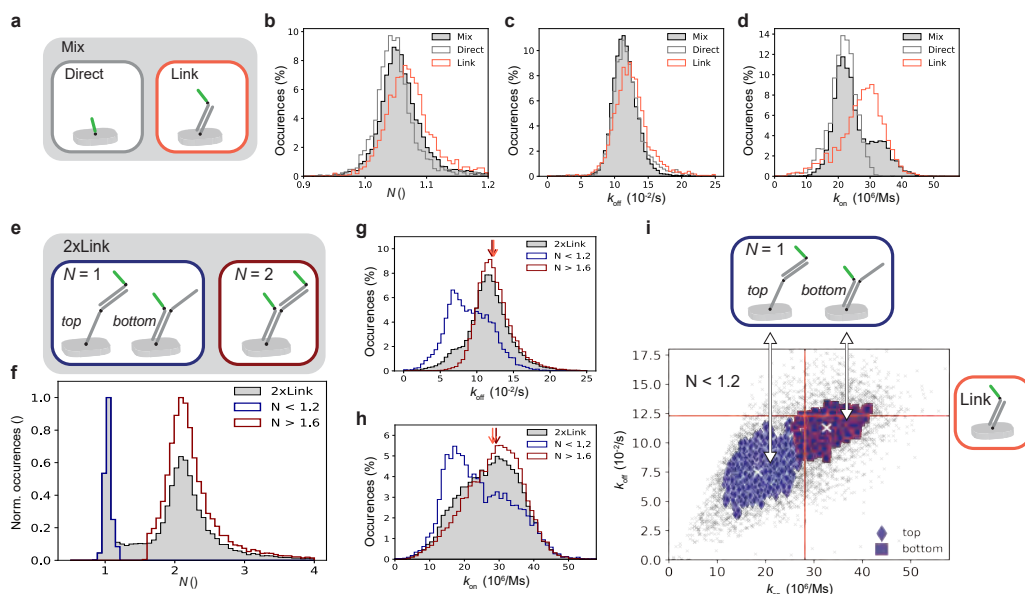


**Figure 5.4. Distinction of nanoscopic DNA assemblies via binding dynamics.** (a) Schematic of the direct incorporation of 5xCTC docking strands into DNA origami (‘Direct’; dark-grey box) and permanent attachment of 5xCTC docking strands via a ‘linker strand’ (A20\*+5xCTC) after folding (‘Link’; orange box). Black dots indicate single stranded TT-spacers. We imaged three samples containing 1) only Direct origami, 2) only Link origami or 3) a mixture of both configurations (‘Mix’; filled grey box). (b) lfFCS+ counting results as obtained from the Direct origami, the Link origami and the mixed sample as illustrated in (a). Direct sample contained # clusters = 2,088; Link: # clusters = 2,780; Mix: # clusters = 9,136. (c) Dissociation rate  $k_{\text{off}}$  as obtained from the same data as shown in (b). (d) Association rate  $k_{\text{on}}$  as obtained from the same data as shown in (b). (e) DNA origami design featuring 2x linker binding sites (referred to as ‘2xLink’). After incubation with linker strands, 2xLink origami can be in three possible states (schematically depicted). The first two states consist of a single linker strand (i.e.,  $N = 1$ ) bound to the 2xLink origami at either the bottom or the top position (blue box). The third state corresponds to both A20 sites being occupied by a linker strand (i.e.,  $N = 2$ ; dark-red box). (f) Total  $N$  distribution obtained from imaging 4 distinct samples of 2xLink origami, which were incubated for 3 min at either 100 nM, 40 nM, 5 nM or 2 nM linker strand concentrations (Supplementary Fig.A.9 shows separate results for each sample). For further analysis, we split the total distribution into into clusters yielding either  $N < 1.2$  (blue) or  $N > 1.6$  (dark red). Total # of 2xLink origami localization clusters from 4 data sets = 27,348;  $N < 1.2$ : # clusters = 6159;  $N > 1.6$ : # clusters = 19,192. (g) Dissociation rate  $k_{\text{off}}$  as obtained from the same data as shown in (f). The dark red arrow indicates the median of the  $N > 1.6$  subpopulation, the orange arrow indicates the median of the Link origami shown in (c). (h) Results analogous to (g) but for the association rate  $k_{\text{on}}$ . (i) Scatter plot of  $k_{\text{off}}$  vs.  $k_{\text{on}}$  for all 2xLink origami yielding  $N < 1.2$ , see (f). Hierarchical density based clustering (hdbscan) [89] (used parameters: metric = ‘l2’, min\_cluster\_size = 500, min\_samples = 8) of the data yielded two groups. The median of each group is marked by a white cross and the corresponding median as obtained from Link origami shown in (c,d) is indicated by the orange lines. We assigned the bottom  $N = 1$  state of the 2xLink origami to the upper right group (dark-blue squares) due to 1) the proximity of its median to the median of the Link origami and 2) its resemblance in design to the Link origami (compare orange box in (a) with blue box in (e)) Vice versa, we assigned the top  $N = 1$  state of the 2xLink origami to the lower left group (dark-blue diamonds). All  $N < 1.2$  origami contained # clusters = 6159; top: # clusters = 2630; bottom: # clusters = 981.



# 6

## Summary and Outlook

Revisiting the initially stated motivation, we will briefly discuss to which extent this work can give answer to the *guiding questions* of this thesis as presented in Section 1.6:

1. *Under which experimental constraints is DNA-PAINT truly decoupled from photo-physical artifacts?*
2. *Is the underlying DNA-hybridization predictable enough to be used for a robust quantitative analysis of DNA-PAINT data?*
3. *Based on DNA-mediated fluorophore exchange, is it possible to create a single molecule label emitting a continuous, ideally uninterrupted, fluorescence signal for prolonged observation times in SPT?*

The short answer to **Question 1** is, that we found that DNA-PAINT indeed suffers from residual photo-physical artifacts, but their implications can be efficiently reduced to a minimum under appropriately chosen experimental conditions.

First, we demonstrated that the photo-induced depletion of docking strands [76] can be almost neglected for short image acquisition times employing sufficiently low laser excitation intensities (see Chapter 3 & 5) and can be further suppressed by addition of oxygen scavenging systems. Remarkably, the employment of low laser excitation intensities in combination with oxygen scavenging systems allowed to uninterruptedly monitor single target molecules over the course of hours (see Chapter 4) underlining the efficiency of the applied measures to reduce photo-damage.

Second, in the comparative study of Chapter 2 we showed that a commonly used inhomogeneous Gaussian excitation profile directly translates into 1) a non-uniform localization detection efficiency, 2) non-uniform fluorescent ON-times and 3) non-uniform localization precisions throughout the FOV. All of these artifacts could already be avoided at the stage of data-acquisition through the simple implementation of a flat-top illumination profile by using a commercially available refractive beam-shaping device [95].

We want to highlight that all of the studies presented focused on sufficiently planar samples allowing imaging in TIRF configuration offering highly selective illumination of thin volumes close to the surface of the sample substrate ( $\leq 200$  nm)[57]. Hence, it is questionable if the found stability of DNA-PAINT regarding photo-physical artifacts still holds true for less selective illumination schemes. Particularly, imager

diffusion barriers due to compartmentalization in e.g. cellular samples might lead to bleaching of the local imaging solution reservoir and hence to a reduction of the effective (fluorescent) imager concentration in such enclosed volumes. An enlarged excited volume of the imaging solution might additionally cause an enrichment of oxygen radicals which are presumed to cause the depletion of docking strands during DNA-PAINT image acquisition [76, 96, 97].

Despite that, we did not only identify potential residual artifacts in DNA-PAINT images but also developed efficient strategies to minimize their impact. Therefore, we believe that our efforts will help to ‘demystify’ recurring uncertainties regarding the interpretation of DNA-PAINT images and will serve as a good starting point for further investigations in more complex scenarios.

In our answer to **Question 2** we introduced an approach termed lbFCS (see Chapter 3) which allowed for the first time *absolute* molecular counting in localization clusters in DNA-PAINT images, without the need of a separate reference measurement and using only minimal theoretical assumptions. However, it 1) required at least two measurements of the same sample at distinct and correctly-adjusted imager concentrations and 2) could only yield *average* values for both the underlying hybridization rates and the counted copy numbers. Additionally, it did not take into account recent advances regarding the ‘speed-up’ of the DNA-PAINT reaction [79–81, 85].

We could overcome these limitations in a revised framework termed lbFCS+ (see Chapter 5) which finally allowed extraction of *absolute* molecular numbers and hybridization rates of *single* DNA-PAINT clusters requiring only a *single* DNA-PAINT image acquisition. lbFCS+ thus provides a solution to the long prevailing problem of ‘molecular counting’ in SMLM without the need of any initial calibration or modeling [24, 32, 48]. Our assessment of the working range indicated that lbFCS+ is suited for an application to well-separated localization clusters containing up to six docking strands.

However, we only demonstrated the applicability of lbFCS+ in proof-of-principle experiments on DNA origami. Since lbFCS+ is not relying on any ensemble averaging it would be ideally suited for the study of heterogeneous samples as expected in e.g. cellular environments. Taking into account its sensitivity to determine local hybridization rates, it could potentially map the varying accessibility of imagers to different cellular parts which could be of general interest for the interpretation of DNA-PAINT images. We hereby reason that studies aiming for the distinction of monomers, dimers or tetramers are a feasible first step. However, high target molecule densities [32], pronounced unspecific binding of imager strands [85, 90] and the optical sectioning capabilities of the used microscope will be major challenges when applying lbFCS+ to cellular targets.

More generally, we demonstrated that lbFCS+ is capable of detecting/distinguishing small differences in imager/docking strand binding dynamics in nanoscopic volumes containing low numbers of molecules requiring only moderate measurement times on the order of tens of minutes. As such, it provides a highly-parallelized and easy-to-implement readout for potential on-chip bio-sensing applications. Especially interesting are applications requiring a direct detection of molecules in low concentration regimes without amplification steps [91, 92]. We want to highlight that the theoretical framework behind lbFCS+ is not limited to the study of DNA hybridization reactions, but can be applied to any reversible binding reaction of fluorescently-labeled

ligands to immobilized receptors.

Our investigations of the main factors influencing the association/dissociation rate of the imager/docking strand binding reaction included its dependency on sequence, temperature and ionic strength/composition, as presented in Chapter 3 & 5 and [79]. The precise control over the DNA-PAINT binding reaction gained via these preparatory studies finally allowed to positively answer **Question 3** with the development of a continuously fluorescent 1:1 labeling approach based on DNA-mediated fluorophore exchange - referred to as tracking handle (TH) - as presented in Chapter 4. It allowed to uninterruptedly monitor DNA-origami moving on SLBs over the course of tens of minutes under live cell compatible conditions.

Although Chapter 4 only focused on a *in vitro* reconstituted system, we believe that our labeling approach can be translated also to cellular targets, such as genetically-tagged [74, 98] membrane proteins with accessible extra-cellular modification sites. Along this way, it will become particularly important to assess and minimize unspecific binding of negatively charged imagers with extracellular components and to overcome the elevated background fluorescence currently limiting the tracking experiments to selective plane illumination schemes such as TIRF microscopy. An interesting solution to the stated obstacles would be the combination of the TH with recently proposed self-quenching fluorogenic imagers for DNA-PAINT [70]. Additionally, a peptide-based PAINT approach has been recently demonstrated inside living cells [72, 73], which could allow genetic engineering of a peptide-based TH for intracellular targets.

We reason that our DNA based labeling approach also bears potential regarding further technical developments. Even a single TH promotes binding of imagers of same sequence but labeled with spectrally distinct dyes. The simultaneous multi-color recording of an individual TH labeled target in a solution containing e.g. two spectrally distinct imagers would result in a single trajectory featuring 1) different step-like intensity levels according to the numbers of imagers bound to the TH and 2) a specific alternating color code enfolded into the detected intensity levels. While the sum of the signals in both color channels represents the complete recorded trajectory of one particle we believe that the specific intensity/color bar-code could be used for further analysis. This includes the distinction of trajectories at crossing points based on a statistical assessment of their specific intensity/color bar-code potentially allowing for increased target molecule densities and finally improved statistics. Following the same line, the specific intensity/color bar-code could also serve for the distinction of multimeric assemblies or getting additional information of the assembly process upon co-localization of trajectories. Finally, the demonstrated prolonged observation times achieved with the TH might open up new opportunities to detect the occurrence of spatiotemporal heterogeneities within the motion of individual diffusing particles or the classification of different diffusive modes [30].

In summary, we are confident that our thorough characterization of the reversible DNA hybridization reaction provides a solid base for the quantitative assessment of DNA-PAINT data. Additionally, our contributions for the design of novel labeling approaches based on the generalized concept of DNA-mediated fluorophore exchange will help future researchers to overcome current limitations in single-molecule microscopy.



**Part IV**  
**Appendix**





## Appendix to Chapter 5

## A.1 Supplementary Figures

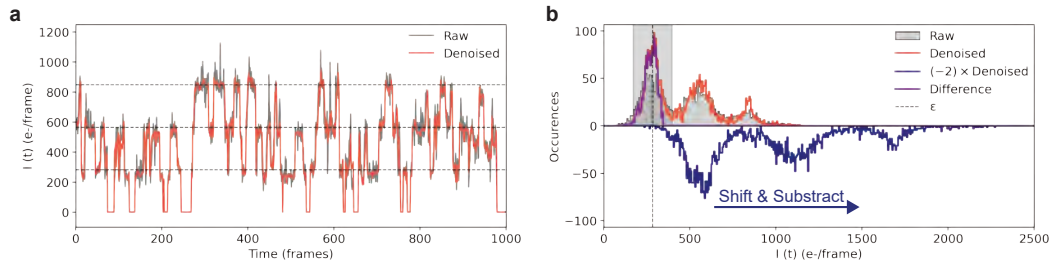


**Figure A.1. Intensity denoising and normalization.** (a) Exemplary raw intensity trace from a localization cluster from a data set containing  $N = 4$  DNA origami (grey). The intensity is given by the total number of photo-electrons contained in the fitted 2D Gaussian PSF during each single molecule localization event, i.e., (# photo-electrons)/frame. The intensity trace exhibits step-like behavior between three intensity levels due to varying numbers of imager strands that are bound to the origami at a given time (i.e., per frame). Smaller intensity fluctuations at each level are due to the noise induced by the camera electronics (readout noise) and due to the stochastic nature of the photon arrivals (shot noise). To regain a close to step-like behavior according to the number of simultaneously bound imagers, a non-linear de-noising filter [87] is applied to the raw intensity trace during analysis; the de-noised intensity trace is shown in red. The dashed lines correspond to multiples of the normalization value  $\epsilon$  as obtained by the following procedure. (b) Photo-electron intensity histograms as obtained from the raw intensity trace (grey) and de-noised intensity trace (red) as shown in (a) both feature three clearly distinguishable peaks, indicating that up to three imagers are bound simultaneously to the origami. The normalization process is based on the histogram of the de-noised intensity trace. Its general idea is to isolate the leftmost peak of the histogram in order to obtain the (cluster specific) intensity value corresponding to a single imager bound to the target. Therefore, the intensity values of the de-noised intensity trace are first multiplied by a factor of  $\times 2$  and the histogram is re-calculated maintaining the original bin size of the de-noised histogram. Subsequently the resulting bin heights are adjusted to approximately match the heights of the original histogram by multiplication with a factor of  $\times 1.5$ . Finally, multiplication of the bin heights with a factor of  $\times (-1)$  yields the ' $(-2) \times$  De-noised' histogram as shown in blue. Now, the ' $(-2) \times$  De-noised' histogram is subtracted from the original histogram (de-noised; red) and subsequently shifted one bin to the right. This 'Shift & Subtract' procedure is repeated  $\times 100$  yielding the difference histogram (turquoise) only consisting of the original leftmost peak. As a next step, all values in the original de-noised histogram not deviating more than 40 % to the median of the difference histogram are selected (light-grey interval). Finally, the intensity value  $\epsilon$  (dashed line) used for normalization is set to the median of the de-noised intensity values within the selected interval.

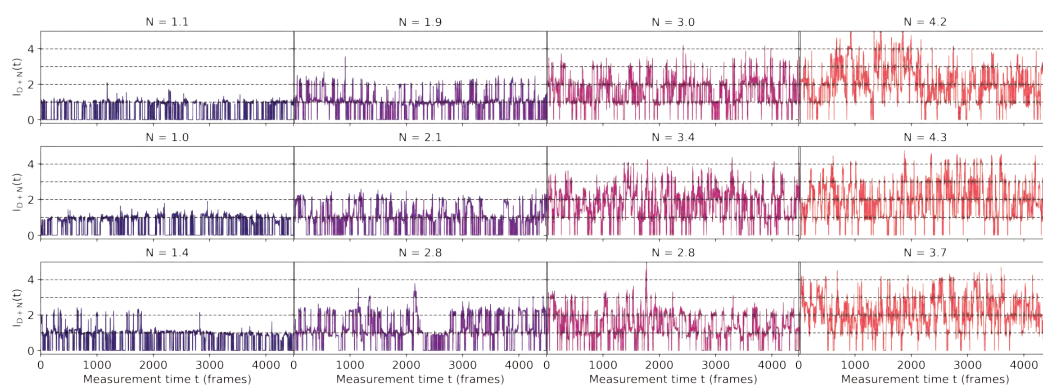


**Figure A.2. Exemplary intensity traces ( $N = 4$ ) corresponding to selected intervals in  $\hat{I}$ .** Exemplary de-noised and normalized intensity traces as obtained from  $N = 4$  origami according to the selected intervals in  $\hat{I}$  as depicted in the left panel of **Fig.5.2e** (i.e., same color code used for traces and intervals in  $\hat{I}$ ). The counting result  $N$  as obtained by lbFCS+ analysis is stated above each trace. As expected, observed intensity levels are located at unit-less integer values (i.e., 1, 2, 3, 4) after the normalization procedure (described in **Supplementary Fig.1** according to the current number of imagers bound to the DNA origami (dashed lines).

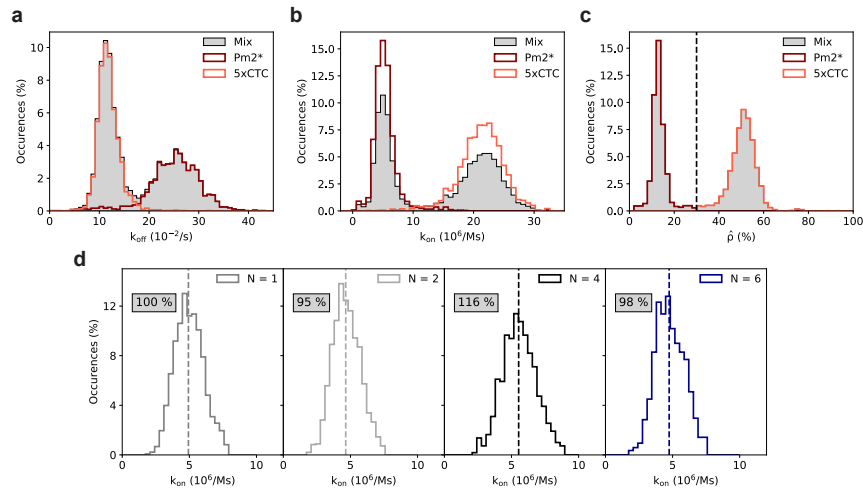


**Figure A.3. Calibration of  $k_{on}$  using Pm2\* reference origami.** (a) Resulting  $k_{off}$  distribution from a sample containing a mixture of origami with either a single (i.e.,  $N = 1$ ) 5xCTC docking strand or a single Pm2\* docking strand (calibration reference) imaged with the same imager Pm2 at a concentration of 5 nM (grey; ‘Mix’). Since imagers bind to Pm2\* docking strands with a higher  $k_{off}$  and lower  $k_{on}$  (due to a repetitive docking strand design, described in refs. [78, 81, 82, 85]) the individual distributions corresponding to either Pm2\* (dark red) or 5xCTC origami (orange) can be easily distinguished using the occupancy  $\hat{\rho}$ ; see (c). The mixed sample contained a total of # clusters = 4,076 with # clusters = 1,833 assigned to Pm2\*, and # clusters = 2,243 assigned to 5xCTC. (b) Same data and analogous analysis as in (a) but for the association rate  $k_{on}$ . (c) Illustration of the isolation of clusters based on the occupancy  $\hat{\rho}$  (dashed line), i.e.,  $\hat{\rho} < 30\%$  corresponds to Pm2\* origami (dark red) and  $\hat{\rho} > 30\%$  corresponds to 5xCTC origami (orange); as used in (a,b). (d) As described in Section 5.3.4 each of the samples shown in Fig.5.1a-d,f contained a subpopulation of Pm2\* reference origami in order to track pipetting errors of the imager concentration affecting the resulting  $k_{on} = \tilde{k}_{on}/c$ . We first isolated the Pm2\* clusters in each sample according to the procedure described in (a-c). Subsequently we compared the resulting median  $k_{on}$  (dashed line) of each subpopulation (same color code as in Fig.5.1a-d,f) to a fixed value of  $\overline{k_{on}} \equiv 5 \times 10^6$  1/Ms. In the final calibration step, the relative deviation of the median  $k_{on}$  for each Pm2\* subpopulation to  $\overline{k_{on}}$  (grey boxes) was then used to correct the  $k_{on}$  as obtained from the target 5xCTC  $N = 1, 2, 4, 6$  origami. Pm2\* reference origami subpopulations contained: # clusters = 1,330 for  $N = 1$ , # clusters = 1,920 for  $N = 2$ , # clusters = 1,098 for  $N = 4$ , # clusters = 845 for  $N = 6$ .

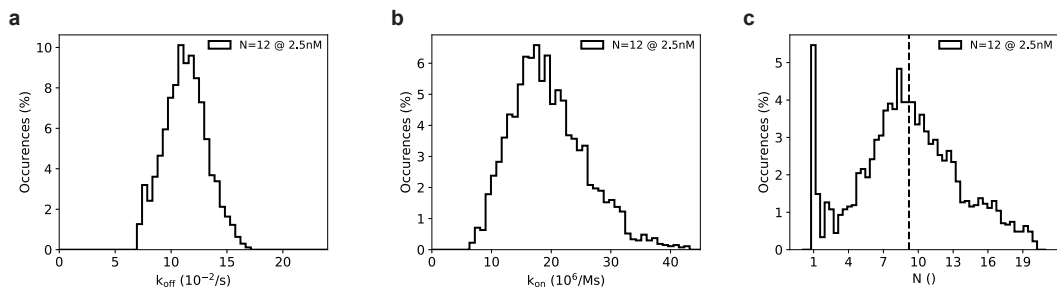


**Figure A.4. lbFCS+ results for  $N = 12$  origami measured at an imager concentration of 2.5 nM.** (a) lbFCS+ results for  $k_{off}$ . (b) lbFCS+ results for  $k_{on}$ . (c) lbFCS+ results for  $N$ . Based on a mean of  $\langle N \rangle = 9.2$  (dashed line) we estimated an average incorporation efficiency of 77% (in good agreement with [74]). Data shown in (a,b,c) contained a total of # clusters = 2,689.

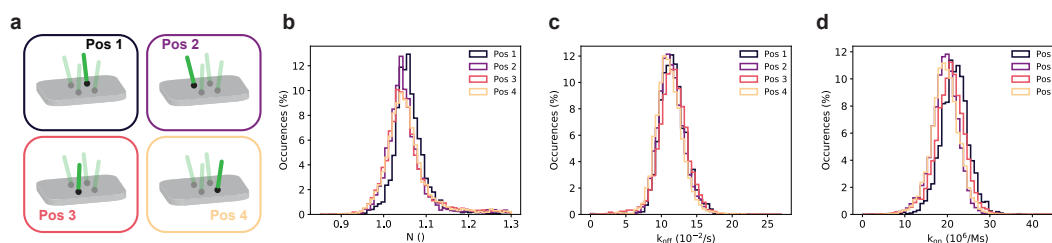


**Figure A.5. Control for position dependency of  $k_{\text{off}}$  &  $k_{\text{on}}$ .** (a) To check for position dependent hybridization rates we folded DNA origami each containing only one of the four docking strands (i.e.,  $N = 1$ ) at every position used for the  $N = 4$  origami (Pos1-4; transparent docking strands indicate other  $N = 4$  positions). (b) Corresponding lbFCS+ results for  $N$  for all origami shown in (a) agree with the expected  $N = 1$ . (c) Corresponding lbFCS+ results for  $k_{\text{off}}$  for all origami shown in (a) did not indicate any position dependent alteration of  $k_{\text{off}}$ . (d) Corresponding lbFCS+ results for  $k_{\text{on}}$  for all origami shown in (a) did not indicate any position dependent alteration of  $k_{\text{on}}$ . Data shown in (b,c,d) contained # clusters = 1,994 for Pos1, # clusters = 3,188 for Pos2, # clusters = 6,428 for Pos3, # clusters = 5,680 for Pos4.

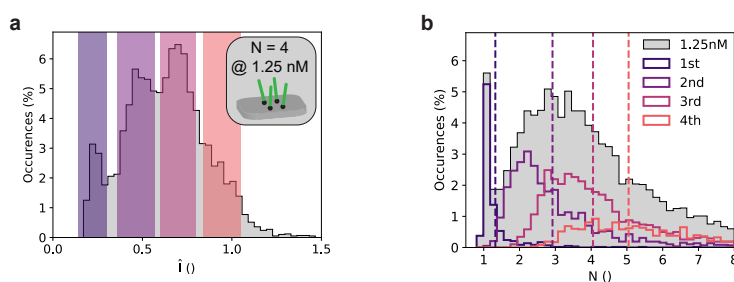


**Figure A.6. Selection of intervals in  $\hat{I}$  for  $N = 4$  origami measured at imager concentration of 1.25 nM.** (a) Selection of intervals in  $\hat{I}$ , analogous to the left panels of Fig.5.2e and Fig.5.3c. (b) Inspection of the counting results for clusters corresponding to the selected intervals in  $\hat{I}$  as shown in (a), analogous to the right panels of Fig.5.2e and Fig.5.3c. Data shown in (a,b) contained # clusters = 5,834.

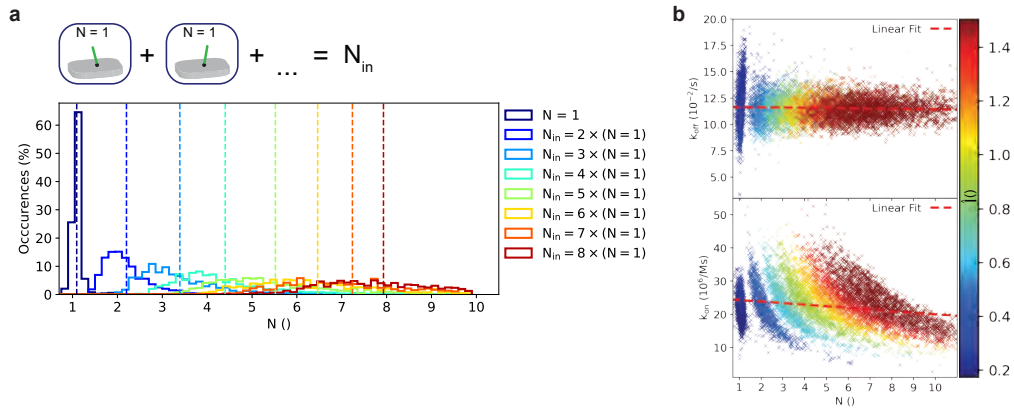


**Figure A.7. Computational combination of  $N = 1$  clusters measured at imager concentration of 1.25 nM.** (a) lbFCS+ counting results obtained from computationally regrouped clusters consisting of up to eight experimental  $N = 1$  clusters measured at an imager concentration of 1.25 nM (i.e.,  $N_{in} = k \times (N = 1)$  up to  $k = 8$ ; # clusters = 1,000 for each  $N_{in}$ ), analogous to Fig.5.3a. (b)  $k_{off}$  &  $k_{on}$  vs.  $N$  scatter plot (color coded by  $\hat{I}$ ) and linear fit (red dashed line) of the same data as shown in (a), analogous to the left panels of Fig.5.3b. Data shown in (b) contained a total of # clusters = 8,648.

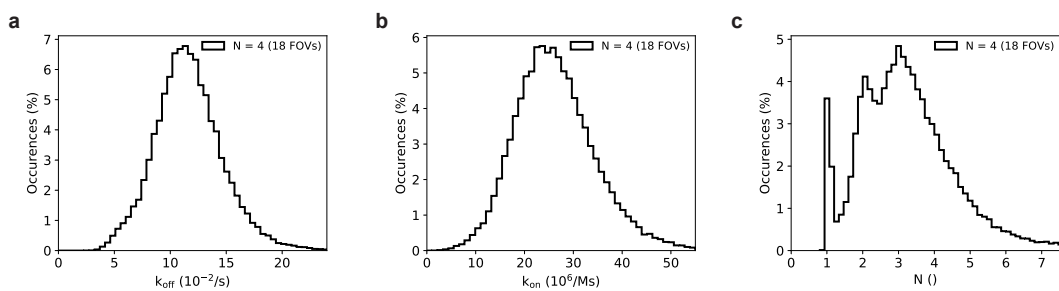


**Figure A.8. Quantitative imaging of 18 FOVs in 3 h.** (a) lbFCS+ results for  $k_{off}$  as obtained from a total of 18 FOVs of a sample containing  $N = 4$  origami (total # clusters = 48,966). Each FOV was measured for 1500 frames (i.e., 10 min) leading to a total of 3 h of measurement time for all 18 FOVs. (b) Same as (a) but for  $k_{on}$ . We want to highlight that this sample did not contain a subpopulation of Pm2\* origami used for calibration of  $k_{on}$ . (c) Same as (a) but for  $N$ .

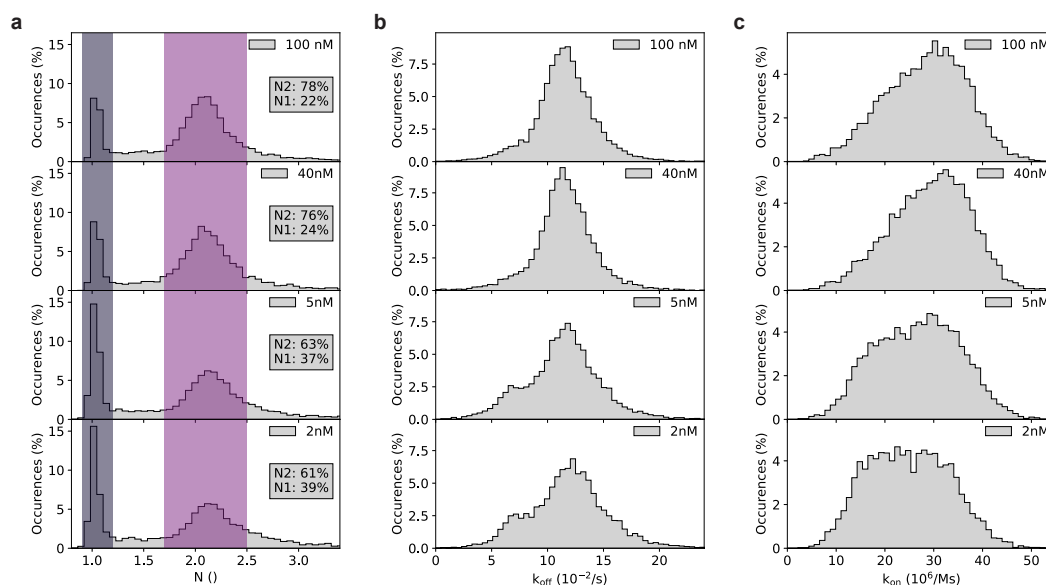


**Figure A.9. 2xLink origami incubated with varying linker strand concentrations.** (a) lbFCS+ counting results for 2xLink origami incubated for 3 min at linker strand concentrations  $c = 100$  nM, 40 nM, 5 nM, 2 nM prior to imaging. We selected 2xLink origami yielding  $0.9 < N < 1.2$  corresponding to the  $N = 1$  configurations (left colored interval) as shown in the blue box of Fig.5.4e, and 2xLink origami yielding  $1.7 < N < 2.5$  corresponding to the  $N = 2$  configuration (right colored interval) as shown in the dark-red box of Fig.5.4e. The grey boxes indicate the ratio of 2xLink origami found in either a  $N = 1$  or  $N = 2$  state (normalized to the total of origami in a  $N = 1$  or  $N = 2$  state). (b) lbFCS+ result for  $k_{off}$  for the same data as shown in (a). (c) lbFCS+ result for  $k_{on}$  for the same data as shown in (a). Data shown in (a,b,c) contained # clusters = 9,372 for 100 nM, # clusters = 5,625 for 40 nM, # clusters = 6,709 for 5 nM, # clusters = 5,298 for 2 nM.

## A.2 Supplementary Tables

**Table A.1. Detailed imaging conditions.** For all presented data the exposure time was set to 400 ms corresponding to the image acquisition duty cycle (see Section 5.3.5). 'Pm2\*' indicates if the sample contained - besides the target 5xCTC origami - a Pm2\* ( $N = 1$ ) origami subpopulation for calibration of  $k_{on}$  (see Section 5.3.4). In case of 'Link' and '2xLink' origami the given concentration indicates the concentration of linker strands during the the 3 min incubation time prior to imaging.

Figure	Sample	Pm2*	Imager conc. (nM)	Irradiance ( $W/cm^2$ )	Frames
Fig.5.2 Fig.5.3b (right panel) SI_Fig.A.3	N = 1,2,4,6	Yes	5	10	4500
SI_Fig.A.1 SI_Fig.A.2 Fig.5.3d,e	N = 4	Yes	5	10	4500
Fig.5.3a Fig.5.3b (left panel)	N = 1, regrouped	Yes	5	10	4500
SI_Fig.A.4	N = 12	Yes	2.5	10	4500
SI_Fig.A.5	N = 1, Pos1-4	Yes	5	10	4500
Fig.5.3c Fig.5.3d,e	N = 4	Yes	2.5	10	4500
SI_Fig.A.6 Fig.5.3d,e	N = 4	Yes	1.25	10	4500
SI_Fig.A.7	N = 1, regrouped	No	1.25	10	4500
Fig.5.3f,g,h	N=4	Yes	5	10	4500 2250 1125 600
SI_Fig.A.8	N = 4, 18 FOVs	No	5	10	1500
Fig.5.4b,c,d	N=1, Direct Link, 100 nM Direct + Link	Yes	10 10 5	10	4500
Fig.5.4f,g,h,i SI_Fig.A.9	2xLink, 100 nM 2xLink, 40 nM 2xLink, 5 nM 2xLink, 2 nM	Yes	5	10	4500

# List of Figures

1.1	Concept of single molecule localization. . . . .	4
1.2	DNA-mediated fluorophore exchange in DNA-PAINT. . . . .	9
5.1	Absolute counting of molecular copy numbers in a single DNA-PAINT experiment. . . . .	113
5.2	Proof-of-principle demonstration on DNA origami. . . . .	117
5.3	Assessing the working range of lbFCS+. . . . .	119
5.4	Distinction of nanoscopic DNA assemblies via binding dynamics. . . . .	125
A.1	Intensity denoising and normalization. . . . .	134
A.2	Exemplary intensity traces ( $N = 4$ ) corresponding to selected intervals in $\hat{I}$ . . . . .	135
A.3	Calibration of $k_{\text{on}}$ using Pm2* reference origami. . . . .	136
A.4	lbFCS+ results for $N = 12$ origami measured at an imager concentration of 2.5 nM. . . . .	136
A.5	Control for position dependency of $k_{\text{off}}$ & $k_{\text{on}}$ . . . . .	137
A.6	Selection of intervals in $\hat{I}$ for $N = 4$ origami measured at imager concentration of 1.25 nM. . . . .	137
A.7	Computational combination of $N = 1$ clusters measured at imager concentration of 1.25 nM. . . . .	138
A.8	Quantitative imaging of 18 FOVs in 3 h. . . . .	138
A.9	2xLink origami incubated with varying linker strand concentrations. . . . .	139

## LIST OF FIGURES

---

# List of Tables

A.1 Detailed imaging conditions. . . . . 140

## LIST OF TABLES

---

## List of Abbreviations

DIC	Differential Interference Contrast Microscopy
FCS	Fluorescence Correlation Spectroscopy
FOV	field of view
FRET	Förster Resonance Energy Transfer
HILO	Highly Inclined and Laminated Optical Sheet
lbFCS	localization-based Fluorescence Correlation Spectroscopy
PAINT	Points Accumulation for Imaging in Nanoscale Topography
PALM	Photoactivated Localization Microscopy
PSF	point-spread function
QD	quantum dot
qPAINT	quantitative PAINT
SDCM	Spinning Disc Confocal Microscopy
SLB	supported lipid bilayer
SMLM	Single-Molecule Localization Microscopy
SNR	signal-to-noise ratio
SPIM	Selective Plane Illumination Microscopy
SPT	Single Particle Tracking
SR	super-resolution
STORM	Stochastic Optical Reconstruction Microscopy
TH	tracking handle
TIRF	Total Internal Reflection Fluorescence

LIST OF ABBREVIATIONS

---

# Bibliography

1. Lichtman, J. W. & Conchello, J.-A. Fluorescence microscopy. *Nat. Methods* **2**, 910–919 (2005) (cit. on p. 3).
2. Shendure, J. & Ji, H. Next-generation DNA sequencing. *Nat. Biotechnol.* **26**, 1135–1145 (2008) (cit. on p. 3).
3. Lazcka, O., Campo, F. J. D. & Muñoz, F. X. Pathogen detection: A perspective of traditional methods and biosensors. *Biosens. Bioelectron.* **22**, 1205–1217 (2007) (cit. on p. 3).
4. Hall, M. D., Yasgar, A., Peryea, T., Braisted, J. C., Jadhav, A., Simeonov, A. & Coussens, N. P. Fluorescence polarization assays in high-throughput screening and drug discovery: a review. *Methods Appl. Fluoresc.* **4**, 22001 (2016) (cit. on p. 3).
5. Daniai, J. S. H., Aguib, Y. & Yacoub, M. H. Advanced fluorescence microscopy techniques for the life sciences. *eng. Glob. Cardiol. Sci. & Pract.* **2016**, e201616–e201616 (June 2016) (cit. on p. 3).
6. Suzuki, T., Matsuzaki, T., Hagiwara, H., Aoki, T. & Takata, K. Recent Advances in Fluorescent Labeling Techniques for Fluorescence Microscopy. *ACTA Histochem. Cytochem.* **40**, 131–137 (2007) (cit. on p. 3).
7. Diederich, B., Lachmann, R., Carlstedt, S., Marsikova, B., Wang, H., Uwurukundo, X., Mosig, A. S. & Heintzmann, R. A versatile and customizable low-cost 3D-printed open standard for microscopic imaging. *Nat. Commun.* **11**, 5979 (2020) (cit. on p. 3).
8. McDole, K., Guignard, L., Amat, F., Berger, A., Malandain, G., Royer, L. A., Turaga, S. C., Branson, K. & Keller, P. J. In Toto Imaging and Reconstruction of Post-Implantation Mouse Development at the Single-Cell Level. *Cell* **175**, 859–876.e33 (Oct. 2018) (cit. on p. 3).
9. Schwille, P., Meyer-Almes, F. J. & Rigler, R. Dual-color fluorescence cross-correlation spectroscopy for multicomponent diffusional analysis in solution. *Biophys. J.* **72**, 1878–1886 (1997) (cit. on p. 3).
10. Bacia, K., Kim, S. A. & Schwille, P. Fluorescence cross-correlation spectroscopy in living cells. *Nat. Methods* **3**, 83–89 (2006) (cit. on p. 3).
11. Waters, J. C. Accuracy and precision in quantitative fluorescence microscopy. *J. Cell Biol.* **185**, 1135–1148 (June 2009) (cit. on p. 3).
12. Hell, S. W. & Wichmann, J. Breaking the diffraction resolution limit by stimulated emission: stimulated-emission-depletion fluorescence microscopy. *Opt. Lett.* **19**, 780–782 (1994) (cit. on pp. 4, 110).
13. Klar, T. A., Jakobs, S., Dyba, M., Egner, A. & Hell, S. W. Fluorescence microscopy with diffraction resolution barrier broken by stimulated emission. *Proc. Natl. Acad. Sci.* **97**, 8206 LP –8210 (July 2000) (cit. on pp. 4, 110).

## BIBLIOGRAPHY

---

14. Betzig, E., Patterson, G. H., Sougrat, R., Lindwasser, O. W., Olenych, S., Bonifacino, J. S., Davidson, M. W., Lippincott-Schwartz, J. & Hess, H. F. Imaging Intracellular Fluorescent Proteins at Nanometer Resolution. *Science* (80-. ). **313**, 1642 LP –1645 (Sept. 2006) (cit. on pp. 4, 7, 110).
15. Rust, M. J., Bates, M. & Zhuang, X. Sub-diffraction-limit imaging by stochastic optical reconstruction microscopy (STORM). *Nat. Methods* **3**, 793–796 (2006) (cit. on pp. 4, 7, 110).
16. Hess, S. T., Girirajan, T. P. K. & Mason, M. D. Ultra-High Resolution Imaging by Fluorescence Photoactivation Localization Microscopy. *Biophys. J.* **91**, 4258–4272 (2006) (cit. on pp. 4, 7, 110).
17. Sharonov, A. & Hochstrasser, R. M. Wide-field subdiffraction imaging by accumulated binding of diffusing probes. *Proc. Natl. Acad. Sci.* **103**, 18911 LP –18916 (Dec. 2006) (cit. on pp. 4, 8, 110).
18. Heilemann, M., van de Linde, S., Schüttpelz, M., Kasper, R., Seefeldt, B., Mukherjee, A., Tinnefeld, P. & Sauer, M. Subdiffraction-Resolution Fluorescence Imaging with Conventional Fluorescent Probes. *Angew. Chemie Int. Ed.* **47**, 6172–6176 (Aug. 2008) (cit. on pp. 4, 7, 110).
19. Jungmann, R., Steinhauer, C., Scheible, M., Kuzyk, A., Tinnefeld, P. & Simmel, F. C. Single-Molecule Kinetics and Super-Resolution Microscopy by Fluorescence Imaging of Transient Binding on DNA Origami. *Nano Lett.* **10**, 4756–4761 (Nov. 2010) (cit. on pp. 4, 8, 9, 110, 111).
20. Schnitzbauer, J., Strauss, M. T., Schlichthaerle, T., Schueder, F. & Jungmann, R. Super-resolution microscopy with DNA-PAINT. *Nat. Protoc.* **12**, 1198–1228 (2017) (cit. on pp. 4, 8, 110, 111, 115).
21. Schermelleh, L., Ferrand, A., Huser, T., Eggeling, C., Sauer, M., Biehlmaier, O. & Drummen, G. P. C. Super-resolution microscopy demystified. *Nat. Cell Biol.* **21**, 72–84 (2019) (cit. on p. 4).
22. Patterson, G., Davidson, M., Manley, S. & Lippincott-Schwartz, J. Superresolution Imaging using Single-Molecule Localization. *Annu. Rev. Phys. Chem.* **61**, 345–367 (Mar. 2010) (cit. on pp. 4, 5).
23. Gelles, J., Schnapp, B. J. & Sheetz, M. P. Tracking kinesin-driven movements with nanometre-scale precision. *Nature* **331**, 450–453 (1988) (cit. on p. 5).
24. Lelek, M., Gyparaki, M. T., Beliu, G., Schueder, F., Griffié, J., Manley, S., Jungmann, R., Sauer, M., Lakadamyali, M. & Zimmer, C. Single-molecule localization microscopy. *Nat. Rev. Methods Prim.* **1**, 39 (2021) (cit. on pp. 5, 10, 110, 111, 123, 128).
25. Betzig, E. Proposed method for molecular optical imaging. *Opt. Lett.* **20**, 237–239 (1995) (cit. on p. 5).
26. Mlodzianoski, M. J., Schreiner, J. M., Callahan, S. P., Smolková, K., Dlasková, A., Šantorová, J., Ježek, P. & Bewersdorf, J. Sample drift correction in 3D fluorescence photoactivation localization microscopy. *Opt. Express* **19**, 15009–15019 (2011) (cit. on p. 5).

- 
27. Wang, Y., Schnitzbauer, J., Hu, Z., Li, X., Cheng, Y., Huang, Z.-L. & Huang, B. Localization events-based sample drift correction for localization microscopy with redundant cross-correlation algorithm. *Opt. Express* **22**, 15982–15991 (2014) (cit. on p. 5).
  28. Nieuwenhuizen, R. P. J., Lidke, K. A., Bates, M., Puig, D. L., Grünwald, D., Stallinga, S. & Rieger, B. Measuring image resolution in optical nanoscopy. *Nat. Methods* **10**, 557–562 (2013) (cit. on p. 5).
  29. Banterle, N., Bui, K. H., Lemke, E. A. & Beck, M. Fourier ring correlation as a resolution criterion for super-resolution microscopy. *J. Struct. Biol.* **183**, 363–367 (2013) (cit. on p. 5).
  30. Manzo, C. & Garcia-Parajo, M. F. A review of progress in single particle tracking: from methods to biophysical insights. *Reports Prog. Phys.* **78**, 124601 (2015) (cit. on pp. 5, 7, 129).
  31. Chenouard, N., Smal, I., de Chaumont, F., Maška, M., Sbalzarini, I. F., Gong, Y., Cardinale, J., Carthel, C., Coraluppi, S., Winter, M., Cohen, A. R., Godinez, W. J., Rohr, K., Kalaidzidis, Y., Liang, L., Duncan, J., Shen, H., Xu, Y., Magnusson, K. E. G., Jaldén, J., Blau, H. M., Paul-Gilloteaux, P., Roudot, P., Kervrann, C., Waharte, F., Tinevez, J.-Y., Shorte, S. L., Willemse, J., Celler, K., van Wezel, G. P., Dan, H.-W., Tsai, Y.-S., de Solórzano, C. O., Olivo-Marin, J.-C. & Meijering, E. Objective comparison of particle tracking methods. *Nat. Methods* **11**, 281–289 (2014) (cit. on p. 6).
  32. Baddeley, D. & Bewersdorf, J. Biological Insight from Super-Resolution Microscopy: What We Can Learn from Localization-Based Images. *Annu. Rev. Biochem.* **87**, 965–989 (June 2018) (cit. on pp. 6, 7, 110, 123, 124, 128).
  33. Thompson, R. E., Larson, D. R. & Webb, W. W. Precise Nanometer Localization Analysis for Individual Fluorescent Probes. *Biophys. J.* **82**, 2775–2783 (2002) (cit. on pp. 6, 110).
  34. Demchenko, A. P. Photobleaching of organic fluorophores: quantitative characterization, mechanisms, protection. *Methods Appl. Fluoresc.* **8**, 22001 (2020) (cit. on pp. 6, 7, 110).
  35. Annibale, P., Vanni, S., Scarselli, M., Rothlisberger, U. & Radenovic, A. Quantitative Photo Activated Localization Microscopy: Unraveling the Effects of Photoblinking. *PLoS One* **6**, e22678 (July 2011) (cit. on pp. 7, 110).
  36. Annibale, P., Vanni, S., Scarselli, M., Rothlisberger, U. & Radenovic, A. Identification of clustering artifacts in photoactivated localization microscopy. *Nat. Methods* **8**, 527–528 (2011) (cit. on pp. 7, 110).
  37. Coltharp, C., Kessler, R. P. & Xiao, J. Accurate Construction of Photoactivated Localization Microscopy (PALM) Images for Quantitative Measurements. *PLoS One* **7**, e51725 (Dec. 2012) (cit. on pp. 7, 110).
  38. Lee, S.-H., Shin, J. Y., Lee, A. & Bustamante, C. Counting single photoactivatable fluorescent molecules by photoactivated localization microscopy (PALM). *Proc. Natl. Acad. Sci.* **109**, 17436 LP –17441 (Oct. 2012) (cit. on pp. 7, 110).

39. Puchner, E. M., Walter, J. M., Kasper, R., Huang, B. & Lim, W. A. Counting molecules in single organelles with superresolution microscopy allows tracking of the endosome maturation trajectory. *Proc. Natl. Acad. Sci.* **110**, 16015 LP–16020 (Oct. 2013) (cit. on pp. 7, 110).
40. Nan, X., Collisson, E. A., Lewis, S., Huang, J., Tamgüney, T. M., Liphardt, J. T., McCormick, F., Gray, J. W. & Chu, S. Single-molecule superresolution imaging allows quantitative analysis of RAF multimer formation and signaling. *Proc. Natl. Acad. Sci.* **110**, 18519 LP–18524 (Nov. 2013) (cit. on pp. 7, 110).
41. Ehmman, N., van de Linde, S., Alon, A., Ljaschenko, D., Keung, X. Z., Holm, T., Rings, A., DiAntonio, A., Hallermann, S., Ashery, U., Heckmann, M., Sauer, M. & Kittel, R. J. Quantitative super-resolution imaging of Bruchpilot distinguishes active zone states. *Nat. Commun.* **5**, 4650 (2014) (cit. on pp. 7, 110).
42. Rollins, G. C., Shin, J. Y., Bustamante, C. & Pressé, S. Stochastic approach to the molecular counting problem in superresolution microscopy. *Proc. Natl. Acad. Sci.* **112**, E110 LP–E118 (Jan. 2015) (cit. on pp. 7, 110).
43. Fricke, F., Beaudouin, J., Eils, R. & Heilemann, M. One, two or three? Probing the stoichiometry of membrane proteins by single-molecule localization microscopy. *Sci. Rep.* **5**, 14072 (2015) (cit. on pp. 7, 110).
44. Ricci, M. A., Manzo, C., García-Parajo, M. F., Lakadamyali, M. & Cosma, M. P. Chromatin Fibers Are Formed by Heterogeneous Groups of Nucleosomes In Vivo. *Cell* **160**, 1145–1158 (2015) (cit. on pp. 7, 110).
45. Hummer, G., Fricke, F. & Heilemann, M. Model-independent counting of molecules in single-molecule localization microscopy. *Mol. Biol. Cell* **27**, 3637–3644 (July 2016) (cit. on pp. 7, 110).
46. Laplante, C., Huang, F., Tebbs, I. R., Bewersdorf, J. & Pollard, T. D. Molecular organization of cytokinesis nodes and contractile rings by super-resolution fluorescence microscopy of live fission yeast. *Proc. Natl. Acad. Sci.* **113**, E5876 LP–E5885 (Oct. 2016) (cit. on pp. 7, 110).
47. Nino, D., Rafiei, N., Wang, Y., Zilman, A. & Milstein, J. N. Molecular Counting with Localization Microscopy: A Bayesian Estimate Based on Fluorophore Statistics. *Biophys. J.* **112**, 1777–1785 (2017) (cit. on pp. 7, 110).
48. Nicovich, P. R., Owen, D. M. & Gaus, K. Turning single-molecule localization microscopy into a quantitative bioanalytical tool. *Nat. Protoc.* **12**, 453–460 (2017) (cit. on pp. 7, 110, 123, 128).
49. Golfetto, O., Wakefield, D. L., Cacao, E. E., Avery, K. N., Kenyon, V., Jorand, R., Tobin, S. J., Biswas, S., Gutierrez, J., Clinton, R., Ma, Y., Horne, D. A., Williams, J. C. & Jovanović-Talisman, T. A Platform To Enhance Quantitative Single Molecule Localization Microscopy. *J. Am. Chem. Soc.* **140**, 12785–12797 (Oct. 2018) (cit. on pp. 7, 110).
50. Pinaud, F., Clarke, S., Sittner, A. & Dahan, M. Probing cellular events, one quantum dot at a time. *Nat. Methods* **7**, 275–285 (2010) (cit. on p. 7).
51. Nirmal, M., Dabbousi, B. O., Bawendi, M. G., Macklin, J. J., Trautman, J. K., Harris, T. D. & Brus, L. E. Fluorescence intermittency in single cadmium selenide nanocrystals. *Nature* **383**, 802–804 (1996) (cit. on p. 7).

- 
52. Kuno, M., Fromm, D. P., Hamann, H. F., Gallagher, A. & Nesbitt, D. J. Nonexponential “blinking” kinetics of single CdSe quantum dots: A universal power law behavior. *J. Chem. Phys.* **112**, 3117–3120 (Feb. 2000) (cit. on p. 7).
  53. Qian, H., Sheetz, M. P. & Elson, E. L. Single particle tracking. Analysis of diffusion and flow in two-dimensional systems. *Biophys. J.* **60**, 910–921 (1991) (cit. on p. 7).
  54. Michalet, X. Mean square displacement analysis of single-particle trajectories with localization error: Brownian motion in an isotropic medium. *Phys. Rev. E* **82**, 41914 (Oct. 2010) (cit. on p. 7).
  55. Shen, H., Tauzin, L. J., Baiyasi, R., Wang, W., Moringo, N., Shuang, B. & Landes, C. F. Single Particle Tracking: From Theory to Biophysical Applications. *Chem. Rev.* **117**, 7331–7376 (June 2017) (cit. on p. 7).
  56. Giannone, G., Hosy, E., Levet, F., Constals, A., Schulze, K., Sobolevsky, A. I., Rosconi, M. P., Gouaux, E., Tampé, R., Choquet, D. & Cognet, L. Dynamic Superresolution Imaging of Endogenous Proteins on Living Cells at Ultra-High Density. *Biophys. J.* **99**, 1303–1310 (2010) (cit. on pp. 8, 10).
  57. Thompson, N. L., Burghardt, T. P. & Axelrod, D. Measuring surface dynamics of biomolecules by total internal reflection fluorescence with photobleaching recovery or correlation spectroscopy. *Biophys. J.* **33**, 435–454 (1981) (cit. on pp. 8, 127).
  58. Tokunaga, M., Imamoto, N. & Sakata-Sogawa, K. Highly inclined thin illumination enables clear single-molecule imaging in cells. *Nat. Methods* **5**, 159–161 (2008) (cit. on p. 8).
  59. Adams, M. C., Salmon, W. C., Gupton, S. L., Cohan, C. S., Wittmann, T., Prigozhina, N. & Waterman-Storer, C. M. A high-speed multispectral spinning-disk confocal microscope system for fluorescent speckle microscopy of living cells. *Methods* **29**, 29–41 (2003) (cit. on p. 8).
  60. Hosny, N. A., Song, M., Connelly, J. T., Ameer-Beg, S., Knight, M. M. & Wheeler, A. P. Super-Resolution Imaging Strategies for Cell Biologists Using a Spinning Disk Microscope. *PLoS One* **8**, e74604 (Oct. 2013) (cit. on p. 8).
  61. Huisken, J., Swoger, J., Del Bene, F., Wittbrodt, J. & Stelzer, E. H. K. Optical Sectioning Deep Inside Live Embryos by Selective Plane Illumination Microscopy. *Science (80-. )*. **305**, 1007 LP –1009 (Aug. 2004) (cit. on p. 8).
  62. Cella Zanacchi, F., Lavagnino, Z., Perrone Donnorso, M., Del Bue, A., Furia, L., Faretta, M. & Diaspro, A. Live-cell 3D super-resolution imaging in thick biological samples. *Nat. Methods* **8**, 1047–1049 (2011) (cit. on p. 8).
  63. Dai, M., Jungmann, R. & Yin, P. Optical imaging of individual biomolecules in densely packed clusters. *Nat. Nanotechnol.* **11**, 798–807 (2016) (cit. on p. 9).
  64. Mücksch, J., Blumhardt, P., Strauss, M. T., Petrov, E. P., Jungmann, R. & Schwille, P. Quantifying Reversible Surface Binding via Surface-Integrated Fluorescence Correlation Spectroscopy. *Nano Lett.* **18**, 3185–3192 (May 2018) (cit. on pp. 9, 12, 115).
  65. Jungmann, R., Avendaño, M. S., Dai, M., Woehrstein, J. B., Agasti, S. S., Feiger, Z., Rodal, A. & Yin, P. Quantitative super-resolution imaging with qPAINT. *Nat. Methods* **13**, 439–442 (2016) (cit. on pp. 10, 110).
-

66. Schueder, F., Strauss, M. T., Hoerl, D., Schnitzbauer, J., Schlichthaerle, T., Strauss, S., Yin, P., Harz, H., Leonhardt, H. & Jungmann, R. Universal Super-Resolution Multiplexing by DNA Exchange. *Angew. Chemie Int. Ed.* **56**, 4052–4055 (Mar. 2017) (cit. on p. 10).
67. Agasti, S. S., Wang, Y., Schueder, F., Sukumar, A., Jungmann, R. & Yin, P. DNA-barcoded labeling probes for highly multiplexed Exchange-PAINT imaging. *Chem. Sci.* **8**, 3080–3091 (2017) (cit. on p. 10).
68. Auer, A., Strauss, M. T., Schlichthaerle, T. & Jungmann, R. Fast, Background-Free DNA-PAINT Imaging Using FRET-Based Probes. *Nano Lett.* **17**, 6428–6434 (Oct. 2017) (cit. on p. 10).
69. Lee, J., Park, S., Kang, W. & Hohng, S. Accelerated super-resolution imaging with FRET-PAINT. *Mol. Brain* **10**, 63 (2017) (cit. on p. 10).
70. Chung, K. K. H., Zhang, Z., Kidd, P., Zhang, Y., Williams, N. D., Rollins, B., Yang, Y., Lin, C., Baddeley, D. & Bewersdorf, J. Fluorogenic probe for fast 3D whole-cell DNA-PAINT. *bioRxiv*, 2020.04.29.066886 (Jan. 2020) (cit. on pp. 10, 129).
71. Schueder, F., Lara-Gutiérrez, J., Haas, D., Beckwith, K. S., Yin, P., Ellenberg, J. & Jungmann, R. Super-Resolution Spatial Proximity Detection with Proximity-PAINT. *Angew. Chemie Int. Ed.* **60**, 716–720 (Jan. 2021) (cit. on p. 10).
72. Oi, C., Gidden, Z., Holyoake, L., Kantelberg, O., Mochrie, S., Horrocks, M. H. & Regan, L. LIVE-PAINT allows super-resolution microscopy inside living cells using reversible peptide-protein interactions. *Commun. Biol.* **3**, 458 (2020) (cit. on pp. 10, 129).
73. Eklund, A. S., Ganji, M., Gavins, G., Seitz, O. & Jungmann, R. Peptide-PAINT Super-Resolution Imaging Using Transient Coiled Coil Interactions. *Nano Lett.* **20**, 6732–6737 (Sept. 2020) (cit. on pp. 10, 129).
74. Strauss, S., Nickels, P. C., Strauss, M. T., Jimenez Sabinina, V., Ellenberg, J., Carter, J. D., Gupta, S., Janjic, N. & Jungmann, R. Modified aptamers enable quantitative sub-10-nm cellular DNA-PAINT imaging. *Nat. Methods* **15**, 685–688 (2018) (cit. on pp. 10, 116, 117, 129, 136).
75. Wade, O., Woehrstein, J., Nickels, P., Strauss, S., Stehr, F., Stein, J., Schueder, F., Strauss, M., Ganji, M., Schnitzbauer, J., Grabmayr, H., Yin, P., Schwille, P. & Jungmann, R. 124-Color Super-resolution Imaging by Engineering DNA-PAINT Blinking Kinetics. *Nano Lett.* **19**. doi:[10.1021/acs.nanolett.9b00508](https://doi.org/10.1021/acs.nanolett.9b00508) (2019) (cit. on p. 11).
76. Blumhardt, P., Stein, J., Mücksch, J., Stehr, F., Bauer, J., Jungmann, R. & Schwille, P. Photo-Induced Depletion of Binding Sites in DNA-PAINT Microscopy 2018. doi:[10.3390/molecules23123165](https://doi.org/10.3390/molecules23123165) (cit. on pp. 11, 110, 112, 127, 128).
77. Stehr, F., Stein, J., Schueder, F., Schwille, P. & Jungmann, R. Flat-top TIRF illumination boosts DNA-PAINT imaging and quantification. *Nat. Commun.* **10**. doi:[10.1038/s41467-019-09064-6](https://doi.org/10.1038/s41467-019-09064-6) (2019) (cit. on pp. 11, 18, 110, 116).

- 
78. Stein, J., Stehr, F., Schueler, P., Blumhardt, P., Schueder, F., Mücksch, J., Jungmann, R. & Schwille, P. Toward Absolute Molecular Numbers in DNA-PAINT. *Nano Lett.* **19**. doi:[10.1021/acs.nanolett.9b03546](https://doi.org/10.1021/acs.nanolett.9b03546) (2019) (cit. on pp. 12, 46, 110–112, 115, 116, 118, 136).
  79. Schueder, F., Stein, J., Stehr, F., Auer, A., Sperl, B., Strauss, M., Schwille, P. & Jungmann, R. An order of magnitude faster DNA-PAINT imaging by optimized sequence design and buffer conditions. *Nat. Methods* **16**. doi:[10.1038/s41592-019-0584-7](https://doi.org/10.1038/s41592-019-0584-7) (2019) (cit. on pp. 12, 111, 128, 129).
  80. Schickingler, M., Zacharias, M. & Dietz, H. Tethered multifluorophore motion reveals equilibrium transition kinetics of single DNA double helices. *Proc. Natl. Acad. Sci.* **115**, E7512 LP –E7521 (Aug. 2018) (cit. on pp. 12, 111, 128).
  81. Strauss, S. & Jungmann, R. Up to 100-fold speed-up and multiplexing in optimized DNA-PAINT. *Nat. Methods* **17**, 789–791 (2020) (cit. on pp. 12, 110, 111, 116, 128, 136).
  82. Stehr, F., Stein, J., Bauer, J., Niederauer, C., Jungmann, R., Ganzinger, K. & Schwille, P. Tracking single particles for hours via continuous DNA-mediated fluorophore exchange. *Nat. Commun.* **12**, 4432 (2021) (cit. on pp. 12, 72, 112, 114, 116, 136).
  83. Stein, J., Stehr, F., Jungmann, R. & Schwille, P. Calibration free counting of low molecular copy numbers in single DNA-PAINT localization clusters. *bioRxiv*, 2021.08.17.456678 (Jan. 2021) (cit. on p. 109).
  84. Deschout, H., Znacchi, F. C., Mlodzianoski, M., Diaspro, A., Bewersdorf, J., Hess, S. T. & Braeckmans, K. Precisely and accurately localizing single emitters in fluorescence microscopy. *Nat. Methods* **11**, 253–266 (2014) (cit. on p. 110).
  85. Clowsley, A. H., Kaufhold, W. T., Lutz, T., Meletiou, A., Di Michele, L. & Soeller, C. Repeat DNA-PAINT suppresses background and non-specific signals in optical nanoscopy. *Nat. Commun.* **12**, 501 (2021) (cit. on pp. 111, 116, 124, 128, 136).
  86. Rothmund, P. W. K. Folding DNA to create nanoscale shapes and patterns. *Nature* **440**, 297–302 (2006) (cit. on p. 111).
  87. Chung, S. H. & Kennedy, R. A. Forward-backward non-linear filtering technique for extracting small biological signals from noise. *J. Neurosci. Methods* **40**, 71–86 (1991) (cit. on pp. 114, 134).
  88. Edelstein, A. D., Tsuchida, M. A., Amodaj, N., Pinkard, H., Vale, R. D. & Stuurman, N. Advanced methods of microscope control using  $\mu$ Manager software. *J. Biol. Methods* **1**, e10 (Nov. 2014) (cit. on p. 116).
  89. McInnes, L., Healy, J. & Astels, S. hdbscan: Hierarchical density based clustering. *J. Open Source Softw.* **2**, 205 (2017) (cit. on pp. 123, 125).
  90. Geertsema, H. J., Aimola, G., Fabricius, V., Fuerste, J. P., Kaufer, B. B. & Ewers, H. Left-handed DNA-PAINT for improved super-resolution imaging in the nucleus. *Nat. Biotechnol.* **39**, 551–554 (2021) (cit. on pp. 124, 128).
  91. Johnson-Buck, A., Li, J., Tewari, M. & Walter, N. G. A guide to nucleic acid detection by single-molecule kinetic fingerprinting. *Methods* **153**, 3–12 (2019) (cit. on pp. 124, 128).
-

92. Chatterjee, T., Knappik, A., Sandford, E., Tewari, M., Choi, S. W., Strong, W. B., Thrush, E. P., Oh, K. J., Liu, N., Walter, N. G. & Johnson-Buck, A. Direct kinetic fingerprinting and digital counting of single protein molecules. *Proc. Natl. Acad. Sci.* **117**, 22815 LP–22822 (Sept. 2020) (cit. on pp. 124, 128).
93. Qian, L. & Winfree, E. Scaling Up Digital Circuit Computation with DNA Strand Displacement Cascades. *Science (80-. )*. **332**, 1196 LP–1201 (June 2011) (cit. on p. 124).
94. Cherry, K. M. & Qian, L. Scaling up molecular pattern recognition with DNA-based winner-take-all neural networks. *Nature* **559**, 370–376 (2018) (cit. on p. 124).
95. Khaw, I., Croop, B., Tang, J., Möhl, A., Fuchs, U. & Han, K. Y. Flat-field illumination for quantitative fluorescence imaging. *Opt. Express* **26**, 15276–15288 (2018) (cit. on p. 127).
96. Sies, H. & Menck, C. F. M. Singlet oxygen induced DNA damage. *Mutat. Res.* **275**, 367–375 (1992) (cit. on p. 128).
97. Matter, B., Seiler, C. L., Murphy, K., Ming, X., Zhao, J., Lindgren, B., Jones, R. & Tretyakova, N. Mapping three guanine oxidation products along DNA following exposure to three types of reactive oxygen species. *Free Radic. Biol. Med.* **121**, 180–189 (2018) (cit. on p. 128).
98. Schlichthaerle, T., Strauss, M. T., Schueder, F., Auer, A., Nijmeijer, B., Kueblbeck, M., Jimenez Sabinina, V., Thevathasan, J. V., Ries, J., Ellenberg, J. & Jungmann, R. Direct Visualization of Single Nuclear Pore Complex Proteins Using Genetically-Encoded Probes for DNA-PAINT. *Angew. Chemie Int. Ed.* **58**, 13004–13008 (Sept. 2019) (cit. on p. 129).

# Acknowledgements

Although I am obliged to place only my name on the cover page of this thesis it would not exist without the support, advice, encouragement and humor of numerous people that have accompanied me during my PhD over the past years.

*Prof. Petra Schwille:* First of all, I would like to thank you for making all of this possible. I deeply appreciate it, that you gave me the freedom and trust to follow my own ideas as a 'fully-grown' researcher, although they were not always completely in line with the agenda of the lab. I have seen many labs during the course of my PhD but none of these was better equipped than ours! All of this allowed me to learn a lot, both scientifically and personally, and I want to thank you for that.

*Prof. Ralf Jungmann:* Thank you for all your input and advice in many perspectives. Without you and the help of your group especially the start into my PhD life would not have been so easy. But also in later projects you always connected me to other researchers bringing in new perspectives and opportunities. It was a pleasure working together with you on all our joint projects.

*Johannes Stein:* It was love at first sight on our first 'working' day at the group retreat on the Zugspitze, a good start. Since then we have been a team in all of our PhD projects, nicknamed 'FloHansi' from the rest of the lab as an expression for the symbiotic nature of our collaboration. While our complementary skills and mutual trust made almost every project a success it was also always a lot of fun to work together since we could laugh about the same bad kind of humor. I have learned a lot from you both in tough times and moments full of joy. I am extremely grateful to have found in you such a close friend.

*Florian Schüder:* We bumped into each other on the first day at LMU and have been friends since then. We traveled together, teamed up to study for tough exams, climbed mountains, had endless discussions about physics and everything else and finally even ended up to do our PhD at the same institute, working again together on joint projects. There is no way to express more than ten years of 'Florri' in a few sentences, I thank you for everything.

*Julian Bauer and Patrick Schüler:* Thank you for spending your master projects with us and for your contributions to the joint publications. You have been patient with us as 'supervisors' allowing us to learn what it means to take this role. Above all, we had a lot of fun with you researching, skiing, partying or just enjoying 4 kg of delicious Mensa food together during lunch.

*Philipp Blumhardt and Jonas Mücksch:* Thank you for introducing us to the 'Schwillies', sharing your know-how, your sincere feedback and your scientific advice. You kept a 'physics attitude' alive in our group and we tried to keep up with it after you left.

*Alexander Auer, Thomas Schlichthärle, Maximilian Strauss, Kimberly Cramer, Sebastian Strauss, Kimbu Wade, Philipp Nickels and Alexandra Eklund:* Thank you for always being available for help, for sharing your know-how as well as for your experimental support during our collaborations.

*Kristina Ganzinger and Christian Niederauer:* Thank you for your input and help during

the joint work on single particle tracking that was finally published after a year of constant struggle.

*Jan-Hagen Krohn and Yusuf Qutbuddin*: Thank you for taking over in such a smooth way, keep the spirit alive!

*Peter Schultz and Frederik Steiert*: Thank you for the pleasant atmosphere in our little desk corner.

*Henri Franquelim*: Thank you for your valuable help and support on anything regarding DNA origami, lipids and membranes.

*Beatrice Ramm, Tamara Heermann*: Thank you for your valuable help and support on anything regarding Mins and SLBs.

*Silke Leuze-Bütün*: Thank you for your unbeatable administrative support regarding all aspects of the scientific life and for taking great care of the people in the lab.

*Frank Siedler, Thomas Weidemann and Helge Vogl*: Thank you for your endless efforts in keeping the lab well-running, safe and functioning.

*Sigrid Bauer and Katharina Nakel*: Thank you for your valuable help regarding chemicals, buffers and DNA origami purification.

Finally, a huge thank you to the whole *Schwille department*.

I am very grateful that I was associated with the *Graduate School of Quantitative Biosciences Munich (QBM)* that organized retreats at amazing locations and introductory courses and provided additional budget for conferences and workshops.

I have also been fortunate to be associated with the *Center for NanoScience* and would like to thank *Susanne Hennig* and *Claudia Leonhardt* for all their efforts in organizing fun, helpful and very interesting scientific events.

Besides the invaluable scientific support, I am deeply thankful to my all my friends who have accompanied me during the inevitable ups and downs of this endeavor.

I am also very thankful to all the musicians I had the opportunity to play with during my PhD since they always helped me to get out of the scientific bubble and back to the rhythm of life. Special thanks to the *AGV Bigband* and *Toller*.

I am very grateful for the love and support from my family *Birgit, Hubert* and *Alexander* and from my 'extended' family *Martina* and *Berthold*.

Finally, I want to thank you, *Ayla*, for your endless love and support. It is you who makes me laugh about myself when I think the world is going to end once again. Without your company my life would not be as colorful, as joyful and not so full of surprises as it is. I feel you take me as I am and manage to drag me out of my cozy comfort zones at the same time. I am deeply grateful that we have been on this trip together and I am looking forward to the next one!